UNIVERSITY OF Southampton

**FACULTY OF ENGINEERING AND PHYSICAL SCIENCES**

Computational Engineering and Design group

# Fabrication and characterisation of novel functionally-graded lattice materials using additive manufacturing

by

**Loris Domenicale**

Thesis for the degree of Doctor of Philosophy

May 2020

**UNIVERSITY OF SOUTHAMPTON**

# ABSTRACT

FACULTY OF ENGINEERING AND PHYSICAL SCIENCES
Computational Engineering and Design group

Thesis for the degree of Doctor of Philosophy

**Fabrication and characterisation of novel functionally-graded lattice materials using additive manufacturing**

by Loris Domenicale

Porous and cellular materials are frequently found in nature as well as applications in biomedical, automotive, and aeronautical engineering. Their unusual properties are a direct consequence of their micro-structure. These materials have proven to be difficult to mimic synthetically. Additive manufacturing is a promising approach to fabricate this class of materials, as it provides great control over the lattice micro-architecture.

A fabrication technique is developed using fused deposition modelling with affordable 3D printers, to produce extrusion with continuously varying cross-sectional size. The novel approach proposed here achieves this by manipulating process parameters. Significant intended variation in the axial and bending stiffness of extrusion is achieved. An excellent agreement between the target diameter of the extruded filament and the diameter of the fabricated filaments confirms a reasonably linear response of the machine following simple incompressible flow of molten material. The adaptability of a fixed bore nozzle to produce variable diameter extrusion was characterised via three quantities $\alpha, \alpha_{\mathrm{S}}, \alpha_{\mathrm{B}}$ that respectively represent adaptable range in geometry, axial stiffness and bending stiffness of the extruded filaments. The ovality of the extruded filaments thus produced was quantified and was seen to have a significant impact on their bending stiffness.

Following successful fabrication of variable diameter extrusions, rectangular bi-layer lattice strips, with spatially varying bending stiffness, were fabricated. Their bending response is asymmetric about their length-wise centre. This asymmetric response was found to be consistent with a simple one-dimensional theory of post-buckled mode shape arising from a functionally graded beam. The response shows high curvature in parts of the structure with relatively softer struts compared to the stiffer regions, which is consistent with expectations. Finally, bi-layer square lattice films with spatially varying stiffness were fabricated. The bent surface of the planar structure shows strong spatial variations in bending response. This asymmetric response is well captured by the linear buckling mode shapes obtained from finite element analysis.

Encouraged by the success in fabrication and analysis, a host of mathematical problems including response of woodpile lattices when properties vary spatially were solved.

# Contents

**Declaration of Authorship**

**Acknowledgements**

**1 Introduction** **1**
1.1 Cellular Materials . . . 3
1.2 Functionally Graded Materials . . . 4
1.3 Additive manufacturing . . . 5
1.4 Tissue Engineering . . . 6
1.5 Aims and objectives . . . 7
1.6 Outline of the thesis . . . 8

**2 Literature Review** **11**
2.1 Cellular Solids . . . 11
2.1.1 Applications of cellular materials . . . 12
2.1.2 Fabrication of porous materials and scaffolds . . . 14
2.1.3 Mechanical properties of lattice structures and their characterisation 14
2.1.4 Bending-dominated and stretch-dominated structures . . . 17
2.1.5 Material-property space . . . 18
2.1.6 Metamaterials . . . 19
2.2 Functionally Graded Materials . . . 20
2.2.1 Applications . . . 21
2.2.2 Fabrication of functionally graded materials . . . 22
2.3 Additive manufacturing . . . 26
2.3.1 Material extrusion methods . . . 26
2.3.2 Powder bed fusion . . . 29
2.3.3 Vat photopolymerisation . . . 31
2.3.4 Bioprinting . . . 31
2.3.5 Other additive manufacturing techniques . . . 32
2.4 Fused deposition modelling 3D printing . . . 33
2.4.1 Parameters of FDM 3D printing . . . 34
2.4.2 Flow rate of material in FDM 3D printing . . . 35
2.4.3 Applications . . . 35
2.5 Tissue Engineering . . . 37
2.5.1 Biomedical scaffolds . . . 38
2.5.2 Pore size requirements for tissue engineering . . . 40
2.5.3 Stress shielding . . . 41

2.6 Manufacturing of functionally graded materials using 3D printing . . . . . 42
2.7 Current state of the biomedical applications of 3D printing . . . . . 43
2.7.1 Tissue and organ regeneration . . . . . 44
2.7.2 Orthopaedic implants . . . . . 45
2.7.3 3D printing for pharmaceutical applications . . . . . 45
2.8 Conclusions . . . . . 46

**3 Adaptable diameter extrusion using fixed bore FDM nozzles 47**
3.1 Methodology of fabrication and characterisation . . . . . 48
3.1.1 Fabrication of variable-diameter filaments . . . . . 48
3.1.2 Methodology to characterise the fabricated filaments using microscopic measurements . . . . . 50
3.1.3 Procedure for validation of under- & over-extrusion by weighing the samples . . . . . 51
3.2 Fabrication of variable-stiffness filaments by controlling process parameters 53
3.2.1 Controlling the fabrication of filament diameter by G-code . . . . . 54
3.3 Microscopic characterisation of the manufactured filaments . . . . . 58
3.3.1 Measured variability in diameter obtained with the 0.25 mm nozzle & linearity of the response . . . . . 59
3.3.2 Capability to control extruded diameter using the 0.4 mm nozzle . 62
3.3.3 Variable diameter extrusion using 0.6 mm nozzle . . . . . 64
3.3.4 Variable diameter extrusion using 0.8 mm nozzle . . . . . 66
3.3.5 Consolidated picture of the adaptable stiffness fabrication capability 68
3.4 Characterisation of average ellipticity of fabricated filaments . . . . . 69
3.4.1 Estimates of ellipticity from weight measurements . . . . . 70
3.4.2 Adaptable diameter extrusion using Ultimaker 3 extended FDM printer . . . . . 76
3.5 Fabrication of complex 3D parts with adaptable extrusion . . . . . 76
3.6 Conclusions . . . . . 79

**4 Analysis, manufacture, and characterisation of structures with spatially varying stiffness 81**
4.1 Spatially varying lattice spacing vs spatially varying strut stiffness . . . . 82
4.2 Mechanics of lattices with spatially varying stiffness . . . . . 84
4.2.1 Assessment of spatially varying stiffness from post-buckled bent shape of a structure . . . . . 85
4.3 Measured asymmetric profiles for lattice structures with axially varying stiffness . . . . . 88
4.3.1 Fabrications of bi-layer lattices with uni-axially varying bending stiffness . . . . . 89
4.3.2 Methodology for the laboratory tests . . . . . 90
4.3.3 Measurement of asymmetric out-of-plane response for variable stiffness bi-layer lattices . . . . . 91
4.4 Analytical response calculations for functionally graded lattice structures . 95
4.4.1 Apparent flexural properties of lattices made of variable diameter filaments . . . . . 95
4.4.2 Approximate flexural response of variable-diameter lattice beams using Rayleigh–Ritz method . . . . . 99

4.4.3 Analysis of woodpile lattice under compression . . . 103
4.5 Conclusions . . . 111

**5 Fabrication & characterisation of bi-directionally graded lattice films 113**
5.1 Fabrication of bi-directionally graded films . . . 115
5.1.1 Methodology . . . 115
5.1.2 Characterisation of the overlap between filaments of different layers 117
5.1.3 The geometry of spatial variation in two dimensions . . . 119
5.1.4 Challenges associated with fabrication . . . 123
5.2 Imaging of two-dimensionally-bent functionally-graded lattice films using Digital Image Correlation (DIC) . . . 125
5.2.1 Fundamentals of Digital Image Correlation (DIC) . . . 126
5.2.2 Materials and methods . . . 127
5.2.3 Results . . . 129
5.3 Computational response calculation of bi-directionally graded lattice structures . . . 134
5.3.1 Finite element modelling of the film with spatially varying stiffness in two dimensions . . . 134
5.3.2 Computational assessment of spatially varying stiffness using finite element analysis . . . 135
5.3.3 Computational results for spatially varying structure & comparisons with experimental measurements . . . 137
5.4 Conclusions . . . 139

**6 Conclusions and future work 141**
6.1 Conclusions . . . 141
6.2 Future work . . . 143

# List of Figures

1.1 The role of cellular architecture in the design of materials. With solid materials only the solid constituent can be changed to vary the properties of the material. Cellular materials, from random to ordered and location-specific, increase the degrees of freedom available during design (image from Schaedler and Carter [2016]) . . . . . 4
1.2 A schematics of the manufacturing process known as Fused Deposition Modelling 3D printing, adapted from Ahn et al. [2009]. The filament is pushed into the printing head, where a heater melts the polymer. The molted polymer is then deposited onto a platform through a nozzle. The printing head moves according to machine instructions generated by a slicing software. . . . . 6

2.1 On the left-hand side, different classes of architected materials are shown and are sorted based on their minimum size scale on the $x$-axis, and structural efficiency on the $y$-axis. The use of cellular materials started with foams and aerogels. Subsequent research and the development of new materials architectures, such as microlattices, improved the structural efficiency of this class of materials. On the left side of the image, the same concept is applied to buildings and structures. The efficiency of structures improved over time, due to the introductions of new materials and new architectures. Image from Schaedler and Carter [2016]. . . . . 13
2.2 (a) The structure of the octet-truss lattice material. The darkened struts represent a octahedral cell, while the nodes with labels form a tetrahedral cell. Adapted from Deshpande et al. [2001a]. . . . . 15
2.3 Material property space created using the CES Selector database website [Granta, 2012]. The plot shows for which combinations of Young's Modulus and Density a material is commercially available. White zones indicate that there is no material available with that combination of Young's modulus and density. . . . . 19
2.4 The re-entrant honeycomb auxetic structure, adapted from Yang et al. [2015]. (a) shows the two-dimensional representation of the design, (b) shows the 3D unit cell of the auxetic structure using this re-entrant honeycomb. . . . . 20
2.5 Scaffolds with different spacing and hence different porosity. µCT and SEM micrographs of scaffold with spacing of 1100 µm (a,d) and 500 µm (b,e). µCT and SEM micrographs of scaffold with a discrete gradation of spacing: four parts with spacing 1100 µm, 900 µm, 700 µm, 500 µm(c,f). Scale bar 2 mm. Image from Di Luca et al. [2016]. . . . . 23

2.6 Scaffold with a gradation in spacing between filaments and hence porosity. Scaffold 'Grad 1' has a spacing that varies linearly form 750 µm at the top and bottom of the scaffold to 100 µm at the centre. 'Grad 2' on the other hand has a porosity that goes from 100 µm at the top and bottom and 750 µm at the centre. 'Homog 1' and 'Homog 2' scaffolds have a constant spacing of 750 µm and 100 µm respectively. Image from Sobral et al. [2011]. 23
2.7 (a) shows the case when the concentric nozzles are all in the 'down' position, resulting in the smallest possible diameter of the nozzle (17). (b) shows the case of a different nozzle size. Here, nozzles number 14 and 15 have been moved to the 'up' position to make the nozzle (17) larger. By varying the height of the nozzle with respect to the buildplate (40), the diameter of the filament can be changed. Images from patent KR101725302B1 [Jin, 2016]. . . . . 25
2.8 Material in the form of a filament (2) is pushed by rollers (3) into a heated element (4) where the material is melted. The movement of the print head, allows the material to be deposited on the build plate (1) according to the commands received via software. In the case of overhangs, support material (5) may be needed. Image from Manufacturing Guide Sweden AB. 28
2.9 Powdered material (1) is spread using a roller (3). A pulsating laser (4) scans the powder according to commands from software and sinters a thin layer of the powder. The build plate (2) then moves down and the process is repeated until the part is complete. Image from Manufacturing Guide Sweden AB. . . . . 30
2.10 The build plate (2) starts from the bottom of the vat of photosensitive resin (1) and raises after every layer is formed. Each layer is formed by means of a light source (3) that hardens the resin to form each layer. Image from Manufacturing Guide Sweden AB. . . . . 32
2.11 3D Bioprinting of tissue and organs. Bioinks are created by combining cultured cells and various biocompatable materials. Bioinks can then be 3D bioprinted into functional tissue constructs for drug screening, disease modeling, and in vitro transplantation. From Sigma-Aldrich. . . . . 33
2.12 (a) Design of the BioPen, which shows the two separate chambers with a motor control. The two chambers are connected to the printing nozzle (insert), which allows the coaxial printing of the two different bioinks in a core/shell distribution. (b) Photograph of the biopen. (c) Representation of the core/shell distribution. (d) Representation of the multiple layer three-dimensional printed block in a criss-cross pattern . Adapted from Bella et al. [2018]. . . . . 39
2.13 Ear scaffold. Designed model on the left and 3D printed part on the right (PCL material, manufactured using a KIMM 3D printer). Different sections have been printed with different parameters, to match the desired mechanical properties. Scale bar 2 mm. From Shahangi [2018]. . . . . 40

3.1 The table shows two shapes that could be used as assumptions for the cross sections. On the left, the elliptical cross section, the one chosen in this work; on the right, the stadium shape, a possible alternative. The idea is to use the microscope measurements as $d_M$, and obtain the second parameter ($d_m$ or $h$, in these examples) making use of the mass $m$ of the sample and the length of extruded filament $L$. . . . . 53

3.2 An extract of G-code to show the main commands: $G10$ to stop extruding material, $G0$ to move the printing-head without extruding, $G11$ to start extruding, $G1$ to move the printing-head while extruding material, $M109$ to change the extrusion temperature, $M106$ to change the speed of the cooling fan. . . . . 54
3.3 A schematic diagram of the extrusion process during over-extrusion: the diameter of the extruded filament, $d$, is greater than the nominal diameter of the nozzle $d_{\text{nozzle}}$, because of the change to the $E$ value. . . . . 57
3.4 The sample used to measure the diameter of the filaments. Twenty of these samples were printed, each with a different value for the process parameter $d_{\text{intended}}$. The filaments running in the direction of the long side are the ones that have been measured. . . . . 59
3.5 The measured diameter of extruded filaments as a function of the process parameter $d_{\text{intended}}$, for the nozzle of diameter 0.25 mm. The measurements obtained from the microscope images are shown as dots and error bars, where the dot represents the mean value for the five measurements taken on the sample, and the error bars represent the standard deviation of these. The pink line shows the ideal scenario where $d = d_{\text{intended}}$, and the solid line is the best fit for the measurements. . . . . 60
3.6 The measured diameter of extruded filaments as a function of the process parameter $d_{\text{intended}}$, for the nozzle of diameter 0.4 mm. The measurements obtained from the microscope images are shown as dots and error bars, where the dot represents the mean value for the five measurements taken on the sample, and the error bars represent the standard deviation of these. The pink line shows the ideal scenario where $d = d_{\text{intended}}$, and the solid line is the best fit for the measurements. . . . . 63
3.7 The measured diameter of extruded filaments as a function of the process parameter $d_{\text{intended}}$, for the nozzle of diameter 0.6 mm. The measurements obtained from the microscope images are shown as dots and error bars, where the dot represents the mean value for the five measurements taken on the sample, and the error bars represent the standard deviation of these. The pink line shows the ideal scenario where $d = d_{\text{intended}}$, and the solid line is the best fit for the measurements. . . . . 64
3.8 The measured diameter of extruded filaments as a function of the process parameter $d_{\text{intended}}$, for the nozzle of diameter 0.8 mm. The measurements obtained from the microscope images are shown as dots and error bars, where the dot represents the mean value for the five measurements taken on the sample, and the error bars represent the standard deviation of these. The pink line shows the ideal scenario where $d = d_{\text{intended}}$, and the solid line is the best fit for the measurements. The last two points on the right are excluded for the calculation of the best fit: no change in diameter is seen when increasing the parameter, a sign that the maximum amount of material that can be extruded has been reached. . . . . 65
3.9 Wave-like filament: the first vertical filament of the left. It was obtained trying to push a large amount of material through the nozzle. No change in cross section is achieved, only an increased length, leading to a wavy filament. . . . . 66

3.10 Summary of measurements for all four nozzles. Each colour represents a different nozzle diameter. Each dot represents the mean value over the five measurements and the error bar their standard deviation. The pink line represents the expected values, that is $d = d_{\text{intended}}$. The points that are considered outliers are marked with a cross. . . . . 69
3.11 Qualitative representation of the cross-section of the manufactured filament. The dashed circle is the expected circular cross-sectional shape, the solid ellipse is the shape deduced combining microscope and scale measurements. If the distance between the nozzle and the build-plate is kept constant ($z_{\text{inc}}$), printing a larger filament would result in a more severe squashing of the filament, hence a filament with an elliptical cross-section. 70
3.12 Summary of measurements for the 0.4 mm nozzle. Major diameters from the microscope (dots and error bars), expected trend (pink line), diameter from mass of sample assuming circular cross-section (diamond markers), minor diameter assuming elliptical cross-section (plus markers). . . . . 71
3.13 Summary of measurements for the 0.6 mm nozzle. Diameters from microscope images (dots and error bars), expected trend (pink line), diameter from mass of samples assuming circular cross-section (diamond markers), minor axis assuming elliptical cross-section (plus markers). . . . . 73
3.14 Comparison of the diameter obtained from the microscope measurements (dots and error bars), and the diameter obtained from the weight of the sample (diamonds), for both the 0.4 mm and the 0.6 mm nozzle. . . . . 74
3.15 (a) shows the values of $\alpha_{\text{S,elliptical}}$ and $\alpha_{\text{B,elliptical}}$ obtained for the 0.4 mm nozzle. (b) shows the values of $\alpha_{\text{S,elliptical}}$ and $\alpha_{\text{B,elliptical}}$ obtained for the 0.6 mm nozzle. . . . . 75
3.16 Calibration of the Ultimaker 3 Extended 3D printer. The red squares represent the mean values obtained for the diameter, calculated from the mass of the three samples manufactured using the same corresponding $d_{\text{intended}}$. The solid red line represents the best linear fit for the data. . . . 77
3.17 On the left, a standard cube made with Solidworks, sliced using Cura and printed with nozzle 0.4 mm. On the right, the same cube as on the left, but its G-code has been manipulated so that the top half is printed with a thicker filament, 0.6 mm. . . . . 78

4.1 A close-up view of a lattice structure that we have manufactured. The four layers of this structure are clearly visible. The large spacing between filaments allows to better appreciate the internal architecture. . . . . 82
4.2 (a) - Apparent shear of the lattice (left) due to bending of the filaments (right); (b) - Bending of the lattice (left) due to tension/compression of the filaments (right). . . . . 84
4.3 (a) Top view of a sample where the filaments running vertically are equally spaced. (b) Top view of a sample where the filaments running vertically are linearly spaced. The response obtained when bending these films along the long filaments (i.e. in the $x - z$ plane) is the same, as the position of the vertically-running filaments does not affect the bending stiffness of the long, horizontal filaments. . . . . 85
4.4 A plot of the buckled shapes, equation 4.18, with different values for $b$ ($b = -0.001$, $b = -0.05$, $b = -0.1$). This shows that, when $b$ approaches zero, the minimum is closer to the line through the midpoint, dashed line. This indicated that the asymmetry decreases, as expected. . . . . 89

4.5 The coarse sample used in the buckling tests has two layers, the one in the $x$ direction is graded. The spacing between filaments is large (compared to the other sample). . . . . 91
4.6 The fine sample used in the buckling tests has two layers, the one in the $x$ direction is graded. The spacing between the filaments is smaller. . . . . 91
4.7 Step 0: test set up. The sample is compressed until it buckles. The picture is taken from the front to study the profile. . . . . 92
4.8 Step 1: calibration of the coordinate system selecting four points on the image and assigning their distance (based on the rulers). . . . . 92
4.9 Step 2: sampling. Clicking on the image, points are created with respect to the coordinate system of the previous step. . . . . 92
4.10 Step 3: data acquisition. Once the points have been selected, their coordinates are exported for post-processing. . . . . 92
4.11 Comparison between the mathematical model (solid line) and the laboratory results for two coarse samples of type 1. The dashed line marks the midpoint of the sample. The average mean square error of these two films is MSE = 0.00129. . . . . 93
4.12 Comparison between the mathematical model (solid line) and the laboratory results for two fine samples of type 1. The dashed line marks the midpoint of the sample. The average mean square error of these two films is MSE = 0.00335. . . . . 93
4.13 Comparison between the mathematical model (solid line) and the laboratory results for two coarse samples of type 2. The dashed line marks the midpoint of the sample. The average mean square error of these two films is MSE = 0.000604. . . . . 93
4.14 Comparison between the mathematical model (solid line) and the laboratory results for a coarse sample (MSE = 0.00262) and a fine sample (MSE = 0.000978) of type 1, in case of large displacement. The dashed line marks the midpoint of the sample. . . . . 94
4.15 Comparison between the mathematical model (solid line) and the laboratory results for a coarse sample of type 2, in case of large displacement. The dashed line marks the midpoint of the sample. The mean square error is MSE = 0.00113. . . . . 94
4.16 A cell of the lattice. The participating filaments, those running in the $x$-direction, show a continuous variation in their diameter; the filaments running in the $y$ direction, which do not participate in bending, are of a diameter that ensures constant dimensions of the cell. The quantity $dx$ is the distance, in the $x$-direction, between the centres of non-participating filaments; $dy$ is the distance, in the $y$ direction, between the centres of participating filaments; $dz$ is the vertical distance between the centres of participating filaments and is also called layer height. . . . . 97
4.17 Cross-section of a lattice structure. $N_y$ is the number of blue circles in the $y$-direction (5, in this example); $N_z$ is the number of blue circles in the z-direction (3, in this example). Transverse filaments, in grey, are not contributing to the bending stiffness. . . . . 98

4.18 (a): end view of a stack of filaments in case of an odd number of participating layers. (b): end view of a stack of filaments in case of an even number of participating layers. Transverse filaments are shown in grey, participating filaments in blue, and the participating filament whose cross section lies on the neutral axis in red. . . . . 98
4.19 A simply supported beam is loaded with two moments $M$ at the two ends. The coordinate $x$ goes form 0 at the left support to $L$ at the right support. We are interested in the transverse displacement $w(x)$. . . . . 100
4.20 In solid black, the transverse displacement of a lattice structure with $N_y = 10$, $N_z = 3$ and $L = 125\,\text{mm}$ plotted using the solution obtained following the Rayleigh–Ritz method. The diameter of the filaments running parallel to the $x$-axis varies from 0.3 mm to 0.8 mm and the moments applied are $M = 0.5\,\text{N m}$. The red solid line has been obtained setting $N_z = 4$, while keeping the other parameters the same, and is then stiffer because of the extra layer along the $z$-axis. . . . . 103
4.21 Front view of a portion of an infinite lattice under compression. Each transverse layer is shifted with respect to the previous one. . . . . 104
4.22 We consider a Timoshenko beam with periodic boundary conditions to mimic an infinite lattice. A force $F$ is applied at a distance $a$ from the left support and at a distance $b$ from the right support. The shaded area is the portion of the beam that is modelled. . . . . 105
4.23 Case of a beam under bending where shear is negligible. The profile of the beam is in solid blue, the rotation of the cross-sections due to bending is in solid orange and the rotation due to shear only is in dashed orange. We can see how the bending due to shear is negligible compared to the rotation of the cross section. . . . . 108
4.24 Case of a beam under bending where the shear is *not* negligible. The profile of the beam is in solid blue, the rotation of the cross-sections due to bending is in solid orange and the rotation due to shear only is in dashed orange. In this case, the rotation due to shear is an important component of the rotation of the cross section. . . . . 109
4.25 Plot of $U_{\text{SH,rel}}$, the ratio of energy due to shear to the energy due to pure bending (left side of inequality 4.70) as the yellow-blue surface. The red surface represents the case $U_{\text{SH,rel}} = 0.1$. The part of the blue surface below the red plane represents the case where $U_{\text{SH,rel}} < 0.1$ (i.e. the energy due to shear is less than 10% of the energy due to pure bending). The green line in the plot represents the range of values of $a$ for which $U_{\text{SH,rel}} < 0.1$, when $r = 0.2\,\text{mm}$. The blue line represents the range of values of $a$ for which $U_{\text{SH,rel}} < 0.1$, when $r = 0.5\,\text{mm}$. The black line represents the range of $r$ that gives $U_{\text{SH,rel}} < 0.1$ when $a = 5\,\text{mm}$ (force is applied at the centre of the beam). The dots represent the extremes of the interval of the same color (where $U_{\text{SH,rel}} = 0.1$). . . . . 111

5.1 On the left, a standard cube made with Solidworks, sliced using Cura and 3D printed with using a nozzle of size 0.4 mm. On the right, a cube obtained with a manipulated version of the G-code. It has been manipulated so that the top half of the cube is printed with a thicker filament, 0.6 mm. 114
5.2 The 2-layer film of interest lies on two larger base layers. This allows the film to be made of two layers with comparable diameters, as the layer printed directly on the print-bed is thinner than the rest of the layers. . . 117

5.3 SEM images of the front view of a lattice, in the case of a large overlap between filaments of subsequent layers, (a), and in the case of small overlap, (b). Case (a) is achieved by setting the value for the layer height about 20% smaller than the value for the filament diameter, while case (b) is achieved by setting the value for the layer height close to the value for the filament diameter. . . . 118
5.4 The four corners are referred to with a pair of letters depending on the thickness of the two layers of the film at that corner. 'T' is used for thick filaments and 't' for thin filaments, hence we have: tt-corner, TT-corner, tT-corner and Tt-corner. The two diagonals are referred to based on the corners that they connect, hence we have a tt-TT diagonal and a tT-Tt diagonal. . . . 119
5.5 Top view of the four corners of the film, at a scale of 10:1 with respect to the film represented in the centre of the image. One layer, along $y$, is shown in grey, while the second layer, along $x$, in blue. Detail A shows the top view of the corner where both layers are made of thin filaments, 0.4 mm in diameter, referred to as tt. Detail B and C show the corners at which one of the layers is 0.4 mm and the other is 0.7 mm, referred to as tT and Tt. Detail D shows the top view of the corner where both layers are made of thick filaments, 0.7 mm in diameter, referred to as TT. . . . 120
5.6 Unit cells of the film graded in two dimensions. The assumption is that, within a cell, the diameter of the filaments can be considered constant. $d_1$ is the diameter of the filaments in the first layer, $d_2$ is the diameter of the filaments in the second layer. The overlap between the two layers, $o$, is 8% of $d_2$, and the spacing between filaments is indicated with $s$. The porosity $\rho$ is the ratio of the void volume to the volume of the cell, as per equation 5.1. . . . 122
5.7 Design pore size variation within the film. At coordinate $(0, 0)$ is the TT corner, while at coordinate $(100, 100)$ is the tt corner. The porosity varies from 0.54 to 0.74. The black lines connect unit cells with the same local porosity, whose value is shown. . . . 123
5.8 Cylindrical deformation due to one of the two layers being stiffer that the other. The first layer that is printed on the print-bed is made of thinner filaments, which are the ones to deform, leaving the filaments in the other direction to remain almost undeformed. . . . 124
5.9 Set-up of the buckling experiment. The film is mounted on the fixtures with the diagonal along the loading axis. . . . 129
5.10 The customised fixture uses a round flat plate with a ridge, over which masking tape was added to prevent the rotation of the sample during testing. 129
5.11 Overlayed deformation of film with an asymmetric response. Image obtained from the software DaVis. . . . 130
5.12 (a) Surface plot of the deformation in Figure 5.11. (b) Side view of the deformed film. The asymmetry of the deformed shape is visible, with respect to position $x = 0$. . . . 130
5.13 The non-normalised stages considered for Sample 2, along the diagonal with symmetric behaviour. . . . 132
5.14 The normalised stages considered for Sample 2, along the diagonal with symmetric behaviour. . . . 133

5.15 The non-normalised stages considered for Sample 2, along the diagonal with asymmetric behaviour. . . . . 133
5.16 The normalised stages considered for Sample 2, along the diagonal with asymmetric behaviour. . . . . 134
5.17 The image shows the full lattice and its axis for reference. The $x-y$ plane represents the plane of the film, while the $z$ direction, parallel to segments $a$ and $b$, is the direction out of plane. Along segment $a$, displacement along $x$ is blocked, while at point $A$ displacement is blocked along $x$ and $z$. The point force is applied at point $A$, in the $y$ direction. Along segment $b$, displacement along $x$ is blocked, while at point $B$ displacement is blocked along all directions, $x$, $y$ and $z$. . . . . 135
5.18 The image shows the mesh used for the simulation, as well as an example of the results obtained from Abaqus. . . . . 136
5.19 The last stage of deformation along the diagonal with non-graded properties, tT-Tt, is shown in solid black. The FE analysis results are reported with black dots. Both are normalised in length and in amplitude for ease of comparison. . . . . 138
5.20 The last stage of deformation along the diagonal with graded properties, tt-TT, is shown in solid black. The FE analysis results are reported with black dots. Both are normalised in length and in amplitude for ease of comparison. . . . . 138

# List of Tables

2.1 Summary of additive manufacturing methods [Ngo et al., 2018, Wang et al., 2017]. . . . . 27

3.1 This table shows, for each nozzle size, the range of intended diameter that has been used and the obtained range of diameter for the extruded filament. 59

3.2 Summary of the capability of adaptive extrusion that can be achieved for each nozzle diameter. The second column shows the gain in the diameter of the fabricated filaments, the third column the gain in the axial stiffness in case of circular cross section, the fourth column shows the gain in bending stiffness assuming circular cross section. The last two columns are an estimate from figure 3.15, and they show the gain in axial and bending stiffness taking into account the ellipticity of the cross section. . . . . 75

5.1 Manufacturing parameters used to manufacture the film (third and fourth layers) and the sacrificial base (layers one and two). The difference in the parameters in each layer is dictated by the need to ensure proper adhesion between layer 1 and 2, reduced adhesion between layer 2 and 3, and proper adhesion between layer 3 and 4. This facilitates the detaching of the base from the film after manufacturing and avoids damaging the film. . . . . 116

## Declaration of Authorship

I, Loris Domenicale, declare that the thesis entitled *Fabrication and characterisation of novel functionally-graded lattice materials using additive manufacturing* and the work presented in the thesis are my own, and have been generated by me as the result of my own original research.

I confirm that:

- this work was done wholly or mainly while in candidature for a research degree at this University;
- where I have consulted the published work of others, this is always clearly attributed; the exception of such quotations, this thesis is entirely my own work;
- I have acknowledged all main sources of help;
- none of this work has been published before submission.

Signed:.....

Date:.....

# Acknowledgements

I would like to offer my deep gratitude to my academic supervisor *Prof. Atul Bhaskar* for the quality and the scientific content of every meeting. I highly appreciate his constant dedication and tireless support while helping me in the transformation from mathematician to engineer. His insightful comments and constructive criticism are of utmost importance for my growth as a PhD student. These made me a better researcher, a better mathematician, a better engineer and a better writer. His contagious passion and attention to detail enabled me to output work of much higher quality, while appreciating the beauty of being thorough and meticulous. I also want to thank my industrial supervisor *Dr. Christopher Lovell* who helped me in the months spent in Lucideon, the industrial partner. I am grateful for the support on two fronts, first for the constructive and inspiring scientific discussions, second, for his efforts to ensure I had access to all I needed while away from University. I also want to thank everyone in Lucideon as I have been welcomed and treated as part of the team from day one. The work presented in this thesis was carried out as part of the HyMedPoly research project, with funding from the European Union's Horizon 2020 research and innovation programme under the Marie Skłodowska-Curie grant agreement No 643050. My thanks are extended to all the members of the HyMedPoly project for the inspiring discussions.

I am grateful to *Dr. Andrew Robinson* for his training, supervision and help in carrying out the experiments in the Testing and Structures Research Laboratory of the University. His expertise helped achieving high-quality results. I would like to express my great appreciation to *Dr. Andrew Hamilton* for giving me access to the Design Workshop of the University. I would also like to thank *Dr. Alessandra Bonfanti* for her active involvement and help, especially during the early stages of my research. I would also like to thank *Ms. Faezeh Shalchy* for being always available for thought-provoking discussions, tips, and help in using a commercial FE code.

My sincere gratitude, admiration and respect go to my parents, *Lorena* and *Giuseppe*, for their unceasing encouragement and for always believing in me. Such supportive and encouraging parents are a gift, for which I am forever grateful. Their attention and care, even from a distance, have always been what keeps me motivated most. None of this would have been possible without their life-long efforts and sacrifices they made for me, *thank you*. I would like to extend a special thank you to my grandfather *Giuseppe*. Unfortunately, I could not rely on his physical presence during this experience, but I would not be who I am today without his boundless love, support, and encouragement during our time together. His contributions to my life will be felt forever. I would also like to offer my special thanks to my girlfriend *Martina* for her support and encouragement throughout. I am particularly grateful to her for her decision to move to the UK after her graduation. Her presence and care were sometimes all I needed to keep going.

# Chapter 1

# Introduction

Porous materials and structures with voids in their microstructure have been used for a very long time in many applications. Lattice structures and porous materials have attracted the attention of engineers and scientists in many sectors of industry such as automotive, aerospace, chemical & catalytic, biomedical, and acoustics. There is a growing interest in improving the manufacturing processes used to build these structures and in understanding their mechanical properties thoroughly. Many manufacturing methods such as foaming have been used to produce lightweight materials and structures that possess random porosity. Additive manufacturing (AM), also known as 3D printing, by contrast, is a promising alternative in that it offers computer control of the porosity and its detailed mesoscopic architecture. The present thesis is motivated by the need to fabricate and characterise this class of materials and structures.

Structured materials with lattice architecture are relatively easily produced using additive manufacturing. However, the use of additive manufacturing for the production of these structures, especially in the biomedical sector, is still limited. Materials capable of 3D printing are limited. Additive manufacturing also has limitations concerning resolution as well as speed of mass manufacture. These are compensated by the quick turn-around times between design and fabrication of a prototype while using 3D printing, one reason why this manufacturing approach is also known as rapid prototyping. Additionally, the ability to fabricate structures with complex external and internal shapes makes the process extremely attractive for future developments. In the biomedical engineering field, the scope of personalising implants and bio-structures is great, leading to advances in personalised medicine in the context of prosthetics and tissue engineering.

A growing sector of industry that has shown great promise both in cellular material and 3D printing is that of biomedical engineering. This new field brings together the classical engineering knowledge with biology and medicine. Engineering alone would not be able to provide patient-ready solutions without adopting this multidisciplinary approach, which is key to unlock new technologies and advance in the quality of patient

care. There is huge interest to harness knowledge in the areas of mechanics, materials, manufacturing and cell biology, and combine them to develop novel biomedical devices. As an example, bone and cartilage scaffolds find many applications in tissue engineering, where they are used as tissue supports for regeneration. Considerations to biological aspects are essential to ensure the correct functionality and safety, while engineering research is required to ensure mechanical function. Porosity plays an important role in the biological function of tissue engineering scaffolds. Once the scaffold is implanted, porosity provides support to the cells and guides them during proliferation. Porosity also plays an important role at this stage in providing the micro-environment for osteoconduction, osteoinduction and nutrient transport as well as that of metabolic waste. The size and distribution of pores are crucial parameters to optimise this micro-environment. In addition to these biological aspects, mechanics of such structures plays an important role in ensuring the mechanical performance in terms of stiffness and strength. In addition to bio-structures, lattice materials are also being considered promising candidates for lightweight structures, acoustic metamaterials, core of sandwich constructions, thermal insulation, and substitutes to a host of applications that make use of foams.

Mechanical properties of lattice structures must be quantitatively understood to be able to make use of these materials in engineering design. Learning how to control the internal architecture of such materials, and hence their properties, would vastly extend the applicability of 3D printing. This is especially true when applied to the most economical and accessible of 3D printing methods, which is fused deposition modelling (FDM). Although there are other additive manufacturing techniques that can achieve stronger, more accurate and more precise parts, FDM has a great potential due to the low cost of the capital and the consumables. Research into establishing structure-function relationships is key in the understanding of their properties and tailoring the internal architecture optimally. Further, the automation that 3D printing is associated with ensures minimal retraining of staff over a range of machines, since they are all driven by nearly device-independent computer codes.

One way of tailoring the mechanical behaviour of lattice structures is to fabricate them with local properties that vary spatially. Common manufacturing processes can manufacture bulk functionally graded materials (FGM), such as centrifugal casting, or are used to coat surfaces, such as chemical vapor deposition (CVD) [Sarathchandra et al., 2018]. Biological tissues adapt to the mechanical and biological requirements of their location and function. Artificial scaffolds and biomedical devices could be improved and optimised by taking into account these function-specific and location-specific requirements, by manufacturing them to mimic the natural tissue. Introducing a functional gradation in a structure introduces several challenges in its design and fabrication that are hard to overcome using conventional non-AM methods. The present work addresses both fundamental and practical challenges, and the understanding of how functional gradation

affects the mechanical behaviour. It also opens the possibility to use a cheaper and simpler method of production, FDM 3D printing, for the production of functionally graded materials (FGMs). The present work is motivated by the need to develop a technique to introduce spatial gradation of stiffness by using any off-the-shelf FDM 3D printer.

With the above considerations, we can see how cellular materials, as a class of materials, possess interesting properties. The concept of functional gradation is present in many natural materials. The lack of a consistent and effective method of production for functionally graded porous materials makes it difficult to use them for industrial and medical applications. The field of tissue engineering, for instance, could substantially benefit from a larger availability of this kind of materials. This work provides a possible approach of producing such materials, using the cheap FDM process.

## 1.1 Cellular Materials

The word *cell* derives from *cella*, a Latin word meaning *enclosed compartment* or *bounded volume*. A material is referred to as *cellular* when it contains a large number of cells that are characterised by structures at a mesoscopic scale, dispersed throughout its mass. Here, by *cells* or *unit cells* we mean an internal architectural unit. For a material such as wood, the structural cell and the biological cell are the same. The interest is in an assembly of cells with solid edges or faces, grouped together so that they fill space [Gibson and Ashby, 1997]. The cells can be randomly dispersed, in which case the material can be called *foam* or *aerogel*, depending on the dimension of the pores, or regularly dispersed, with the materials called *periodic cellular materials* or *lattice materials* [Schaedler and Carter, 2016].

Cellular materials have been used for centuries, starting with natural materials, such as cork, back in Roman times (Horace, 27 BC), and continuing with structured materials engineered today. The main reason why cellular materials are of interest lies in their unique properties, which is a consequence of their internal architecture. For synthetic cellular materials, it is possible to *design* the internal architecture as well as the external shape, in order to tune and optimise the elastic response. This structural hierarchy can play a major role in tailoring the bulk material properties [Lakes, 1993]. Cellular materials with regularly dispersed cells, in particular, are easily fabricated by means of additive manufacturing.

The process of designing a lattice structure for production using this technique is not limited to the choice of the constituent material, rather, parameters of its mesoscopic architecture—pore size, filament diameter, filament orientation—can be used to achieve the material design objectives [Valdevit et al., 2011]. The presence of pores, coupled with the possibility to enhance and tune performance, are the main features that allow to manufacture a material that can exhibit low density and high stiffness and strength.

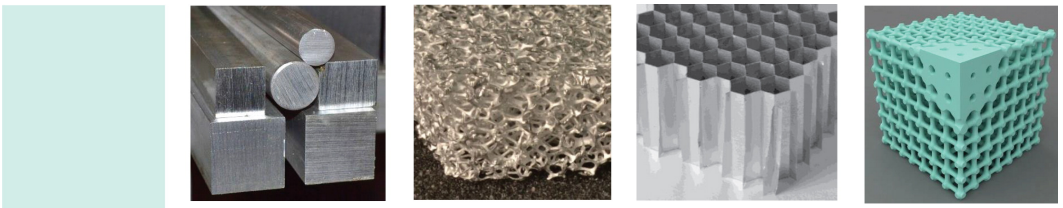

| | | | | |
|---|---|---|---|---|
| **Cellular architecture** | None | Random | Ordered | Ordered and location specific |
| **Properties** | Continuous and homogeneous | Homogeneous at scales > cell | Homogeneous and highly anisotropic | Inhomogeneous and highly anisotropic |
| **Design degrees of freedom** | Solid constituent | Solid constituent, cell size | Solid constituent, cell size, and orientation | Cell size/shape, node topology, ligament shape, material... |

Schaedler TA, Carter WB. 2016.
Annu. Rev. Mater. Res. 46:187–210

Figure 1.1: The role of cellular architecture in the design of materials. With solid materials only the solid constituent can be changed to vary the properties of the material. Cellular materials, from random to ordered and location-specific, increase the degrees of freedom available during design (image from Schaedler and Carter [2016])

There is an ever increasing interest in making use of these materials [CMI Inc., 2019, CellMat, 2015]. A lightweight structure with superior structural performance is needed in many applications, such as in the automotive, aerospace and medical sectors. These are some of the reasons why research in the area of synthetic cellular materials is currently very active. The current production methods of porous structures and scaffolds, however, focus mostly on foams and aerogels. As stated before, these materials are characterised by a random distribution of pores throughout their volume. The dimension of these pores can be controlled approximately and statistically within specific ranges, but precise control is impossible. In figure 1.1, different kinds of architectured materials can be seen. Materials with random cellular architectures are characterised by an extra degree of freedom with respect to solid materials, the cell size. Ordered cellular materials add one more degree of freedom in their internal design, the orientation of the internal structure. In the last column of figure 1.1, we can see another type of cellular architecture that gives even more design freedom: a material with ordered and *location specific* architecture, which we will introduce in the next section.

## 1.2 Functionally Graded Materials

Functionally graded materials, or FGMs, are innovative materials characterised by properties that vary spatially (see last column in Figure 1.1). Often the variation of properties is realised by a spatial variation in the chemical or material composition. Here we are

interested in materials with spatially varying mechanical properties achieved by structuring their internal architecture, rather than by chemical composition. This spatial gradation in the structure allows the *apparent* mechanical properties to also vary from point to point. Tailoring the architecture, the properties of the material can be varied to match location-specific requirements dictated by the specific application or purpose for that part. Thus this class of materials can be called designer material.

Bone is a natural material that shows a graded porosity. This suggests that a functionally graded architecture in a synthetic material would mimic properties more closely. This is considered beneficial, because minimising the differences between the properties of the bone and that of the surrounding material, in case of bone grafts for instance, could reduce the shear stress between the two, an important aspect that will be discussed in Section 2.5.3, known as stress shielding. Functionally graded materials are also very useful for weight reduction in aerospace and automotive sectors. The density of a load-bearing structure can be varied by adjusting pore dimensions to optimise the balance between weight and mechanical properties. This reduces mass and saves material. Without the use of functional gradation, the properties of the whole structure would have to match those needed in the point of highest local load [Schaedler and Carter, 2016], resulting in excess material being used where not necessary.

The methods of production of porous materials, structures and scaffolds can be broadly divided into conventional subtractive methods [Leong et al., 2008] and modern additive techniques. The conventional techniques lack precise control over the microstructure, when the pores need to be much smaller than the bulk dimensions of a structure, and are best suited for random architectures. Also, it is difficult to obtain a regular pattern using these methods. This is something that additive manufacturing techniques can easily overcome.

## 1.3 Additive manufacturing

Additive manufacturing, also known as 3D printing, widely varies in the manufacturing methods, depending on the materials used, the power source, and the characteristics of the final structures. This class of manufacturing methods is characterised by a repetitive addition of material, usually layer-wise, until the final product is complete. Manufacturing methods in this category will be discussed in the next chapter, and the need for an affordable manufacturing process for structured cellular materials will be brought out. Among those methods, FDM stands out due to its affordability and ease of use.

Fused Deposition Modelling (FDM), also known as Fused Filament Fabrication (FFF), is now one of the cheapest and most widely used methods for 3D printing. In this manufacturing process, a representation of which can be seen in Figure 1.2, each layer is produced by the deposition of melt extruded filaments. A spool of thermoplastic polymer

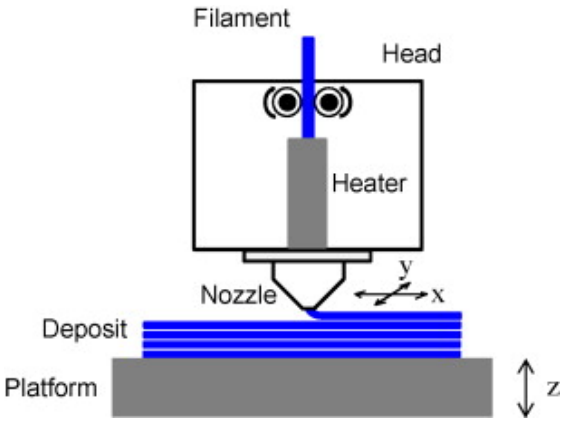


Figure 1.2: A schematics of the manufacturing process known as Fused Deposition Modelling 3D printing, adapted from Ahn et al. [2009]. The filament is pushed into the printing head, where a heater melts the polymer. The molted polymer is then deposited onto a platform through a nozzle. The printing head moves according to machine instructions generated by a slicing software.

is fed into the printer to supply material to the printing-head (or extrusion-head). The polymers most frequently used for this are polylactic acid (PLA), acrylonitrile butadiene styrene (ABS), polycarbonate (PC) and nylon. The polymer is heated above its melting temperature, extruded through a nozzle and deposited following a series of commands, known as G-code (see Section 3.2). We will see why this technique is well suited for the fabrication of graded architectures, despite a few limitations.

Currently, only some of the more advanced and sophisticated AM techniques are used in industry, beyond research stage, for the production of cellular materials. FDM was traditionally considered more of a prototyping technique rather than a technique capable of manufacturing final parts. However, this is changing fast. FDM has the potential to be used in many sectors due to its ease of use and affordability. Recently, the use of FDM printers has increased significantly in the medical sector, where the adaptability and the ability to customise the parts are the main selling points.

## 1.4 Tissue Engineering

Due to trauma or ageing, tissues and organs are frequently repaired or replaced by artificial organs, bio-structures, prosthetics, and implants. This procedure is likely to gain further importance in the future—the associated technology is known as Tissue Engineering (TE). One of its most promising solutions is to grow cells on a biodegradable scaffold—for example, made with additive manufacturing techniques—which is then implanted in the damaged area to provide support to the cells and guide them during cell adhesion, proliferation and growth. Once the new and healthy tissue is formed, the scaffold finally degrades. A simpler example of the use of additive manufacturing is the work

of e-NABLE, an online community of volunteers who use their 3D printers to make free and low-cost prosthetic limb devices for children and adults in need, making use of the open-source designs created by the same volunteers [e-NABLE, 2020].

The properties of human tissues depend on their function and often show gradients spatially to match specific needs. An example of this can be found in bone tissue engineering. The same tissue in different locations has different properties due to the mechanical and biological requirements in that particular region. To increase the chances of success of a bone implant, it must fulfil the local structural and biological requirements of the target tissue, hence, it should mimic the graded architecture [Leong et al., 2008]. This may also affect how cells respond, grow, proliferate or differentiate. Another fundamental aspect is porosity. A porous structure provides an ideal microenvironment for osteoconduction, osteoinduction and for the transportation of nutrients and metabolic waste [Hutmacher, 2000a], facilitating osteogenesis. An example of this can be the work by Shahangi [2018], where an auricular structure has been printed in six sections, each with different properties to mimic the real properties of the replaced cartilage.

## 1.5 Aims and objectives

The present work aims to design and fabricate novel structures in which porosity and mechanical properties can be tailored in response to the demands of the application at hand. The focus is to use Fused Deposition Modelling as the manufacturing process, to achieve novel ways to tailor the stiffness in 3D printed parts. The aim is also to characterise and model the mechanical properties of such structures, in order to optimise their mechanical performance. Here we focus on the relationships between the mechanical response and the internal architecture of structured material. In particular, fabrication of lattice structures with spatially varying stiffness and its theoretical and experimental characterisation is addressed. This will enable engineers to design and manufacture the internal architecture of a structure as well as its external shape according to the desired application and required mechanical properties. This work also aims to carry out innovative research in the area of FDM 3D printing addressing a wide range of applications; especially in biomedical engineering. An innovative technique to produce functionally graded lattices using FDM machines will be presented. Additionally, models of the mechanical behaviour of these novel structures have been developed to enhance the understanding of structure–property relationships.

To explore the possibility of creating structures with variable stiffness, we pursue the following specific objectives:

- To develop a technique that can extend the capability of FDM 3D printing to obtain filaments with variable stiffness extruded from a fixed diameter of FDM nozzle;

- To characterise the variation in filament diameter and be able to relate it to the manufacturing parameters;
- To extend the technique developed to obtain filaments with a stiffness that varies continuously throughout the length;
- To apply the technique to obtain structures with filaments of variable stiffness in one and two dimensions;
- To test the manufactured films to verify the effectiveness of the technique;
- To develop mathematical models or perform finite element analysis, whose results can be compared to the results obtained experimentally.

These intermediate steps would ensure that the technique developed is capable of manufacturing structures with graded properties, as well as that the graded properties obtained can be predicted using simple models or finite element analysis.

## 1.6 Outline of the thesis

- The main concepts and the context of this work are presented here in Chapter 1. A brief introduction and the description of the key topics underlying this research are presented.
- Chapter 2 gives an in-depth review of the current state of the art of the research in the main topics introduced in the first chapter. Starting from the basic concepts, gaps in knowledge that this research will address are highlighted.
- Chapter 3 focuses on a single 3D printing filament. The dependence of the filament diameter with respect to a process parameter of FDM 3D printing is studied. This leads to successful manufacture of variable-diameter filaments using fixed-diameter nozzles. This chapter also describes the measurements that have been taken and the procedure followed for calibration of the 3D printer parameters with respect to variable extruded bead stiffness. The calibration process for two 3D printers is described, which can be followed by users with any 3D printers to find the calibration curve specific for their printers.
- Chapter 4 describes how we applied the results from the previous chapter to the production of a functionally graded structure with variable stiffness along one direction. Mathematical models have also been developed, with the aim to predict the mechanical behaviour of the functionally graded architectures produced.
- Chapter 5 extends the manufacturing of functionally graded films to lattice films graded in two dimensions. Films with a 2D variation of stiffness have been successfully manufactured, tested, and stiffness compared to finite element analysis for validation.

- Chapter 6 summarises the main conclusion that can be drawn from this work. Additionally, extensions and ways in which this work may further evolve have also been collected in this last chapter.

# Chapter 2

# Literature Review

This chapter provides an up-to-date review of the literature relevant to this work and the research outlined in the previous chapter. The context of the research relates to several interdisciplinary fields connecting materials, structures, manufacturing and tissue engineering. Of particular interest are cellular and porous solids, functionally graded materials, 3D printing and tissue engineering. Their connection to the present work will be discussed. Gaps in knowledge will be identified leading to the technical challenges addressed in this work.

## 2.1 Cellular Solids

Many materials found in nature display unique combinations of properties and hierarchical architectures. They are characterised by a micro-structure that shows an interconnected network of struts. These materials have been proven difficult to mimic synthetically, although in the last decade these have been successfully produced using polymers, metal or glass, and have been studied extensively [Ashby, 2006]. The work from Wegst et al. [2014] provides a review of the most important design motifs and discusses the difficulties related to their design and fabrication. The most common manufacturing methods for bio-mimetic materials are reviewed. Additive manufacturing (AM) is recognised as a production method that could enable fabrication of the bio-inspired materials of the future. Two of the main challenges that have been identified are the narrow palette of material available and the lack of additive manufacturing processes able to print nanoscale features combined with the large macroscopic scale of many practical components. However, what is referred to as the 'Achilles heel' of additive manufacturing techniques is the difficult control over the microstructure of individual layers and segments. Research in the field of additive manufacturing would enhance the control and the reliability of the manufacturing methods, to achieve the mechanical properties and the microstructure characteristics that are required for a consistent use of AM in

the production of cellular materials. We now review the main applications for cellular materials to date, as well as their main fabrication techniques.

### 2.1.1 Applications of cellular materials

Cellular materials are widely used. Their application ranges from energy absorption and dissipation, sound absorption, thermal insulation and biomedical engineering. This class of materials mainly started with the use of foams and aerogels, but subsequent research and development allowed to obtain materials with improved efficiency, as represented in Figure 2.1. In the field of high-performance cooling, the cores of cold plates, heat pipes and heat exchangers have been fabricated from various cellular and periodically structured materials because they enable designs with improved performance [Lu et al., 2005, Tian et al., 2007]. Cellular materials can also be used as energy-absorbing materials, where they are used for protection against impact and shock. In this application, an intervening medium is required to be capable of large volume decrease to reduce the incoming pressure by extending the impulse duration, and cellular materials are an excellent choice due to the voids within them. This feature is sought in a wide range of applications, from helmets to crashworthy vehicle structures and sporting gear. Cellular materials, here, are necessary because dense solids and fluids have relatively small compressibility [Evans et al., 2010]. Another important application of these structured materials is as cores for sandwich panels. Sandwich structures are widely used in lightweight designs, especially in aerospace engineering, but also increasingly in sporting and automotive applications. In sandwich constructions, the core, made of foam or cellular material, lies between two thin and stiff face sheets. The separation between these face sheets, due to the thickness of the cellular core in between, provides the structure with a higher second moment of area under bending load. This allows to increase the bending stiffness with a relatively low impact on the overall weight. The core between the two face plates provides transverse shear stiffness and resistance to transverse compression [Schaedler and Carter, 2016]. Acoustic damping is another application, in particular using closed-cell metal foams [Li and Crocker, 2006, Golovin and Sinning, 2003].

The interest in cellular structures has also increased in the bioengineering field, especially for tissue engineering applications. The importance of their use mainly arises from the freedom and flexibility in design that allows balancing the weight to the desired strength and stiffness. In the field of bone tissue engineering, significant challenges must be addressed to ensure favourable interaction of the implant with the surrounding biological environment [Salgado et al., 2004, Chen and Thouas, 2015]. Osseointegration is the process that allows an implant to become naturally fused, or bonded, to the surrounding bone. For this to happen, the implant must facilitate attachment and growth inside, thus promoting vascularisation of the new tissue. More details on this will be given in Section 2.5. Another application is the possibility to use these *graspable* 3D objects to overcome

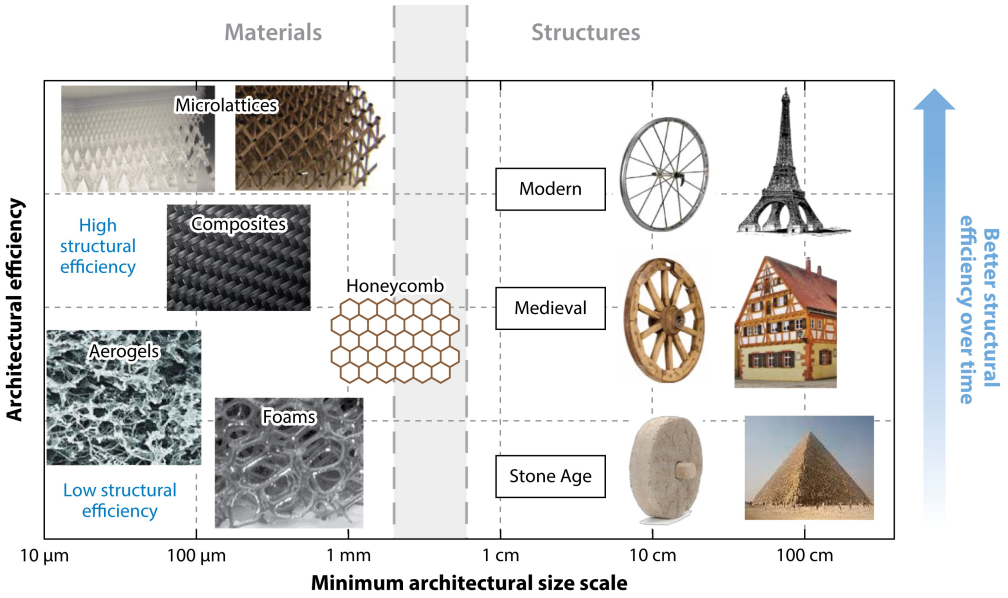


Schaedler TA, Carter WB. 2016.
Annu. Rev. Mater. Res. 46:187–210

Figure 2.1: On the left-hand side, different classes of architected materials are shown and are sorted based on their minimum size scale on the $x$-axis, and structural efficiency on the $y$-axis. The use of cellular materials started with foams and aerogels. Subsequent research and the development of new materials architectures, such as microlattices, improved the structural efficiency of this class of materials. On the left side of the image, the same concept is applied to buildings and structures. The efficiency of structures improved over time, due to the introductions of new materials and new architectures. Image from Schaedler and Carter [2016].

the limitation of 3D visualisation in the field of medical training and clinical practice [Rengier et al., 2010]. This could greatly improve patient-clinician interactions because of the easier connection that can be established when the patient fully understands and is aware of the procedures; however, also medical and surgical education, training and research could benefit from a tangible 3D model, rather than a 3D image visualised on a screen.

Success in enhancing the flexibility and the capabilities of cellular materials, as well as gaining more freedom in tweaking the properties of the manufactured materials could positively affect all of the mentioned applications. In bioengineering, in particular, it could lead to having at our disposal faster and cheaper ways to enhance the quality of patient life. To achieve this, we first need a reliable and flexible industrial method to manufacture porous or cellular materials with the desired properties. In the next section we take a look at some of the most relevant fabrication methods for porous scaffolds.

### 2.1.2 Fabrication of porous materials and scaffolds

The work from Yeong et al. [2004] gives a good overview of how rapid prototyping was seen a decade and a half ago, compared to the conventional manufacturing methods, with particular motivation from the field of tissue engineering. It also comprises a comprehensive review of the conventional fabrication methods at the time, as well as rapid prototyping techniques. The conventional fabrication techniques reviewed are reported to have inherent limitations regarding the ability to control the geometry of the porous materials manufactured, such as size of the pores, interconnectivity and their distribution. These techniques include: solvent casting and particulate leaching [Mikos et al., 1994], gas foaming [Mooney et al., 1996], fibre meshes and fibre bonding [Freed et al., 1994], phase separation [Lo et al., 1995], melt moulding [Thomson et al., 1995], emulsion freeze drying [Whang et al., 1995], solution casting and freeze drying [Hsu et al., 1997]. Rapid prototyping or additive manufacturing techniques, on the other hand, are separated into two categories: melt-dissolution deposition technique and the particulate bonding technique. The first includes those where each layer is formed by extrusion of molten material deposited in a predetermined pattern. Fused Deposition Modelling (FDM) techniques belong to this category and are reported to be a feasible method for the fabrication of functional scaffolds. However, the resolution for FDM at the time was 250 µm. Some progress has been made as far as resolution is concerned, which can now be as low as 50 µm, as a more recent review reports [Yuan et al., 2019].

The work of Yuan et al. [2019] focuses mostly on porous metal implants. Porous metallic implants have been created using various manufacturing methods. Some of them include powder metallurgy [Chen et al., 2017], metal foaming [Gu et al., 2009] and space holder methods [Bram et al., 2000]. However, this work also states that the main two issues with these techniques, despite the fact that they show great potential, is that they are high-cost and time-consuming. A recent work from Maiti et al. [2016] compares the long-term mechanical properties of 3D printed cellular solids and random foams: 3D printed structures are shown to have better long-term stability and mechanical performance. Imaging both microstructures and performing finite element analysis on them indicate that this may be due to a wider stress variation in the stochastic foam, where points of higher local stress are present, compared to the 3D printed cellular solid. Therefore, research into 3D printing especially aimed at more accessible, easier to operate and faster manufacturing is required. One may be able to achieve a broader range of materials to be used, have a better control over the parameters and achieve higher resolution.

### 2.1.3 Mechanical properties of lattice structures and their characterisation

The formal and analytical strudy of the mechanical properties of lattices and foams started with the works by Gibson and Ashby. In their work Gibson L. J., Ashby M.

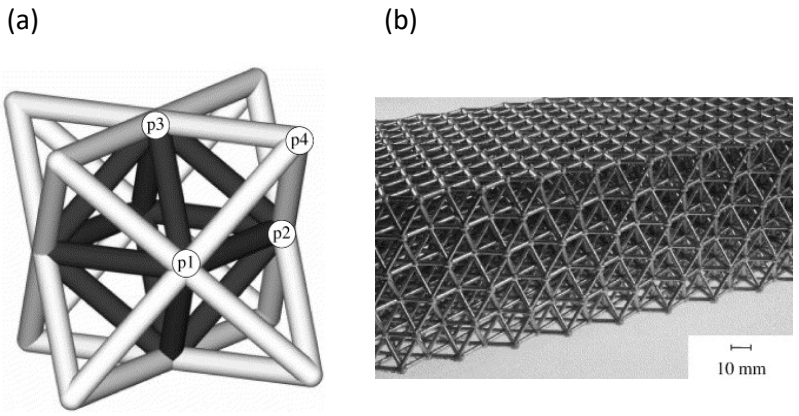


Figure 2.2: (a) The structure of the octet-truss lattice material. The darkened struts represent a octahedral cell, while the nodes with labels form a tetrahedral cell. Adapted from Deshpande et al. [2001a].

F., Schajer G. S., Robertson C. I. [1982], the mechanical properties of honeycombs were analysed and compared with experiments. The properties are described in terms of the bending, elastic buckling and plastic collapse of the beams that make up the cell walls. Another of their most important work is Gibson I. J., Ashby M. F. [1982], which is concerned with the study of three dimensional cellular solids or foams. This work relates the mechanical properties to the properties of the cell wall and to the cell geometry. Hence, the models developed in these works address the problem of 2D lattices and 3D foams. Lattices in three dimensions cannot be modelled using the two dimensional approach used in the works just mentioned. However, these works sparked the interest in these kind of materials within the scientific community. These two studies led to the first comprehensive treatise of mechanics of cellular materials Gibson and Ashby [1997]. Shortly afterwards, various ordered cellular architectures with improved mechanical properties were studied [Evans et al., 1999, Wadley et al., 2003]; for example, the octet truss lattice with ideal linear scaling of mechanical properties [Deshpande et al., 2001a] that can be seen in Figure 2.2. These pioneering works sparked the interest in these topics, leading to more complex architectures to be studied in the years since. These structures have also been studied by means of finite element analysis, as a method of discovering the role that the cellular topology plays in the resulting mechanical properties. One of the main conclusions drawn is that in some high-connectivity topologies, stiffness and strength were significantly influenced when the regularity of the microstructure was compromised [Alkhader and Vural, 2007]. This stresses the importance of studying the relationship between the parameters of the manufacturing process and the resulting properties, to achieve a structure that is as close as possible to the intended design.

A review on metallic micro-lattices [Rashed et al., 2016] presents an overview of their

modelling approach first. Further, they present an overview of the manufacturing and processing of these, together with the corresponding mechanical properties. Finite element analysis has been used in conjunction with several modelling approaches. The structures can be modelled as a continuum—where the structure is assumed to have homogenised properties—or modelling the individual struts, which allows to include imperfections. However, it is important to check how the variations in dimensions of the individual struts affect the mechanical properties obtained. Modelling the individual struts and comparing the predictions with experiments is then a way to check how the imperfections introduced by the manufacturing process affect the properties of the final result. A comprehensive review on the properties and performance of lattice structures manufactured using Selective Laser Melting is available Maconachie et al. [2019]. In this work, data available in literature on the experimental results obtained on such lattices is summarised and analysed. Correlations between relative density and mechanical properties have been found consistent with the predictions of the Gibson-Ashby model.

Physical realisation of porous materials have several technological impacts. Their ever-increasing use necessitates their experimental, theoretical and computational characterisation. Tissue engineering in recent years has rapidly increased the use of cellular materials. Three main reasons can be identified why the use of porous scaffolds has increased for orthopaedic applications [Ryan et al., 2006]. It is possible to improve fixation when bone tissue grows into and through a porous matrix. Their low elastic modulus could reduce the problems associated with stress shielding. Finally, their porosity and interconnectivity can improve body fluid flow, resulting in an improvement of bone ingrowth. The review by Ryan et al. [2006] summarises methods of fabrication for porous metallic scaffolds, both that possess open-cell and closed-cell architectures. However, limitations exist in the control of the porous material parameters. Most methods can control the characteristics of the whole structure or a large area, but not of specific locations within the matrix. In case of FDM 3D printing, works concerning the mechanical properties of 3D printed structures started soon after the development of the RepRap open-source prototyper [Tymrak et al., 2014]. However they were mostly concerned with the tensile strength of the overall structure or its elastic modulus. A similar work has also been carried out on dense 3D printed parts manufactured using ink-jet printing of a binder [Giordano et al., 1997]. Here, the effects of the amount of binder used were analysed, as well as the effect of low and high molecular weight of the base material on the properties, for which the maximum tensile strength did not show significant difference. This work also takes into account the way a part is treated and processed after being printed, which plays a role in the properties of the manufactured part, and is usually overlooked. The time elapsed between deposition of the material and its solidification is also responsible for the final dimensions and characteristics of the final print. An example of this characterisation is in the work by Smay et al. [2002]. Here, structures with a range of features have been manufactured using colloidal inks, and the deflection of these has been used

to probe the relationship between gel strength, deposition speed and shear rate profiles in the nozzle.

The works by Cuan-Urquizo [2016], Cuan-Urquizo et al. [2015] deal with the characterisation of regular 3D printed lattice structures. The mechanical properties of these have been studied in the case of tensile, flexural and torsional load. The case of a compressive force in the stacking direction has also been studied. These works provide mathematical models for the prediction of the mechanical properties of regular lattices, hence no variation in the diameter of the filaments is allowed. Additionally, the contributions due to shear are not considered. For these reasons, the models developed are applicable to lattices made of filaments with one single diameter where the spacing between the filaments is large compared to the diameter of the filaments (to ensure shear is negligible).

Dimensional accuracy is another aspect of manufacturing that needs to be characterised. It is important not to introduce irregularities and imperfections in the cellular materials. The manufacturing process must also ensure that it does not introduce irregularities that greatly affect the mechanical behaviour. Non-stochastic lattices were fabricated using electron beam melting (EBM) and their properties tested in compression and bending [Cansizoglu et al., 2008]. It was found that modification to the geometry of the lattice would be of value, to improve the response to shear forces. In this work, the minimum achievable strut thickness was 0.7 mm. The discrepancy between the strut dimensions in the CAD model and the actually fabricated struts was responsible for a slightly lower value for the stiffness of the lattice. This stresses the importance of a good control over the properties of the object to be manufactured, and also shows the need to improve the knowledge on how the parameters of the porous structure and of the manufacturing process affect its mechanical properties. The importance of predicting and modelling the effects of imperfections introduced by the manufacturing process is highlighted in the work by Harbusch-Hecking and Öchsner [2016], where small alterations in the simulated mesh are introduced and their impact on the properties is characterised. The Young's modulus of the simulated part decreased over 70% after about 2.15% of the elements were deleted. On the other hand, the effect of shifting nodes had little to no influence on the performance, unless the nodes are shifted of an amount close to the size of an element.

### 2.1.4 Bending-dominated and stretch-dominated structures

Cellular solids deform by a combination of deformation mechanisms of the cell walls—bending and stretching being such two important mechanism. When the dominant mechanism is the bending of the cell walls, the cellular solids are referred to as bending-dominated. Random cellular architectures of foams and aerogels result in bending-dominated deformation of the cell walls when the architecture is kinematically mobile,

resulting in a rapid decrease in strength and stiffness as porosity is increased [Deshpande et al., 2001b]. On the other hand, certain ordered cellular architectures can have nearly optimal stretching-dominated deformations, resulting in materials in which the strength and stiffness scale proportionally to the solid volume fraction of the material [Zheng et al., 2014]. Note however, that high stiffness is not a requirement for all applications. Indeed flexible structures are desirable at times. In the recent review by Tan et al. [2017] on metallic cellular scaffolds, a characterisation of bending- and stretch-dominated topologies as well as a review on manufacturing, designs, mechanical properties and biocompatibility, is provided. A bending-dominated translationally repetitive structure consists of $b$ struts and $j$ frictionless joints that satisfy the Maxwell's criterion $M = b - 3j + 6b < 0$; this unit cell is characterised by the cell struts bending upon loading. A stretch-dominated unit cell structure, on the other hand, satisfies the Maxwell's criterion $M = b - 3j + 6 \geq 0$ [Tan et al., 2017]. Its struts are loaded in tension-compression when load is applied to the structure.

### 2.1.5 Material-property space

Properties of materials can be conveniently displayed on the so-called material property map which attempts to classify all available materials on a plane spanned by their properties. This provides us with a convenient visual way of comparing relative merits or deficiencies of different materials and material groups (e.g. metals vs ceramics vs polymers, etc) within the *material kingdom*. Considering all the commercially available materials and plotting their Young's modulus against their density (Figure 2.3), it is possible to visualise the combinations of Young's modulus and density for which a material is available. Fixing the desired Young's modulus, for example, one can find the range of densities of the available materials with that modulus. Equivalently, fixing the desired density it is possible to see the range of moduli for which a material is available [Granta, 2012].

White areas in this material property space represent combinations of modulus and density for which a material is not yet available. Continuous effort is being made to populate these white areas of the diagram—especially the top-left corner, as it represents materials with low density but high elastic modulus. With the technological improvements in the manufacturing processes, in particular with the advent of additive manufacturing, the bounds of what can be produced are expanding. Further improvements in the architectures and manufacturing processes could lead to new regions on the diagram, achieved without the need for a chemically-new material but by tailoring the internal architecture. These are the main reasons why the properties of complex architectures and microstructures are interesting theoretically and practically.

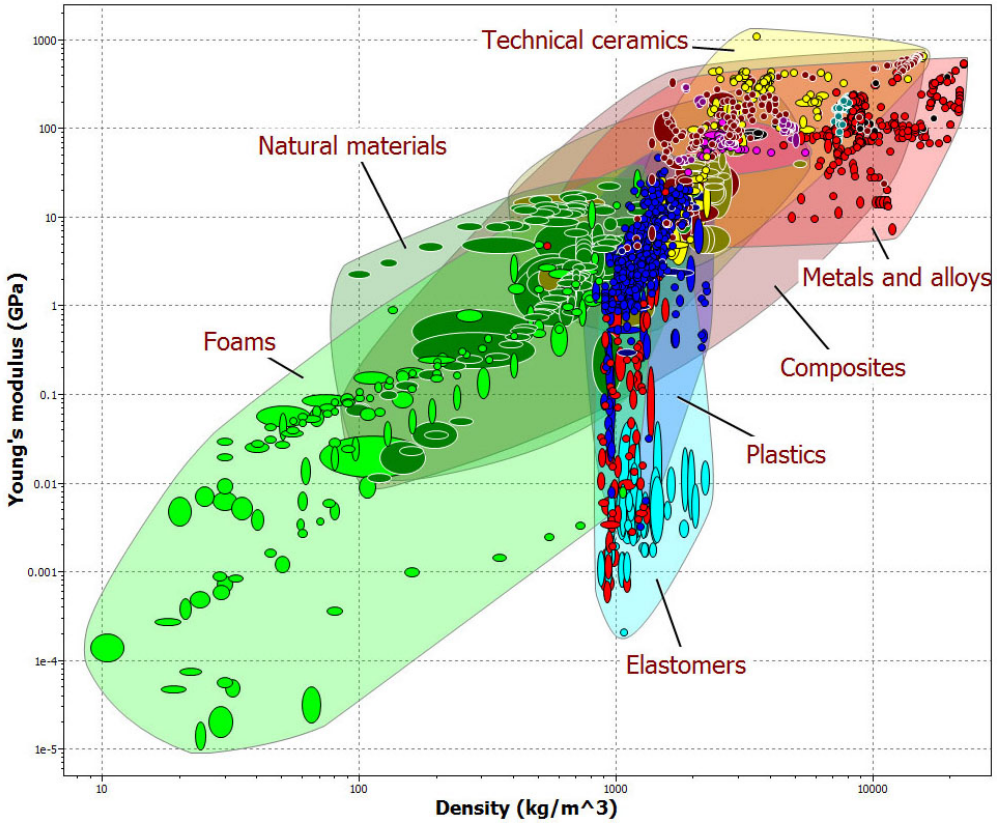


Figure 2.3: Material property space created using the CES Selector database website [Granta, 2012]. The plot shows for which combinations of Young's Modulus and Density a material is commercially available. White zones indicate that there is no material available with that combination of Young's modulus and density.

### 2.1.6 Metamaterials

The possibility to produce architectured materials has given rise to intense activity in the area of *metamaterials*. This class of materials exhibit properties that are usually not associated with naturally occurring materials but are due to their *engineered* internal structure. This field arose with the controlled propagation of electromagnetic waves, including optics, and has matured over the last two decades [Sievenpiper et al., 1996]. Nevertheless, recently, the term *mechanical metamaterial* has been used to describe materials with unusual mechanical properties achieved by controlling their internal structure [Christensen et al., 2015]. By tailoring this internal architecture, the properties of the metamaterial can be controlled, and uncommon and sometimes unexpected properties can be achieved. Auxetic materials are an interesting class of metamaterials with such unique properties [Novak et al., 2016, Evans and Alderson, 2000]. As a consequence of the structural deformation of their internal cellular structure they exhibit a negative Poisson's ratio, i.e. they increase in size laterally when stretched. This is associated with increase in volume upon extension—it can be shown that $\frac{\Delta V}{V} = \epsilon_x(1 - 2\nu)$, where $V$ is the volume of the material, $\epsilon_x$ is the strain in the direction of stretching and $\nu$ is

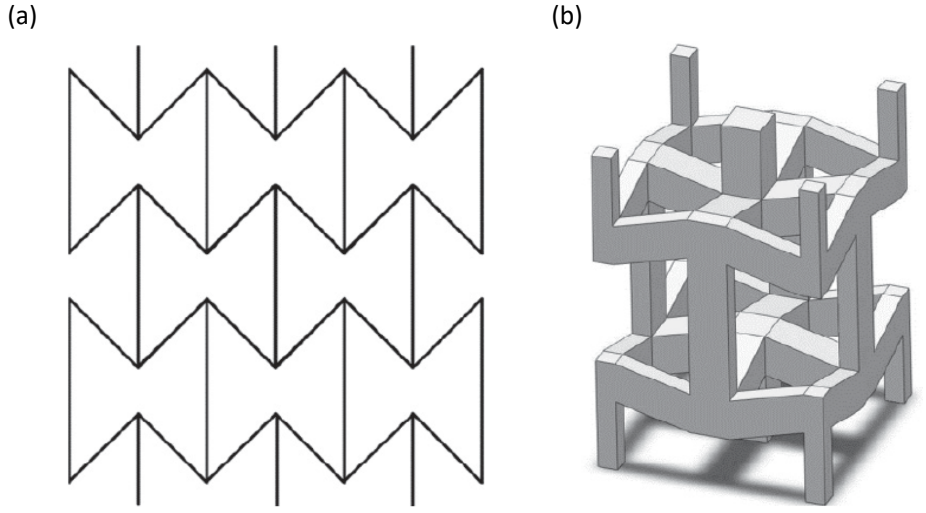


Figure 2.4: The re-entrant honeycomb auxetic structure, adapted from Yang et al. [2015]. (a) shows the two-dimensional representation of the design, (b) shows the 3D unit cell of the auxetic structure using this re-entrant honeycomb.

the Poisson's ratio of the material. One example of a structure which exhibits auxetic behaviour is the re-entrant honeycomb shown in Figure 2.4 [Yang et al., 2015]. An important application for auxetic materials in the field of bioengineering is in patches for heart tissue. In this situation, when the heart tissue contracts, the synthetic material attached must shrink *in all directions*; this desirable response can be achieved with the use of auxetic materials.

Recently, development of a new class of metamaterials has taken off, in relation to the advent of 4D printing. 4D printing has attracted tremendous attention since its first conceptualisation in 2013 [Kuang et al., 2019]. As opposed to the static objects created with 3D printing, the structures created with 4D printing change configuration or function in time, when subjected to external stimuli, such as temperature or water. Obtaining such customised materials and behaviours has been possible thanks to research in 3D printing; this process still needs to be fully explored, especially from the point of view of the manufacturing process itself, both hardware or software, but it is a clear example of how research can enhance and improve a manufacturing process.

## 2.2 Functionally Graded Materials

Cellular materials are a great example of how nature managed to come up with a way to obtain lightweight materials with interesting properties. Natural cellular materials allow us to gain an understanding of how nature creates materials needed to fulfil specific

requirements through the evolutionary process. It can easily be observed that natural materials tend to have a spatial variation in their properties based on their function and location. For this reason, one of the enhancements of many manufacturing processes that manufacture porous materials has been the idea of adding a variation in the porosity. Materials with spatial variation in properties are called Functionally Graded Materials, or FGMs. Usually, the term functional gradation refers to a gradation of porosity or spatially varying chemical composition. However, its effect on the variation of mechanical properties is usually overlooked [Ryan et al., 2006]. The variation in composition or properties can either gradually vary throughout the volume, in which case the variation is continuous, or it can be discrete, where different portions of the volume have different properties, however they remain constant within each portion. This creates an interface between the portions where there is a sharp variation in the properties. A continuous gradation is preferred because it allows to avoid stress concentration around interfaces between sections with different properties [Shah et al., 2014]. In the next sections, we will present the main application for this kind of materials and their most common methods of fabrication.

### 2.2.1 Applications

Functionally graded materials (FGMs) are a class of high-performance materials that have quickly developed in the last three decades Gupta and Talha [2015] and that have the potential for wider applications in the future. FGMs have been initially used in the aerospace sector, however, applications in other fields have quickly developed. The aerospace sector uses FGMs for thermal applications. Specifically, to avoid stress concentration due to different thermal expansion coefficients at the interfaces between materials with different properties (for example when coating metals with ceramics). Between these two materials, a FGM can be used to make the properties vary gradually at the interface. In the optoelectronics sector, an example of application can be found in the modulation of refractive index, achieved through functional gradation of material properties. In semiconductors, it has been found that many parameters depend on local material functions. However, in this field, the concern is with optical and electromagnetic properties. The extensive review from Gupta and Talha [2015] presents the structural response for functionally graded materials as well as an overview of different fabrication methods, discussed in the next section. Additionally, several studies have been carried out, as discussed in a recent review [Sola et al., 2016a], on the basis that FGMs can improve the mechanical properties of implants as well as their interaction with the host biological environment [Pompe et al., 2003].

The biomedical sector has become more and more interested in this class of materials. Gradients in properties are being used in the biological and medical fields for specific purposes. It has been shown that an ambient with gradation in properties, for example

pore size, improves the response of cells. Di Luca et al. [2016] showed that designing structural porosity gradients may be an appealing strategy to support gradual osteogenic differentiation of adult stem cells. In this work, scaffolds with homogeneous spacing have been manufactured, as well as scaffolds with a discrete variation in the spacing of filaments throughout the scaffold, see Figure 2.5. This work shows that the differentiation of hMSCs cultured in mineralisation media was improved in gradient scaffolds. In the work by Sobral et al. [2011], scaffolds with pore-size gradients were found to improve cell seeding efficiency. The scaffolds that have been manufactured and tested in this work can be seen in Figure 2.6. Here, the pore size gradient scaffolds improved seeding efficiency from about 35% in homogeneous scaffolds to about 70% under static culture conditions. Anisotropic cell distribution was also shown in the presence of a scaffold with pore-size gradients in another work [Woodfield et al., 2005a]. In the work by Singh et al. [2010], a gradient in composition has been introduced, which results in a gradient in stiffness, for functional regeneration of interfacial tissue (direct the differentiation of hMSCs) using controlled infusion of polymeric and composite microspheres.

The works presented in this section all show how manipulation of the internal architecture of the scaffold can lead to improved biological performance. This is obtained either with a change in composition or a change in porosity. However, the focus is on the improvements that can be achieved from a biological standpoint. The change in mechanical response as a result of the changes in porosity is usually overlooked. The methods presented in these works give an understanding of the requirements in terms of porosity but a characterisation of the properties and a method to tailor the mechanical properties of scaffolds is identified as a gap in the literature. It could be argued that in order to change the stiffness it would be sufficient to cluster multiple filaments together (i.e. spacing $= 0$), however, using this technique would only result in clusters with a width that is a multiple of the width of the starting filaments, while the thickness would not change. Assuming a diameter of the filaments $d$, this technique would not be a viable solution for obtaining filaments with diameters in the range $[d, 2d]$. Additionally, when a change in porosity is used to improve biological performance, the mechanical properties are a consequence of the change in porosity rather than being controlled separately.

### 2.2.2 Fabrication of functionally graded materials

There are occasional situations within conventional processing, dating back to several decades in cutting tool manufacturing, that can be technically called functionally graded. One of them is carburising, which provides hardness at the surface of a cutting tool due to the high carbon content, usually achieved by charcoal diffusion or carbon monoxide [Edenhofer et al., 2015]. Such layers are only a few microns to fractions of a few millimetre. When such a tool is quenched, the surface is brittle but hard, whereas the bulk of the core of the cutting tool remains tough, which is resistant to impact and fracture.

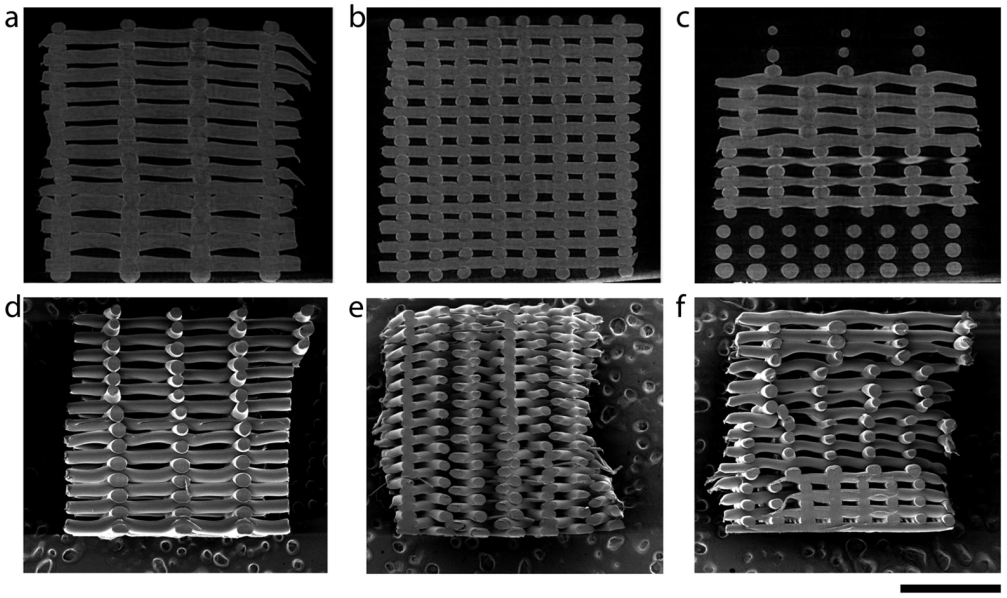


Figure 2.5: Scaffolds with different spacing and hence different porosity. µCT and SEM micrographs of scaffold with spacing of 1100 µm (a,d) and 500 µm (b,e). µCT and SEM micrographs of scaffold with a discrete gradation of spacing: four parts with spacing 1100 µm, 900 µm, 700 µm, 500 µm(c,f). Scale bar 2 mm. Image from Di Luca et al. [2016].

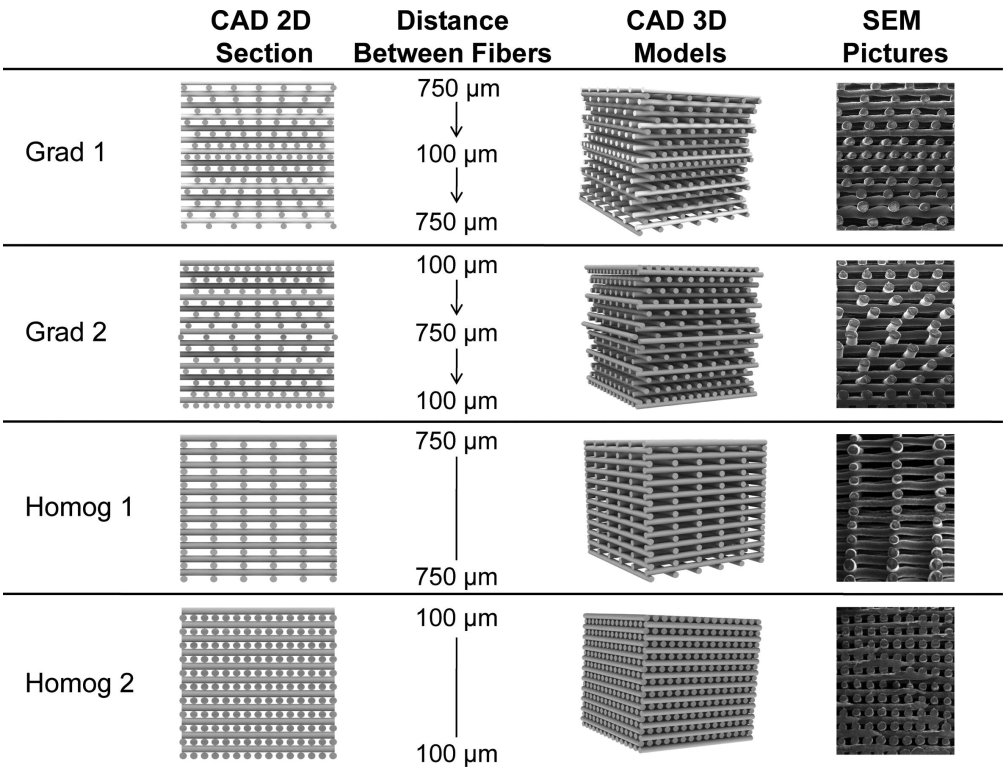


Figure 2.6: Scaffold with a gradation in spacing between filaments and hence porosity. Scaffold 'Grad 1' has a spacing that varies linearly form 750 µm at the top and bottom of the scaffold to 100 µm at the centre. 'Grad 2' on the other hand has a porosity that goes from 100 µm at the top and bottom and 750 µm at the centre. 'Homog 1' and 'Homog 2' scaffolds have a constant spacing of 750 µm and 100 µm respectively. Image from Sobral et al. [2011].

The profile of material properties such as hardness or local modulus of elasticity rapidly decays into the depth of the material.

Methods of production of functionally graded porous structures and scaffolds can be divided into conventional processing & subtractive methods vs additive 3D-printing techniques [Leong et al., 2008]. Standard methods of production could be further divided into physical or chemical methods [Gupta and Talha, 2015]; some of these involve powder processes, techniques involving metal melts or processing of graded polymers. The review from Kieback et al. [2003] also describes the techniques to model the processes involved in manufacturing these materials, from gradient formation, to sintering and drying.

The *conventional methods* do not generally provide full control of the macro- and microstructure of the produced material but they have been successful in producing scaffolds with gradients in porosity and pore size. Volatile sintering additives have been added in different proportions throughout the powder mixture used to build structures [Werner et al., 2002], which would leave pores when disappearing during sintering. Another method makes use of powders with different degrees of crystallinity by impregnating cellulosic sponges into hydroxyapatite (HA) slurries [Tampieri et al., 2001]. Self-foaming followed by pyrolysis has also been explored [Zeschky et al., 2005]. Here, the use of a low foaming temperature allowed control of bubble nucleation and hence porosity. Centrifugation is another conventional method for fabrication of functionally graded parts. This method allows the separation of the components of the suspension, then the spinning mixture is rapidly frozen to lock the component separation. The frozen solvent phase is then removed via sublimation [Harley et al., 2006]. The centrifugal mixed-powder method [Watanabe et al., 2009] is a novel method for the production of FGMs. It is derived from the centrifugal solid-particle method, an application of the technique of centrifugal casting, in which it is hard to produce FGMs containing nano-particles. This novel technique, on the other hand, can obtain FGMs containing nano-particles. A deeper discussion on these non-3D-printing-related techniques for the fabrication of functionally graded materials is available in a recent review by Sola et al. [2016b]. FGMs still require advances in materials, manufacturing and modelling for a full development of their potential. To this end, 3D printing looks very promising, especially from the perspective of customisation options and ease of use.

The main *3D-printing techniques* that have been used for creating functionally graded parts are: Theriform$^{TM}$, resulting in semi-continuous gradient in porosity; Fused Deposition Modelling (FDM) and 3D Fibre deposition (3DF), resulting in discrete gradients. Theriform$^{TM}$ is a 3D printing process that has been used to fabricate composite scaffolds for articular cartilage repair [Sherwood et al., 2002]. This technique makes use of a porogen, particles that are dissolved after the structure solidifies, leaving pores in the material. The use of this kind of chemical process requires the use of a laboratory and the knowledge of the underlying chemistry to be able to engineer products with the desired features. Additionally, the variation in porosity obtained is discrete. A zone of transition

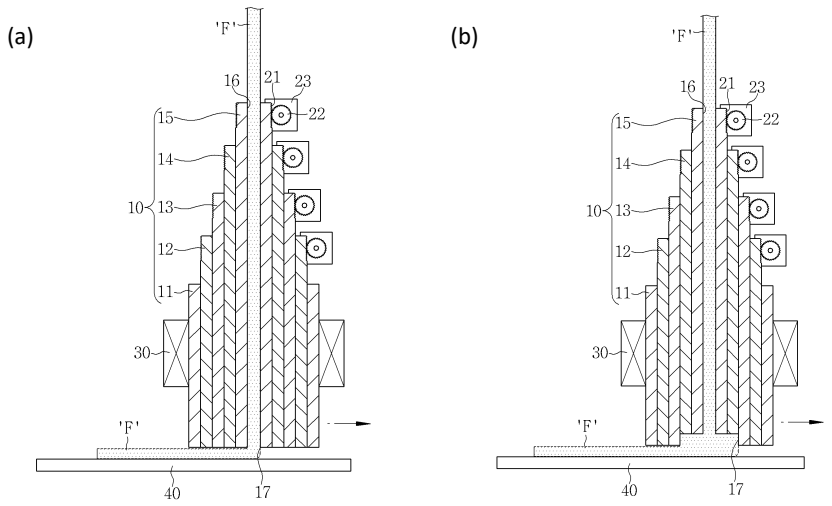


Figure 2.7: (a) shows the case when the concentric nozzles are all in the 'down' position, resulting in the smallest possible diameter of the nozzle (17). (b) shows the case of a different nozzle size. Here, nozzles number 14 and 15 have been moved to the 'up' position to make the nozzle (17) larger. By varying the height of the nozzle with respect to the buildplate (40), the diameter of the filament can be changed. Images from patent KR101725302B1 [Jin, 2016].

was added to avoid delamination: a gradient of materials was added to avoid the sharp interface between the two regions. *Fused deposition modelling* has been used to produce a cylindrical scaffold with concentric regions of different porosity to mimic the average bone composition [Kalita et al., 2003], however the porosity variation was discrete and not continuous. *3D fibre deposition*, where the input material is in pellet form rather than a filament, generates graded structures by varying the fibre spacing [Woodfield et al., 2004, 2005b], which can have, as we will see in a later chapter, a counter-intuitive effect on the mechanical properties. Another possibility is to use a 3D printer that is fitted with a variable-nozzle head [Jin, 2016]. A series of concentric nozzles that can be raised or lowered are used to obtain filaments of different diameters, see Figure 2.7. Although this method removes the need to change nozzles manually, no continuous variation can be achieved.

All of these manufacturing methods move one step closer to the production of FGMs using 3D printing. However, none of these methods provide a *continuous* variation of mechanical properties using standard equipment. The use of porogens or chemicals require a specific setup to work and requires professional staff to manufacture the pieces. Similarly, standard 3D printers have only been used to manufacture FGMs with discrete variation in properties. Lastly, the use of a variable nozzle requires the use of bespoke expensive hardware, which makes the method usable only by those with the specific equipment. A gap in the knowledge can be identified here: the lack of a consistent and

cheap method to manufacture functionally graded material using standard, out-of-the-box equipment. This would allow anyone with minimal training to take advantage of FGMs. This can also greatly impact their development and help their spread.

## 2.3 Additive manufacturing

Additive manufacturing, also referred to as 3D printing, is a manufacturing method that builds 3D objects by addition of layers of material. Great interest has been generated in the recent years, not only within the scientific community, but also the general public. The relatively low cost of some of the methods and the ever increasing number of resources available make 3D printing very accessible. Many specialised websites now provide set-up guides and introductions to the main methods [3DPrintingIndustry, Markforged] as well as to the most common method for desktop applications: Fused Deposition Modelling [3DHubs]. The illustrative images in this section are from the Manufacturing Guide website Manufacturing Guide Sweden AB.

The inherent technology for additive manufacturing widely varies, depending on the process, which limits the materials used and on the power source, greatly impacting the characteristics of the final structures. These methods are all characterised by a subsequent addition of material, hence the name *additive* manufacturing, until the final product is complete. This family of techniques makes use of a computer code, known as *Slicer*, that slices a three-dimensional object in a series of stacked layers. A machine then reads the geometry of each layer and uses a nozzle, dispenser or optical source to build the object, layer by layer. Different 3D-printing techniques can be differentiated by the different ways in which the layers are built. The many methods that are included under the term 3D printing are discussed in the following. The most commonly used additive manufacturing techniques are: material extrusion, powder bed fusion, vat photopolymerization, inkjet printing, directed energy deposition, laminated object manufacturing and bioprinting [Wang et al., 2017, Ngo et al., 2018, Zhang and Chen, 2019].

Table 2.1 gives an overview of the most common manufacturing processes for architected cellular materials along with the respective materials that can be used. In the following, we discuss some of the most relevant of these manufacturing processes, and we touch on the other main methods at the end of this section. Bioprinting, on the other hand, will be introduced in this section, but will be also discussed in later sections in this chapter.

### 2.3.1 Material extrusion methods

Manufacturing processes in the material extrusion category are characterised by the extrusion of molten material through a nozzle and layered in a specified pattern, to form the part, as shown in Figure 2.8. In case of ceramics, extrusion of slurries and pastes,

| **Category** | **Methods** | **Materials** |
|---|---|---|
| Material extrusion | Fused deposition modelling (FDM), also called Fused filament fabrication (FFF) | Filaments of thermoplastic polymers such as polylactic acid (PLA), acrylonitrile butadiene styrene (ABS), polycarbonate (PC) |
| | Continuous filaments fabrication (CFF) and Fibre-reinforced additive manufacturing (FRAM) | Same as FFF plus reinforced fibres within (carbon, glass) |
| | Atomic diffusion additive manufacturing (ADAM) | Ceramic or metallic powder within a polymeric matrix |
| Powder bed fusion | Selective laser sintering (SLS) | PCL and polyammide powder |
| | Direct metal laser sintering (DMLS) | Metal alloys |
| | Selective laser melting (SLM) | Titanium alloys, Cobalt-Chrome alloys, Stainless steel, Aluminium |
| | Electron Beam Melting (EBM) | Metal alloys |
| Vat photo-polymerisation | Stereolithography (SLA) | Photocurable resins |
| Inkjet printing (powder adhesion) | Material jetting | Mainly ceramics |
| | Binder jetting | Mainly ceramics |
| Directed energy deposition (DED) | Many different names: directed energy deposition (DED), laser engineered net shaping (LENS), laser solid forming (LSF), directed light fabrication (DLF), direct metal deposition (DMD) | Metal alloys |
| Lamination | Laminated object manufacturing (LOM) | Polymers, metals, ceramics, paper |
| Bioprinting | Bioprinting | Living cells, hydrogels, bioinks |

Table 2.1: Summary of additive manufacturing methods [Ngo et al., 2018, Wang et al., 2017].

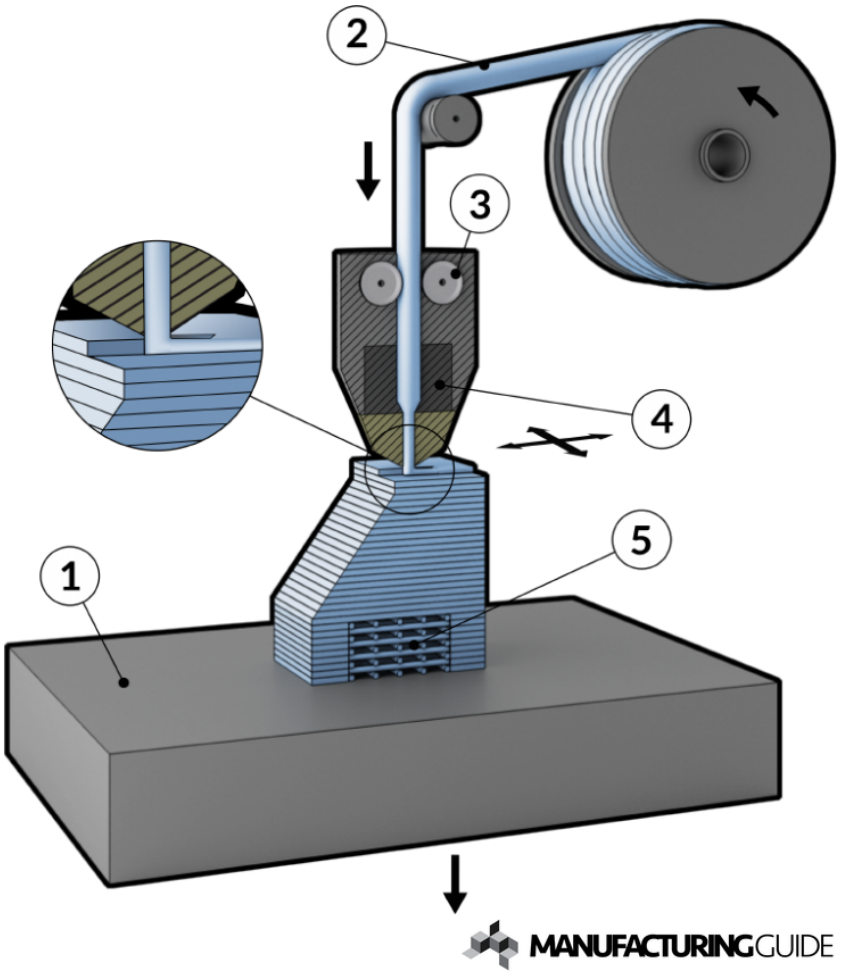


Figure 2.8: Material in the form of a filament (2) is pushed by rollers (3) into a heated element (4) where the material is melted. The movement of the print head, allows the material to be deposited on the build plate (1) according to the commands received via software. In the case of overhangs, support material (5) may be needed. Image from Manufacturing Guide Sweden AB.

rather the molten material, is also used. All of the methods in this category derive from fused deposition modelling (FDM) or paste extrusion. Fused Deposition Modelling (FDM), also known as Fused Filament Fabrication, is now one of the most affordable and widely used methods for 3D printing. In this process, each layer is produced by the deposition of melt extruded filaments. A spool of thermoplastic polymer is fed into the printer to supply material to the printing-head (or extrusion-head). The polymer is heated above its melting temperature and extruded through a nozzle. The polymers that are most frequently used for this, depending on the application, are polylactic acid (PLA), acrylonitrile butadiene styrene (ABS), polycarbonate (PC) and Nylon, depending on the required properties. The path in which this filament is deposited is determined by the slicing software and is written as a series of G-code commands (see Section 3.2). G-codes constitute a set of instructions that move a machine tool—the nozzle, in this case—usually generated by a computer-aided manufacturing (CAM) software.

Some of the main limitations of the FDM process will now be discussed, as they led to the development of modified versions of the FDM process aimed at addressing them. A thin support, that can later be removed, must be designed for part of the structure with overhang, so that these are supported during the printing process. The process of breaking away the support structures affects the surface finish of the fabricated parts adversely and requires additional processing. Other current limitations of FDM are the range of materials that can be processed and poor mechanical properties of the printed parts [N. Turner et al., 2014, Ngo et al., 2018], especially for high strength and stiffness applications where metallic parts outperform polymers. Continuous filament fabrication (CFF) and Fibre-Reinforced Additive Manufacturing (FRAM) attempt to improve the mechanical properties of 3D printed parts by inserting strands of reinforced fibres between layers printed with FDM-like techniques [Plocher and Panesar, 2020]. Atomic diffusion additive manufacturing (ADAM), on the other hand, extends FDM capabilities to metals and ceramics. Here, the filaments that is used for extrusion is a mix of ceramic or metallic powder with a polymeric matrix. After printing the part, a sintering process removes the polymeric matrix and binds together the ceramic or metallic powder [Galati and Minetola, 2019].

Improved mechanical properties, a greater flexibility in the design and range of materials are essential to ensure a broader applicability of FDM manufacturing. Therefore, research into each of these topics is necessary due to the promising potential. The process parameters and their relation to the mechanical properties of the printed part, in particular, are of great current interest. In the present work, we explore novel capabilities of the FDM process and study the mechanics of the parts thus printed. The ease of use of this technique would also allow a much wider range of users to benefit from it, without the need, for instance, for a constant presence of specialised technicians as opposed to the methods described later. In the rest of this section, we are going to introduce the other common additive manufacturing techniques. The next section (Section 2.4) will focus on the manufacturing technique that will be used in the rest of this work: Fused Deposition Modelling 3D printing.

### 2.3.2 Powder bed fusion

Powder bed fusion is a 3D printing approach that works by fusing together grains of powdered material using an energy source. The techniques that belong to this family can be divided based on the source of energy used. In one of the most successful *powder bed fusion* methods in the market, the metal powder is typically melted with either a laser or an electron beam to create each layer [Horn and Harrysson, 2012]. One of the methods is called *Selective Heat Sintering* (SHS). In this process, layers of thermoplastic powder are treated with high-precision heat: when one layer is complete, the bed moves downwards, a roller adds a new layer of powder and the next layer can be sintered.

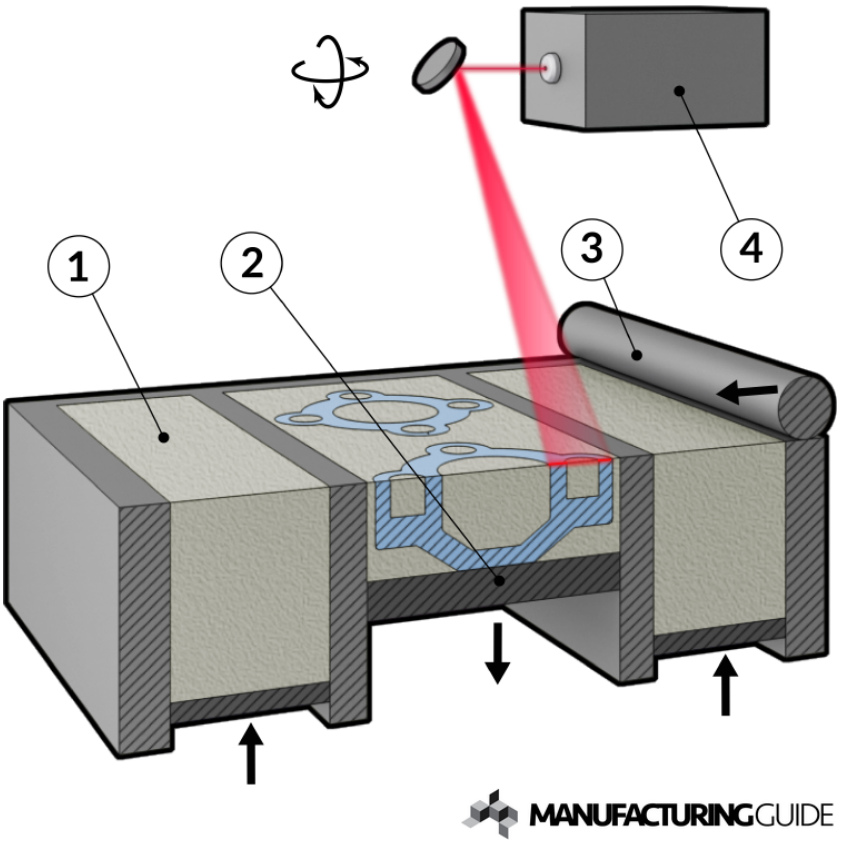


Figure 2.9: Powdered material (1) is spread using a roller (3). A pulsating laser (4) scans the powder according to commands from software and sinters a thin layer of the powder. The build plate (2) then moves down and the process is repeated until the part is complete. Image from Manufacturing Guide Sweden AB.

When the energy comes from a laser, instead, the techniques are called Laser Sintering techniques. This makes the process more accurate but more expensive [Sahasrabudhe et al., 2018]. Laser sintering techniques include *Selective Laser Sintering* (SLS), see figure 2.9, usually used for polymers, and *Direct Metal Laser Sintering* (DMLS), for metals. *Selective Laser Melting* (SLM) is another technique in this category. Here the powder reaches the melting point and thus fuses, instead of being sintered by means of a high-energy laser. Layer by layer, a fully dense material is created. The effects on the final printed part of process parameters of SLM, such as exposure time and laser power, have been studied [Ahmadi et al., 2017]. The results showed that the rate of change in mechanical and topological properties with respect to exposure time was non-linear, while it was linear with respect to the laser power. *Electron beam melting* (EBM) is yet another similar type of additive manufacturing technology for metals, however the energy comes from an electron beam in a high vacuum.

Powder bed fusion methods are generally dimensionally more accurate than FDM-like methods. Additionally, this family of processes uses the powder to support overhangs and thin walls in the part being produced, thus eliminating the need for support structures.

However, costs are still very high: the price for a 3D printer in this category is roughly 50–100 times the price for an FDM 3D printer. Furthermore, the upkeep of these machines is very high and an extensive training is required for their use and maintenance. These are also the most studied methods, given their precision and quality of the printed parts. Certainly there are applications where this is a requirement, but many applications would benefit from a cheaper, more accessible and immediate method, such as FDM-like techniques.

### 2.3.3 Vat photopolymerisation

This category of printing processes is characterised by a vat of material in liquid state that is hardened, or cured, using light or a laser. *Stereolithography* (SLA) uses photopolymerization to produce a solid part from a liquid, usually a type of photosensitive resin [Melchels et al., 2010]. The parts printed with this process are generally printed upside-down: a build-plate is lowered into a vat or liquid resin which is exposed to light under controlled conditions from below the vat. This causes a thin layer of the exposed liquid resin to harden due to photopolymerisation. Then, the build-plate moves upwards. The liquid resin then fills the gaps between the layer that just hardened and the bottom of the tank, and is then exposed to light again to form the next layer—this process repeats until the object is complete. The part is then removed from the build-plate, drained and cleaned [Jacobs et al., 1992].

*Self-propagating photopolymer waveguide production* is a method that takes advantage of an optical effect that traps the UV light in a waveguide, as the index of refraction changes on polymerisation [Jacobsen et al., 2007]. *Continuous liquid interface production* uses digital image projection to expose the resin at a persistent liquid interface [Tumbleston et al., 2015]. *Two-photon lithography* enables 3D printing of polymers at a much higher resolution than that achieved through the standard SLA process. Such resolution, as low as 150 nm [Nanoscribe GmbH, 2007], enables the fabrication of structured materials at the nanoscale [Schaedler and Carter, 2016, Maggi et al., 2017]. The main problem with this technology is related to cost—even though it is cheaper than the sintering techniques—and to the long time needed to produce an object. The speed of the prints is of the order of a few millimetres per hour. Additionally, as mentioned, the polymer is in liquid state. This results in a printed object that is wet once finished, which requires a specific laboratory where the objects can be post-processed, which can include washing and curing.

### 2.3.4 Bioprinting

The use of living cells as a material for additive manufacturing gave birth to what is known as 3D bioprinting, a method that has emerged powerful in regenerative medicine.

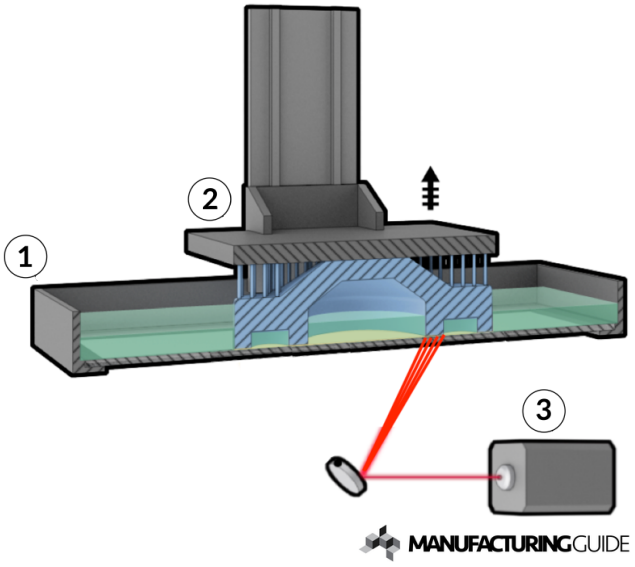


Figure 2.10: The build plate (2) starts from the bottom of the vat of photosensitive resin (1) and raises after every layer is formed. Each layer is formed by means of a light source (3) that hardens the resin to form each layer. Image from Manufacturing Guide Sweden AB.

In this process, layers are generally made of living cells, deposited onto a gel medium or sugar matrix, providing nutrients to prevent the death of the living material that is printed. The layers are slowly deposited to form the three-dimensional part. A representation of the process can be seen in figure 2.11. Further review of this topic will be provided in the following sections, however, two works in particular stand out as examples of the applicability of this manufacturing technique.

3D bioprinting has been used to print a human bi-layered skin using bio-inks containing human plasma, as well as primary human fibroblasts and keratinocytes that were obtained from skin biopsies [Cubo et al., 2017]. A novel way to combine bioprinting with FDM in a manufacturing method has been develop [Wang et al., 2019, Liu et al., 2019]. The coaxial extrusion process presented in these works is characterised by two nozzles coupled together, so that one is inside the other. The inner nozzle extrudes sensitive materials, such as living cells, while the material extruded by the external nozzle protects and supports the sensitive material within (extruded from the other nozzle).

### 2.3.5 Other additive manufacturing techniques

The most relevant methods for the production of structures with internal architecture have been discussed in the sections above. However, in the case of metals and ceramics,

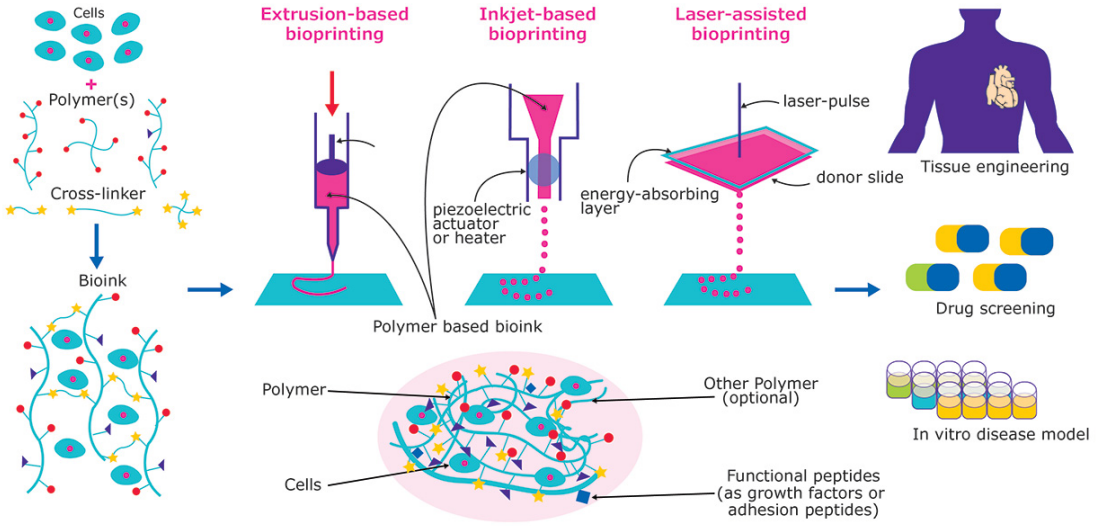


Figure 2.11: 3D Bioprinting of tissue and organs. Bioinks are created by combining cultured cells and various biocompatable materials. Bioinks can then be 3D bioprinted into functional tissue constructs for drug screening, disease modeling, and in vitro transplantation. From Sigma-Aldrich.

two more techniques are promising: directed energy deposition (DED) and binder jetting. *Directed energy deposition*, also known as *laser-engineered net shaping* or *direct metal deposition* is suitable for the production of large structures, as opposed to the methods mentioned before, which can generally produce only small parts. DED methods have some similarities with FDM, in that they do not make use of a powder bed, but the material is melted before deposition in a layer-by-layer fashion. In *binder jetting*, one of the few methods to print with ceramics, the model is built by selective deposition of a liquid binder agent onto ceramic powder [Deckers et al., 2014, Zocca et al., 2015]. This process results in what is known as a green part: a part that then requires firing for the powder particles to fuse. The binder is the agent that holds the part together temporarily, before firing. Similar to this method is the *material jetting* method [Yap et al., 2017]. In this case it is the material that is being deposited, in the form of small droplets, as opposed to the binder. This material is then cured using a UV light. Due to the very small thickness of these droplets, high accuracy as well as a good surface finish are achieved. This method is similar to the classic 2D ink-on-paper printers on the market. Instead of depositing droplets of ink on paper, this method deposits droplets of material that are cured with UV light.

## 2.4 Fused deposition modelling 3D printing

After introducing the most common and widely adopted additive manufacturing techniques, we now focus our attention on the manufacturing method that will be used in the following: Fused Deposition Modelling (FDM) 3D printing. We present here the most

important parameters that are involved in this manufacturing technique, in particular, we focus on the flow rate of material. Additionally, we will review the applications of this manufacturing technique that can be found in literature and that are relevant for this work.

### 2.4.1 Parameters of FDM 3D printing

Designing a part to be 3D printed using Fused Deposition Modelling requires, first of all, the selection of the material to be used. Some materials require a controlled environment or higher temperatures that may or may not be achievable by the machine available to the user. Each material is characterised by an optimal temperature of extrusion: this is the temperature to which the material should be heated in order to obtain the optimal viscosity for 3D printing. However, this is not the only temperature that should be considered. The temperature of the printing bed and the ambient temperature also play a role, especially with some higher-end materials (for example, polycarbonate) as this affects proper adhesion to the buildplate as well as retention of shape during solidification. A high printing bed temperature and ambient temperature, usually achieved by adding a front enclosure to the printer, ensure the correct cooling profile to avoid warping and to ensure adhesion to the build plate. Another important parameter is the printing speed. This can either be interpreted as the speed at which the print head moves, or the speed at which the stock filament is pushed into the printing head. These two definitions of printing speed are equivalent, as they are related by a simple conservation of mass relation between the filament fed into the printing head and the filament extruded from the nozzle. An in-depth discussion on the topic can be found on the work by Go et al. [2017]. A lower printing speed requires less material to be extruded in a fixed amount of time, improving the finish of the part and the accuracy of the movements. With some materials (for example PLA), it is possible to achieve higher-than-standard speeds by slightly increasing the extrusion temperature to ensure proper flow of material, provided that the extruded material is cooled effectively and rapidly to avoid unwanted deformations. Cooling is another parameter: the printing head is usually equipped with a fan, the speed of which can be controlled. The parameters mentioned in this section are particularly important not to overlook when the part to be printed has overhangs, with or without support, or tall sections that are far apart. This is because in the case of overhangs, the material needs to be cooled before gravity can deform the part; while in the case of sections that are far apart, when the printer stops the extrusion to move to a new location on the build plate to continue the print, material can ooze from the nozzle, leaving unwanted thin strings of material between separate parts of the print (this is usually referred to as *stringing*). A lower printing speed, adjustments to the extrusion temperature and a higher speed during repositioning of the print head are usually sufficient to solve the issue (see All3DP for more information).

### 2.4.2 Flow rate of material in FDM 3D printing

We now refer back to Figure 2.8 and we focus our attention on detail (3) of the figure: these rollers are responsible for pushing the stock material in filament form into the heating element. These rollers are responsible for pulling the filament from the spool of stock material and pushing it into the heating element. The stepper motor that drives these rollers is calibrated so that the correct rotational speed is applied, to achieve the required dimensional control over the parameters of the extruded filaments [N. Turner et al., 2014, Gold and Turner, 2015]. Two main limitations can be identified here. The motors are characterised by a maximum speed at which they can rotate and by a maximum torque that they can apply. This limits the maximum flow rate of material, together with possible loss of traction, causing the filament to slip with respect to the rollers. For instance, with a large nozzle, the amount of material that needs to be extruded may require a speed that the rollers cannot achieve. Similarly, when the nozzle is small, the pressure drop through the liquefier increases, increasing the necessary torque to push the material out. In this case, it is possible that the motors cannot apply the amount of torque needed, that the filament buckles under the compressive load given by these motors [Go et al., 2017] or that the filaments slips when the rollers rotate, due to the pressure build-up inside the nozzle. These concept will be relevant in the following, when we explore the possibility to alter the flow rate of the material to obtain filaments of arbitrary diameter using a fixed-nozzle machine.

### 2.4.3 Applications

FDM as a manufacturing process has been used in a wide variety of sectors. A common application is the production of physical 3D models of prototypes. This can be used, for example, by physicians to communicate effectively with the patient, informing them and empowering them. The model can be used as an effective and cheap visualisation aid for immediate understanding of an operation or of an anatomical issue that needs to be well understood by the patient for their therapy and recovery, or by the clinicians themselves. The same idea can be applied to other engineering sectors, for example as a visualisation aid to compare surface roughness, or any laboratory test that generates data points that can be converted into 3D models.

As mentioned before, many applications come from methods that are a modified version of FDM. Some of these modifications come in the form of software optimisation, others come in the form of material optimisation. In the first case, once the design has been optimised, then a standard FDM technique can be used to manufacture the part. Modelling allows us to optimise the structure in order to produce physiologically realistic constructs that mimic real tissue structure and function [Shipley et al., 2009]. In this work, biomedical scaffolds that host strands of gel containing cells are considered, and

the effective flow and transport properties of such a scaffold system are determined using asymptotic homogenisation. Another method of this kind has been developed to create an infill pattern for 3D printing that resembles the internal structure of bones. An optimisation process is performed on the infill of a 3D printed object in order to approach bone-like porous structures [Wu et al., 2018]. The work by Schumacher et al. [2015] proposes a method for fabricating deformable objects with spatially varying elasticity using 3D printing. However, no material modifications are made, rather a microstructural optimisation is carried out. Pre-computed small-scale structures are assembled via interpolation to obtain an internal architecture of the object to be manufactured using rapid prototyping that is optimised based on the loading chosen. These small-scale structures are chosen from a pre-computed database, and then an optimisation process takes place to interconnect them and build the final optimised microstructure. In this work by Schumacher et al. [2015], due to some manufacturing constraints, the AM method chosen is SLS (selective laser sintering), however, once the microstructure is optimised, any AM technique that satisfies the requirements could be used.

Other modifications to FDM attempt to enhance the mechanical properties of the printed parts, especially when they are load-bearing. Fibre-reinforced polymer structures are widely used for lightweight structural applications [Brenken et al., 2018]. The size of the machine also increased considerably, as well as the dimensions of the parts that can be printed. Some applications include the manufacturing of moulds and tooling. Their production, however, is energy- and labour-intensive. A novel approach, that makes use of 3D printing to generate light structures with hierarchical architecture by orienting the molecular domains with the printing path, has recently been proposed [Gantenbein et al., 2018].

As we have seen before, the accuracy and precision at which it is possible to manufacture parts is possibly the most relevant aspect of the characterisation of FDM parts. There are many factors that affect how accurately the manufactured part represents its intended CAD model. The successful manufacturing of parts using fused deposition modelling can depend on the orientation of the part, the temperature of the process and the material chosen, as well as the machine. Therefore, it is essential to be able to characterise the process. The relationship between these parameters and the resulting properties must be determined. The work by Gold and Turner [2015] reviews the materials and dimensional accuracy for FDM and similar extrusion-based AM processes, together with methods for evaluating performance parameters. A study on the physical limits (rate limits) of fused deposition modelling 3D printing and guidelines for this kind of systems is also available [Go et al., 2017]. This study exploits limits on the build rate, the maximum throughput and the speed of the actuators. It is important to learn how to improve the manufacturing process and the machine design. This understanding, as well as its continuous expansion, are essential to improve extrusion processes such as FDM

expanding their range of applicability and enhancing the mechanical properties of the final parts.

Despite many improvements in manufacturing, there have been works demonstrating the capability of AM techniques to produce biomedical scaffolds with tailored properties. 3D fibre deposition was used to fabricate well-defined and custom-made scaffolds for tissue engineering with 100% connected pores [Moroni et al., 2005]. This work examines the influence of co-polymer composition in terms of their swelling on dynamic mechanical properties of the scaffold. The results indicate that by coupling structural and chemical characteristics, the viscoelastic properties may be fine-tuned to achieve the desired properties.

## 2.5 Tissue Engineering

*Tissue Engineering* (TE) is undergoing rapid advances. The main reasons for this are the development of manufacturing methods like 3D printing and 3D bioprinting, which helped in achieving a degree of customisation, design and patient-specific features that greatly improved the applicability and customisation capabilities. Despite these important developments, there is still a long way to go before complex organs can be synthetically produced. Many novel ideas are still at laboratory level and require further developments before they can be used in operating theatres or implanted.

The main issues to date with tissue engineering come from two fronts: the technology barriers and the ethical or regulatory barriers. Technology barriers refer to all of the limitations imposed by the current state of technology, be it in the manufacturing process and materials or in the specific subject knowledge necessary to achieve clinical applicability [Bonfield, 2006]. A recent review by Francis et al. [2018] looks at the technology barriers in the four major components of the field of cartilage tissue engineering: cells, scaffolds, chemical and physical simulations. Due to these limitations, there have not yet been human clinical trials using 3D printed cartilage tissue, for instance. The second front regards ethical barriers and regulatory issues [Gilbert et al., 2018]. These arise from questions such as whether there is a limit as to what should be bioprinted and whether the risks of harm to humans during testing is justifiable. Other questions that arise regarding the irreversibility of the treatment—due to how the patient's cells grow inside the scaffolds, it is not easy to withdraw from trial—but also the loss of treatment opportunity—accessing a new and superior treatment in the future might not be possible due to technical and biological reasons. Although the ethical issues must be addressed, the technological barriers should be brought forward. Until the technology develops enough to be able to manufacture grafts and scaffolds with satisfactory properties capable of carrying out some preliminary tests, it is unlikely the ethical and regulatory questions can be satisfactorily answered.

Manufacturing is a key technological barrier that currently limits the applicability of materials in medicine. A key point is the combination of tissue engineering with 3D printing. The idea of applying 3D printing to tissue engineering usually comes in the form of porous or solid scaffolds made of polymers or metals; however, recently, the advent of 3D bioprinting pushed the boundaries even more. This renders even more important advances in 3D printing manufacturing processes as these could have a strong impact on bioprinting. Both 3D printing and 3D bioprinting have had a huge impact in the field of tissue engineering. An example of how these methods can be used, both as a research tool, as well as for the medical sector is the BioPen [Bella et al., 2018]. The BioPen is a hand-held device that can be used by doctors directly in the operating theatres and can be seen in Figure 2.12. It makes use of coaxial extrusion to deliver bioscaffold and cultured cells directly in vivo to the location of the cartilage defect. This device develops from the 3D printing pens available on the market. Additionally, the development of this medical device made use of standard 3D printing for the prototyping and testing stages of development. Another example of developments in the field of 3D printing and tissue engineering is the work by Marga et al. [2007]. Here, a novel approach is presented to build 3D living structures, in which cell aggregates are printed instead of individual cells, assuring a significant gain in speed. This work makes use of the differential adhesion hypothesis [Steinberg, 1963] to illustrate the role that tissue fusion and tissue liquidity play in the process of manufacturing.

### 2.5.1 Biomedical scaffolds

Musculoskeletal tissue, bone and cartilage are under extensive investigation in tissue engineering research [Hutmacher, 2000b]. The work of Simske et al. [1997] reviews the pertinent aspects of bone morphology and metabolism, and the subsequent engineering considerations. This review sees composites as the future of porous materials in bone tissue engineering. A recent review from Do et al. [2018] provides an overview of the developments of 3D printing in the field of tissue engineering, as well as points out the main hurdles that still need to be overcome, such as the preservation of tissues and cells for long-term storage, and the prevention of tissue and cell rejection.

Issues regarding the vascularisation of scaffolds make cartilage regeneration particularly appealing for AM technologies. This tissue-type does not have a dense net of capillaries inside and it only contains very few resident stem cells, meaning that the chance of self repair is very little. This application is then very promising for additive manufacturing, as vascularisation remains one of the biggest challenges. Additionally, scaffolds that are currently manufactured with non-additive-manufacturing technologies, lack the control and the ability to completely customise the microstructure that are inherent of AM technologies. Many of the conventional methods for the production of scaffolds fall short of AM technologies, as they cannot achieve structures with the same control over the

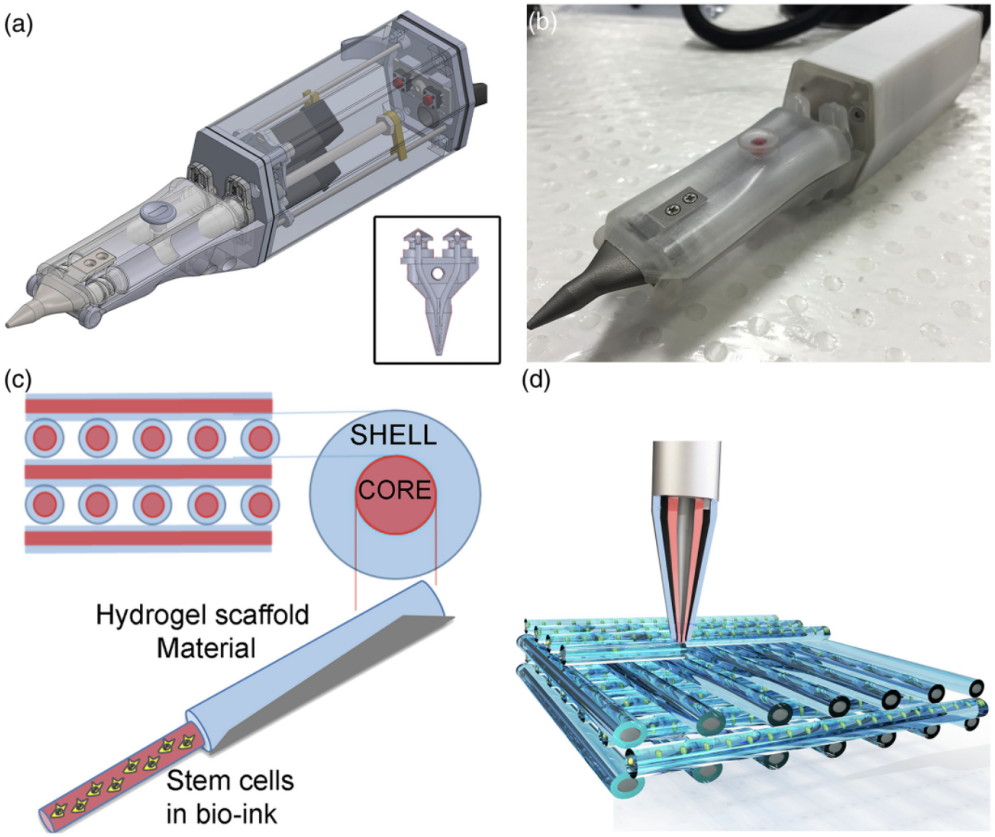


Figure 2.12: (a) Design of the BioPen, which shows the two separate chambers with a motor control. The two chambers are connected to the printing nozzle (insert), which allows the coaxial printing of the two different bioinks in a core/shell distribution. (b) Photograph of the biopen. (c) Representation of the core/shell distribution. (d) Representation of the multiple layer three-dimensional printed block in a criss-cross pattern . Adapted from Bella et al. [2018].

parameters. Examples of methods used in the past include the formation of macro pores using additives to cement powders that are then chemically treated to obtain $CO_2$ bubbles [del Real et al., 2002], and the construction of a synthetic biomaterial of ICPC (injectable calcium phosphate cement) combined with recombined bone xenograft granules [Weimin et al., 2013]. Solvent casting is another viable method. Here, 2D films or 3D scaffolds are fabricated by evaporation of a solvent in a polymeric solution [Haider et al., 2020].

Additive manufacturing, on the other hand, provides excellent control over the microstructure. Metal foams and ceramic porous scaffolds obtained with laser sintering methods are commonly found in literature [Duan et al., 2010, Yuan et al., 2019]. However, these methods are expensive, both for the machine that is needed and for its maintenance and use. Fused deposition modelling (FDM) on the other hand is cheap, easy to use and accessible. An early example of the use of FDM as a production method for novel scaffold architectures can be found in Zein et al. [2002], where layers of directionally aligned microfilaments were used to produce 3D scaffolds with controllable porosity and channel size. Mechanical tests were used to better understand the anisotropic nature

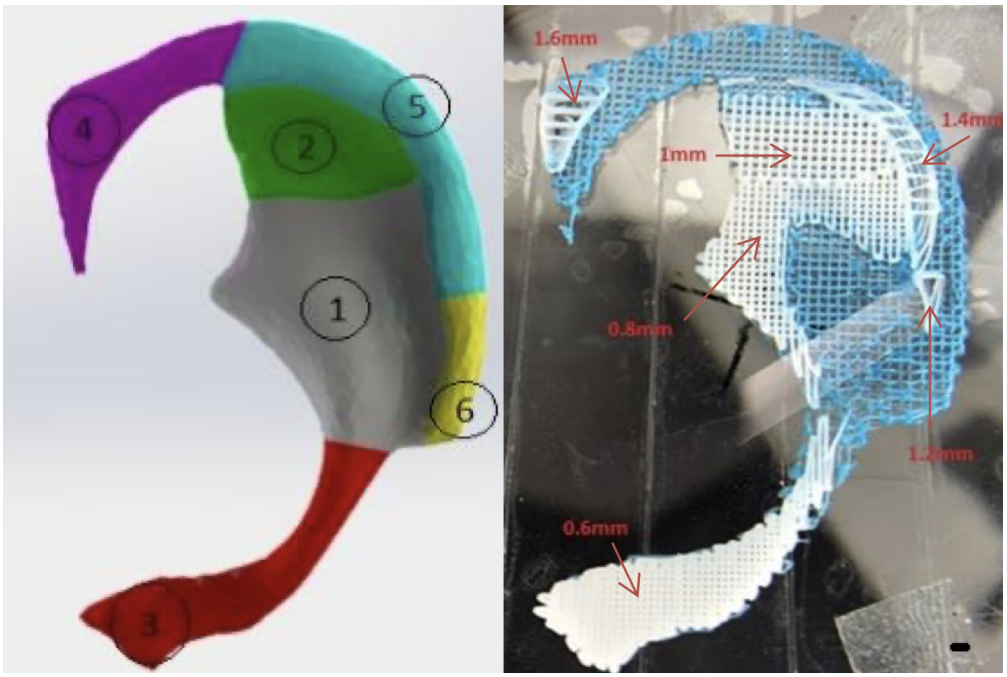


Figure 2.13: Ear scaffold. Designed model on the left and 3D printed part on the right (PCL material, manufactured using a KIMM 3D printer). Different sections have been printed with different parameters, to match the desired mechanical properties. Scale bar 2 mm. From Shahangi [2018].

of the designs. The mechanical properties were found to be generally dependent on the porosity, regardless of the design patterns and channel size, in agreement with theoretical concepts on the structure-property relationships of porous solids. A more recent example is the work of Shahangi [2018], who produced, using 3D printed polycaprolactone (PCL), an auricular structure divided into six parts, each printed with a different diameter and spacing to achieve the desired mechanical properties. Data from CT scans were used for the modelling of the structure and FEA analysis was performed for validation. This work makes use of a single material and does not need to modify the appearance of the ear, as can be seen in figure 2.13. A review by Ng et al. [2019] provides an analysis of the improvements in the 3D printing of biological tissues and scaffolds. In this review, special attention is given to the role of polymers and how they help overcome some of the major impediments in the field of organ printing.

### 2.5.2 Pore size requirements for tissue engineering

From the point of view of the interaction of the scaffolds with living cells, the majority of the works in the literature have focused on the interaction with 2D substrates with stiffness ranging from a few kPa to hundreds of MPa [Cui et al., 2009, Fu et al., 2011, Hulbert et al., 1970, Johnson and Herschler, 2011, Karageorgiou and Kaplan, 2005]. Only one work [Maggi et al., 2017] considers cell viability and functionality in 3D scaffolds with compressive moduli in the MPa range and with strut dimensions on the order of a few

microns. The parameter space in 3D is more complex; it involves the effects of relative density, effective surface area and the scaffold's structural stiffness on cell function (usually correlated with the deposition of collagen and calcium phosphate). Investigations about the effect of micro-porosity on osseointegration are also available [Hing et al., 2005]. The results indicate that the microporosity can accelerate osseointegration and elevate the equilibrium volume of bone.

Additive manufacturing is beginning to possess the capability of manufacturing porous materials at fairly small length scales, with the potential of easily tuning properties. Conventional manufacturing techniques such as foaming could result in a structure with pores that are not completely interconnected, leading to a poor diffusion of nutrients [Genzer, 2005, Bidan et al., 2013]. In order to create three-dimensional structures with controlled macro- and micro-structures, alternatives to AM have been considered, for example cryogenic prototyping [Lim et al., 2010]. In this work, micro pores of 90 µm were used, together with 300 µm channels to enhance cellular infiltration and vascularisation.

The ideal pore size is not easy to universalise—it depends on many factors depending on the application. Zadpoor [2015] reports a minimum pore size of 100 µm and a suggested pore size larger than 300 µm for bone tissue regeneration. Additionally, a single value of porosity may not even be the right choice: the work by Di Luca et al. [2016] suggests that designing porosity gradients may be an appealing strategy to support gradual osteogenic differentiation of adult stem cells. A focus on the functional gradation of scaffolds should then be considered. Additionally, porosity distribution should not be the only gradient to be studied. Mechanical properties of scaffolds can also be graded for the best structural benefits from material at different regions of a structure. It is, therefore, necessary to understand how the variations in porosity affect the mechanical properties and vice-versa, to achieve an effective material or scaffold.

### 2.5.3 Stress shielding

The most widely adopted materials for bone implants have been titanium alloys for a long time. They have excellent biocompatibility, high strength, high fracture toughness and strong corrosion resistance [Zhang and Chen, 2019]. However, there are many issues that remain unresolved. These materials have an elastic modulus on the order of ∼100–200 GPa [Nag and Banerjee, 2012]. The modulus of bone ranges from 0.2–10 GPa for trabecular bone, and from 22–26 GPa for cortical bone [Rho et al., 1997, Kopperdahl and Keaveny, 1998]. This mismatch in moduli leads to a phenomenon known as *stress shielding* [Ridzwan et al., 2007a]. The significance of stress shielding has been noticed in the past, however, the long-term effects were not known [Huiskes et al., 1992]. This phenomenon is related to the adaptive remodelling of bone due to a variation in the loading applied to it. Clinical data highlights the importance of load application to bone cells because an adequate mechanical load causes the osteoblasts to remodel the tissue,

forming denser and stronger bone over time [Maggi et al., 2017]. No load transfer from the implant to the surrounding tissues, on the other hand, leads to the activation of osteoclasts, which break down bone tissue, resulting in bone resorption. This generates weaker bone that increases the chances of fracture recurrence [Nag and Banerjee, 2012, Ridzwan et al., 2007a, Frost, 1994]. As an example, normally the femur carries external loads from the femoral head, through the femoral neck, to the cortical bone [Ridzwan et al., 2007b]. When a stiffer material is inserted into the bone, there are parts of the cortical tissue around the implant with reduced load. Consequently the bone responds by remodelling itself, in this case reducing bone mass because of the reduced stresses it has to withstand. This leads to a weakening of the bone and possible re-fracture.

As the issue is more prominent the larger the mismatch in elastic modulus between the implant and the surrounding bone, reducing the mismatch could help prevent recurring fractures. A possible solution to the issue of the mismatch in moduli could be the use of polymers and implants with porous internal structure, which may provide mechanical properties closer to those of bone, thus reducing the contrast in stiffness between the graft and the adjacent tissue. This is thought to lead to a distribution of load closer to that in the original bone, reducing the remodelling due to the presence of the implant. Secondly, polymers can be easily processed using affordable techniques, such as 3D printing, which offers the possibility to meet patient-specific requirements in terms of geometry and cut the cost considerably [Mota et al., 2015]. In this case, the idea of introducing functional gradation in the mechanical properties may help to further reduce the gap between the properties of the bone and the properties of the scaffold. Such clinical needs form the basis for the present work where tissue engineering requires subtle aspects of structural mechanics to inform implant design.

## 2.6 Manufacturing of functionally graded materials using 3D printing

A review by Sing et al. [2016] presents the progress of selective laser melting (SLM) and electron beam melting (EBM) in the field of manufacturing metallic orthopaedic implants. This work also explains how single-materials scaffolds, with their uniform structure, cannot easily satisfy the requirements needed for implants. The paper then goes on to introducing the idea of functional gradation as a method to overcome this issue. Several works regarding functional gradation have been carried out. A novel optimisation strategy has been developed for designing functionally graded cellular structures with desired mechanical properties [Li et al., 2018]. In this work, a variable-density gyroid structure is created, then optimised using graded structure optimisation. A very recent work by Scaffaro et al. [2020] presents another useful application of functional gradation, the controlled release of substances. Functionally graded laminates were manufactured

by direct electrospinning onto dense substrates achieved by solvent casting. An increase in stiffness was achieved, as well as a reduction of burst delivery of carvacrol.

The majority of the works in this area seem to focus on the porosity from biological perspective, rather than from the point of view of the mechanical properties. Laser-engineered net shaping (LENS) has also been used in the past for the production of a complex-shaped metallic implant with functionally graded porosity [Krishna et al., 2007]. The variation in porosity results in a structure with spatially varying properties, however, the direct connection with mechanical properties is not usually explored. It has been shown that a gradation in stiffness can affect the response of cells [Singh et al., 2010]. This is the local stiffness, whereas often the bulk stiffness may also need to be functionally graded for optimal structural performance. To be able to achieve this, a direct control over the properties is necessary. A novel method for the production of functionally graded structures is needed, which does not focus on porosity as the parameter to control the mechanical properties of the structures. Rather, porosity and mechanical properties should be controlled separately and independently to achieve the desired results. Additionally, the conventional fabrication methods mainly provide a way for the porosity to be discretely varied, rather than continuously. The third issue is in the traditional manufacturing processes as they are expensive, very elaborate and complex. Fused Deposition Modelling can overcome many of these issues. Additionally, being a cheap and accessible method, research in this area can grow much more rapidly, helping this manufacturing method to achieve its potential.

## 2.7 Current state of the biomedical applications of 3D printing

3D printing has greatly evolved since its initial use as pre-surgical tool, which made it available to many applications in the biomedical world: devices, implants, scaffolds, as well as diagnostic platforms and drug delivery systems [Chia and Wu, 2015]. A recent review by Durfee and Iaizzo [2019] provides an overview on 3D printing and how it has been used in various medical applications, from cardiac 3D printing, to low-cost limb prosthetics and orthotics. The ability of 3D printing to produce customised medical devices has been demonstrated and practical applications are rapidly replacing laboratory-level attempts [Tofail et al., 2018]. For example, a customised bioresorbable tracheal splint, created from the computed tomographic image of the patient's airway, was implanted in an infant with tracheobronchomalacia [Zopf et al., 2013]. However, not all of the applications are for implantation. 3D printed hearts have been used to effectively illustrate a range of heart conditions for education and training. Another interesting story comes from the University of Minnesota [Con, 2017], where the connected hearts of two twins have been imaged and a 3D model has been 3D printed. This tangible model of the connected hearts helped the surgeons in planning the surgery for their separation.

Many limitations of additive manufacturing in the context of biomedical engineering still needs to be addressed, mainly due to the limited number of materials available that have sufficient mechanical properties as well as the required biocompatibility and biodegradation properties, but also the need to address lower resolution features in the manufactured parts. Due to the increasing number of applications and the improvements in materials and manufacturing processes, research in the area of materials and manufacturing can only be beneficial to this fast-growing sector. There are three main bioengineering areas where 3D printing is ever more present: the field of tissue and organ regeneration, orthopaedic implants, and pharmaceuticals.

### 2.7.1 Tissue and organ regeneration

3D printing and 3D bioprinting have both seen tremendous advances in the past few years, and their applicability in the field of tissue and organ regeneration drastically increased. Soft-tissue prosthesis moulds have been successfully produced using a desktop 3D printer [He et al., 2014] through a method known as SPPC—Scanning Printing Polishing Casting. The anatomy is scanned, a mould is designed and 3D printed, the mould is chemically polished to remove the staircase effect (due to the layering of the manufacturing process) and obtain a smooth surface. This method turns out to be much cheaper than the current fabrication methods for soft prosthesis. 3D bioprinting has been used not only for the generation and transplantation of several tissues [Murphy and Atala, 2014]—like skin, bone [Bose et al., 2013, Inzana et al., 2014], heart tissue and cartilaginous structures—but also to develop tissue models for research.

A variety of interesting applications of 3D printing for tissue regeneration can be found in literature. A 3D printed bionic ear was successfully developed by [Mannoor et al., 2013]. Here, the ability to interweave biological tissue with functional electronics is exploited. The result is an enhancement of the auditory sensing for radio frequency reception, and the possibility to listen to stereo audio with complementary left and right ears. There has also been research to create a network of blood vessels in 3D engineered tissues [Miller et al., 2012]. In this work, a network of carbohydrate glass was printed and used as a sacrificial template for the creation of cylindrical networks that could form a system of blood vessels. In the work from Noor et al. [2019], thick and perfusable cardiac patches have been manufactured using 3D printing. This work demonstrated, for the first time, the use of fully personalised 3D-printable bioinks, made from fatty tissue of the same patients.

### 2.7.2 Orthopaedic implants

Manufacturing of orthopaedic implants using 3D printing is very often achieved using powder-based techniques with ceramic materials [Butscher et al., 2011] or metallic powders such as titanium [Ryan et al., 2008]. Examples of combination of techniques are also available: a screw-like porous scaffold has been produced by means of 3D printing, then coated with hydroxyapatite (HA) to improve its osteocondcutivity [Liu et al., 2016]. A recent review by Sing et al. [2016] takes a closer look at the processes, materials and design of metallic implants obtained with laser and electron beam melting. This review reports how strength and biocompatibility are not desired to be uniform: a single composition with uniform structure cannot satisfy the requirements needed for implants [Watari et al., 1997]. A recent review on this topic [Mahmoud and Elbestawi, 2017] describes important aspects of functionally graded materials and their applications in additive manufacturing of orthopaedic implants. It also points out the importance of optimisation in the manufacturing process to obtain high quality lattice structures and implants.

### 2.7.3 3D printing for pharmaceutical applications

Together with the manufacturing process itself, the production of polymers for 3D printing is also of utmost importance for many applications. A recent study [Melocchi et al., 2016] developed and manufactured filaments to be used on 3D printers which were considered potentially suitable for printing capsules and coating layers for immediate or modified release. Another work combines fused deposition modelling with hot-melt extrusion (HME) technology to fabricate tablets with extended drug release properties [Zhang et al., 2017]. There are advantages compared to the traditional processes (milling extrudates, sieving, compressing and coating), such as an increased solubility and bioavailability of drugs, as well as a production of more complex-structured dosage forms and personalised drug products.

Tablets with different infills have been 3D printed and tested for dissolution. Different release profiles were found in [Solanki et al., 2018]. Improvements in this area could include studies on the link between the process parameters of 3D printing and the release profile of drugs from the tablets. This would allow to optimise the process parameters based on the release profile as demanded by pharmocological considerations. A similar strategy can be applied to mechanical properties. Being able to determine the connection between the response and the process parameters enhances the applicability of 3D printing as a manufacturing process. Additionally, researching the manufacturing processes themselves makes possible to push the boundaries further and achieve applications that were not possible before.

## 2.8 Conclusions

The current state of technology regarding the manufacturing of porous structures, especially by means of additive manufacturing technology was reviewed in this chapter. This includes the comparison between additive manufacturing and conventional methods of manufacturing. It has been shown how additive manufacturing technologies have several advantages, because of the personalisation capabilities, quick turn around time between design and manufacture, ability to deal with geometric complexity of shape, and the freedom of design. Gaps in knowledge have been identified, such as a relatively narrow range of materials available for fabrication, as well as the challenges due to the understanding of the connection between the mechanical properties of 3D printed parts and the manufacturing parameters.

Here is a summary of the key points:

- Additive manufacturing technology has shown great potential for many engineering and medical applications;
- Functional gradation, which means spatially varying stiffness for present, is likely to improve the structural performance for many applications;
- Improvements in the usable materials and in the manufacturing processes themselves are necessary to enhance the applicability of these methods;
- Some of the most widespread methods of additive manufacturing lack the simplicity and the availability of other methods, namely methods such as Selective Laser Sintering and similar, which require trained staff and expensive equipment, as opposed to Fused Deposition Modelling, which is accessible and easy to implement;
- Fused Deposition Modelling has disadvantages over some of the more sophisticated methods but with research, the potential of this method can grow immensely;
- Not all applications require sophisticated and expensive methods;
- Processing parameters are linked to the mechanical properties of the resulting object: a clear evaluation of this link could lead to microstructure optimisation leading to an even higher applicability of the process.

To conclude, this works focuses on Fused Deposition Modelling 3D printing and on the link between the processing parameters of this manufacturing process and the resulting mechanical properties. This will be exploited to innovative ways of producing functionally graded lattice structures. We will focus on the difference between gradients in porosity and in mechanical properties, as well as provide a novel technique for the production of functionally graded materials control of process parameters.

# Chapter 3

# Adaptable diameter extrusion using fixed bore FDM nozzles

Functionally graded materials are often found in nature. For example, the internal structure of a bone is characterised by hard tissue with decreasing density and increasing pore size towards the centre. Reproducing this spatial variation in the properties to mimic the original tissue is important in the field of biomedical engineering. This could reduce the risks of subsequent fractures. Another possible application for FGMs is in weight reduction for specified function of a structure. The possibility to tailor the properties based on the local requirements can save material. Otherwise, the whole structure would need to have the properties required for the highest local load, resulting in excess material where not necessary. We have seen this in Chapter 2, where a number of works make use of materials that exhibit a spatial variation in their porosity. This can be achieved by adjusting the polymer melt viscosity during foaming via temperature [Zeschky et al., 2005], by centrifugation of a solution that is then quickly solidified [Harley et al., 2006] or by means of porogens [Werner et al., 2002]. Additive manufacturing techniques have also been used to produce composite scaffolds for articular cartilage repair [Sherwood et al., 2002] and scaffolds with concentric regions of different porosity to mimic the average bone composition [Kalita et al., 2003]. However, the lack of a consistent, reliable, yet affordable method for production of functionally graded materials is the motivation behind this course of research. Current additive manufacturing techniques have failed to deliver structures with continuously graded properties, even when specific hardware modifications were adopted.

This work explores the possibility of manufacturing novel structures with spatially varying stiffness using existing FDM hardware, such as a standard desktop 3D printer. Here we propose to achieve this by controlling a process parameter, responsible for the amount of material that is extruded during the printing process. The proposed approach requires

systematically characterising the response to variations in the input commands. The essential idea is simple. Extrusion-based printers have a nominal nozzle diameter. Actual velocity of extrusion can be controlled by the volume flow rate independently. Therefore a limited amount of control on the diameter of the extruded material can be envisaged by under-extruding or over-extruding using the pressure of the machine that can be controlled using a computer code. The rheology of the molten polymer is complex, with a velocity profile through the cross-section, which is expected to result in the diameter of the solidified extruded material with size that is variable for a fixed nominal diameter of the nozzle. In this way, if successful, one would be able to use an affordable and conventional FDM machine as if it had *variable-diameter nozzle*. This research hypothesis that extrusion of material can produce spatially varying stiffness by the use of under- and over-extrusion, runs through the present work starting with the simplest validation of the idea to producing and characterising complex lattice structures.

In this chapter, we present the manufacture of single filaments by controlling the process parameter that affects the extrusion rate and characterise the cross-section of the extruded filaments. This characterisation has been carried out on two different FDM machines. By following the procedure presented here, users of other 3D printers can find the correct calibration for their machines, and make use of our technique. The aim of this work is to produce filaments with continuous spatial variation of mechanical stiffness. This chapter presents the basics for the use of this method, i.e. how to vary the diameter of the extruded filament in fused deposition modelling 3D printing, by controlling the code that drives the machine. Subsequent chapters will make use of the technique presented here, for the production of films with continuously varying properties.

## 3.1 Methodology of fabrication and characterisation

### 3.1.1 Fabrication of variable-diameter filaments

The fabrication of variable-diameter filaments was achieved using two commercial desktop FDM 3D printers: Ultimaker 2+ (UM2) and an Ultimaker 3 Extended (UM3) (see Ultimaker [2011] for specifications). Ultimaker 2+ can be fitted with interchangeable nozzles of four different diameters: 0.25 mm, 0.4 mm, 0.6 mm, 0.8 mm. Ultimaker 3 does not support interchangeable nozzles but is equipped with a cartridge-like 0.4 mm print core. The procedure for fabrication using these 3D printers requires a 3D model to be sliced by the use of a software, which then saves a G-code file that contains the list of commands that the 3D printer needs to follow, to obtain a 3D printed version of the 3D model. G-codes are instructions for tool path generation and have been used in conventional machining such as CNC milling machines. The language provides very basic instruction for the movement of tool path. The same language has been adopted by

the 3D printing manufacturers, so that a CAD drawing generates G-codes to control the path of the nozzle of FDM printers.

In this work, a bespoke MATLAB [MATLAB, 2016] script was created, which directly generates an ASCII-file containing the machine code, known as G-code, that drives the 3D printer, details of which will be given in Section3.2. This code drives the FDM nozzle path, in addition to controlling some other process parameters. To produce variable-diameter filaments, process parameters within the G-code were overridden, so that over-extrusion, or under-extrusion, could be realised. The details of this are presented in Section 3.2, and involve a process parameter $E$ that is responsible for controlling the amount of extruded material and consequently the diameter of the extruded filament. Due to the different ways in which this parameter $E$ is interpreted by different machines, the MATLAB code required adjustments based on the machine. There exist slightly different versions of G-code in different "dialects" of the machine language, and also the internal handling. These different versions are often referred to as different *flavours* of G-code. Both printers were fed with standard Ultimaker PLA, polylactic acid feeder material, either in white or grey colour. Although no difference in the fabricated structures or their mechanical properties was observed for materials of different colours, the samples used for testing have always been manufactured using white PLA.

The in-house developed MATLAB script mentioned above takes manufacturing parameters as input and returns a G-code file as output. These manufacturing parameters, related to the lattice to be 3D printed, are: the number of layers in the $z$-direction, the number of filaments along the overall $x$ and $y$ axes, the nominal diameter of the nozzle fitted on the machine and the $x$ and $y$ dimensions of the required sample. This allows us to fabricate rectangular lattices of any dimension and spacing. The value for the nozzle diameter can also be modified in the code without physically changing the nozzle on the machine, to induce the printer to over- or under-extrude, resulting in thicker or thinner printed filaments. For the fabrication and experimental characterisation carried out in this chapter, we manufacture several samples of filaments with fixed diameter first; each filament has a specified diameter that differs from the nominal nozzle diameter. Samples of filaments with spatially varying stiffness are presented in future chapters.

Together with the manufacturing parameters related to the lattice, there are a number of process parameters related to FMD 3D printing that need to be chosen. The four essential parameters that need to be chosen are: the printing temperature, the printing speed, the temperature of the print bed and the speed of the cooling fan. Unfortunately these parameters depend of several factors, mainly ambient temperature and humidity, which need to be taken into account. This means that there is no single value for these parameters that can be used, even for the same exact print. However, a range of values can be given. The printing temperature is probably the most consistent of these parameters: a value of about 210 °C has been used throughout this work. Minor tweaks to the temperature may be needed if the printing speed is increased (215 °C)

or if the part to be printed has large overhangs (205 °C). The printing speed depends on the desired precision and on the amount of overhangs that are present in the part to be manufactured. A good range for the type of lattices manufactured in this work has been found to be 800–1200 mm/ min, where the speed represents the speed at which filament is fed into the printing head (the speed of the printing head is handled by the machine automatically, through conservation of mass). It has been observed that a value of 1000 mm/ min usually leads to good results for lattices with overhangs up to five-ten times the diameter of the filaments. The temperature of the print bed was usually chosen to be 40–60 °C, however, especially with PLA material, the heating of the print bed is not essential. If no heated printed bed is used, especially for 3D printers with a glass print bed, tape is used to cover the surface, to ensure proper adhesion of the part. The speed of the cooling fan is usually expressed as a number between 0 and 255 in the G-code: generally, a value of 100 was used, indicating then about 40% fan speed. If deformation is observed on the part, this number is increased. When deformation is still present with fan speeds close to 100%, then it is necessary to reduce the print bed temperature or the extrusion temperature.

### 3.1.2 Methodology to characterise the fabricated filaments using microscopic measurements

Following the manufacturing phase, a characterisation was carried out to demonstrate if the proposed technique has been successful. There is no guarantee that this would be the case, because the process of extruding pressurised filaments, followed by solidification at the atmospheric pressure, is characterised by a complex flow profile within the molten material. Hence, the response of the FDM machine to the demand dictated by G-code, which has a mismatch with the nominal nozzle size, and the complex interaction with the movement of the nozzle are difficult to theorise and predict. Here we test the simplest hypothesis that the machine dispenses material volume as per rate demanded and the diameter of the extruded material upon solidification approximately obeys simple flow continuity, i.e. the diameter increases or decreases to compensate for a variable extrusion rate. Indeed, with so many complexities involved, this may not be true and instead of modelling the flow, the controller of the machine, or the solidification process, here we propose to fabricate filaments produced by changed demands of extrusion through a fixed diameter nozzle and then to test if over-extrusion or under-extrusion is at all possible using these standard FDM machines. Once this is established, we then go on to quantitatively test this against the simple hypothesis of solidified diameter approximately compensating the enforced changes in the flow rate. This allows us to calibrate the machine so that a specific diameter can be obtained just by modifying the parameter in the G-code.

Twenty samples were manufactured, each with a different, but *fixed* value for the process parameter, resulting in a set of twenty samples with varied intended diameter of the filaments with which they were manufactured. Over-extrusion and under-extrusion was carried out for different nozzles (each of fixed diameter again). A microscope was then used to image the manufactured filaments together with a scale given by a stage micrometer. Post-processing of the image was carried out using an image processing software (Adobe® Photoshop® software, see Photoshop [2019]). A scale could be set, based on the stage micrometer in the frame, and a measurement of the filament could be taken. The images were $2448 \times 2050$ pixels with the 0.1 mm stage micrometer spanning 144 pixels, resulting in a scale of 1440 pixels/mm. Five measurements were taken at five random locations in each sample, giving us five values of filament diameter for each value of the parameter. This gives an idea on the variability of the diameter and also provides a mean value for the filament diameter to be associated with the value of the process parameter used to manufacture the sample. Plotting these results against the expected theoretical relation, we obtain a master curve that can be used as calibration for the printer, allowing users to obtain filaments of the desired diameter (within a specific range).

### 3.1.3 Procedure for validation of under- & over-extrusion by weighing the samples

The method described above to measure the diameter of the filaments using an optical microscope assumes circular cross-section, which is not strictly correct, because the observed cross-section has ovality due to the creeping flow under gravity. There is no guarantee that cross-sectional shapes are circular, and with only five measurements taken for each sample, the average behaviour and response of the printing machine requires another independent measurement. Microscopic measurements taken in total were around 400, only for the Ultimaker 2+: this arises from a combination of 4 nozzles, 20 samples for each nozzle, and five measurements for each sample. The benefits of taking more measurements would not be comparable to the amount of time needed for production, testing and post-processing. Another possible method to study the cross-sectional shape of the printed filaments could have involved the use of a Scanning Electron Microscope (SEM). This, however, would be highly dependent on the position where the sample is broken: the cross-section of the filaments of the first layer is affected by the distance between the nozzle and the print bed, while filaments in subsequent layers are affected by whether the cross section is taken in the hanging portion of a filament or close to where the filament interacts with the layer on which it rests. This section explains the method used to address these issues, by weighing samples. The averaging effect of considering the mass of the samples gives a good idea of the average extrusion rate of the 3D printer from start to finish.

We consider 3D-printed lattices that consist of a set of extruded filaments arranged in a woodpile fashion: filaments running orthogonally in alternate layer are stacked over each other. The sum of the lengths of the extruded filaments, $L$, is calculated by the MATLAB script that generates the tool path, hence it is known. The mass of the samples can be easily converted into the volume of extruded material, $V$, by means of the density of PLA filament material. The density is known to be $\rho = 1.24\,\mathrm{g/cm^3}$, from the technical data sheet of PLA, directly from the Ultimaker website [Ultimaker, 2011], alternatively, the density can also be calculated weighing a given amount of filament and using Archimedes' principle. The volume of extruded material can be converted into the average cross sectional area, $A$, making use of the total length of extruded filament. To summarise, if $m$ is the mass of the sample, we can write $m = \rho V = \rho L A$, so that

$$A = \frac{m}{\rho L}. \tag{3.1}$$

Assuming that the cross section of the filament is circular with radius $d$, we then have $A = \frac{1}{4}\pi d^2$, which combined with the previous expression gives

$$d = \sqrt{\frac{4m}{\pi \rho L}}. \tag{3.2}$$

This assumes that the volume of the extruded material is arranged in a set of cylinders of a length equal to the total length of extrusion $L$, as given by the MATLAB script, and with a uniform circular cross-sectional area, $A$. Discrepancies between the diameter measured with the optical microscope as explained in the previous section, and the diameter obtained using the average cross-sectional area as just explained led to the consideration that the cross section is not always circular. We accounted for these deviations by allowing for the cross-section to be elliptical.

The measurements taken on the microscope images correspond approximately to the major axis diameter of an ellipse, $d_M$, because gravity flattens circular cross-sections in a manner that the minor axis is vertical and the major axis is horizontal. Since microscopic measurements are in the top view, one measures the major axis diameter of such elliptical cross-section. Then, from the mass of the sample, one could find the minor axis diameter $d_m$, so that the volume matches that of extruded material. We can take equation 3.1 and use the substitution $A = \frac{1}{4}\pi d_\mathrm{m} d_\mathrm{M}$, where $d_\mathrm{M}$ is the microscope measurement and $d_\mathrm{m}$ is the only unknown. This leads to the expression for the minor axis diameter

$$d_m = \frac{4m}{\pi \rho L d_M}. \tag{3.3}$$

Instead of elliptical cross-section, any other cross-sectional shape described by two parameters could be used and assumed to be the cross-sectional shape, using the procedure above to find the unknown *height* of the shape (*width* of the shape is the microscope measurement). For example, the stadium shape, shown in Figure 3.1, as seen in the

| shape | ELLIPSE | STADIUM |
|---|---|---|
| sketch | 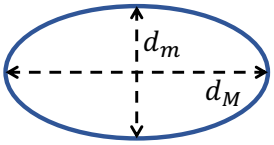  | 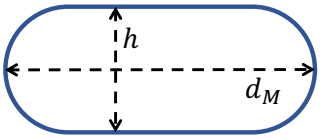  |
| area | $A = \frac{\pi\, d_m d_M}{4}$ | $A = \frac{\pi\, h^2}{4} + h(d_M - h)$ |
| *height* given width and mass | $d_m = \frac{4\, m}{\pi\, \rho\, L\, d_M}$ | $h = \frac{-d_M + \sqrt{d_M^2 + 4(\frac{\pi}{4}-1)\frac{m}{\rho L}}}{2(\frac{\pi}{4}-1)}$ |

Figure 3.1: The table shows two shapes that could be used as assumptions for the cross sections. On the left, the elliptical cross section, the one chosen in this work; on the right, the stadium shape, a possible alternative. The idea is to use the microscope measurements as $d_M$, and obtain the second parameter ($d_m$ or $h$, in these examples) making use of the mass $m$ of the sample and the length of extruded filament $L$.

work by Serdeczny et al. [2018] could have been assumed as cross-sectional shape. Figure 3.1 shows the elliptical shapes and its dimensions and the stadium shapes and its dimensions; additionally, their area and the value of the height parameter given the mass of the sample, are presented in the table.

## 3.2 Fabrication of variable-stiffness filaments by controlling process parameters

We have seen in Chapter 2 that the conventional manufacturing processes produce functionally graded materials mainly using composites, hence multiple materials, to achieve localised properties. Although these techniques lead to a structure with properties that vary in space, it is often unclear or not specified how *mechanical* properties are affected or under what *loading conditions* these mechanical properties vary in space. In this section we present a novel technique for manufacturing lattice structures with graded *mechanical properties*. Two main factors contributed to the development of the proposed approach: the identification of a process parameter responsible for the amount of material pushed out of the 3D printer nozzle, and the ability to directly create the G-code that drives the printer. This combination allows us to achieve variable-diameter filaments during the

```
1 M109 S210
2 M106 S100
3 G10
4 G0 F12000.00 X60.00000 Y50.00000 Z0.60000
5 G0 F1000.00000 X60.00000 Y50.00000
6 G11
7 G1 X60.00000 Y175.00000 Z0.60000 E238.762456
```

Figure 3.2: An extract of G-code to show the main commands: $G10$ to stop extruding material, $G0$ to move the printing-head without extruding, $G11$ to start extruding, $G1$ to move the printing-head while extruding material, $M109$ to change the extrusion temperature, $M106$ to change the speed of the cooling fan.

printing process, resulting in continuously varying stiffness throughout the 3D printed body.

Computer Numerical Control (CNC) refers to automation of machine tools operated by a software. CNC systems are used for process that can be described as a series of movements and operations. G-code (international standard ISO 6983) is the most widely used numerical control programming language in the area of computer-aided manufacturing. It is a set of machine-readable instructions used for controlling the path of a tool and other associated parameters. The first implementation of a numerical control programming language was developed at the Massachusetts Institute of Technology (MIT) Servomechanisms Laboratory in the late 1950s. Since then, many implementations have taken place and this language has become very popular to control a range of manufacturing hardware. Due to G-code being already used in the manufacturing industry, their use as instructions for tool-path programming has continued in additive manufacturing. Even though the spatial information in modern CAD systems might use software tools specific to the management of spatial information of a 3D object, the machine instructions that they generate to drive the printing-head is invariably a G-code. The next section introduces this programming language and explains how this relates to the technique of fabricating variable stiffness filaments as proposed here.

### 3.2.1 Controlling the fabrication of filament diameter by G-code

An example of a series of G-code commands is shown in figure 3.2. This extract is taken from the G-code used on an Ultimaker 2 3D printer. While most features of this programming language are fairly universal, there are aspects of the dialect of the language that are machine specific. Minor differences in these dialects of programming language mainly account for machine-specific purposes and features. The lines of code are numbered here for convenience; these numbers do not appear in a G-code file (these line would all start with G or M).

The simple G-code instructions in figure 3.2 contain some of the most important commands regularly used for 3D printing, one per line. Commands can be differentiated by their first letter: *M* for commands that change parameters and functions of the machine, *G* for commands that involve movement of the printing head. Two of the most important M-commands regularly seen in G-code can be seen in line 1 and 2. The command *M*109 sets the extruder temperature and tells the machine to wait until that temperature is reached. The temperature is given in degrees Celsius after the option *S* when one wants to increase the temperature, or after the option *R* when one wants for the machine to wait for a lower temperature (cool down). The command in line 1 of the figure then tells the machine to set the extruder temperature to 210 °C and wait to reach the temperature. This command is usually seen in the first lines of the G-code as the heating elements needs to be heated to the desired extrusion temperature before starting the print, however, this command can be used anywhere in the code to alter the temperature (remembering to use option *R* instead of *S* to reduce the temperature). *M*106 sets the speed of the cooling fan: the speed is given after the option *S* as a number between 0 and 255, corresponding to the range 0%-100% relative to the maximum fan speed. In the example we then have a fan speed set to 100, which, to clarify, does not mean 100%. The maximum speed would be 255, hence that corresponds to a fan speed of approximately 40% (of the maximum speed of the fan).

Instructions starting with the letter *G* (*G*0, *G*1, *G*10, *G*11) are the main instructions; they command the machine as to *what* to do. The fields that follow the instructions starting with *G* include the parameters, or options, and they tell the machine *how* to perform the operation. We start here by explaining the commands first and we'll introduce later the options that they accept. Line 3 of the code, *G10*, instructs the machine to stop extruding. More specifically, it retracts the filament out from the printing-head, stopping the extrusion of melted material from the nozzle. When the command is given on its own, as in line 1, a default option is used. Otherwise, the length of the retraction could come as an option after this instruction: it is possible to specify *S0* for 'short retract' or *S1* for 'long retract' (the line of code would be "*G*10 *S*0"). The *G*0 instruction in lines 4, 5 is a rapid linear move used to move the printing head *without* extruding any material. A rapid movement is necessary to avoid what is known as stringing—the presence of very thin strings of polymer left during in-air movements of the nozzle. The *G*11 instruction in line 6 is the command to unretract, which is the opposite of *G*10, as it appears in *line* 3. When executing the *G*11 instruction, the printer pushes the filament back into the heated nozzle to restart the extrusion of melted material. To conclude, the *G*1 instruction found in line 7 is used for linear movements while the printer is extruding. This instruction allows the movement to be controlled precisely, accounting for the quality of the printed object, as opposed to the quick and abrupt movement executed when performing a *G*0 command.

The first four parameters following the *G0* and *G1* commands are *F*, *X*, *Y*, *Z* (see lines 4,

5 and 7 in figure 3.2). Each of these letters corresponds to a parameter and the number following them is the value for that parameter. $F$ is the feed rate, measured in mm/min, referring to the speed at which the stock filament in the spool is pushed into the printing head for extrusion. The speed of the printing head is directly related to this feed rate, adapted by the controller of the printer. For some 3D printers, parameter $F$ refers directly to the speed of the printing head. The next three parameters, $X$, $Y$ and $Z$, refer to the coordinates of the point to which the print head must move to, in the coordinate system of the 3D printer. Note that any of these options can be left out. In which case, the machine uses the last assigned value. If no new value is given to update the $X$, $Y$ or $Z$ parameters, there will be no movement in that direction. For example, the instruction in *line* 4 means "perform a fast move, $G0$, at speed 12 000 mm/min, $F12000.00$, moving to the point (60 mm, 50 mm, 0.6 mm) in the ($X$, $Y$, $Z$) reference system of the 3D printer". On *line* 5 the speed is updated to 1000 mm/min, $F1000.00000$, and the $Z$ value is missing. This means that the printing head will not move in the $z$-direction, so the nozzle movement is planar. Note that, since the $X$ and $Y$ values are the same as in the line before, such a line of code is used to update the speed $F$ only.

The next parameter, $E$ (see line 5 in figure 3.2), is related the amount of material being extruded. However, the way that its numerical value is calculated is often machine specific. We will now focus on how this parameter is calculated for the Ultimaker 2 3D printer, where its value specifies the *volume* of material extruded—we will see later in this section another possible definition. In this case, more specifically, its value is a cumulative value of the volume of material extruded in $\text{mm}^3$, from the beginning of the print. For each movement, the value of this parameter is increased by the volume of material to be used for the current movement. If $d_{\text{nozzle}}$ is the diameter of the nozzle fitted on the 3D printer and if the print head is performing a movement of length $l$ from point $A = (x_1, y_1)$ to point $B = (x_2, y_2)$, the value for $E_{\text{nominal}}$ is increased by

$$\Delta E_{\text{nominal}} = A_{\text{nozzle}}\, l = \left(\pi d_{\text{nozzle}}^2/4\right) \sqrt{(x_2 - x_1)^2 + (y_2 - y_1)^2}, \tag{3.4}$$

where $A_{\text{nozzle}}$ is the area of the nozzle and $d_{\text{nozzle}}$ its diameter. The parameter $E$ is useful for printers that have nozzles that can be changed: when a nozzle of a different diameter is fitted, a different amount of material needs to be extruded, depending on the nozzle diameter, for a given print speed. For example, four times the amount of material needs to be extruded for the same nozzle movement, if the nominal diameter is doubled. For printers with a fixed nozzle, it is possible that the value following the option $E$ be just the length of the movement, as the diameter of the nozzle is not a variable.

The diameter of the nozzle, $d_{\text{nozzle}}$, and the diameter of the extruded filament, $d$, will be different when we under-extrude or over-extrude, as illustrated in figure 3.3 for over-extrusion. We do this by controlling the extrusion rate via the process parameter $E$ in the G-code. By controlling this rate, we obtain a filament with a diameter $d \neq d_{\text{nozzle}}$. If we rewrite equation 3.4 using an arbitrary value $d_{\text{intended}}$ in place of $d_{\text{nozzle}}$, we obtain

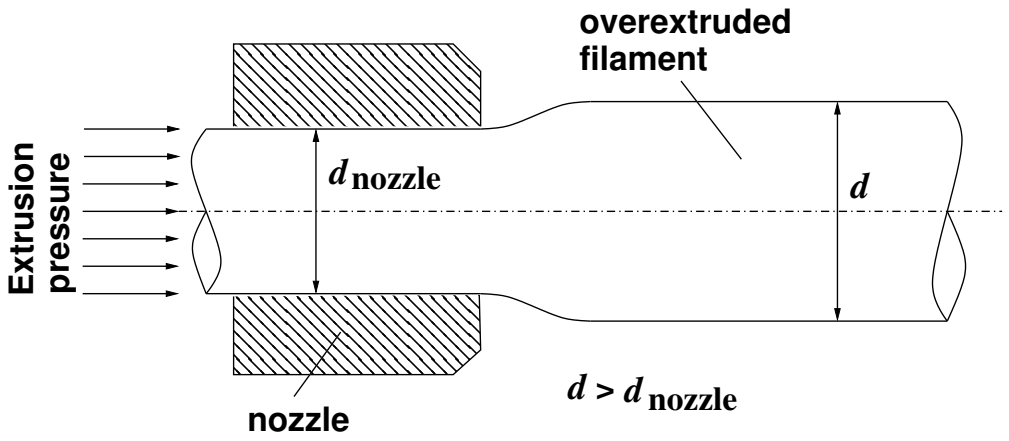


Figure 3.3: A schematic diagram of the extrusion process during over-extrusion: the diameter of the extruded filament, $d$, is greater than the nominal diameter of the nozzle $d_{\text{nozzle}}$, because of the change to the $E$ value.

a value for $\Delta E$ that differs from the nominal value:

$$\Delta E = \frac{\pi d_{\text{intended}}^2}{4} l \neq \Delta E_{\text{nominal}} = \frac{\pi d_{\text{nozzle}}^2}{4} l. \tag{3.5}$$

The subscript 'nominal' refers to the value calculated using the nominal nozzle diameter, $d_{\text{nozzle}}$; on the other hand, $d_{\text{intended}}$ refers to the value we choose to use to calculate the new value of $E$. The symbol $d$, with no subscript, refers to the diameter of the extruded filament, which may have undergone a deliberate under-extrusion or over-extrusion (see Figure 3.3). The hypothesis is that the value chosen as $d_{\text{intended}}$ will be the same as the diameter of the extruded filament $d$, or that at least a relation between the two could be established. The chosen diameter $d_{\text{intended}}$ corresponds only in theory to the diameter of the extruded filament $d$: a characterisation is necessary to establish whether this is true, or to obtain a master curve that can give indication on what value to choose as $d_{\text{intended}}$ to obtain a certain value for $d$, in case they differ. This process is what we refer to as calibration, and will be dealt with in the rest of this chapter. In the following we will plot the obtained filament diameter $d$ against the value chosen $d_{\text{intended}}$ and we will compare these results to the line $d = d_{\text{intended}}$ which represents the ideal theoretical relation between the two.

The approach of fabricating variable diameter filaments using a fixed diameter nozzle by controlling the extrusion parameters is then implemented on Ultimaker 3 Extended 3D printer next. Ultimaker 3 Extended is a fused deposition modelling 3D printer that uses a different definition of the extrusion parameter $E$ within its G-code. As opposed to the *volume* of the extruded material, as for the Ultimaker 2, the value of $E$ is now defined as the *length* of filament fed into the machine from the spool of material at the back of the printer. We introduce a new symbol, $d_{\text{spool}}$ representing the diameter of the filament in the spool of material at the back of the printer. For Ultimaker machines this value is usually $d_{\text{spool}} = 2.85\,\text{mm}$, but for some machines it could also be $d_{\text{spool}} = 1.75\,\text{mm}$. The

G-code for this model of printers would look exactly like the one showed in the previous section (figure 3.2), only the numerical value for the parameter $E$ would be interpreted differently by the machine, according to the definition just given. As an example, let us consider the diameter of the filament in the spool of material $d_{\text{spool}}$ and the diameter of the nozzle $d_{\text{nozzle}}$. During a movement between two points at a distance $l$ from each other, it is possible to equate the volume of material before and after extrusion, using $L$ as the length of filament fed into the printer from the back—which by the definition just given is the value of the parameter $E$—to obtain:

$$l\pi\left(\frac{d_{\text{nozzle}}}{2}\right)^2 = L\pi\left(\frac{d_{\text{spool}}}{2}\right)^2. \tag{3.6}$$

Considering the new definition just given for the parameter $E$ ($L = \Delta E_{\text{nominal}}$) we can obtain the value of $\Delta E_{\text{nominal}} = L$

$$\Delta E_{\text{nominal}} = L = l\left(\frac{d_{\text{nozzle}}}{d_{\text{spool}}}\right)^2. \tag{3.7}$$

In this expression, we can then substitute the diameter of the nozzle $d_{\text{nozzle}}$ with a different value to be used as a parameter to control the amount of extruded material. The altered $\Delta E$ then becomes

$$\Delta E = l\left(\frac{d_{\text{intended}}}{d_{\text{spool}}}\right)^2. \tag{3.8}$$

Again, the hypothesis that a manipulation of the parameter $E$ actually leads to a variation in the diameter of the extruded filament must be verified experimentally. This will also be tested in the subsequent sections for the Ultimaker 3 machine, and the structure thus fabricated will be characterised.

## 3.3 Microscopic characterisation of the manufactured filaments

In this section, the proposed approach for printing filaments of different diameters will be implemented and quantitatively evaluated. We used an Ultimaker 2+ desktop 3D printer [Ultimaker, 2011] and followed the methodology presented in section 3.1.2. The results are then presented plotting the diameter $d$ of the filaments measured using the microscope images, against the value chosen for the parameter $d_{\text{intended}}$, which is the intended diameter of the filament. In the following plots within this chapter, a pink line will represent perfect fidelity between the intended diameter of the filament and that of the produced filament, i.e. $d = d_{\text{intended}}$, representing the ideal situation of a

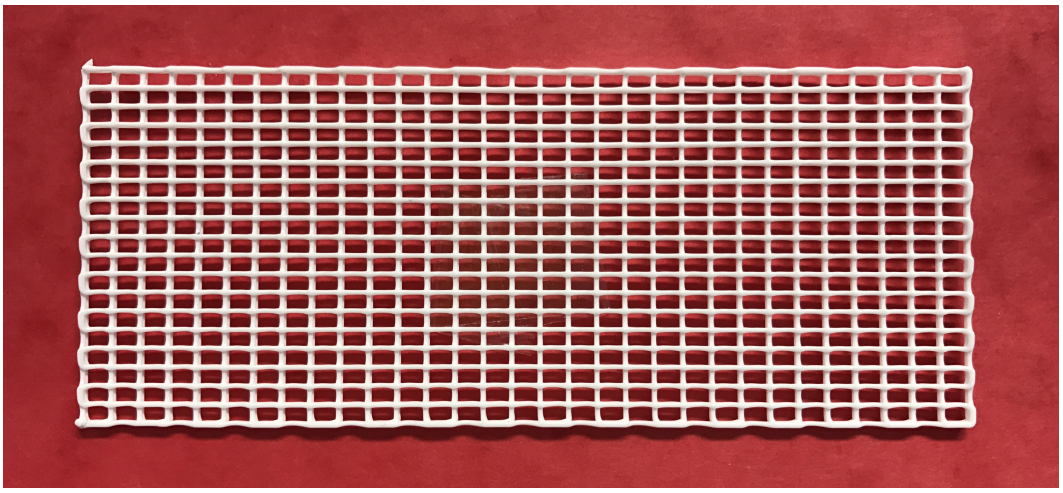

Figure 3.4: The sample used to measure the diameter of the filaments. Twenty of these samples were printed, each with a different value for the process parameter $d_{\text{intended}}$. The filaments running in the direction of the long side are the ones that have been measured.

| $\boldsymbol{d_{\text{nozzle}}}$ (mm) | $\boldsymbol{d_{\text{intended,min}}}$ (mm) | $\boldsymbol{d_{\text{intended,max}}}$ (mm) | $\boldsymbol{d_{\text{min}}}$ (mm) | $\boldsymbol{d_{\text{max}}}$ (mm) |
|---|---|---|---|---|
| **0.25** | 0.18 | 0.51 | 0.23 | 0.55 |
| **0.40** | 0.30 | 0.83 | 0.35 | 1.05 |
| **0.60** | 0.44 | 1.22 | 0.45 | 1.20 |
| **0.80** | 0.59 | 1.68 | 0.60 | 1.21 |

Table 3.1: This table shows, for each nozzle size, the range of intended diameter that has been used and the obtained range of diameter for the extruded filament.

manufactured filament of the exact same diameter $d$ as the value chosen as parameter $d_{\text{intended}}$.

This preliminary characterisation shows the range of $d_{\text{intended}}$ that gives significant achievable variations in the diameter of the filaments for each nozzle of fixed size. The range of interest of the target value of the diameter of the fabricated filament $d_{\text{intended}}$ is reported, for each nozzle, in table 3.1. An overview of the resulting range in achievable diameter is also presented there, in turn, for each of the four nozzle sizes used: 0.25 mm, 0.4 mm, 0.6 mm, 0.8 mm.

### 3.3.1 Measured variability in diameter obtained with the 0.25 mm nozzle & linearity of the response

Figure 3.5 shows the measurements obtained from samples printed using the 0.25 mm nozzle, where the resulting diameter of the manufactured filament is plotted against

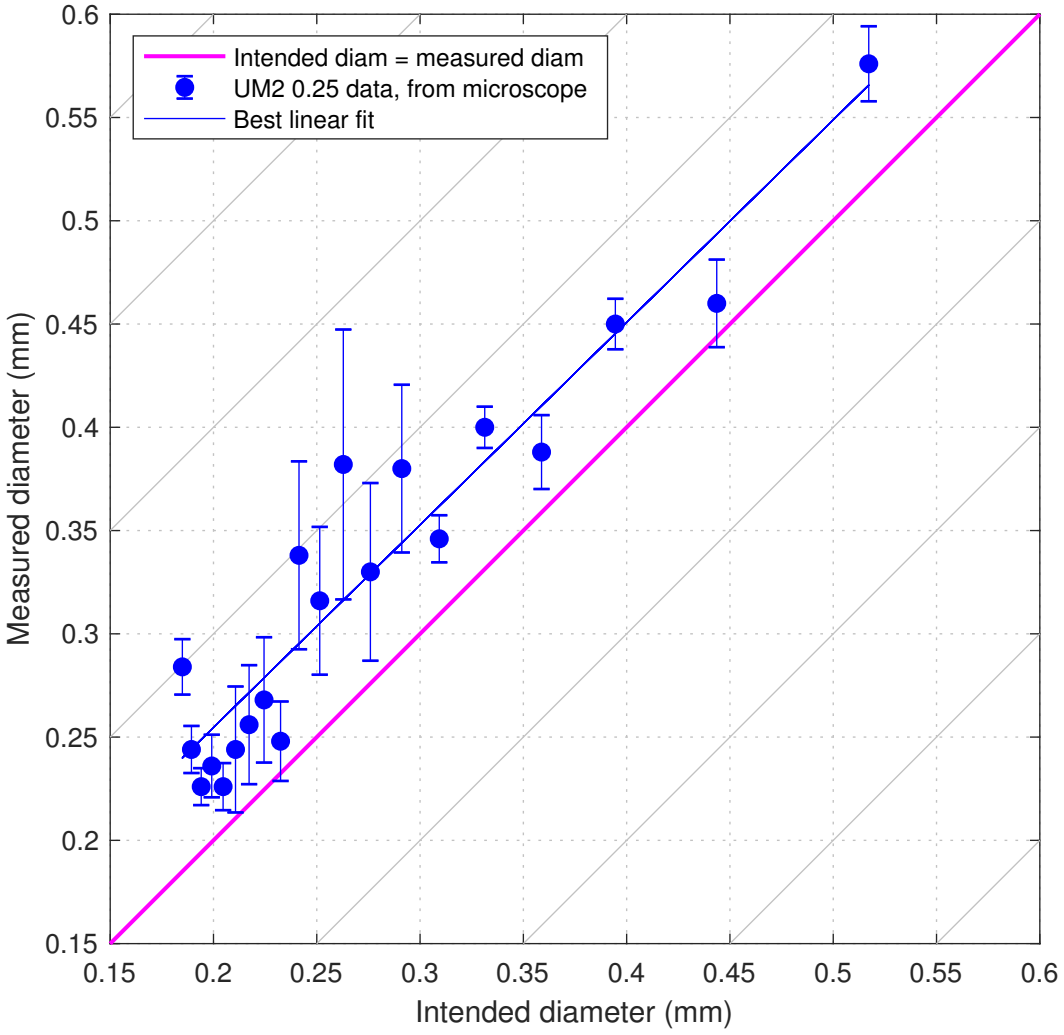


Figure 3.5: The measured diameter of extruded filaments as a function of the process parameter $d_{\text{intended}}$, for the nozzle of diameter 0.25 mm. The measurements obtained from the microscope images are shown as dots and error bars, where the dot represents the mean value for the five measurements taken on the sample, and the error bars represent the standard deviation of these. The pink line shows the ideal scenario where $d = d_{\text{intended}}$, and the solid line is the best fit for the measurements.

the intended value. Each blue dot represents the mean of the five measurements on one sample, plotted against $d_{\text{intended}}$—the value used to create the G-code to print that sample. All the points would fall on the pink line if the measured values of the extruded filaments matched $d_{\text{intended}}$. The solid blue line is the best linear fit for the measurements, confirming a linear trend that follows the pink line although slightly shifted up.

Three main observations can be made from figure 3.5: the first is that almost all of the measurements are above the pink line. Secondly, measured values for the diameter show some fluctuations around a mean trend. Thirdly, the width of the error bars representing standard deviation has fairly large values for some cases. Explanations of these are multiple. Firstly, all affordable machines have precision of moderate level that one has

to accept. Then the control on the manufacturing processes is only limited, because samples were made in normal conditions over several days with fluctuating ambient temperature and humidity. Fused Deposition Modelling works by means of a printing-head that extrudes a filament of melted polymer. A layer, made up of this filament, hardens and is then ready to function as a base for the next layers. The filament, just after it is extruded from the nozzle, has a circular cross-section. Once it deposits onto the base, it will be *squashed* by the printing nozzle as it is very close to the base. In addition, the rheology of the solidifying polymer distorts the cross-sectional shape. The ellipticity of the filament cross-section may be the reason why, when imaged from above, the measurements are consistently larger than the diameter of the intended circular extrusion. When an elliptical cross-section is measured from the top—which is the case when the diameter is measured with the microscope—the measurement obtained corresponds to its major axis diameter, larger than the diameter of a circle of the same area. Section 3.4.1 will provide a method to further investigate this aspect of the fabrication. The shift in the plot suggests that experimental calibration of the filament diameter as a function of the process parameter $d_{\text{intended}}$ may need to be carried out, in case the assumption $d = d_{\text{intended}}$ were found not to hold. Nevertheless, the feasibility of the fabrication of variable diameter filaments is firmly established, as a 0.25 mm nominal diameter nozzle is capable of producing filaments in the approximate range 0.2 mm and 0.5 mm. Although this is only about 2.5 times variation in the range of the diameter values, the bending stiffness achieved by the nozzle, which scales as the fourth power of diameter, is in a range nearly 40 times! The axial stiffness $EA$ of a filament scales as per the square of the diameter, hence a factor of 2.5 in diameter leads to a range of 6.25 in altering the axial stiffness. We propose to call this factor—the ratio of the maximum achievable diameter during fabrication to the minimum—as the *adaptability* factor $\alpha^{\max}$ of the nozzle, which is a measure of the adjustability of a fixed nozzle for variable diameter printing. This is not a universal parameter, but a function of the technology and processes as well as potentially the material. We can also define similar ranges of the stiffness of the extruded filament under *stretch* that can be adapted by the nozzle—the parameter $\alpha_{\text{S}}^{\max} = (\alpha^{\max})^2$ describes this flexibility of a fixed diameter nozzle. Likewise, we can define a factor $\alpha_{\text{B}}^{\max} = (\alpha^{\max})^4$ to describe the achievable adaptability of the fixed diameter nozzle for producing variable *bending* stiffness extrusions. These simple scaling relationships between $\alpha^{\max}$, $\alpha_{\text{S}}^{\max}$, and $\alpha_{\text{B}}^{\max}$ assume circular cross section of the extrusion, any deviations would lead to different relationships.

Fluctuations in the measured diameter due to inconsistencies are unintentional and pronounced for small nozzles, because the fabrication process becomes more sensitive to the variations in the manufacturing conditions as well as process parameters. Measurement errors are also accentuated for small diameter. We will see that these oscillations will become much smaller as the nozzle size increases. Other than our intentional variation as a result of the modification of $d_{\text{intended}}$, factors that affect the volume of extruded material are limited control in feeding the spool material, the speed of the printing process

and the response of the actuators. For these reasons, this technique gives better results with larger nozzle size that are less affected by these. As the machines and the materials improve, more consistent fabrication even for small diameter nozzles is expected.

The height of the error bars is the third important aspect of the statistical discrepancy to be considered. The reasons are similar to those for the fluctuations in the mean values—all associated with imprecision in fabrication using affordable machines as well as measurements. Note that fluctuations from the intended values are not the same as intended variability by deliberately controlling the process parameters. Relative Standard Deviation, $\sigma_{\text{rel}}$, can be taken as a measure of the spread of the five measurements taken for each sample, relative to their mean value. The formula used is $\sigma_{\text{rel}} = 100\sigma/\bar{d}$, where $\sigma$ is the standard deviation of the five measurements and $\bar{d}$ is their mean value. Very wide error bars suggest a high variability in the resulting filament diameter. This means that if we fix a value for $d_{\text{intended}}$, the diameter of the extruded filament cannot be predicted with sufficient precision. The Relative Standard Deviation ($\sigma_{\text{rel}}$) is lowest in the region $0.3\,\text{mm} \lesssim d_{\text{intended}} \lesssim 0.5\,\text{mm}$. The diameter of the fabricated filaments in this region is $0.35\,\text{mm} \lesssim d \lesssim 0.55\,\text{mm}$. The rest of the plot is characterised by wider error bars with a relative standard deviation in the range of $10 - 17\%$. For example, for $d_{\text{intended}} \approx 0.26\,\text{mm}$ the diameter of the filament extends from 0.32 mm to 0.45 mm, when its expected value is approximately 0.3 mm. This corresponds to a 43% relative error (width of the error bar relative to the expected value). Because of lack of consistency while using this nozzle, larger diameter nozzles will be used in later work.

### 3.3.2 Capability to control extruded diameter using the 0.4 mm nozzle

The measured diameter of the extruded filaments as a function of $d_{\text{intended}}$ for the 0.4 mm nozzle are summarised in figure 3.6. The dots represent the mean value of the five measurements taken from each sample, while the error bars represent their standard deviation. The solid red line is the best linear fit for the measurements. The right-most point on the plot has a measured value that is more than 25% off the intended value, probably due to the squashing of the filament. However, the point follows the linear trend (red line), confirming the capability of the process to produce large variations in the diameter. As for the results obtained with the 0.25 mm nozzle, the ellipticity of the cross-section is also one possible explanation for the fact that almost all measurements are above the pink line. However, in this case, the measurements have a smaller relative standard deviation $\sigma_{\text{rel}} \lesssim 8\%$ for all values of the parameter $d_{\text{intended}}$. The statistical variability in the diameter of the extruded filament is significantly less than that achieved using the nozzle of 0.25 mm bore. Additionally, the fluctuations that were present in that case are no longer so severe. This calibration allows to obtain a relation between the parameter $d_{\text{intended}}$ and the diameter of the manufactured filaments, with an acceptable RSD ($\sigma_{\text{rel}} \lesssim 8\%$). We also want to point out that the actuators of the machine are

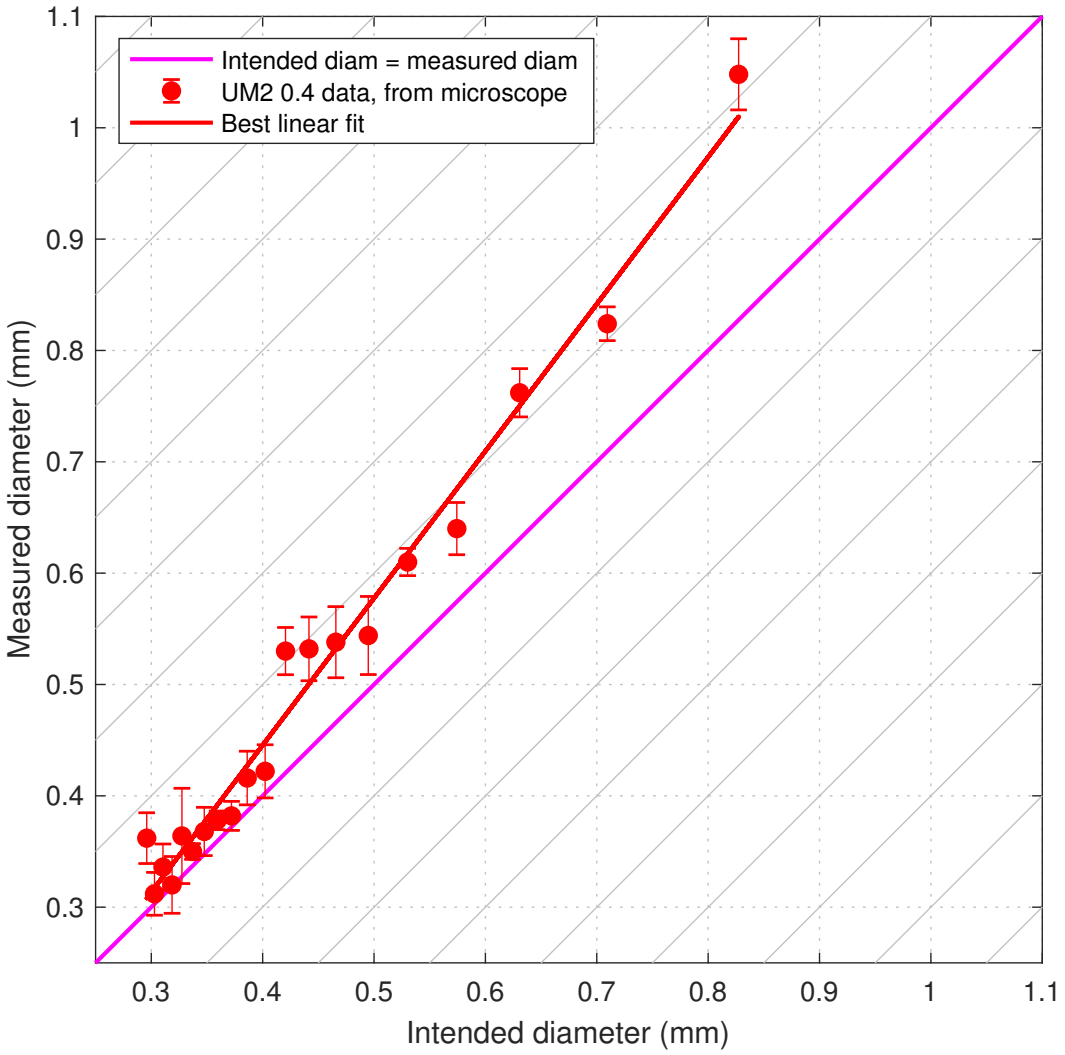


Figure 3.6: The measured diameter of extruded filaments as a function of the process parameter $d_{\text{intended}}$, for the nozzle of diameter 0.4 mm. The measurements obtained from the microscope images are shown as dots and error bars, where the dot represents the mean value for the five measurements taken on the sample, and the error bars represent the standard deviation of these. The pink line shows the ideal scenario where $d = d_{\text{intended}}$, and the solid line is the best fit for the measurements.

not built with this technique in mind, so they might have been optimised only for the required nozzle sizes. Advancements on this could lead to even lower RSD values. The adaptability $\alpha^{\max}$ of this nozzle within the range studied is approximately 3. This gives us a huge flexibility in tailoring the axial stiffness by a factor of $\alpha_{\text{S}}^{\max} \approx 9$ and $\alpha_{\text{B}}^{\max} \approx 81$, which is huge. We are approximating the values to nearest whole numbers, since it is an approximate measure of the manufacturing capability, rather than being a precise physical property.

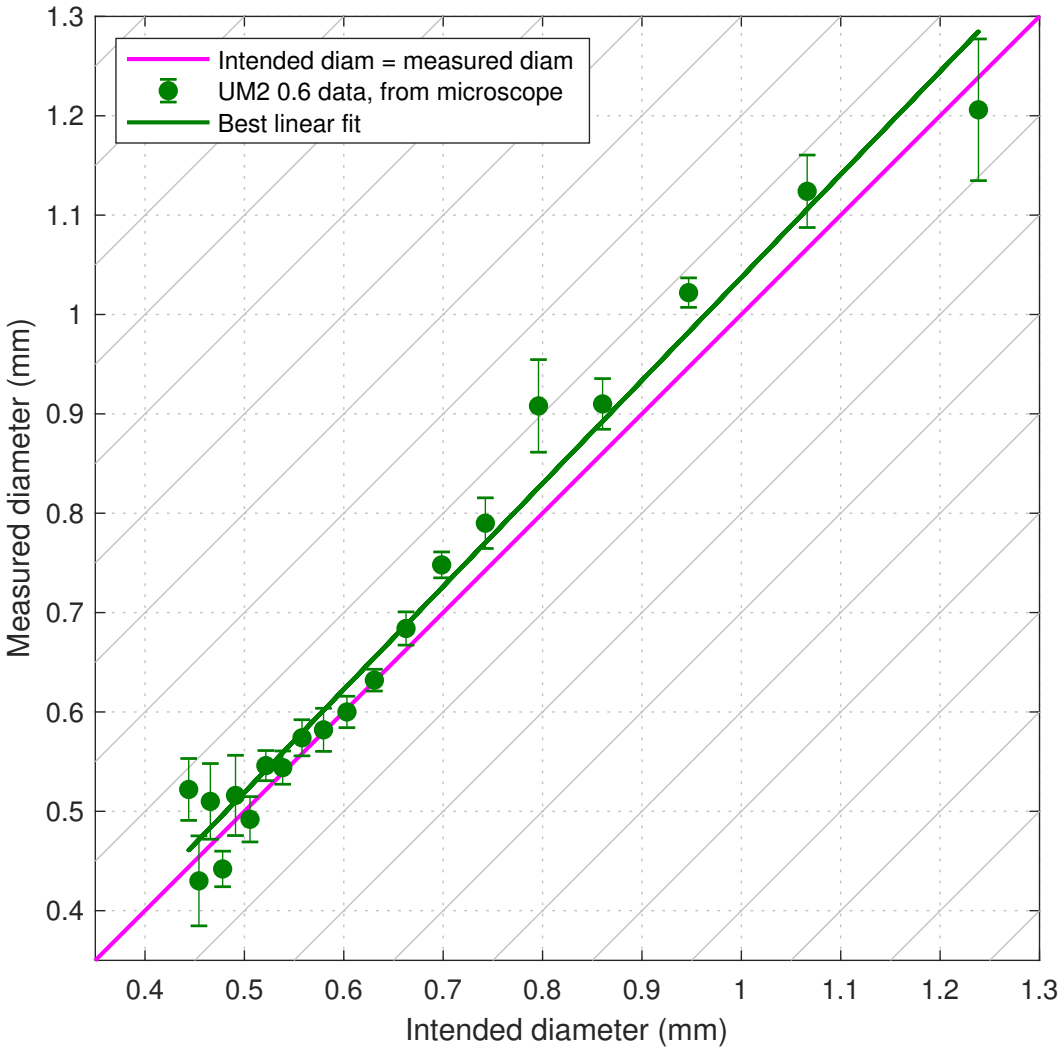


Figure 3.7: The measured diameter of extruded filaments as a function of the process parameter $d_{\text{intended}}$, for the nozzle of diameter 0.6 mm. The measurements obtained from the microscope images are shown as dots and error bars, where the dot represents the mean value for the five measurements taken on the sample, and the error bars represent the standard deviation of these. The pink line shows the ideal scenario where $d = d_{\text{intended}}$, and the solid line is the best fit for the measurements.

### 3.3.3 Variable diameter extrusion using 0.6 mm nozzle

The measured diameters of the fabricated filaments using the 0.6 mm nozzle are shown in figure 3.7, as plotted against the indented diameter. The relative standard deviation in the variability of fabrication $\sigma_{\text{rel}}$ in this case is below 6% for the whole range of $d_{\text{intended}}$ considered. This is the most consistent $\sigma_{\text{rel}}$ obtained with the available nozzle sizes. Note that the variability describing the unreliability of the process and the machine is not to be confused with the intended range of diameter variation, as quantified by $\alpha^{\max}$. With this nozzle size, a reliable fabrication is now possible in the range of diameter $0.45 \lesssim d \lesssim 1.2$, giving us $\alpha^{\max} \approx 2.7$, i.e. $\alpha_{\text{S}}^{\max} \approx 7.3$ and $\alpha_{\text{B}}^{\max} \approx 53$. Again, most

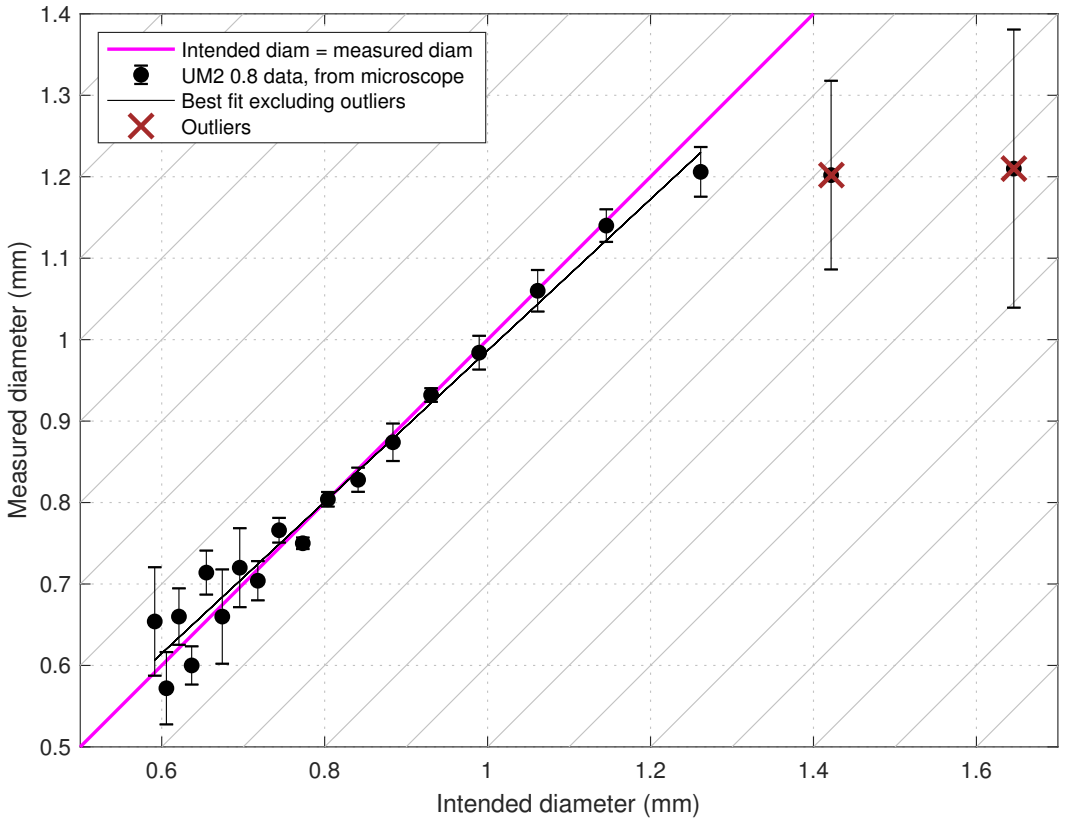


Figure 3.8: The measured diameter of extruded filaments as a function of the process parameter $d_{\text{intended}}$, for the nozzle of diameter 0.8 mm. The measurements obtained from the microscope images are shown as dots and error bars, where the dot represents the mean value for the five measurements taken on the sample, and the error bars represent the standard deviation of these. The pink line shows the ideal scenario where $d = d_{\text{intended}}$, and the solid line is the best fit for the measurements. The last two points on the right are excluded for the calculation of the best fit: no change in diameter is seen when increasing the parameter, a sign that the maximum amount of material that can be extruded has been reached.

measured values of diameter are slightly above the intended values. However, both the slope and the position of the trend line are in very good agreement with the slope and the position of the line of expected values. These results also show even less random fluctuations than the results obtained with the 0.4 mm nozzle and the best fit is very close to the expected trend line (pink line). These results are a further proof of concept of our proposed approach of fabrication: not only varying $d_{\text{intended}}$ in the G-code results in a variation in the diameter $d$ of the fabricated filaments, but the behaviour is close to the ideal case where the parameter chosen $d_{\text{intended}}$ corresponds to the diameter $d$ of the filaments produced.

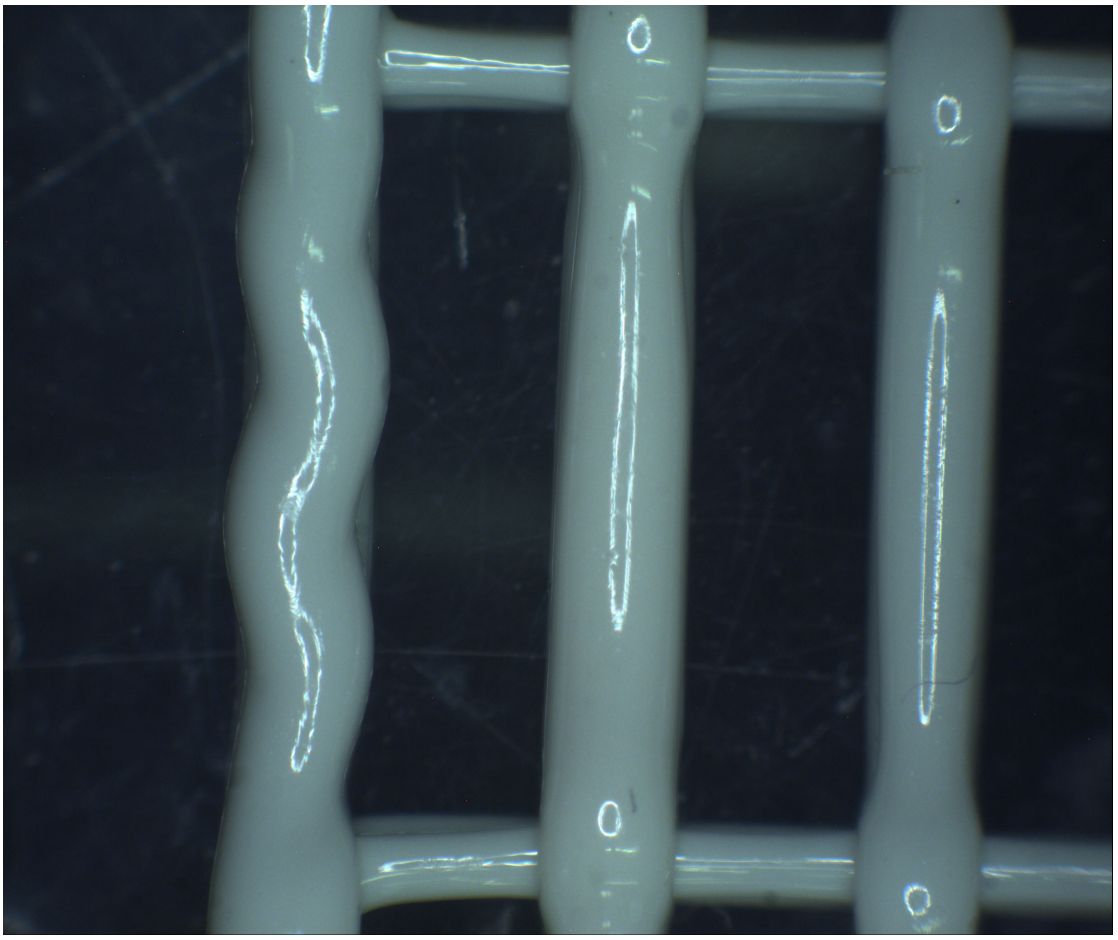

Figure 3.9: Wave-like filament: the first vertical filament of the left. It was obtained trying to push a large amount of material through the nozzle. No change in cross section is achieved, only an increased length, leading to a wavy filament.

### 3.3.4 Variable diameter extrusion using 0.8 mm nozzle

Figure 3.8 shows the results for the size of the fabricated filaments, manufactured using a nozzle of 0.8 mm. The results are very promising, showing reliable fabrication of adaptable diameter filaments, a best fit almost overlapping the line of intended values (pink line), and a very small standard deviation. In the central region of the plot, $0.7 \lesssim d_{\text{intended}} \lesssim 1.2$, the relative standard deviation is only about 2% for most of the values, with some values less than 1%). This shows consistency in the measured diameters, demonstrating the reliability of the technique. The absence of a gap between the trend line and the line of expected values suggests that the distance from the nozzle to the build-plate was optimal for this nozzle, reducing the ellipticity of the cross-section due to squashing. However, a new behaviour appears: the last three data points on the plot ($d_{\text{intended}} \approx 1.25$, $d_{\text{intended}} \approx 1.4$, $d_{\text{intended}} \approx 1.65$) seem to all correspond to a manufactured filament diameter of 1.2 mm. This plateau likely derives from the fact that the printer cannot extrude the quantity of material we are prescribing it to extrude–this

is a technology issue related to the machine, rather than a scientific one. The limit was discussed in section 2.4.2 as reported by N. Turner et al. [2014], Gold and Turner [2015]. We saw that this is likely due to a limit in the amount of pressure that the motors can overcome (above which the rollers that push the filament may slip and cause the pressure to drop, hence altering the extrusion rate), from the buckling of the feedstock filament. The 1.20 mm diameter seems to correspond to the limit, in volume of material (due to pressure, as just explained) that the actuators of the 3D printers can extrude. A second possibility could be that from this diameter of the filament, if we further increase the extrusion rate, we obtain a variation in the *length* of the filament rather than in its cross-section. Figure 3.9 shows a wavy filament (first vertical filament of the left), obtained as a result of increasing the volume of material extruded. This wavy filament has approximately the same cross section as the one next to it, but its length has increased. It is possible that this upper limit in the diameter could be tweaked, for example by reducing the speed of the printing-head.

From the flow continuity relation $\dot{V} = Av$, where $V$ is the volume, $\dot{V}$ is the volume extruded per unit of time, $A$ is the cross-sectional area and $v$ is the speed of extrusion, we conclude that, for a fixed $\dot{V}$, by decreasing the speed, the area can increase. This could mean that reducing the speed, the limit in the maximum diameter achievable increases, assuming a fixed value for the maximum extrusion rate. The speed of the printer, though, cannot be decreased at will: the filament needs to remain straight without sagging (when overhanging) or becoming wavy. This can happen if we push *a lot* of material and move slowly. The first filament to the left in figure 3.9 is an example of this. We can see from the middle and rightmost filaments, on the other hand, that the filaments become straight again increasing the speed of the printer or reducing the amount of extruded material.

Figure 3.9 also shows how the diameter of the filaments vary due to the interaction with the layer below. In this figure we have three filaments running vertically that belong to the top layer and two transverse filaments running horizontally that are part of the bottom layer. Excluding the left-most, wavy filament, we can see how the middle filament is thinner towards the top transverse filaments while the right-most vertical filament is thinner towards the bottom. This is an indication of the direction of print. The middle filament was extruded while the print head moved from top to bottom, while the right-most filament was extruded in the opposite direction. This change in diameter happens because while the top filament is being extruded, when in reaches the filament in the layer below, it sticks to it, resulting in a force that pulls on the filament being extruded, making it initially thinner. All of the measurements taken in this work are obtained from the middle part of the filaments, to ensure that this thinning effect is not affecting the measurements.

### 3.3.5 Consolidated picture of the adaptable stiffness fabrication capability

The left end of all the plots in the previous section is characterised by a widening of the error bars, denoting a greater variability in the diameter of the fabricated filament. In this region, the diameter of the extruded filaments is smaller than the nominal size of the nozzle used. This means that the nozzle does not act as a guide to shape the extruded filament, which increases the variability of its diameter. Due to the high variability of the results compared to the rest of the plots, manufacture should be avoided in this range, if precision of the produced part is of utmost importance. When the printed filaments have a diameter in the range $[d_{\text{nozzle}}, 2d_{\text{nozzle}}]$, the fabrication has greater reliability ($d_{\text{nozzle}}$ denotes the nominal diameter of the nozzle). This is a length scale that is not achievable otherwise with an off-the-shelf 3D printer. The only option would be to extrude multiple filaments adjacent to one another to produce a thicker strand of material. This method however, would not be able to manufacture filaments in the range that we achieved, and also, the *thickness* of the strand would be the same as that of the single filaments, whereas with our technique, the thickness is also altered. This two-fold increase in diamter, $\alpha^{\max} = 2$, would still give a four-time increase in axial stiffenss, $\alpha_{\text{S}}^{\max} = 4$, and a 16-time increase in bending stiffness, $\alpha_{\text{B}}^{\max} = 16$.

The data of intended diameter vs measured diameter, for nozzles of all four bores, are shown for the Ultimaker 2+ machine in figure 3.10. As in the previous plots, each dot and its error bar represent the mean value and the standard deviation over five measurement, respectively. Measured values are plotted as a function of $d_{\text{intended}}$ on the horizontal axis. Markers with four different colours represent data for the four nozzles. From figure 3.10, we can note how $0.3 \lesssim d \lesssim 1.2$ is the region where error bars are the smallest, $\sigma_{\text{rel}} \lesssim 6\%$, and the measurements are very close to, sometimes overlapping with, the pink line that represents perfect fidelity with the kinematics of flow rate continuity. Since the match between the data and the intended values is excellent, this pink line is taken as the *master-curve* for driving the demand to produce variable diameter extrusion.

Since it is possible to achieve a filament with diameter $d \approx 0.3\,\text{mm}$ with the 0.4 mm nozzle, and due to the lower quality of the result obtained with the 0.25 mm nozzle, the nozzle of size 0.25 mm becomes of little interest. Additionally, for each nozzle, except 0.25 mm nozzle, in the region around the nominal diameter, measurements are close to the line of expected values with small variability, as should be expected, presumably because printers are optimised to work in this region. We have thus demonstrated that it is possible to control the filament diameter using fixed diameter nozzles by controlling the process parameter $E$, directly linked to $d_{\text{intended}}$. The potential for fabrication of functionally graded structures is immediate and will be explored in the next chapter.

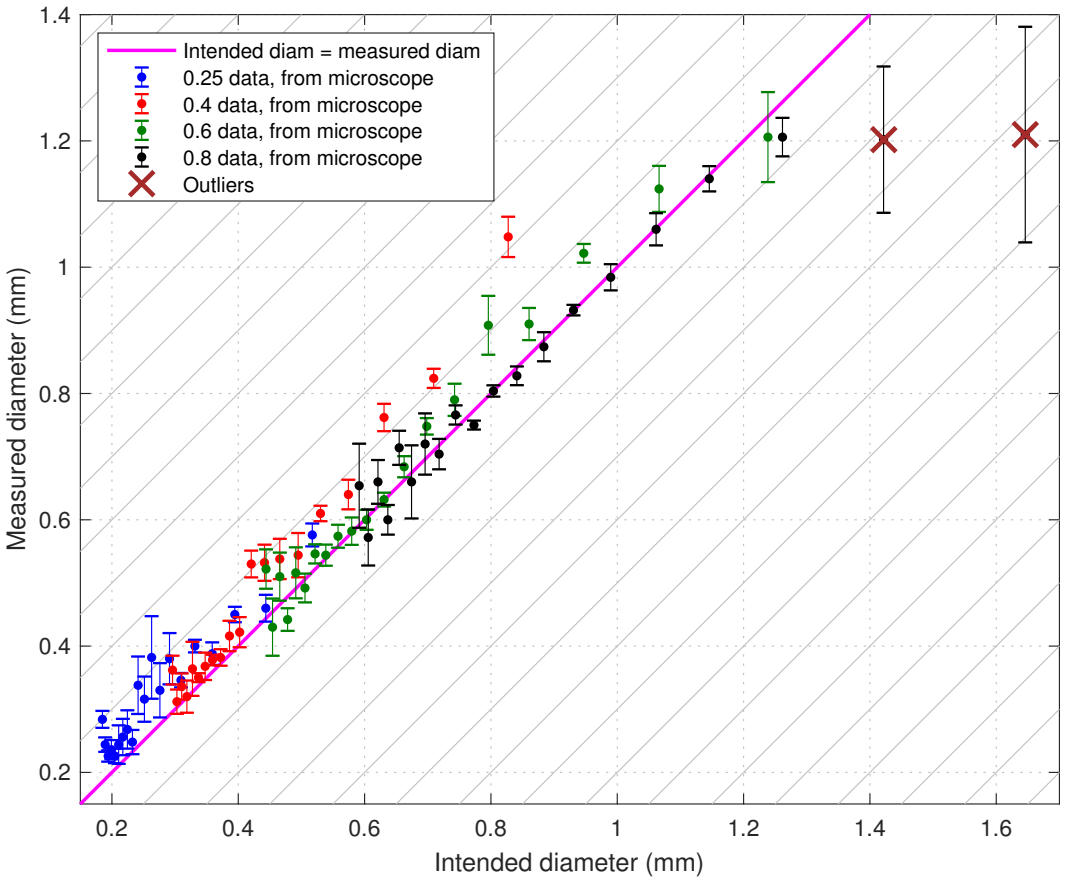


Figure 3.10: Summary of measurements for all four nozzles. Each colour represents a different nozzle diameter. Each dot represents the mean value over the five measurements and the error bar their standard deviation. The pink line represents the expected values, that is $d = d_{\text{intended}}$. The points that are considered outliers are marked with a cross.

So far, microscopic measurements on the fabricated filaments formed the basis of our discussion. The next refinement in the geometric characterisation is that of the cross-sectional shape. While detailed studies using technologies such as micro-CT are possible, here we take a simple approach of combining bulk volume estimates by weighing samples with the microscopic major-axis measurements. This provides us with estimates of ovality on the extrusions—the flattening of circular sections is attributed to the inevitable mechanical pressure applied by the nozzle, and also to the gravity driven creeping flow during the solidification process.

## 3.4 Characterisation of average ellipticity of fabricated filaments

In this section, we characterise the ellipticity of the cross section. As the diameter of the printed filament is increased, the distance from the nozzle to the buildplate remains

fixed. This progressively increases the squashing of the filament, which results in a cross-section that becomes less and less circular. A qualitative representation of this can be seen in figure 3.11. Here we show the difference between the expected circle (dashed line) and the elliptical cross-section (solid line) for two cases: a case in which the diameter of the filament is comparable to that of the nozzle, on the left, and a case in which the diameter of the filament is larger than that of the nozzle, on the right. This section quantifies the ellipticity of the cross section combining the measurements obtained using the microscope and the weight of the samples.

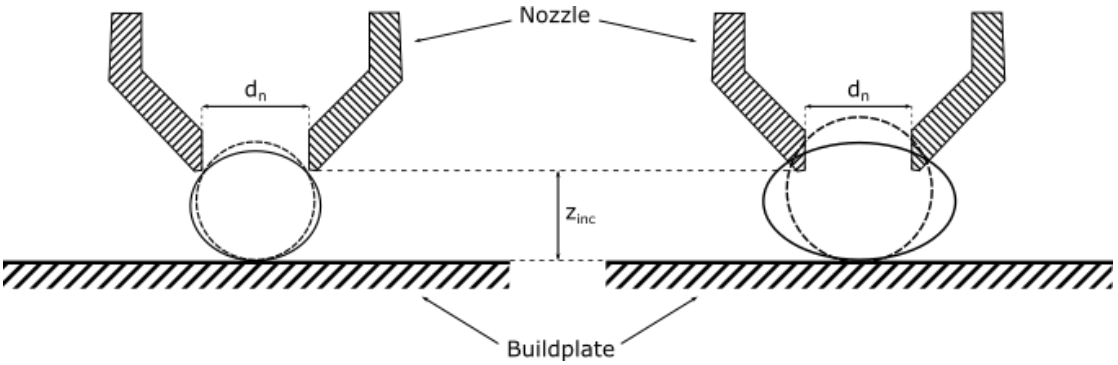


Figure 3.11: Qualitative representation of the cross-section of the manufactured filament. The dashed circle is the expected circular cross-sectional shape, the solid ellipse is the shape deduced combining microscope and scale measurements. If the distance between the nozzle and the build-plate is kept constant ($z_{\text{inc}}$), printing a larger filament would result in a more severe squashing of the filament, hence a filament with an elliptical cross-section.

### 3.4.1 Estimates of ellipticity from weight measurements

The 0.25 mm nozzle, as stated before, covers a range that is almost all covered by the 0.4 mm nozzle, while the 0.8 mm nozzle is considered quite large for most applications. Therefore, we focus on the nozzles of diameter 0.4 mm and 0.6 mm only.

To obtain the average cross-sectional area of the filament used to print the samples, we make use of the *mass* of the samples, using the methodology described in section 3.1.3. Plotting the results for the 0.4 mm we obtain figure 3.12, while the results for the 0.6 mm nozzle are shown in figure 3.13. The summary of measurement for both nozzles is presented in figure 3.14.

In the plots, the major diameter measured with the microscope is again shown with dots and error bars like in the previous section, and the diameter obtained by the mass of the samples (see equation 3.2) is shown with a diamond marker. These values are again plotted against the parameter $d_{\text{intended}}$. The pink line represents again the case where the chosen parameter $d_{\text{intended}}$ equals the diameter of the manufactured filaments.

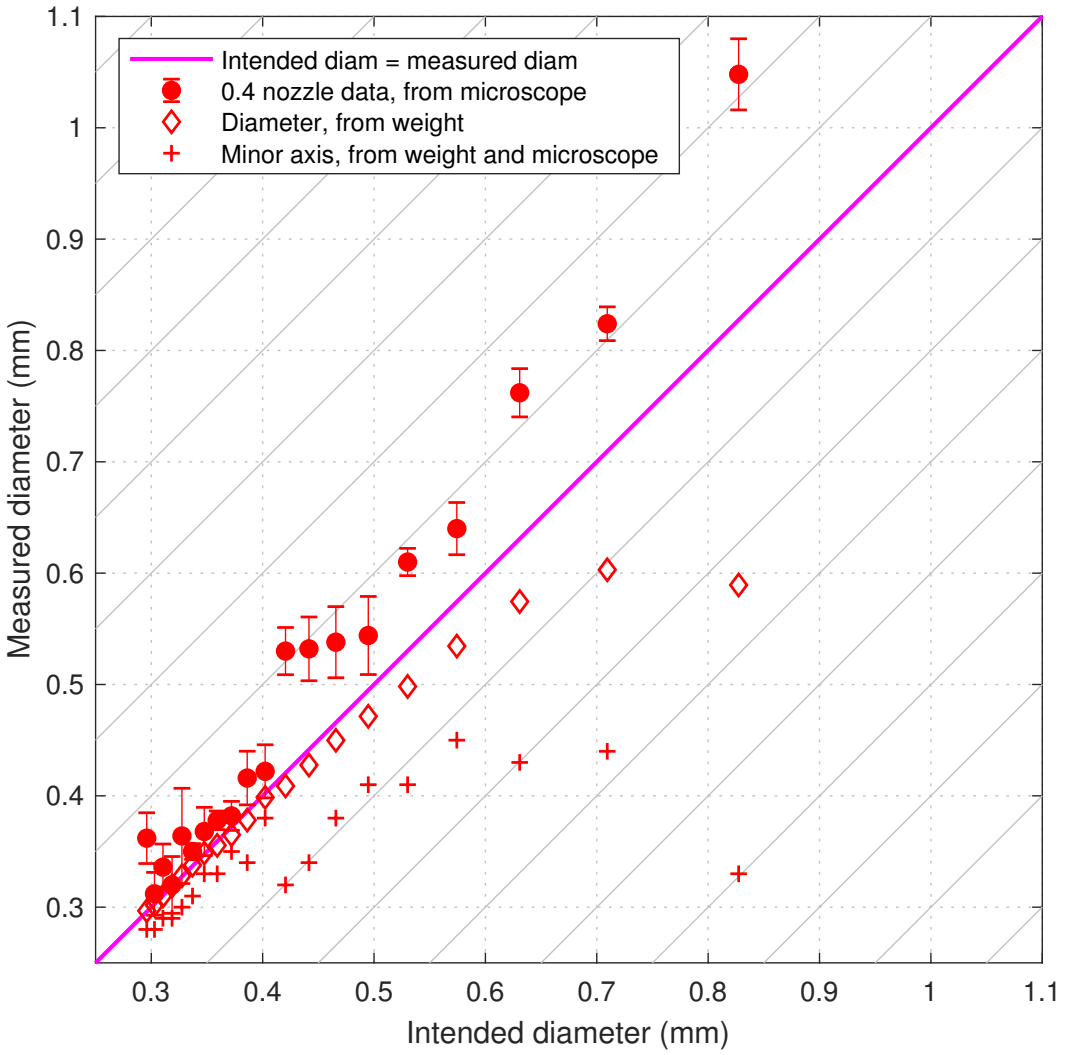


Figure 3.12: Summary of measurements for the 0.4 mm nozzle. Major diameters from the microscope (dots and error bars), expected trend (pink line), diameter from mass of sample assuming circular cross-section (diamond markers), minor diameter assuming elliptical cross-section (plus markers).

While printing, the nozzle is at a fixed distance from the build-plate, or from the previous layer, which is expected to squash the freshly extruded filament. A practical rule that is often used is that the distance of the nozzle with respect to the printing bed or to the previous layer, is 80% of the *nominal* nozzle diameter—$z_{\text{inc}} = 0.8 d_{\text{n}}$. This allows the filament to be slightly pushed against the previous layer, ensuring adhesion and compactness of the final result. When we over-extrude, the filament is pushed more against the previous layer—this leads to the flattening of the cross-section. We now assess the ellipticity of the cross section as described in section 3.1.3. The calculated values for the minor axis diameter of the ellipse $d_{\text{m}}$ (see equation 3.3 for its expression) are represented by a plus marker on the plots. The values used as $d_{\text{M}}$ are the values measured with the microscope. In section 3.3 these were interpreted as diameter of a circle, while we now know that there is significant ovality, hence we use these measurements here as

major-axis diameters.

The diamond markers, representing the diameter assuming circular cross-section, obtained from the mass of the samples, come very close to the pink line of expected trend in the region of $0.3 \lesssim d_{\text{intended}} \lesssim 0.6$ in figure 3.12, and in the region of $0.45 \lesssim d_{\text{intended}} \lesssim 0.9$ in figure 3.13. In these regions we could then assume that the assumption of circular cross-section approximately holds. However, it is possible to further divide these regions in two. We can distinguish between the right part and the left part of these regions. On the left-hand side, the distance between the microscope measurements (dots, now representing the major axis diameter of ellipses) and the plus markers (minor diameter of ellipses obtained from weight of the samples) is small. The major and the minor diameters of the ellipse are then very close, hence, the cross-section is close to being circular. On the right end of the plot, the difference increases consistently between minor and major diameters. Excluding the last couple of points, the amount of extruded material has a clear trend closely aligned with the pink line, meaning that on average the 3D printer extrudes the intended amount of material. In the region of $d_{\text{intended}} \gtrsim 0.6$ for figure 3.12 and in the region of $d_{\text{intended}} \gtrsim 0.9$ for figure 3.13, the gap between the two axes of the ellipse becomes very large, confirming elliptical cross-section. The dimension of the minor diameter stops increasing in both cases: this could be a further indication of the fact that the distance from the nozzle to the previous layer needs to be increased according to the amount of material pushed and not according to the nominal diameter.

To illustrate the importance of accounting for ovality of the cross-sections before evaluating mechanical properties, we compare an ellipse with axes of length $d_{\text{M}} = 2a = 0.55\,\text{mm}$ and $d_{\text{m}} = 2b = 0.4\,\text{mm}$ to a circle with the same area, $d = \sqrt{d_{\text{m}} d_{\text{M}}} = 0.469\,\text{mm}$. This apparently small difference results in a relative difference in the second moment of area of approximately 27%:

$$I_{\text{circle}} = \frac{\pi}{4} r^4 = \frac{\pi}{4} \cdot 0.003\,025\,\text{mm}^4; \tag{3.9}$$

$$I_{\text{ellipse}} = \frac{\pi}{4} a b^3 = \frac{\pi}{4} \cdot 0.0022\,\text{mm}^4; \tag{3.10}$$

$$I_{\text{rel}} = 100 \frac{I_{\text{circle}} - I_{\text{ellipse}}}{I_{\text{circle}}} = 27\%. \tag{3.11}$$

By contrast, ovality has no effect on the axial stiffness $EA$ of a filament, if the flattening process is assumed to be approximately area preserving.

The gain in the axial and bending stiffness can now be evaluated accounting for the ellipticity of the cross section. We can now define $\alpha_{\text{S,elliptical}}$ as the ratio of the axial stiffness to the minimum axial stiffness. This is not the same as the maximum range in the axial stiffness achievable, rather it is the gain for a specific value of the targeted diameter, as calculated over smallest extrusion. Similarly, we can define $\alpha_{\text{B,elliptical}}$ as the ratio of the bending stiffness for a given target diameter to the minimum bending stiffness. Using figures 3.12 and 3.13, we consider the dots as the major diameter of

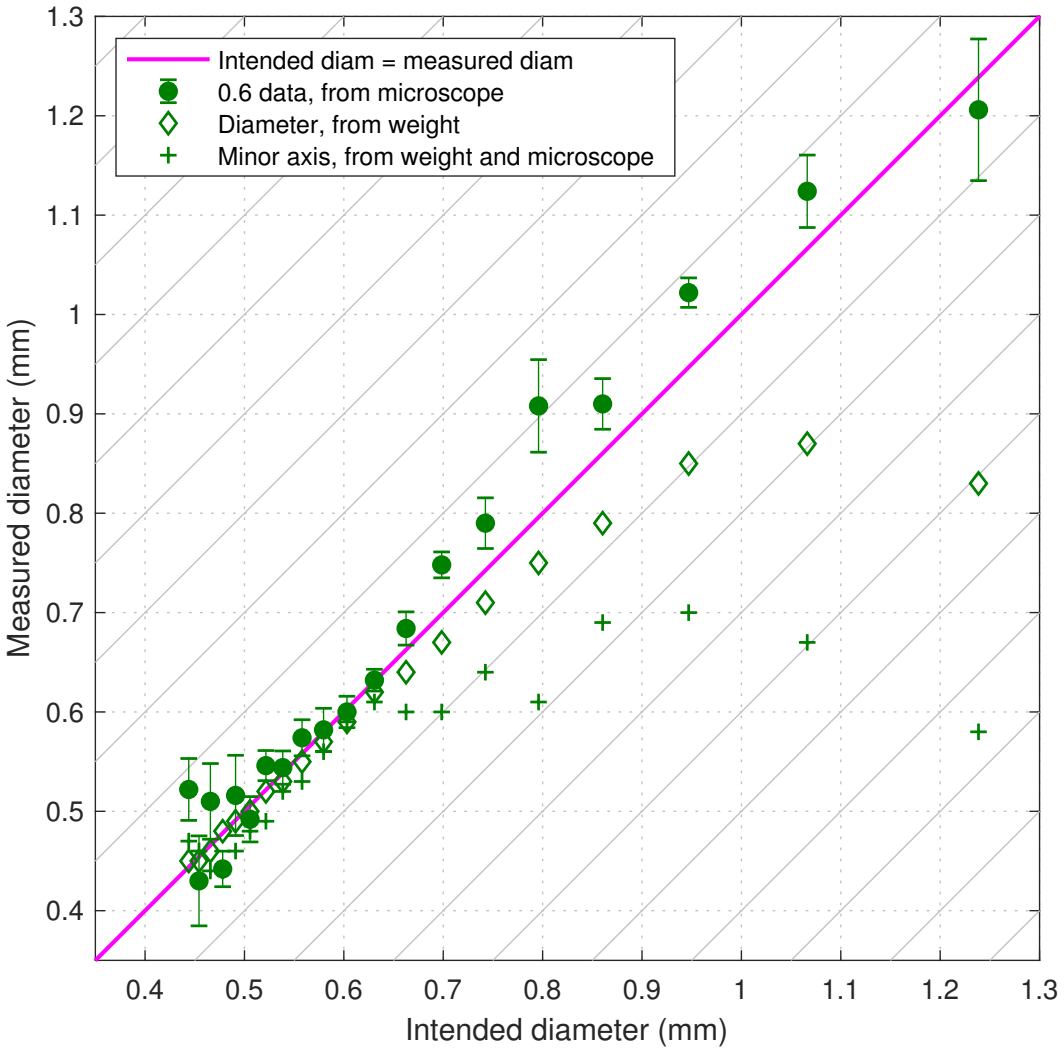


Figure 3.13: Summary of measurements for the 0.6 mm nozzle. Diameters from microscope images (dots and error bars), expected trend (pink line), diameter from mass of samples assuming circular cross-section (diamond markers), minor axis assuming elliptical cross-section (plus markers).

an ellipse and the plus signs as the minor. We can then calculate the area and the second moment of area at each point. We can then normalise these, dividing each by their respective minimum value. We thus obtain the figures in 3.15. Here, (a) shows the values for $\alpha_{\mathrm{S,elliptical}}$ and $\alpha_{\mathrm{B,elliptical}}$ calculated using the data in figure 3.12, obtained from samples made with the 0.4 mm nozzle. Similarly, (b) makes use of data in figure 3.13, obtained from samples manufactured using the 0.6 mm nozzle. In both cases, we note that axial stiffness up to around 4 times the minimum value can be obtained, i.e. $\alpha^{\mathrm{max}}_{\mathrm{S,elliptical}} \approx 4$. Likewise, the bending stiffness can reach 14 times its minimum value ($\alpha^{\mathrm{max}}_{\mathrm{B,elliptical}} \approx 14$) using the 0.4 mm nozzle, and 12 times with the 0.6 mm nozzle size. These clearly demonstrate significant adaptability in variable size extrusion from a fixed bore FDM nozzle.

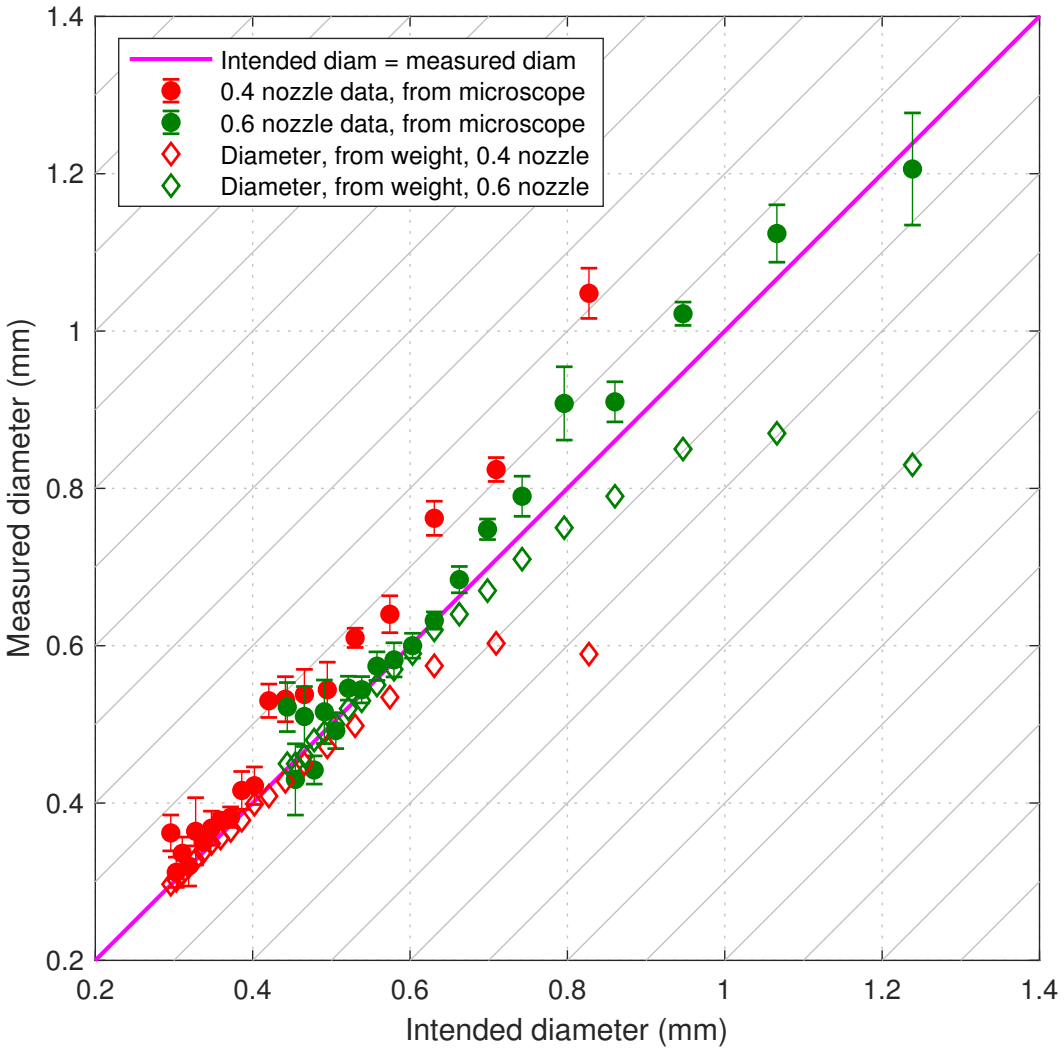


Figure 3.14: Comparison of the diameter obtained from the microscope measurements (dots and error bars), and the diameter obtained from the weight of the sample (diamonds), for both the 0.4 mm and the 0.6 mm nozzle.

### Summary of adaptive extrusion capability

The capability of adaptive extrusion is summarised in table 3.2. For each nozzle size, first column, we report the gain in the manufactured diameter in the second column, the gain in axial stiffness in the third column, the gain in bending stiffness in the fourth column. These last two columns are overoptimistic: these would have been the values if the cross sections were circular. On the other hand, the fifth and sixth columns show the gain in axial and bending stiffness respectively, estimated from figure 3.15. This takes into account the ellipticity of the cross section. As the characterisation of the elliptical cross section has been carried out only for the samples manufactured with nozzles of size 0.4 mm and 0.6 mm, values in the two last columns are present only for these nozzle sizes. The second moment of area is sensitive to the thickness of the filament, hence the larger drop is in the gain in the bending stiffness.

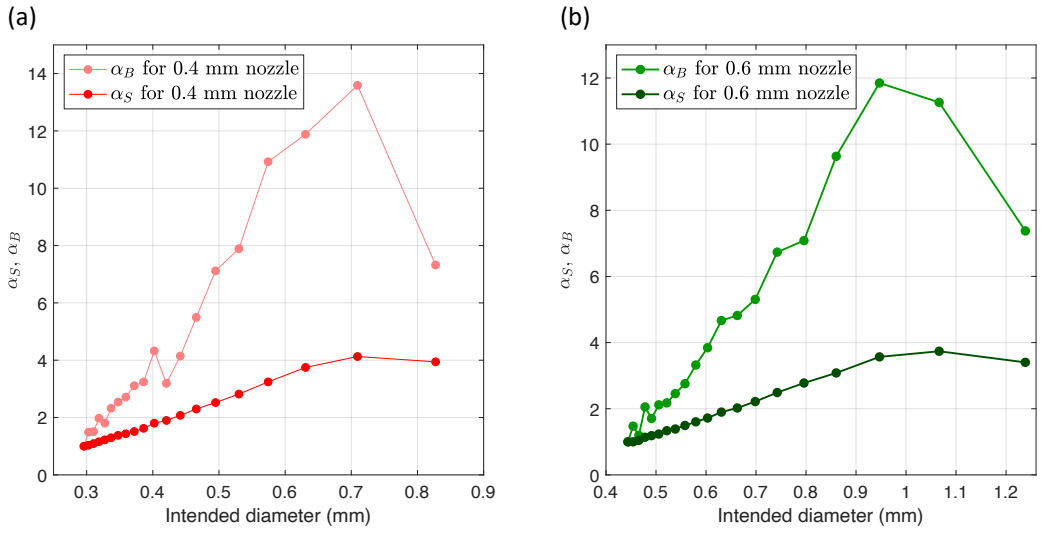


Figure 3.15: (a) shows the values of $\alpha_{\mathrm{S,elliptical}}$ and $\alpha_{\mathrm{B,elliptical}}$ obtained for the 0.4 mm nozzle. (b) shows the values of $\alpha_{\mathrm{S,elliptical}}$ and $\alpha_{\mathrm{B,elliptical}}$ obtained for the 0.6 mm nozzle.

This stresses the importance to obtain filaments of circular cross section when interested in a high gain in bending stiffness. The samples manufactured for this chapter have been printed with a constant layer height, which might be responsible for the cross section becoming elliptical. To further improve the manufacturing and to aim at a less prominent ellipticity, in the next chapters the layer height will be varied based on the diameter of the fabricated filament, which should reduce the squashing of the filament.

| $\boldsymbol{d_{\mathrm{nozzle}}}$ (mm) | $\boldsymbol{\alpha}^{\mathrm{max}} = \left(\frac{d_{\mathrm{max}}}{d_{\mathrm{min}}}\right)$ | $\boldsymbol{\alpha}_{\mathrm{S}}^{\mathrm{max}} = \left(\frac{d_{\mathrm{max}}}{d_{\mathrm{min}}}\right)^2$ | $\boldsymbol{\alpha}_{\mathrm{B}}^{\mathrm{max}} = \left(\frac{d_{\mathrm{max}}}{d_{\mathrm{min}}}\right)^4$ | $\boldsymbol{\alpha}_{\mathrm{S,elliptical}}^{\mathrm{max}}$ | $\boldsymbol{\alpha}_{\mathrm{B,elliptical}}^{\mathrm{max}}$ |
|---|---|---|---|---|---|
| **0.25** | 2.4 | $\sim 5.8$ | $\sim 33.0$ | - | - |
| **0.40** | 3.0 | 9.0 | 81.0 | $\sim 4.0$ | $\sim 14.0$ |
| **0.60** | 2.7 | $\sim 7.3$ | $\sim 53.0$ | $\sim 4.0$ | $\sim 12.0$ |
| **0.80** | 2.0 | 4.0 | 16.0 | - | - |

Table 3.2: Summary of the capability of adaptive extrusion that can be achieved for each nozzle diameter. The second column shows the gain in the diameter of the fabricated filaments, the third column the gain in the axial stiffness in case of circular cross section, the fourth column shows the gain in bending stiffness assuming circular cross section. The last two columns are an estimate from figure 3.15, and they show the gain in axial and bending stiffness taking into account the ellipticity of the cross section.

### 3.4.2 Adaptable diameter extrusion using Ultimaker 3 extended FDM printer

The fabrication and measurements presented so far demonstrate the capability of FDM process to produce adaptable diameter extrusion. This was followed by the characterisation of the extruded material, when Ultimaker 2 printer was used. In this section, we implement the strategy of over- and under-extrusion with the Ultimaker 3 Extended machine. Fabrication using this machine will also be used in the next chapter for the production of lattices and films. The main thing that we wish to establish is whether the behaviour can be modelled with the line of expected trend $d = d_{\text{intended}}$. The test that has been chosen is the one that gives the averaged cross-section, hence diameter, based on the weight of the samples, following equation 3.2, where the size of the extruded filament is estimated by treating the filament as cylindrical (i.e. of circular cross section).

We choose 10 values of the intended diameter of the filament. This is implemented by adjusting the machine parameter $E$ within the G-code, via equation 3.8. Three samples for each value of $d_{\text{intended}}$ were manufactured using the Ultimaker 3 Extended and weighed. Again, the G-code prescribes the length of extruded material and, together with the weight of the sample, it is possible to find the average cross-sectional area and hence the diameter. In figure 3.16, the diameter obtained from the mass, equation 3.2, is plotted against $d_{\text{intended}}$.

There are some generic similarities with fabrication using Ultimaker 2. The averaged results lie below the expected trend line (pink line) and the discrepancy between these becomes greater as the diameter increases, same behaviour that was also found for the Ultimaker 2+ (figures 3.12 and 3.13). The proximity of the results obtained to the pink line of expected trend makes possible to consider the pink line as master curve for the machine to drive the G-code. If strong device-dependent features do need to be incorporated into the G-code, or if the dimensional accuracy needs to be ensured, then the slight non-linearity in the measured diameter vs intended diameter relationship can be incorporated. Also, the way that the actuators, responsible for moving the filament back and forth, respond to changed extrusion demand need optimisation for the proposed technique. We are not concerned with such modifications of existing 3D printing hardware in this work.

## 3.5 Fabrication of complex 3D parts with adaptable extrusion

As a simple proof of concept, we present a method to take the G-code of *a complex 3D part* obtained with a Slicer software and introduce variability in the diameter of the filaments within the part, *as per a prescribed function of position*. This would allow

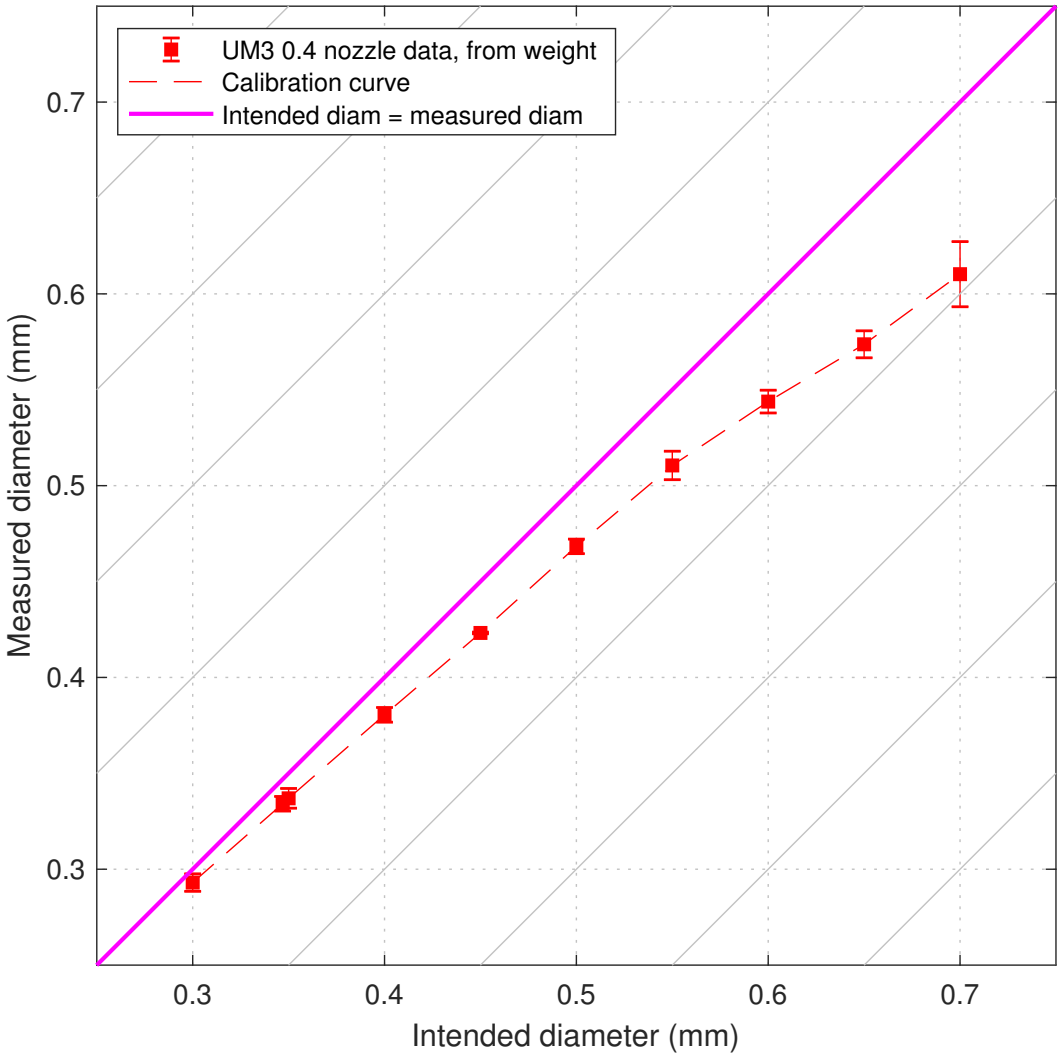


Figure 3.16: Calibration of the Ultimaker 3 Extended 3D printer. The red squares represent the mean values obtained for the diameter, calculated from the mass of the three samples manufactured using the same corresponding $d_{\text{intended}}$. The solid red line represents the best linear fit for the data.

to modify the diameter of the filaments locally within the part. The bespoke MATLAB scripts used throughout this work generates G-code to manufacture lattice structures, starting from a few parameters, such as the dimension of the lattice, the spacing of the filaments and their diameter. Our scripts have been completely independent of any slicing software. The technique presented in this section, on the other hand, enables printing arbitrary objects with variable diameter filaments, starting from existing G-code. This technique, after proper development, could be implemented into any of the slicing software available, such as Cura, PrusaSlicer, OctoPrint, Repetier, Slic3r, etc. This, however, is outside the scope of this work. To summarise, a MATLAB script has been developed that reads the non-functionally-graded version of the G-code of any part (as generated by a slicing software) and *transforms* it into a functionally graded version. This can then be run on a 3D printer to obtain the FG version of the object.

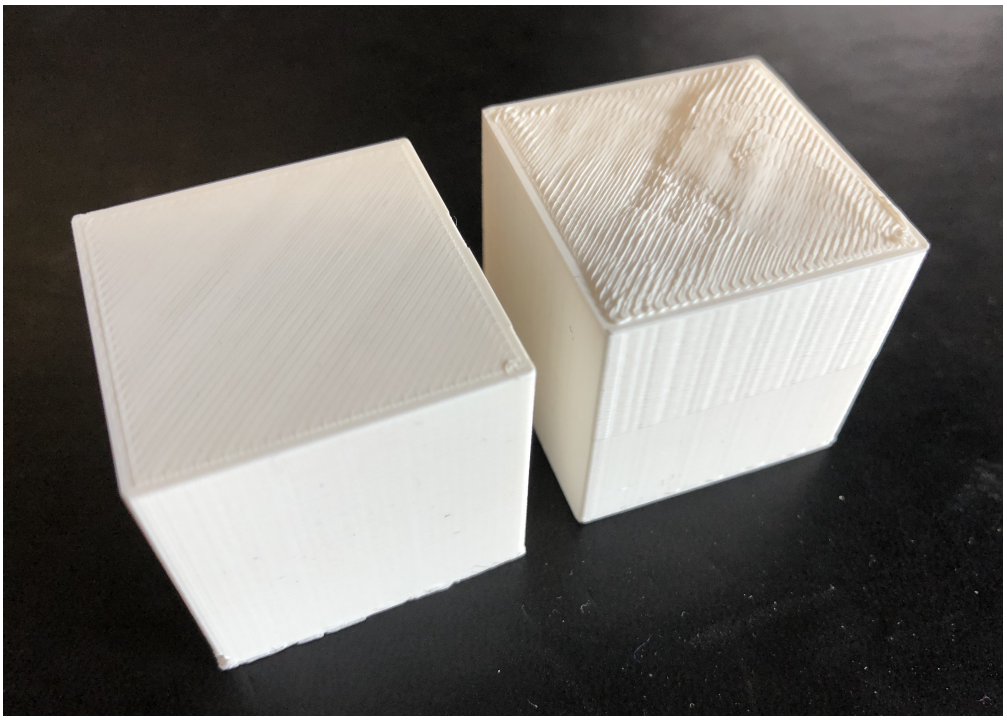

Figure 3.17: On the left, a standard cube made with Solidworks, sliced using Cura and printed with nozzle 0.4 mm. On the right, the same cube as on the left, but its G-code has been manipulated so that the top half is printed with a thicker filament, 0.6 mm.

**Method.** The basic approach is to read one line of the input G-code at a time. Then take the ones starting with $G1$ (movements with extrusion) to re-calculate their value for $E$. The functional gradation is expressed as a function that prescribes the filament diameter given the position of the print-head: $d(x, y, z)$. This means that when the software reads one line of G-code, it knows from where to where the print-head will have to move when executing this command from the X, Y and Z values of the line, then it can use the function $d(X, Y, Z)$ to calculate the value of the filament diameter to assign to that movement. Each time a new line is read, the software calculates the diameter to be assigned to that region, and uses that value to recalculate the value of $\Delta E$ for that line. One complication that arose and has since been solved, is that each movement given by a G command in the G-code takes a fixed amount of material to be extruded during that movement. This means that in order to manufacture a filament with varying diameter, this filament could not be manufactured using a single command. Hence, a maximum length for each movement needed to be implemented, so that filaments could be extruded using a series of commands, each with a different extrusion rate based on the position of that segment within the part. In other words, long movements need to be separated into smaller movements, each with a different value for the chosen diameter, recalculated from the given function $d(X, Y, Z)$. This solution is also the one implemented in the next chapters for the production of continuously graded films. The idea is that these consecutive filaments extruded with different diameters

would not have any interface between them due to the flowing nature of the extruded polymer which would smoothen the variation between sections with different diameters. This will need to be verified experimentally to ensure that this is enough to obtain filaments with a mechanical response that resembles that of filaments with continuously varying diameter. This is what is meant with the term *continuously varying diameter*. Strictly speaking, we obtain the variation using multiple parts of constant diameter, hence the variation is not continuous in a strict sense. However, what we aim to obtain is a variation that makes the filaments behave as if they had a continuous variation in their diameter. In other words, the filaments are mechanically continuous.

**Geometric considerations.** The current issue with this method is that the height of each layer needs to be adjusted to take into account the diameter of the filaments in the layers directly below each point. Currently only an approach has been outlined and details of implementation would require further work on computational geometry of space filling with variable diameter extrusion. This would be potential future development; only a proof of concept is presented here. This approach may be well suited for the inner parts of the objects, what is usually referred to as infill, for two main reasons. Changing the diameter of the filament while printing, makes it difficult to control the surface finish. One option to overcome this issue would be to only use the variable diameter printing for the infill of the print, while the outer layers need to be printed with a constant diameter throughout, to avoid visual differences in the surface finish. The issue with the height of the layers mentioned above, can easily be overcome by adding extra layers of the correct thickness where needed to make the layers even.

**Results.** As a proof of concept a simple geometry and a simple function have been used to test the script. A cube with a side of 20 mm was sliced in Ultimaker Cura to obtain the input G-code. A simple function was chosen, so that the bottom half of the cube be printed with a diameter of 0.4 mm while the top half of the cube with a filament diameter of 0.6 mm. The result can be seen in Figure 3.17. A tangible difference can be seen between the two halves of the cube, which proves the concept described in this chapter.

## 3.6 Conclusions

Adaptable diameter extrusion using a fixed bore nozzle was experimentally realised. This was achieved by controlling process parameters within additive manufacturing instructions, so that material dispensed is either under-extruded, or over-extruded. The resulting size of extrusion was characterised experimentally, when extrusion of a filament of an intended diameter—that is different from the nominal bore of the nozzle—is carried out. This demonstrates the capability of the proposed process. The size of the extrusion is fairly consistent with the intended size in case of over-extrusion. This agreement

validates not only the feasibility of the proposed fabrication approach qualitatively, but also that the output of the fabrication process can be controlled quantitatively.

Caution should be used in case of under-extrusion, as, in this case, the nozzle is larger than the filament. This means that the shape of the filament is not guided by the shape of the nozzle during extrusion. This increases the variability of the results. However, especially for relatively large nozzles sizes, these variations are smaller compared to the diameter, hence the technique is effective in manufacturing filaments of a diameter smaller than the nozzle diameter, although not recommended.

The recommended range of diameters that can be obtained with the technique presented is $[d_{\text{nozzle}}, 2d_{\text{nozzle}}]$. This ensures minimum variability in the results. Additionally, this is a length scale that cannot be achieved otherwise with an off-the-shelf 3D printed. It could be argued that in some cases by extruding multiple adjacent filaments, an effect similar to that obtained with our technique can be achieved. However, that would only produce strands with a width that is a multiple of the filament diameter. It would not be possible to manufacture filaments with a width in the range $[d_{\text{nozzle}}, 2d_{\text{nozzle}}]$. Additionally, multiple adjacent filaments would only increase the *width* of extruded material, while the *thickness* would remain constant. The technique we developed and presented overcomes both of these issues: we can achieve filaments in the range $[d_{\text{nozzle}}, 2d_{\text{nozzle}}]$ and, even accounting for the filaments to be elliptical, an increase in thickness is also achieved.

Measured data for the diameter of the fabricated filaments align well along a linear trend based on simple incompressible material flow continuity, for nozzles of different diameter covering a wide size range. Three parameters $\alpha, \alpha_{\text{S}}, \alpha_{\text{B}}$, describing (i) gain in diameter over its smallest value, (ii) gain in axial stiffness $EA$, and (iii) the gain in bending stiffness $EI$, respectively, were defined. The maximum values of these are intended to be approximately $\alpha^{\max} \approx 3$, $\alpha_{\text{S}}^{\max} \approx 9$ and $\alpha_{\text{B}}^{\max} \approx 81$ if extruded cross-section remained circular. This is practically compromised because of the flattening of the extruded material, which lowers the bending stiffness of the extruded filament significantly. Ellipticity was estimated by measuring the major diameter microscopically and weighing the samples. In spite of flattening, which practically reduces capability of under-extruding and over-extruding, $\alpha_{\text{S,elliptical}}^{\max} \approx 4$ and $\alpha_{\text{B,elliptical}}^{\max} \approx 14$ was achieved. The general capability of the proposed approach of adapting the diameter of extrusion was demonstrated on two different 3D-printing hardware. Finally, a simple proof of concept showing point-to-point spatial variation in the diameter of FDM extruded filaments was presented.

Having successfully established the capability of the proposed process to enable tailoring of stiffness of extruded material significantly, the possibility of additively manufacturing structures that possess continuously varying stiffness opens up. This is taken up in the next chapter.

# Chapter 4

# Analysis, manufacture, and characterisation of structures with spatially varying stiffness

We introduced a novel approach to extrude material with a diameter different from the nominal bore size of the nozzle in the previous chapter (chapter 3). The demonstration of the process capability was for a single filament with *constant* diameter that is different from the nominal nozzle bore size. In this chapter, we control the spatial variation of the diameter by a prescribed function and fabricate a structure with continuously varying stiffness. Given the functional dependence of the spatially varying diameter, flexural response of such structures is theoretically obtained. A mathematical model for the response of films with variable diameter along one direction is derived and presented in the first part of this chapter, while in the second part, an experimental characterisation of structures of spatially varying stiffness is carried out. Following the successful fabrication and validation, in the third part of the chapter, a host of mathematical models have been developed for functionally graded lattices.

Lattice structures with uniform filament stiffness have been studied in Cuan-Urquizo [2016]. However, the introduction of functional gradation in our work poses new manufacturing and modelling challenges. This chapter develops models for such lattice structures with *spatially varying stiffness*. We will focus mainly on bending properties, often the most important mechanisms of deformation. A mathematical model that can predict the behaviour is sought because it would be desirable to assess the stress and deflection response of the final product at the stage of design, *before* it is manufactured. A simple theory, allows to have a quick, quantitative understanding of the response. Simple models that capture the essential behaviour of a structure are useful for practical applications as they are often amenable to analysis and also often contain sensitivity information analytically. Models of increasing complexity can be developed when the need for a

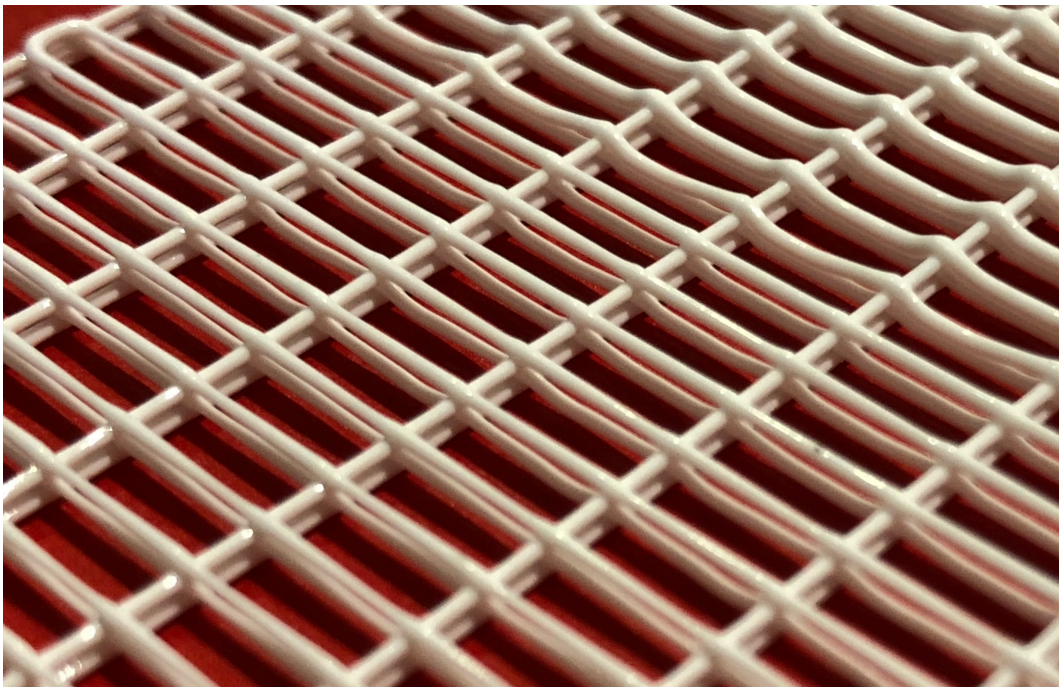

Figure 4.1: A close-up view of a lattice structure that we have manufactured. The four layers of this structure are clearly visible. The large spacing between filaments allows to better appreciate the internal architecture.

better quantitative analysis arises. For the experimental characterisation, we will first present how the manufacturing technique proposed in the previous chapter can be used to produce structures with continuously varying stiffness. The structures considered are the usual regular arrangement of filaments as in Figure 4.1. However, in this chapter we will attempt to introduce a continuous gradation in the properties of the filaments along one direction. Then, we test the manufactured films and compare these results to those obtained from analysis. These laboratory experiments can inform us both on the effectiveness of the fabrication technique as well as how well the mathematical model derived can predict the mechanical behaviour of such structures.

## 4.1 Spatially varying lattice spacing vs spatially varying strut stiffness

Lattice structures are frequently described by apparent deformation and properties. The *apparent* properties of a lattice or micro-structured solid refer to the homogenised properties that would give the same response of the structure, if the properties of the continuum had some effective values. For lattices with spatially varying properties, as presently is the case, such apparent properties would also be spatially varying. Before we develop continuum models for such spatially graded lattice structures, we discuss the mechanisms of strut deformation and their relationship with the overall (i.e. apparent) deformation

of such structures. We also highlight the important distinction between lattices that have been obtained by variable filament spacing vs those with uniform spacing but variable stiffness properties along the filaments.

### Mechanisms of strut deformation in lattice structures

The overall deformation of lattice structures is associated with various deformation mechanisms of the constituent filaments in their internal architecture. The deformation mechanism of struts results in a different apparent deformation of the lattice. In figure 4.2(a), it is illustrated that when the apparent deformation of the lattice is shear, the struts are in bending. In the same way, figure 4.2(b) show that when the apparent deformation of the lattice is bending, the filaments actually deform in tension and compression. In particular, filaments above the neutral axis, shown in blue, are in tension. Filaments below the neutral axis, shown in red, are in compression. In these figures, the apparent response of the structure is shown on the left, in grey, and the micromechanics of the deformation of the filaments is shown on the right. In yellow, the cross-sections of filaments running perpendicular to the plane of the paper appear in their end views. The arrows represent the relative movement of these struts during elastic deformation. The bending of lattice structure is, in general, a combination of these two mechanisms of strut deformation.

Bending of lattice beams involves bulk flexure and apparent shear of the structure. A model that only accounts for the flexure of the lattice can describe with enough accuracy the behaviour in case of small spacing between the filaments, or small displacements. On the other hand, the *apparent shear* of the lattice is significant when bending in the filaments becomes non-negligible, as in the case of large spacing. In this chapter we present the first step in developing a model of this kind, in which we consider a structure where the mechanical response is dominated by the bending of the lattice, neglecting the contributions due to shear. Apparent lattice shear, which manifests as filament bending, can be accounted for.

### Lattices with non-uniform strut spacing

A way to grade the properties of lattices that has been used in the past is to progressively change the lattice spacing. For instance, the spacing could be uniform, as in figure 4.3(a), or could linearly increases, as in figure 4.3(b). This approach is valid to vary the porosity of the lattices, however, the *bending* properties *in the direction of variable spacing* are not affected by this change. It so turns out that the filaments running parallel to the $y$-axis do not participate in bending that occurs in the $x$–$z$ plane. It was established [Berariu, 2016] that the filaments running parallel to the $x$-axis dominate the apparent lattice bending. Hence, the pattern in figure 4.3(b) is not a valid solution to realise bending

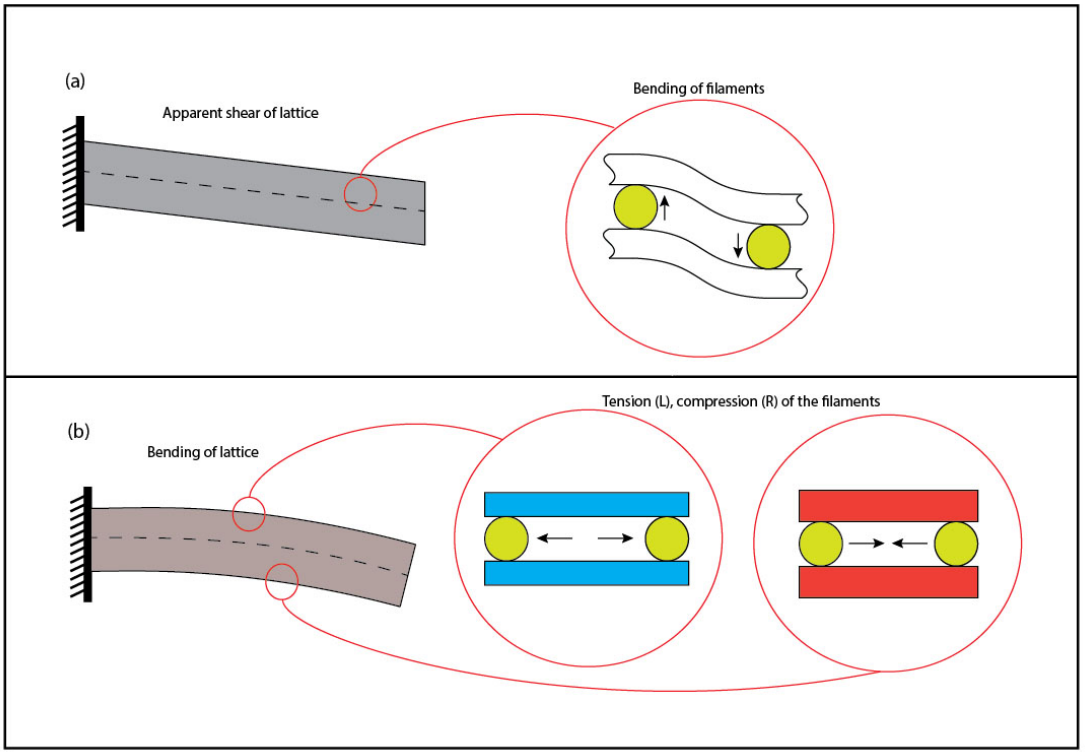


Figure 4.2: (a) - Apparent shear of the lattice (left) due to bending of the filaments (right); (b) - Bending of the lattice (left) due to tension/compression of the filaments (right).

stiffness variation in the $x$-direction, as could be mistakenly assumed. Indeed, it could be shown that such a variable spacing in the $x$-direction leads to stiffness variations in the $y$-direction—the reason being bending in the $y$–$z$ plane is unaffected by struts running parallel to the $x$-axis. In this work, we tailor the stiffness of the lattice in the $x$-direction by being able to continuously vary the bending stiffness of each filament running parallel to the $x$-axis. This would be achieved by realising spatially varying *filament diameter*, which we have been able to physically realise using 3D printing, using the approach of continuously variable extrusion from fixed bore nozzles, as presented in the previous chapter.

## 4.2 Mechanics of lattices with spatially varying stiffness

A novel technique to print functionally graded lattices was described in Chapter 3. Such fabrications are inspired by the potential of using materials with spatially varying properties. Therefore, there is a scientific need to understand the mechanical properties of such lattice structures. Here we develop simple models that provide response of such functionally graded structures. A mathematical model for lattice structures under bending was developed by Cuan-Urquizo [2016], but only for the case of filaments with uniform

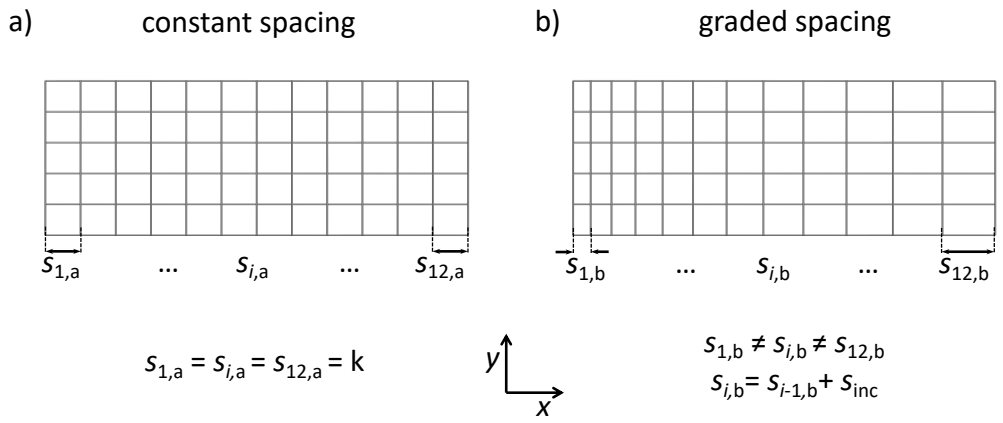


Figure 4.3: (a) Top view of a sample where the filaments running vertically are equally spaced. (b) Top view of a sample where the filaments running vertically are linearly spaced. The response obtained when bending these films along the long filaments (i.e. in the $x - z$ plane) is the same, as the position of the vertically-running filaments does not affect the bending stiffness of the long, horizontal filaments.

bending stiffness, i.e. with constant cross-section. Here, we develop models that expand the capabilities of the available models to lattices with variable-diameter filaments.

Here we restrict ourselves to an orthogonal criss-cross of two layers of struts first. The out-of-plane bending response of such a flat two-dimensional lattice is considered first. Following this, we will proceed to experimentally characterise the manufactured films in the next section.

### 4.2.1 Assessment of spatially varying stiffness from post-buckled bent shape of a structure

Having established the feasibility of fabricating structures with spatially varying stiffness opens up the possibility of experimentally testing the response of structures with variable-diameter filaments and comparing them against analysis. When the struts in the length direction of a bi-layer structure (length much greater than the width) have spatially varying stiffness, the bent shape would be asymmetric even for a loading that is symmetric with respect to the centre of such a structure. We will address manufacturing later in this chapter, while we focus here on testing methodology. While 3-point and 4-point bending tests are a popular choice for experiments, due to the softness of the bi-layer lattice structure, the experimental determination of the asymmetric bent shape is difficult. Instead, the sought asymmetry could be easily brought out by buckling the bi-layer structure and observing it in its edge view, where the asymmetric bent profile can be recorded and characterised.

Motivated by this, we carried out buckling experiments to observe the asymmetric post-buckled bent shape. In this section, we develop a theory to determine such asymmetric buckling mode shapes of a structure with axially varying stiffness. The results of this theoretical analysis will be compared with experimentally measured asymmetric profiles. Note that the theoretical analysis is kept simple, i.e. linear buckling modes are obtained here, which is valid for small post-buckled deflections, whereas experimentally observed post-buckled shapes have significant transverse deflection. Still, it is reasonable to make such comparisons without getting into the higher order effects such as non-linear post-buckling modes. Only mode shapes, and not the buckling forces, are of our interest, as they confirm the successful fabrication of spatially varying stiffness within the lattice.

The analysis presented here is adapted from Wang et al. [2005], where the solution for the case of Euler Column with variable cross section under end concentrated load is derived. Since the struts running perpendicular to the loading direction do not participate in the deformation, their contribution to the mechanics is ignored, if we assume the bi-layer to undergo cylindrical bending (unlike that of plate bending where Poisson-coupling between the two curvatures takes place). Euler column buckling with axially varying cross-section is described by

$$\frac{\mathrm{d}^2}{\mathrm{d}x^2}\left[EI(x)\frac{\mathrm{d}^2 w}{\mathrm{d}x^2}\right] + P\frac{\mathrm{d}^2 w}{\mathrm{d}x^2} = 0, \tag{4.1}$$

where $x$ runs along the axis of the column, $w(x)$ is the post-buckled transverse deflection, $EI(x)$ is the variable stiffness as a function of axial position—a consequence of the variable cross-section—and $P$ is the compression load. This is a second order linear ordinary differential equation with *non-constant coefficients*. Note also that the variable coefficient term $EI(x)$ is inside the outer double differentiation. Double integration of equation 4.1 gives the following non-homogeneous second-order linear differential equation

$$EI(x)\frac{\mathrm{d}^2 w}{\mathrm{d}x^2} + Pw = C_1 + C_2 x. \tag{4.2}$$

The solution to this non-homogeneous differential equation can be written as a sum of the complementary function associated with the homogeneous part, $w_h(x)$, and a particular solution $w_p(x) = \frac{C_1}{P} + \frac{C_2}{P}x$; the sum of these gives the complete solution

$$w(x) = w_h(x) + \frac{C_1}{P} + \frac{C_2}{P}x, \tag{4.3}$$

where $w_h(x)$ is the solution to the corresponding homogeneous equation

$$EI(x)\frac{\mathrm{d}^2 w_h}{\mathrm{d}x^2} + Pw_h = 0. \tag{4.4}$$

If we now write the expression for the bending stiffness $EI(x)$ of a column with circular cross section, using a radius that varies *linearly*, $r(x) = B + Ax$, we obtain

$$EI(x) = E\frac{\pi}{4}r^4(x) = \frac{E\pi}{4}\left(B + Ax\right)^4, \tag{4.5}$$

which can be rewritten using the substitutions

$$\alpha = \frac{E\pi B}{4} \tag{4.6}$$

$$b = \frac{-A}{B}, \tag{4.7}$$

as

$$EI(x) = \alpha\left(1 - bx\right)^4. \tag{4.8}$$

This can be used to rewrite the homogeneous equation 4.4 as

$$\alpha\left(1 - bx\right)^4 \frac{\mathrm{d}^2 w_h}{\mathrm{d}x^2} + P w_h = 0. \tag{4.9}$$

Note that the stiffness here is that of a single column. For this reason, as we will see for the laboratory tests, this result will be used with structures that are made up of a single layer of filaments along the $x$ axis. The modelling of the response of structures with more layers will be dealt with in the last part of this chapter. The solution to equation 4.4 can be found in Murphy [1960]. Plugging the homogeneous solution into the general solution 4.3, we have

$$w(x) = \frac{C_1}{P} + \frac{C_2}{P}x + C_3\mathscr{U}(z) + C_4\mathscr{V}(z), \tag{4.10}$$

where

$$z(x) = 1 - bx, \tag{4.11}$$

$$k = \tfrac{P}{\alpha b^2}, \tag{4.12}$$

$$\mathscr{U}(z) = \sqrt{z}\; J_{-1/2}(\sqrt{k}\, z^{-1}), \tag{4.13}$$

$$\mathscr{V}(z) = \sqrt{z}\; J_{1/2}(\sqrt{k}\, z^{-1}), \tag{4.14}$$

and $J$ represents Bessel functions. It is worth noting that this solution is valid under the assumption that $1 - bx > 0$, which needs to be checked. To do so, we need to consider the expression for $r(x) = B + Ax$. When the radius varies linearly, the case here, along a length $L$ from a value $r_0 > 0$ at one end to a value of $r_1 > 0$ at the other end, the values of $A$ and $B$ would be:

$$A = \frac{r_1 - r_0}{L} \tag{4.15}$$

$$B = r_0. \tag{4.16}$$

Because of the fact that $B = r_0 > 0$ and remembering that $b = \frac{-A}{B}$, the assumption $1 - bx > 0$ is equivalent to $B + Ax > 0$. This is always true as the value $B + Ax = r(x)$ which cannot be negative. It is now possible to apply, to a structure of length $L$, four boundary conditions (pinned ends) in order to find the critical loads. This means writing a system of four equations in four unknowns, which leads to a set of homogeneous algebraic equations. For non-trivial solutions, the determinant must be set to zero. The expression for this, found in Wang et al. [2005], is $\mathscr{U}[z(L)]\mathscr{V}[z(0)] - \mathscr{V}[z(L)]\mathscr{U}[z(0)] = 0$. The critical buckling load is thus obtained as

$$P_{crit,n} = \frac{\alpha\pi^2(1 - bL)^2 n^2}{L^2}. \tag{4.17}$$

Buckling mode shape corresponding to $P_{crit,1}$ can be obtained by determining the constants $C_1$, $C_2$, $C_3$ and $C_4$ in 4.10 up to an undetermined arbitrary scaling. The nature of the problem, does not allow for *all* the constants to be found: the calculation of the critical loads is carried out by setting to zero the determinant of the system of the boundary conditions. This means that one of the four equations can be left out as it is linearly dependent on the other three. The system of boundary conditions reduces to a system of three equations in three unknowns with one constant chosen arbitrarily—in this case, set to 1. The three boundary conditions that are kept are $w(0) = 0$, $w(L) = 0$ and $w''(0) = 0$, with the constant $C_4$ set to one. Solving this system, the constants become $C_1 = 0$, $C_2 = 0$, $C_3 = \tan\left[\frac{(bL-1)\pi}{L|b|}\right]$ and $C_4 = 1$. The buckled shape is then obtained as

$$w(x) = \tan\left[\frac{(bL-1)\pi}{L\,|b|}\right]\mathscr{U}(z) + \mathscr{V}(z) = \frac{\sqrt{2}\,bL(bx-1)\sec\left[\frac{\pi}{bL}\right]\sin\left[\frac{(bL-1)\pi x}{L(bx-1)}\right]}{\pi\sqrt{L|b| - bL^2|b|}}. \tag{4.18}$$

This result only depends on the parameter $b$, a measure of the gradation of the column (see equation 4.5). Fixing the length $L$, it is now possible to plot the buckled shape assigning a value to the parameter $b$. As an example, in the case of a diameter that varies from $r_1 = 0.8\,\text{mm}$ to $r_0 = 0.4\,\text{mm}$ along a length $L = 100\,\text{mm}$, we obtain—using equations 4.7, 4.15, 4.16—that $b = -0.01$. Figure 4.4 shows that with $b$ approaching zero (setting $b = 0$ is not possible due to $\sec\left[\frac{\pi}{bL}\right]$ in the expression for $w(x)$), the shape becomes more and more symmetrical, a quick and effective way to check the model.

## 4.3 Measured asymmetric profiles for lattice structures with axially varying stiffness

A simple bi-layer structure, with variable-diameter struts, is tested to record the post-buckled bent profile. This is followed up with comparisons with the theoretical predictions presented in the previous section. In the previous chapter, the fabrication technique

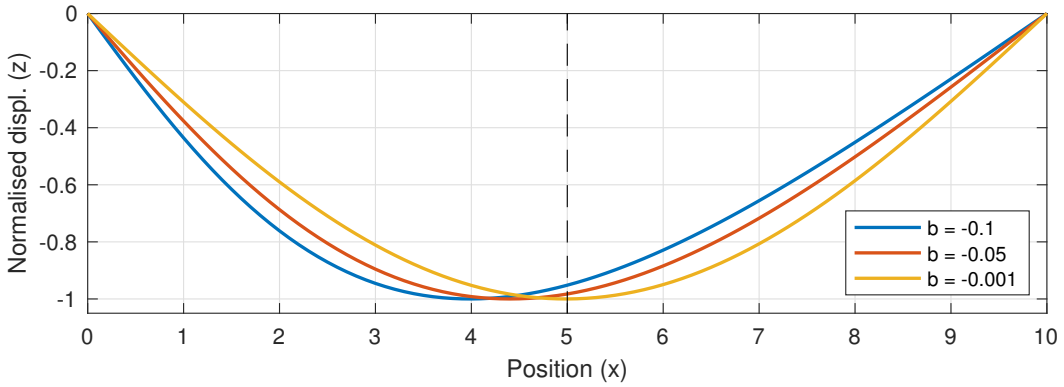


Figure 4.4: A plot of the buckled shapes, equation 4.18, with different values for $b$ ($b = -0.001$, $b = -0.05$, $b = -0.1$). This shows that, when $b$ approaches zero, the minimum is closer to the line through the midpoint, dashed line. This indicated that the asymmetry decreases, as expected.

was proposed to realise variable extrusion using fixed bore FDM nozzles. Here continuously varying struts are fabricated within lattices, the spatial variation in a lattice only in its length direction. Such bi-layer functionally graded filaments have been manufactured. Buckling profiles are easy to characterise. By contrast, spatial variation of asymmetric response in tension/compression is very hard to capture experimentally. Likewise, 3-point and 4-point bending tests were abandoned due to practical difficulties encountered in ensuring correct support conditions and also in capturing the bent profile.

### 4.3.1 Fabrications of bi-layer lattices with uni-axially varying bending stiffness

The proposed approach of 3D printing variable stiffness extrusions, as presented in the previous chapter, enabled us to drive the manufacture as per a chosen function for diameter variation along the print direction with smooth transitions due to the flow nature of the molten polymer. If we imagine a single filament of length $L$, we can obtain a variable diameter by dividing this filament into sub-segments—similar to discretisation in numerical analysis, and extruding each sub-segment using a different value of the intended diameter as demanded by a specified function according to which functionally graded structure needs fabricating. The fabricated extrusion is smoothened further because of the rheology of the extruded material in its molten state. The resulting filaments are then a concatenation of short extrusions of fixed but different diameter, smoothened by the fluid-like properties of the polymer. Due to this we do not have the perfectly linear variation that we assume ($r(x) = B + Ax$), however, the aim of the work is to establish whether the variation in the diameter introduced is mechanically continuous. This means that we aim to find out whether the mechanical response of the lattice under bending can be predicted by assuming continuous variation in the diameter of the filaments. If

this is true, then we say that we have achieved continuous variations in the properties and the diameter.

The samples used for these tests have two layers. Filaments in one layer run in the $x$ direction and are graded in that direction. Filaments of the other layer run perpendicular to the first. The films have been manufactured using a feed rate $F \approx 1100\,\text{mm}\,\text{min}^{-1}$ and an extrusion temperature of 210 °C. Two different samples were manufactured, coarse or fine, depending on the spacing between the filaments (see figures 4.5 and 4.6). The coarse samples are identified by the letter C and are characterised by a spacing between the filaments $s \approx 3.2\,\text{mm}$, see figure 4.5. The fine samples, denoted by letter F, have smaller spacing between filaments, $s \approx 1.6\,\text{mm}$, as can be seen in figure 4.6. For each of these two types, six samples with three different specified gradations (variation in diameter from one end to the other) were 3D-printed. Samples denoted by type 0 have no variation, which are then constant stiffness samples; two samples of type 1 have been printed, with $0.35\,\text{mm} < d_{\text{intended}} < 0.6\,\text{mm}$, and two samples of type 2, with $0.42\,\text{mm} < d_{\text{intended}} < 0.6\,\text{mm}$. To further clarify the notation with examples, sample 1F would identify a sample with small spacing (identified by F), printed with $0.35\,\text{mm} < d_{\text{intended}} < 0.6\,\text{mm}$ (identified by 1); sample 0C would identify a sample with no gradation ($d_{\text{intended}} = d_{\text{nozzle}} = 0.4\,\text{mm}$) printed with large spacing.

### 4.3.2 Methodology for the laboratory tests

Experimental test were performed on the bi-layer samples described in the previous section. One layer is made up of graded filaments ($x$ direction), the other orthogonal layer, is formed of non-graded filaments ($y$-direction). A total of twelve lattice films were manufactured using the process developed, and tested past buckling using a Tinius Olsen H5KS Benchtop Tester in displacement control mode. The sample was placed between two flat plates which were then brought closer together by 12 mm. This allowed the samples to buckle, and the deformed shape was captured with a camera. The samples were photographed in their edge view to capture the buckled profile (see Figure 4.7). Every effort was made to minimise the effects of parallax error. The next steps involve the use of a software, WebPlotDigitizer [2010], to extract the data points from the images and plot the experimental profile against those obtained with the analysis presented in the previous section.

In addition to demonstrating the fabrication capability of continuously varying extrusion in FDM 3D-printing, a purpose of experimental measurement of the bent profile is also to validate the analysis for this class of functionally graded structures. The mode shape associated to the first critical load is used for comparisons. Since the amplitude of mode shapes is arbitrary, both the experimental and theoretical buckled shapes have been normalised using their respective maximum deflection for shape comparisons.

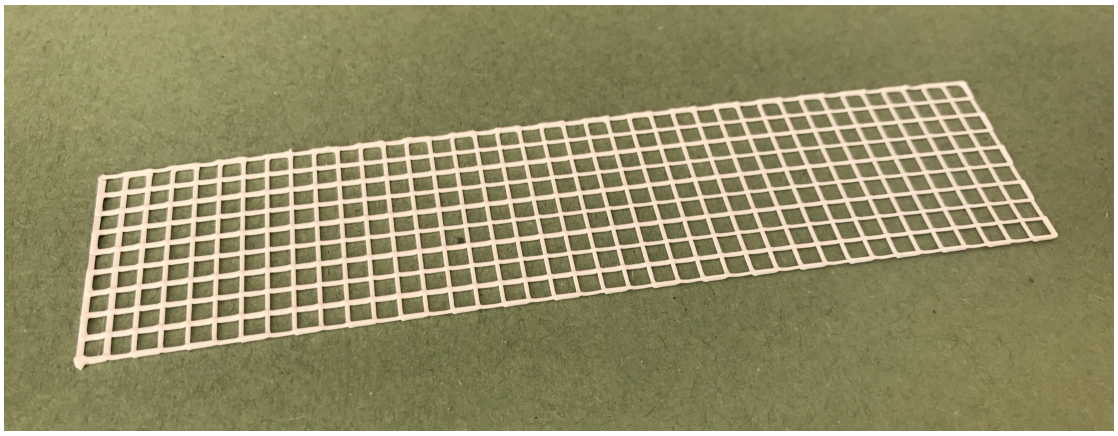

Figure 4.5: The coarse sample used in the buckling tests has two layers, the one in the $x$ direction is graded. The spacing between filaments is large (compared to the other sample).

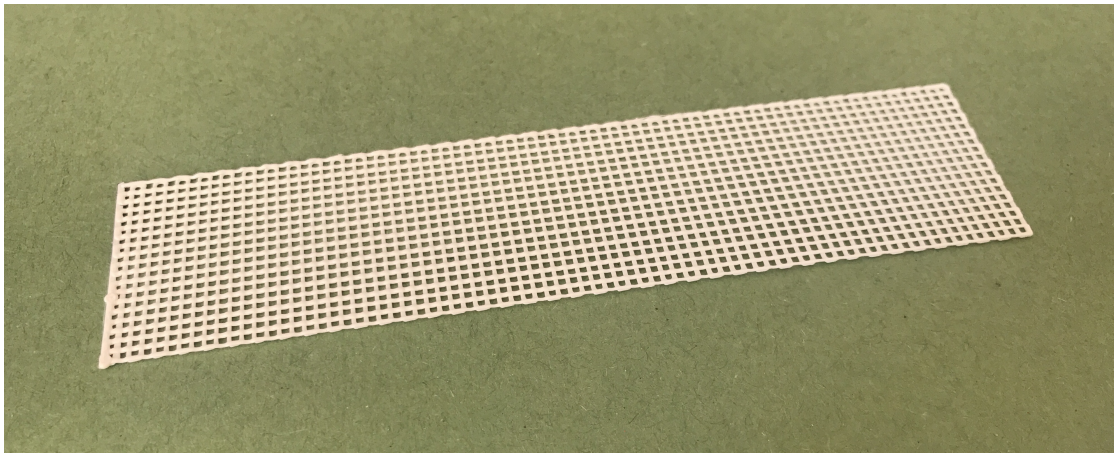

Figure 4.6: The fine sample used in the buckling tests has two layers, the one in the $x$ direction is graded. The spacing between the filaments is smaller.

### 4.3.3 Measurement of asymmetric out-of-plane response for variable stiffness bi-layer lattices

We now describe the laboratory set up for the experiments and show the results obtained, followed by a comparison with the theory developed in the previous section. Within a tensile testing machine equipped with two flat plates, samples were put vertically and compressed until buckling occurs. Once the sample buckles, an image of the profile was taken. An example is presented in figure 4.7. The images were then processed to obtain the shape of the profile. To do so, the images such as those shown in figure 4.7, were uploaded on WebPlotDigitizer [WebPlotDigitizer, 2010]. On this web-based image processing tool, it is possible, in three simple steps (figures 4.8, 4.9, 4.10), to place points on the images and get the coordinates with respect to a reference. In step 1, figure 4.8, the rulers in the images are used to set a known distance between two points so that a scale and direction for two axes can be defined; in our case, resulting in a scale of

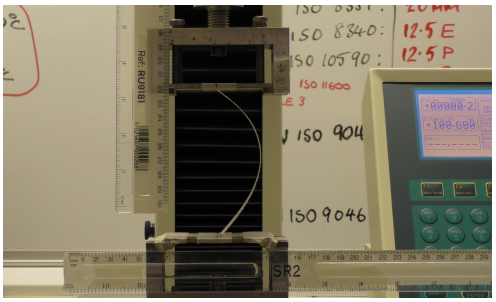


Figure 4.7: Step 0: test set up. The sample is compressed until it buckles. The picture is taken from the front to study the profile.

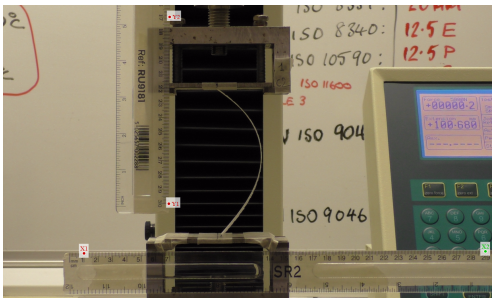


Figure 4.8: Step 1: calibration of the coordinate system selecting four points on the image and assigning their distance (based on the rulers).

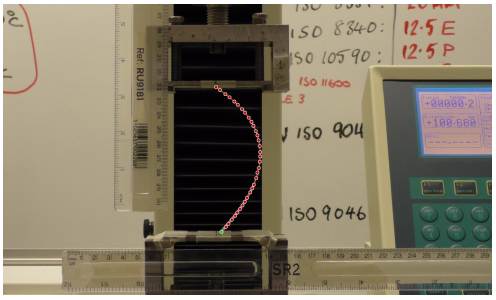


Figure 4.9: Step 2: sampling. Clicking on the image, points are created with respect to the coordinate system of the previous step.

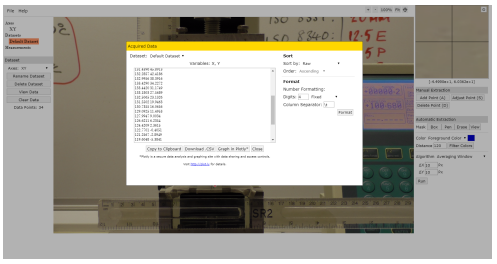

Figure 4.10: Step 3: data acquisition. Once the points have been selected, their coordinates are exported for post-processing.

approximately 114 pixels/cm. In step 2, figure 4.9, the user selects points on the image. In step 3, figure 4.10, the coordinates of these points are exported to a text file that can then be post-processed. The exported data can now be used to plot the deformed shapes. With a simple transformation of coordinates, the shape can be plotted on an $x$–$y$ coordinate system that matches that of the theoretical model, for ease of comparison.

Results obtained are shown in figures 4.11 to 4.15. Note the asymmetric curvature for both theoretical and the measured bent profiles. The computed profile also shows greater curvature on the left side of the plot, where the stiffness is lower, as expected. Successful prediction of the bent profile and asymmetry of the shape confirm the modelling and manufacturing capabilities presented here. We start by comparing films of type 1 labelled with C, Figure 4.11—where the spacing is $s \approx 3.2\,\text{mm}$—to those labelled with F, figure 4.12—where the spacing is $s \approx 1.6\,\text{mm}$. The Mean Square Error (MSE) will be used in the following as a mean of comparison and is defined as the averaged sum of the squares of the distances between theoretical and experimental results. The MSE is smaller for the C-films, where the average is MSE = 0.00129 between the two samples, compared to the F-films, characterised by an average MSE = 0.00335. The coarse samples giving the best match may hint at the fact that the interaction between transverse filaments, ignored

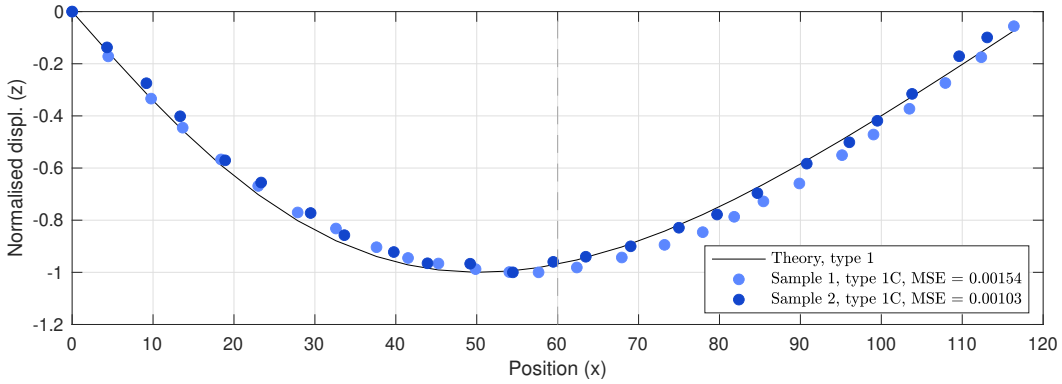


Figure 4.11: Comparison between the mathematical model (solid line) and the laboratory results for two coarse samples of type 1. The dashed line marks the midpoint of the sample. The average mean square error of these two films is MSE = 0.00129.

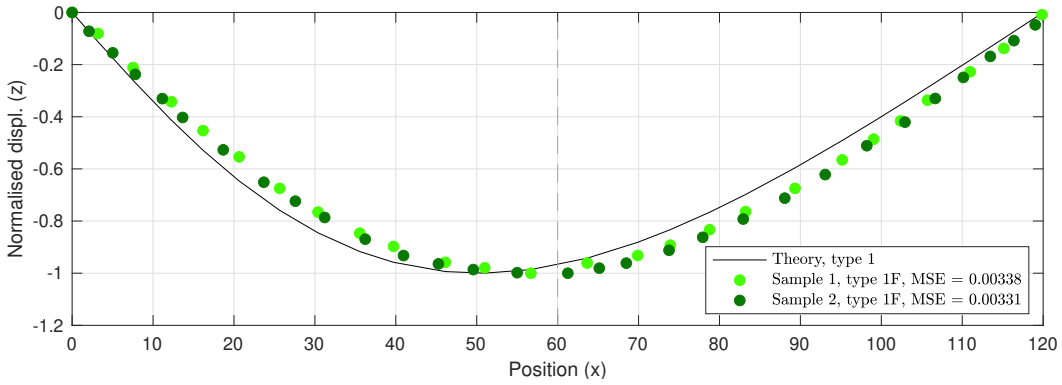


Figure 4.12: Comparison between the mathematical model (solid line) and the laboratory results for two fine samples of type 1. The dashed line marks the midpoint of the sample. The average mean square error of these two films is MSE = 0.00335.

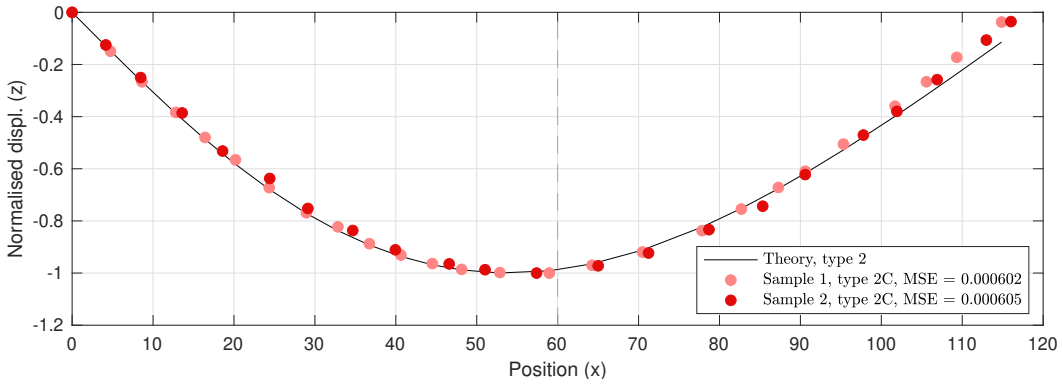


Figure 4.13: Comparison between the mathematical model (solid line) and the laboratory results for two coarse samples of type 2. The dashed line marks the midpoint of the sample. The average mean square error of these two films is MSE = 0.000604.

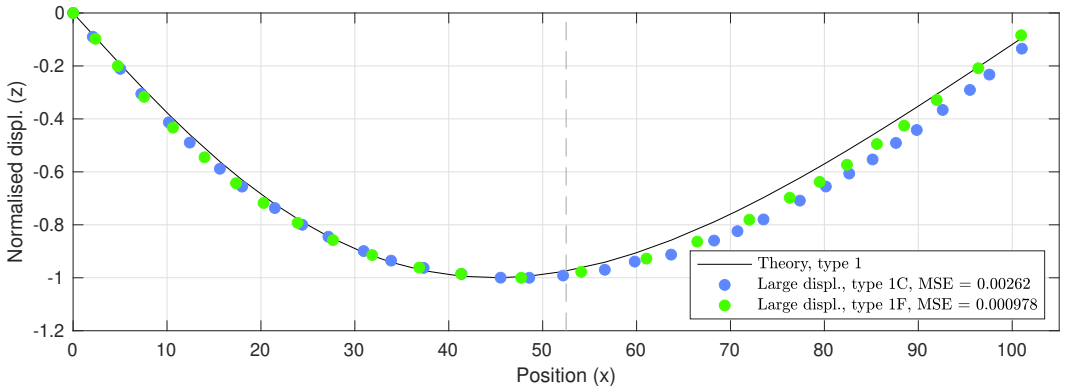


Figure 4.14: Comparison between the mathematical model (solid line) and the laboratory results for a coarse sample (MSE = 0.00262) and a fine sample (MSE = 0.000978) of type 1, in case of large displacement. The dashed line marks the midpoint of the sample.

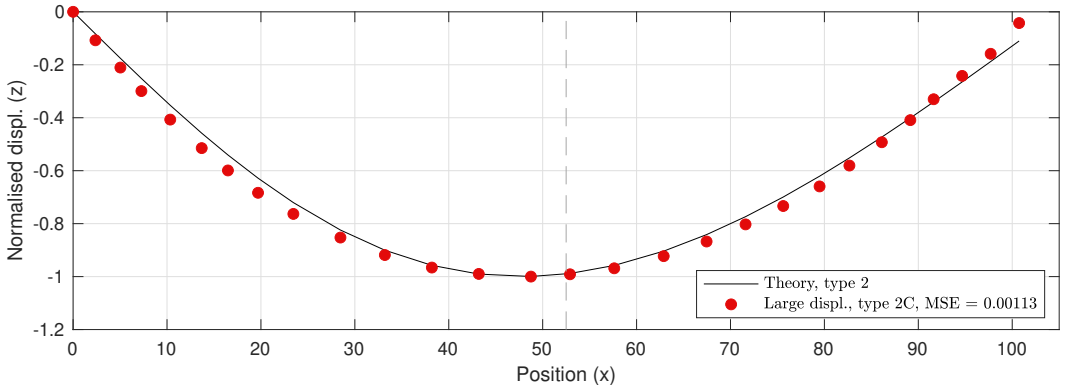


Figure 4.15: Comparison between the mathematical model (solid line) and the laboratory results for a coarse sample of type 2, in case of large displacement. The dashed line marks the midpoint of the sample. The mean square error is MSE = 0.00113.

in this analysis, may become relevant the smaller the spacing. Next, we compare coarse films (C-films) of type 1, figure 4.11, and type 2, figure 4.13. We remind that films of type 1 have a variation in the diameter of their filaments $0.35\,\text{mm} < d_{\text{intended}} < 0.6\,\text{mm}$, while films of type 2 are characterised by $0.42\,\text{mm} < d_{\text{intended}} < 0.6\,\text{mm}$. The best match, in this comparison, is for the films of type 2, where the average MSE = 0.000604. This suggests that the variation in diameter for filaments of type 2 is more consistent with what is expected, while for samples of type 1 the expected range in diameter may not be reproduced correctly by the 3D printer. The reason for this may be the inability of the 3D-printer to cope with the commands when the variation is large or the inaccurate diameters for under-extruded filaments. We can observe that in figures 4.11 and 4.12, the mathematical model predicts slightly more asymmetry than the corresponding laboratory results. This can be an indication of the fact that the variation in the filament diameter of the printed samples is smaller that expected.

Potential discrepancies between theoretical and laboratory results can be attributed to

three main sources. One of them is the measurement error. The second is modelling error, i.e. there are known unmodelled mechanics such as the presence of shear. Finally, it is hard to make measurements for infinitesimal transverse displacement, which means that the measured profile has non-linear effects in it, whereas the theory used is linear. Considering all these, the match between the theoretical profile and the experimentally measured ones is excellent.

To highlight the last point, results obtained for large displacement, figures 4.14 and 4.15, are shown. Excluding films of type 1 with smaller spacing,where the MSE was very large for small displacement as well, the other films all show a worst match in the case of large displacement. The linear mathematical model does not use large displacement analysis. Mode shapes obtained with linear analysis depend only on the variation in the diameter, which gives more or less asymmetry (figure 4.4), on the other hand, for large displacements, the amplitude of the displacement should also be a parameter for the mode shape. The mismatch in this case is different from the mismatch visible in figure 4.11, for example. In that case, we obtain a result that is less asymmetric than expected due to the variation in diameter not being reproduced correctly; in this case, instead, the asymmetry is not the main issue, rather, the *shape* is.

## 4.4 Analytical response calculations for functionally graded lattice structures

Having presented feasibility to fabricate functionally graded lattice materials, and validated a theory for a simple 1D problem of a bi-layer lattice flexure, we are ready to look at a host of problems in this class of functionally graded lattice materials. The rest of this chapter is devoted to such analytical studies. All the problems considered here are within the scope of 1D elasticity. No experimental validation of any of the theoretical work presented in the remaining part of this chapter will be carried out. In the next chapter, a bi-directionally graded film will be considered, where fabrication, testing and computational modelling will be carried out.

The following suite of problems concerning lattice elasticity are considered now: (i) bending of lattice beams with several layers, each filament being functionally graded; (ii) lattice beam response with apparent spatially varying bending stiffness; (iii) compression of woodpile lattice structures.

### 4.4.1 Apparent flexural properties of lattices made of variable diameter filaments

Filaments stacked in a woodpile arrangement are frequently used in many applications. Their mechanics is of great interest. In this subsection, we consider the bending response

of a slender structure with internal architecture as of a woodpile.

Apparent elastic properties are convenient to describe the elastic behaviour of architectured materials. The structured matter is imagined to be loaded remotely. The response can be viewed as one of the apparent strain in the lattice. This apparent strain may not be related to all of the material points in the lattice structure, rather it is due to the displacement field at certain key points in the lattice. The apparent elastic properties relate the apparent strain quantities with the remote stresses applied. The bending stiffness of a solid slender structure is given by $B = EI$, where $E$ is the Young's modulus of the material and $I$ is the second moment of area of the cross-section around its neutral axis. Here we determine the apparent bending stiffness of a slender lattice structure $\langle B \rangle = E \langle I \rangle$. We want to find an expression for $\langle I \rangle$ such that, multiplied by the Young's modulus of the base material (material of which the filaments are made), it gives the apparent bending stiffness of the lattice. This model has been developed here for *functionally graded lattices*, hence the bending stiffness depends on the position $x$ along the length, given by $\langle B \rangle (x) = E \langle I \rangle (x)$.

Figure 4.16 shows a unit cell of the lattice. This cell is not strictly repeated as it is, which is usually the case when the term unit cell is used, rather, the diameter of the blue filaments changes based on the position of the cell within the film. We refer to the filaments running in the $x$-direction, in blue, as participating filaments, for the reasons described in Section 4.1. The assumption made is that the dimensions of a cell, given by $dx$, $dy$ and $dz$, are constant. The diameter of the filaments running along the length vary and the diameter of the perpendicular filaments, in grey, is chosen so that the cell dimensions are kept constant. The radius of the filament that does not participate in bending at $x = x_0$ is chosen as $\frac{dz}{2} - r(x_0)$, where $r(x_0)$ is the radius of the participating filament at $x = x_0$. The bending moment, $M$, is acting on the $xz$-plane.

Having introduced the single cell and its dimensions, consider the end view of the cross-section of the lattice, shown in figure 4.17. The blue circles represent the cross-sections of the filaments participating in bending, while the grey filaments, running transversely, and they do not contribute to lattice deformation. The number of active filaments in the $y$ and $z$ directions are $N_y$ and $N_z$ respectively. Taking one single stack of filaments, hence, one of the $N_y$, we obtain figure 4.18. In the following calculations, it is necessary to divide the cases of odd (figure 4.18(a)) and even (figure 4.18(b)) number of filaments in the stack, $N_z$. We will refer to these cases with the subscripts ODD and EVEN.

Consider figure 4.18. We separate two cases: when $N_z$ is an odd integer, or when it is even. In the first case, shown in figure 4.18(a), we can sum the second moment of area of the red coloured circle with the second moment of area of the blue coloured circles. The second moment of area of the red circle can be immediately found as it lays on the neutral axis; the second moment of area of the blue circles, instead, must be found using the parallel axis theorem. When $N_z$ is an even integer, as in figure 4.18(b), no circle

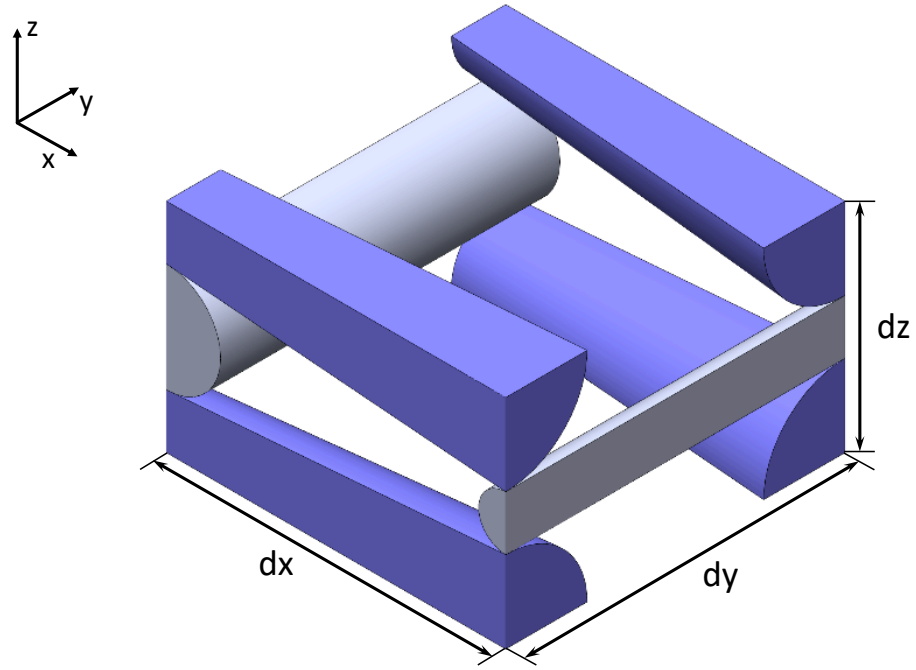


Figure 4.16: A cell of the lattice. The participating filaments, those running in the $x$-direction, show a continuous variation in their diameter; the filaments running in the $y$ direction, which do not participate in bending, are of a diameter that ensures constant dimensions of the cell. The quantity $dx$ is the distance, in the $x$-direction, between the centres of non-participating filaments; $dy$ is the distance, in the $y$ direction, between the centres of participating filaments; $dz$ is the vertical distance between the centres of participating filaments and is also called layer height.

is on the neutral axis, so to account for the second moment of area contributions from every circle, parallel axis theorem needs to be used. The expressions for the two cases become

$$\langle I \rangle_{\text{ODD}}(x) = N_y \left[ I(x) + 2 \sum_{i=1}^{\frac{N_z-1}{2}} \left[ I(x) + A(x) \left( i\, dz \right)^2 \right] \right], \tag{4.19}$$

$$\langle I \rangle_{\text{EVEN}}(x) = N_y \left[ 2 \sum_{i=0}^{\frac{N_z-2}{2}} \left[ I(x) + A(x) \left( \frac{dz}{2} + i\, dz \right)^2 \right] \right], \tag{4.20}$$

where $I(x)$ is the second moment of area of the cross section of one filament, at position $x$, and $A(x)$ is its cross-sectional area. Using the relations

$$\sum_{i=1}^{\frac{N_z-1}{2}} i^2 = \frac{1}{24} N_z (N_z^2 - 1), \tag{4.21}$$

$$\sum_{i=0}^{\frac{N_z-2}{2}} (1+2i)^2 = \frac{1}{6} N_z (N_2^2 - 1), \tag{4.22}$$

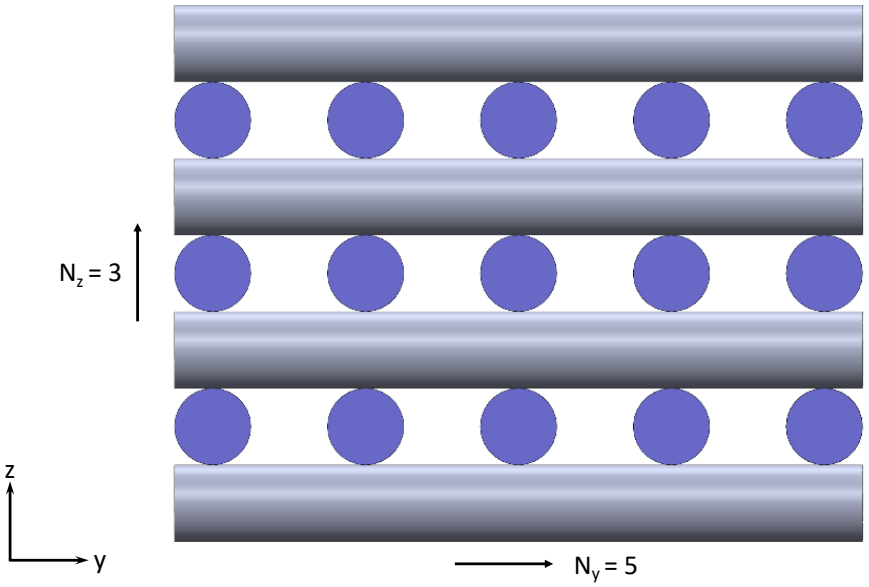


Figure 4.17: Cross-section of a lattice structure. $N_y$ is the number of blue circles in the $y$-direction (5, in this example); $N_z$ is the number of blue circles in the z-direction (3, in this example). Transverse filaments, in grey, are not contributing to the bending stiffness.

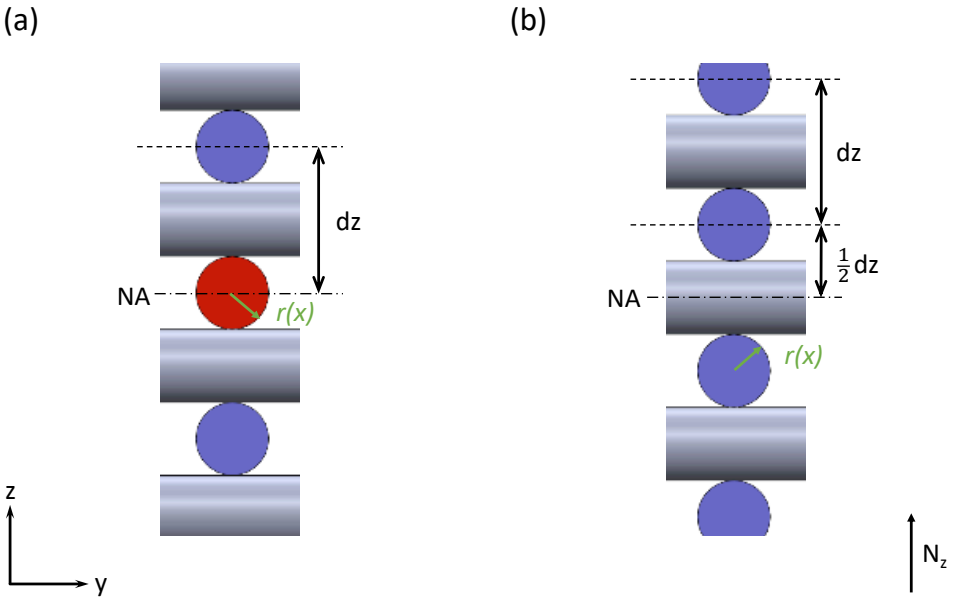


Figure 4.18: (a): end view of a stack of filaments in case of an odd number of participating layers. (b): end view of a stack of filaments in case of an even number of participating layers. Transverse filaments are shown in grey, participating filaments in blue, and the participating filament whose cross section lies on the neutral axis in red.

the apparent second moment of area can be written as a single expression for both cases:

$$\langle I \rangle (x) = N_z N_y \left[ I(x) + \frac{1}{12} dz^2 \left( N_z^2 - 1 \right) A(x) \right]. \tag{4.23}$$

Consider variable cross-section of *circular* shape, we have expressions for position dependent second moment of area and the cross-sectional area as

$$I(x) = \frac{\pi}{4} r^4(x), \tag{4.24}$$

$$A(x) = \pi r^2(x). \tag{4.25}$$

Thus, relation 4.23 now becomes:

$$\langle I \rangle (x) = \frac{\pi}{12} N_y N_z \left[ 3r^4(x) + dz^2 (N_z^2 - 1) r^2(x) \right]. \tag{4.26}$$

This result allows us to treat the lattice architecture as a solid material characterised by this property. The quantity $E \langle I \rangle (x)$ is the apparent *functionally graded* bending stiffness of the lattice, where $E$ is the Young's modulus of the base material and $\langle I \rangle (x)$ is the apparent second moment of area of the lattice structure.

### 4.4.2 Approximate flexural response of variable-diameter lattice beams using Rayleigh–Ritz method

Here we provide an approximate solution based on an energy method known as the Rayleigh-Ritz method. The approach is to write the displacement field in an assumed form with some free parameters known as the generalised coordinates of the problem. Following this, the total potential energy needs to be minimised with respect to these unknown generalised co-ordinates, in order to satisfy equilibrium.

Equation 4.26 provides the functional form of the apparent bending stiffness of lattice beams, as derived in the previous subsection. This can be written in the following form as a function of the axial position $x$

$$\langle B \rangle (x) = E \langle I \rangle (x) = E_1 r^4(x) + E_2 r^2(x), \tag{4.27}$$

where the two constants $E_1$ and $E_2$ are given by

$$E_1 = \pi E N_y N_z / 4,$$
$$E_2 = A dz^2 (N_z^2 - 1)/3.$$

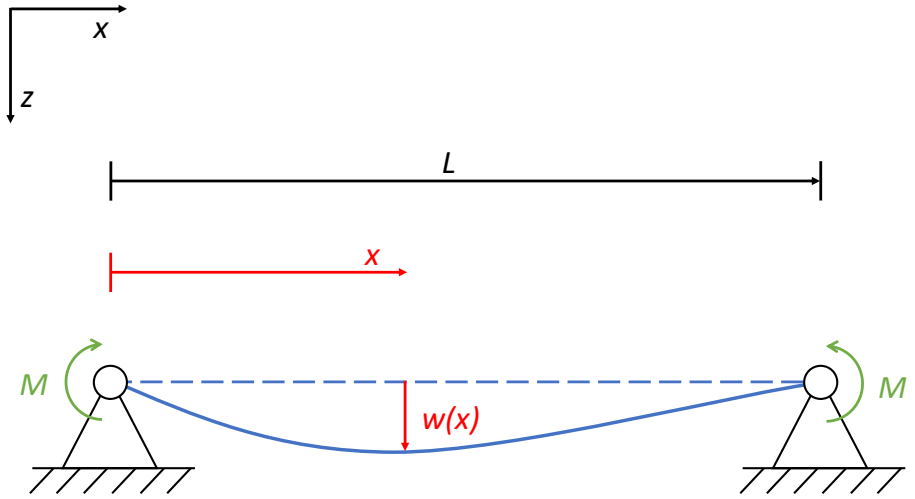


Figure 4.19: A simply supported beam is loaded with two moments $M$ at the two ends. The coordinate $x$ goes form 0 at the left support to $L$ at the right support. We are interested in the transverse displacement $w(x)$.

If we assume that the radius of filaments within the lattice varies linearly with $x$, i.e. $r(x) = B + Ax$, we can further rewrite $\langle B \rangle (x)$ as:

$$\langle B \rangle (x) = E_1(B + Ax)^4 + E_2(B + Ax)^2. \tag{4.28}$$

In this section we obtain the bending response of lattice beams with filaments of axially varying cross-sections, with bending stiffness given by equation 4.28. The aim is to find an approximate solution for the transverse displacement $w(x)$, see figure 4.19, with an approach on the lines of the Rayleigh–Ritz method. A filament—represented by the dashed blue line—is supported between two ends and is loaded by two end moments $M$ acting on the $xz$-plane. This causes the filament to deform transversely. The final bent shape is represented by the solid blue line. Note that we expect the blue line not to be symmetric with respect to its mid–point (its minimum is not at $x = L/2$); this is due to the functional gradation—a theme running through this thesis with regards to manufacture, measurements and analysis.

The application of the Rayleigh–Ritz method starts with an ansatz: i.e. a family of guessed functions for the vertical displacement $w(x)$ that are kinematically admissible. Then, we use the Principle of Minimum Total Potential Energy to find the configuration at equilibrium and derive the values of the parameters. It is a requirement for the method to choose the assumed basis functions so that they satisfy all the *geometric boundary conditions* of the problem. The term geometric boundary conditions refers to those boundary conditions dictated by the *geometry* of the problem. In this case, the

geometry dictates that there cannot be transverse displacement at the two ends, hence $w(0) = 0$ and $w(L) = 0$. The asymmetry in the deflection profile is a feature that we want to capture, hence the family of function we choose must allow this. The easiest functions to start with are polynomials in $x$. The minimum order to respect the geometric boundary conditions and the asymmetric behaviour is 3: a linear function cannot respect the geometric boundary conditions and a parabola would be symmetric. The family of functions that was chosen is then $w(x) = a_0 + a_1 x + a_2 x^2 + a_3 x^3$. After the application of the geometric boundary conditions, the cubic becomes

$$w(x) = x(x - L)(q_1 + q_2 x). \tag{4.29}$$

This has two unknowns $q_1$ and $q_2$ that can be treated as the generalised coordinates of the problem following the proposed Rayleigh-Ritz approximation. The **Principle of Minimum Total Potential Energy**, referred to as PMTPE in the following, states that "out of all the possible displacements, the configuration of equilibrium is one that minimises the total potential energy of the system". In mathematical terms, it can be expressed as

$$\Pi(q_1', \ldots, q_n') = \min_{q_1, \ldots, q_n} \Pi(q_1, \ldots, q_n), \tag{4.30}$$

where $\Pi = U + V$ is the total potential energy, sum of the potential energy and the potential energy of external loading; $q_1, \ldots, q_n$ are the generalised coordinates and $q_1', \ldots, q_n'$ are the coordinates of the configuration of equilibrium. PMTPE can be applied to find $q_1', \ldots, q_n'$. Using variational calculus, one can show that a minimisation of $\Pi$ (in the variational sense) with respect to the generalised coordinates is equivalent to satisfying the following

$$\frac{\partial \Pi}{\partial q_i} = 0 \qquad i = 1, \ldots, n. \tag{4.31}$$

This principle can be applied to the structure in Figure 4.19. First, we need to express the total potential energy $\Pi$ of the system as a function of the generalised coordinates. This is obtained by summing the potential energy $U$ and the potential energy of external loads $V$. The expression of the potential energy for a beam in bending is given by:

$$U = \frac{1}{2} \int_0^L E \langle I \rangle (x) \left[ w''(x) \right]^2 \mathrm{d}x, \tag{4.32}$$

where $w''(x) = \frac{\mathrm{d}^2 w}{\mathrm{d}x^2}$. The potential energy of external loading, $V$, equals the negative of the work done by external forces. In our case, we have two moments $M$ applied at the two ends, so

$$V = -W = Mw'(0) - Mw'(L). \tag{4.33}$$

With the assumed form of the expression for $w(x)$ that we have chosen (equation 4.29), expressions for $U$ and $V$ become:

$$U = \frac{1}{2}\int_0^L \left[E\left\langle I\right\rangle(x)\right]\left[w''(x)\right]^2 \mathrm{d}x = \\ = \frac{1}{2}\int_0^L \left[E_1(B+Ax)^4 + E_2(B+Ax)^2\right]\left[6q_2x + 2(q_1 - q_2L)\right]^2 \mathrm{d}x, \tag{4.34}$$

$$V = M[w'(0)] - M[w'(L)] = M[-q_1L] - M[3q_2L^2 + 2L(q_1 - q_2L) - q_1L]. \tag{4.35}$$

We can now apply the PMTPE to find the values of $q_1'$ and $q_2'$. The results of partial differentiation—obtained using Mathematica—are:

$$q_1' = \frac{N_{q_1'}}{D_{q_1'}}; \tag{4.36}$$

$$N_{q_1'} = 5M\left[210B^4E_1 + 560B^3E_1AL + 42B^2\left(17E_1A^2L^2 + 5E_2\right) + \right. \\ \left. 140B\left(3E_1A^3L^3 + +2AE_2L\right) + 94E_1A^4L^4 + 119A^2E_2L^2\right]; \tag{4.37}$$

$$D_{q_1'} = 2100B^8E_1^2 + 8400B^7E_1^2AL + 280B^6E_1\left(53E_1A^2L^2 + 15E_2\right) + \\ + 2520B^5E_1AL\left(6E_1A^2L^2 + 5E_2\right) + 60B^4\left(165E_1^2A^4L^4 + 273E_1A^2E_2L^2 + \right. \\ \left. + 35E_2^2\right) + 40B^3\left(110E_1^2A^5L^5 + 294E_1A^3E_2L^3 + 105AE_2^2L\right) + \\ + 60B^2\left(22E_1^2A^6L^6 + 81E_1A^4E_2L^4 + 49A^2E_2^2L^2\right) + 120B\left(2E_1^2A^7L^7 + \right. \\ \left. + 9E_1A^5E_2L^5 + 7A^3E_2^2L^3\right) + 20E_1^2A^8L^8 + 108E_1A^6E_2L^6 + \\ + 105A^4E_2^2L^4; \tag{4.38}$$

$$q_2' = \frac{N_{q_2'}}{D_{q_1'}}; \tag{4.39}$$

$$N_{q_2'} = 70AM(2B + AL)\left(10B^2E_1 + 10BE_1AL + 4E_1A^2L^2 + 5E_2\right); \tag{4.40}$$

$$w(x) = -\frac{N_w}{D_{q_1'}}; \tag{4.41}$$

$$N_w = 5Mx(L-x)\left[210B^4E_1 + 280B^3E_1A(2L-x) + 42B^2\left(E_1A^2L(17L + \right. \\ \left. - 10x) + 5E_2\right) + 28BA\left(3E_1A^2L^2(5L-3x) + 5E_2(2L-x)\right) + \\ + A^2L\left(2E_1A^2L^2(47L-28x) + 7E_2(17L-10x)\right)\right]. \tag{4.42}$$

These expressions can then be used to obtain the transverse displacement for a lattice structure under bending, by simply giving values to the parameters within the expressions. As an example, we consider the end view of the lattice as represented in Figure 4.17 and we set $N_y = 10$ and $N_z = 3$. We also set a length for the lattice $L = 125\,\mathrm{mm}$ and the moments applied are $M = 0.5\,\mathrm{N\,m}$. The representative variation in the diameter of the filaments running along the $x$ axis that has been selected is a linear variation from $0.3\,\mathrm{mm}$ at the left end ($x = 0$) to $0.8\,\mathrm{mm}$ at the right end ($x = 125$). The bent profile of such a sample is represented by a black solid line in figure 4.20. Similarly, the red line on

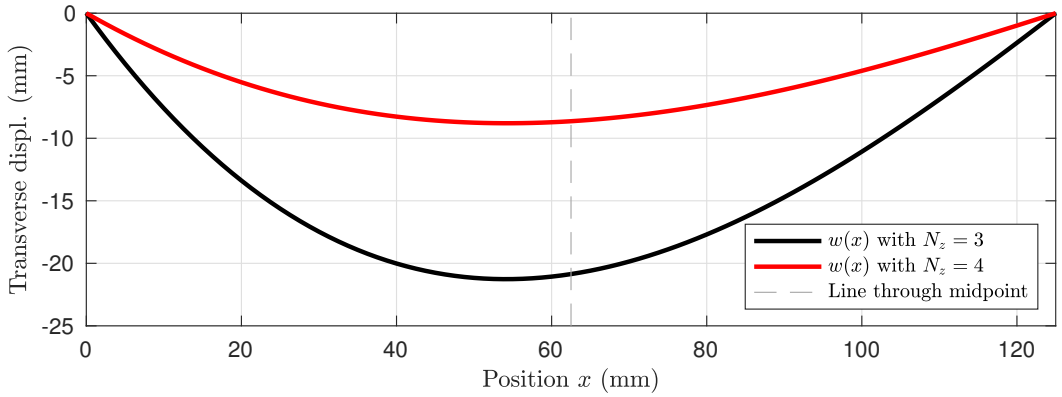


Figure 4.20: In solid black, the transverse displacement of a lattice structure with $N_y = 10$, $N_z = 3$ and $L = 125\,\text{mm}$ plotted using the solution obtained following the Rayleigh–Ritz method. The diameter of the filaments running parallel to the $x$-axis varies from 0.3 mm to 0.8 mm and the moments applied are $M = 0.5\,\text{N m}$. The red solid line has been obtained setting $N_z = 4$, while keeping the other parameters the same, and is then stiffer because of the extra layer along the $z$-axis.

the same image has been obtained setting $N_z = 4$. The rest of the parameters have the same values just presented. The effect of spatial variation of stiffness is apparent from the asymmetry of the deflection profiles. Further, since the stiffness increases from left to right, the curvature is greater on the left half than that of the right half, consistent with expectations.

### 4.4.3 Compressive stiffness of woodpile lattices in the stacking direction: shear correction for dense lattices

Consider the lattice in figure 4.21. It is compressed transversely by a pressure $p$ and the transverse filaments, represented by the circles, are at an offset from one layer to another. Such woodpile lattices are known as *staggered*. Note also that the alternate layers may not be symmetrically staggered, i.e. each piece of strut between two supports below is loaded by a strut above, which is not symmetrically placed. This loaded elastic lattice can be modelled by considering the single longitudinal filaments subject to periodic loading and periodic supports. The underlying mechanism by which the response is dictated is the bending of the filaments, when the lattice is in compression in the stacking direction. This reduces this 3D compression problem to a 1D bending problem of a single filament.

The models found in literature so far are based on the Euler–Bernoulli beam theory. In Cuan-Urquizo [2016], a study on the compression of woodpile lattices is present, however, no contributions due to shear are accounted for. The main assumption is then that a cross-section that is normal to the neutral axis before deformation remains normal after the deformation. The ratio between the spacing between the supports and the characteristic dimension of the cross-section—for example, the diameter for a

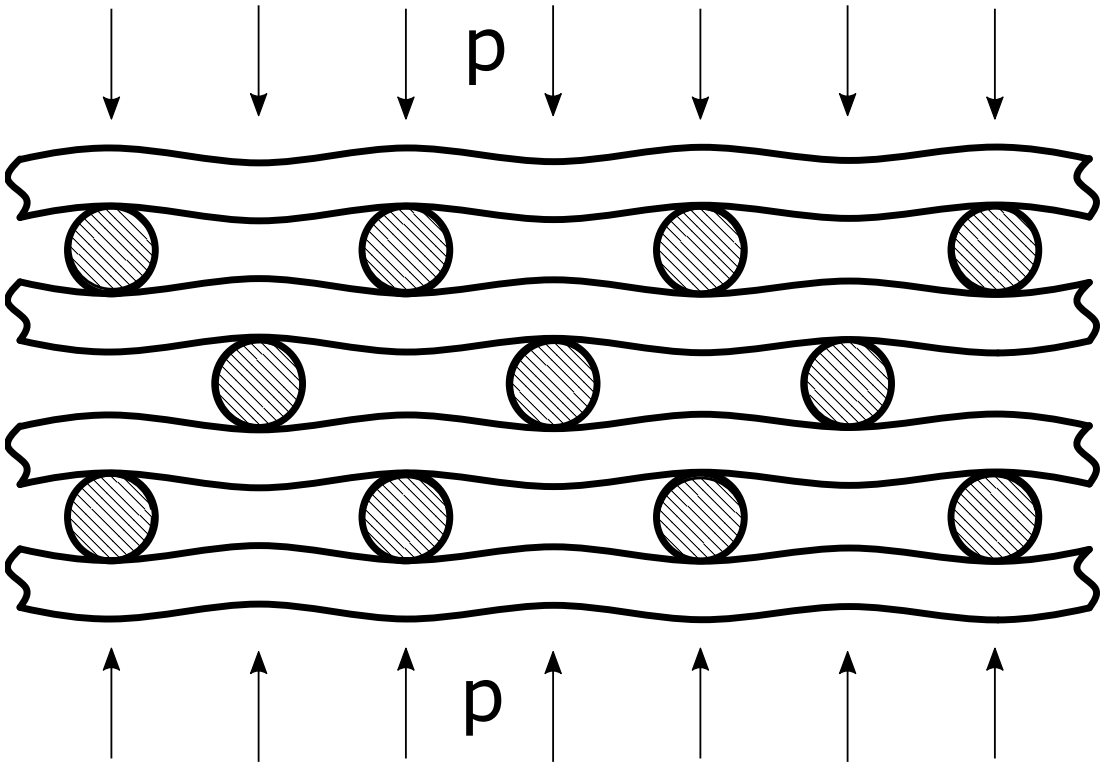


Figure 4.21: Front view of a portion of an infinite lattice under compression. Each transverse layer is shifted with respect to the previous one.

beam with circular cross-section—is usually the quantity used to determine whether this assumption holds. When this assumption does not hold, hence when the spacing is comparable to the diameter of the filament, it is necessary to use the Timoshenko beam theory to take into account the deformations due to shear. In the following, an example explaining how to calculate whether shear is negligible will be shown. Before developing a model for this scenario that involves variable diameter, a possible future work, a model that includes contributions of shear is developed here, for a lattice with filaments of constant diameter. The Timoshenko model describes the system using two quantities: the transverse deflection $w(x)$ as in the Euler–Bernoulli theory, and the rotation of the cross-section, $\psi(x)$. In the following, we adapt the Timoshenko model for the problem of an infinite, periodic beam. This is an improvement on the available models, as well as a step forward in the direction of functionally graded lattices. Another assumption is that the supporting filaments do not deform: the circular cross-sections in figure 4.21 will remain circular after deformation, instead of accounting for the deformation of the cross section due to compressive stresses.

The problem for half of the filament between two supports becomes that of a Timoshenko beam—clamped at one end and loaded at the other by a point force. This is true when the staggering is *symmetric*, because rotation at the supports is zero due to symmetry. When that is not the case, supports can no longer be taken as rotation-free points and

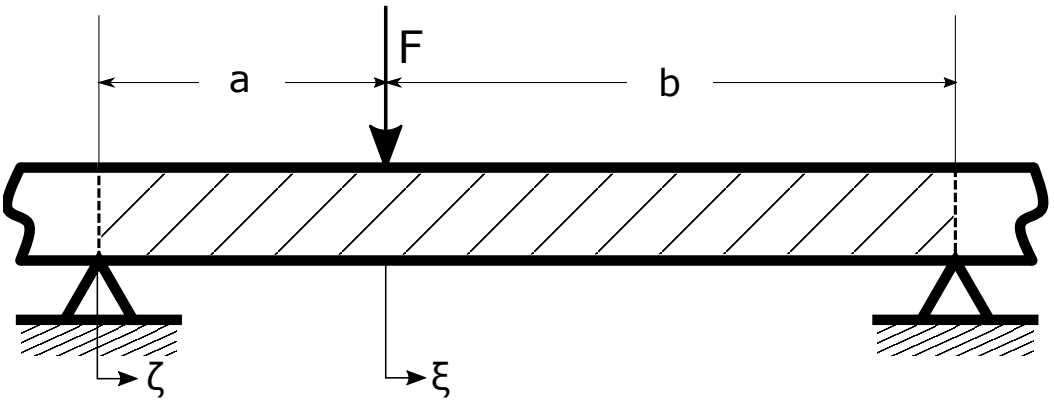


Figure 4.22: We consider a Timoshenko beam with periodic boundary conditions to mimic an infinite lattice. A force $F$ is applied at a distance $a$ from the left support and at a distance $b$ from the right support. The shaded area is the portion of the beam that is modelled.

we need to solve the problem in two parts with four matching conditions at the point of loading.

We start from the the displacement field $u_x(x,y,z) = -z\psi(x)$, $u_y = 0$, $u_z(x) = w(x)$, where $w(x)$ is the transverse displacement of the beam, $\psi(x) = w'(x) - \Phi(x)$ is the rotation of the cross-section due to bending only, $\Phi(x)$ is the shear angle of the cross-section, and $x$ is in the direction of the axis of the beam. Derivation is indicated as follows: $w'(x) = \frac{\mathrm{d}w(x)}{\mathrm{d}x}$. Using the expressions $\sigma_{xx} = E\epsilon_{xx}$, $\sigma_{xz} = 2G\epsilon_{xz}$, $\epsilon_{xx} = -z\psi'(x)$ and $\epsilon_{xz} = \frac{1}{2}[w'(x) - \psi(x)]$, it is possible to evaluate the total potential energy as sum of the potential energy of the beam $U = \frac{1}{2}\int_L \epsilon_{ij}\sigma_{ij}dV$ and the potential energy due to external loading $V = -W = -Fw(L)$, if a force were applied at a distance, say $L$ from the reference end. Applying the PMTPE, $\delta\Pi = 0$, yields the field equations

$$w''(x) - \psi'(x) = 0 \tag{4.43}$$

$$\psi''(x) + \alpha\left[w'(x) - \psi(x)\right] = 0, \tag{4.44}$$

where $\alpha = \frac{\kappa GA}{EI}$. These equations, when paired to the correct boundary conditions, can be used to solve one side of the system in Figure 4.22, that is, from a support to the point load. Using one set of equations for each side of the beam and taking care of the continuity of the solution in the point where the load is applied, a solution can be found. In this context, $x$ is again in the direction of the axis of the beam, with $x = 0$ at the left support, $x = a + b$ at the right support.

The interaction between the filament under bending and the transverse filament on top (Figure 4.21) is modelled as a point force, as in sketch 4.22. We then write two separate

systems, one for each portion of the filament—the point force marking the separation—and use continuity conditions to find the solution for the whole filament (the beam of the Timoshenko model).

The left portion of the filament—from the leftmost support to the point-force—has length $a$ and $\zeta$ is its local coordinate ($\zeta = 0$ at the left support, $\zeta = a$ at the point where the force is applied). The quantities referring to this portion of the filament are characterised by the subscript 1. The right side of the filament runs from the point where the force is applied, $\xi = 0$, to the rightmost support, $\xi = b$, and it has length $b$. The subscript 2 relates to quantities related to this portion of the filament. The field variables are:

$$\begin{aligned} &\psi_1(\zeta), w_1(\zeta) \qquad 0 \le \zeta \le a \\ &\psi_2(\xi), w_2(\xi) \qquad 0 \le \xi \le b, \end{aligned} \tag{4.45}$$

that satisfy the following two sets of field equations

$$\begin{aligned} &w_1''(\zeta) - \psi_1'(\zeta) = 0, \qquad \psi_1''(\zeta) + \alpha\left[w_1'(\zeta) - \psi_1(\zeta)\right] = 0 \\ &w_2''(\xi) - \psi_2'(\xi) = 0, \qquad \psi_2''(\xi) + \alpha\left[w_2'(\xi) - \psi_2(\xi)\right] = 0. \end{aligned} \tag{4.46}$$

The solutions are expressed in terms of 8 unknown constants $c_1, \ldots, c_8$ as follows:

$$\begin{aligned} w_1(\zeta) &= c_4 + (c_1 + c_3)\zeta + \frac{c_2}{2}\zeta^2 - \frac{\alpha c_1}{6}\zeta^3 \\ \psi_1(\zeta) &= c_3 + c_2\zeta - \frac{\alpha c_1}{2}\zeta^2 \end{aligned} \qquad \text{for } 0 \le \zeta \le a \tag{4.47}$$

$$\begin{aligned} w_2(\xi) &= c_8 + (c_5 + c_7)\xi + \frac{c_6}{2}\xi^2 - \frac{\alpha c_5}{6}\xi^3 \\ \psi_2(\xi) &= c_7 + c_6\xi - \frac{\alpha c_5}{2}\xi^2 \end{aligned} \qquad \text{for } 0 \le \xi \le b. \tag{4.48}$$

The correct boundary conditions must be applied to find the 8 unknowns. The 8 boundary conditions are:

$$w_1(\zeta = 0) = 0 \tag{4.49}$$

$$w_2(\xi = b) = 0 \tag{4.50}$$

$$\psi_1(\zeta = 0) = \psi_2(\xi = b) \tag{4.51}$$

$$\psi_{1,\zeta}(\zeta = 0) = \psi_{2,\xi}(\xi = b) \tag{4.52}$$

$$w_1(\zeta = a) = w_2(\xi = 0) \tag{4.53}$$

$$\psi_1(\zeta = a) = \psi_2(\xi = 0) \tag{4.54}$$

$$\psi_{1,\zeta}(\zeta = a) = \psi_{2,\xi}(\xi = 0) \tag{4.55}$$

$$EI\alpha\left[w_{1,\zeta}(\zeta = a) - \psi_1(\zeta = a)\right] = EI\alpha\left[w_{2,\xi}(\xi = 0) - \psi_2(\xi = 0)\right] + F. \tag{4.56}$$

The first two, 4.49 and 4.50, are the kinematic boundary conditions, while the next two are due to the periodicity: 4.51 imposes the continuity of rotation due to bending and 4.52 imposes the continuity of moment. The next four boundary conditions are due to

the continuity at the interface, the point where the force is applied: 4.53 is the continuity of vertical displacement, 4.54 is the continuity of rotation due to bending, 4.55 represents the continuity of moment and 4.56 represents the continuity of shear.

The application of these boundary conditions leads to the linear system of algebraic equations

$$\begin{bmatrix} 0 & 0 & 0 & 1 & 0 & 0 & 0 & 0 \\ 0 & 0 & 0 & 0 & b-\frac{b^3\alpha}{6} & \frac{b^2}{2} & b & 1 \\ 0 & 0 & 1 & 0 & \frac{b^2\alpha}{2} & -b & -1 & 0 \\ 0 & 1 & 0 & 0 & b\alpha & -1 & 0 & 0 \\ a-\frac{a^3\alpha}{6} & \frac{a^2}{2} & a & 1 & 0 & 0 & 0 & -1 \\ -\frac{a^2\alpha}{2} & a & 1 & 0 & 0 & 0 & -1 & 0 \\ -a\alpha & 1 & 0 & 0 & 0 & -1 & 0 & 0 \\ EI\alpha & 0 & 0 & 0 & -EI\alpha & 0 & 0 & 0 \end{bmatrix} \begin{Bmatrix} c_1 \\ c_2 \\ c_3 \\ c_4 \\ c_5 \\ c_6 \\ c_7 \\ c_8 \end{Bmatrix} = \begin{Bmatrix} 0 \\ 0 \\ 0 \\ 0 \\ 0 \\ 0 \\ 0 \\ F \end{Bmatrix}, \tag{4.57}$$

which gives $c_1 = \frac{bF}{\alpha(a+b)EI}$, $c_2 = \frac{abF}{2(a+b)EI}$, $c_3 = \frac{b(-a^2+ab)F}{12(a+b)EI}$, $c_4 = 0$, $c_5 = -\frac{aF}{\alpha(a+b)EI}$, $c_6 = -\frac{abF}{2(a+b)EI}$, $c_7 = \frac{b(-a^2+ab)F}{12(a+b)EI}$, $c_8 = \frac{b(12a+a^2b\alpha)F}{12\alpha(a+b)EI}$. Substituting these values into equations 4.47 and making use of the single variable $0 \leq x \leq a+b$ for both portions of the filament, we obtain the solution

$$\begin{aligned} w_1(x) &= \frac{bFx[12-a^2\alpha-2x^2\alpha+a(b+3x)\alpha]}{12(a+b)EI\alpha} \\ \psi_1(x) &= \frac{bF[-a^2-6x^2+a(b+6x)]}{12(a+b)EI} \end{aligned} \qquad \text{for } 0 \leq x < a \tag{4.58}$$

$$\begin{aligned} w_2(x) &= \frac{aF(b-x)(12+ab\alpha+b\alpha x-2x^2\alpha)}{12(a+b)EI\alpha} \\ \psi_2(x) &= \frac{aF(-ab+b^2-6bx+6x^2)}{12(a+b)EI} \end{aligned} \qquad \text{for } a \leq x \leq a+b. \tag{4.59}$$

It is now possible to plot the deflection profile resulting from the solutions of the two pairs of equations, the solution being 4.58 and 4.59, after inserting values of the geometric and materials parameters of the structure. We obtain the profile of the filament, together with the rotation of the cross-section with respect to the vertical line. Figures 4.23 and 4.24 show the profile of the filament in blue, the rotation of the cross-section in solid orange, and the rotation due to shear only in dashed orange. Figure 4.23 shows a case in which the rotation of the cross-sections obtained with a Timoshenko model is comparable to that obtained with the Euler–Bernoulli beam theory, as shear is negligible. On the other hand, figure 4.24 shows a case where the rotation of the cross-sections predicted by Timoshenko has a large contribution of rotation due to shear. Additionally, using Timoshenko theory, the transverse displacement can have a discontinuity in its first derivative at the point where the force is applied. The blue dots represent the position

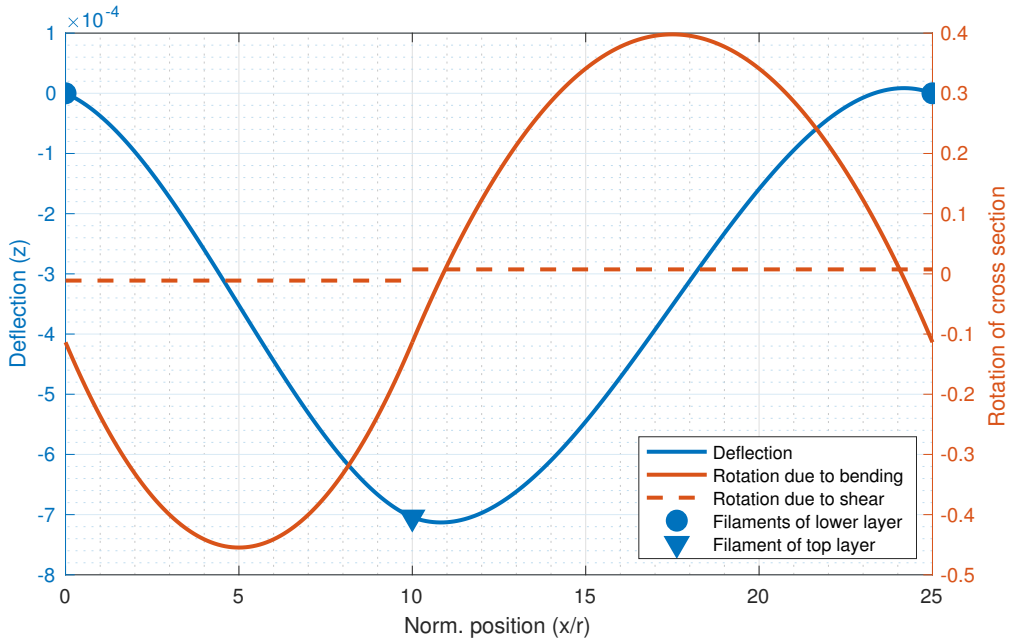


Figure 4.23: Case of a beam under bending where shear is negligible. The profile of the beam is in solid blue, the rotation of the cross-sections due to bending is in solid orange and the rotation due to shear only is in dashed orange. We can see how the bending due to shear is negligible compared to the rotation of the cross section.

of filaments that are below the plotted filament and act as supports. The blue triangle represents the position of a filament in the top layer that acts as point force.

An interesting and useful relation is the ratio of potential energy due to shear to the total potential energy. This would show how the diameter of the filament and the span of the overhangs in the structure affect the contributions of shear. This can give an idea of what parameters play a role in the potential energy due to shear, allowing to infer whether a model with shear correction is necessary or not. We introduce the expressions for the potential energy due to shear, $U_{\mathrm{SH}}$, and the potential energy of a beam under pure bending, $U_{\mathrm{PB}}$, using the quantities $w(x)$ and $\psi(x)$:

$$U_{\mathrm{SH}} = \frac{1}{2}\int_0^{a+b} \kappa G A \left[w'(x) - \psi(x)\right]^2 \mathrm{d}x, \tag{4.60}$$

$$U_{\mathrm{PB}} = \frac{1}{2}\int_0^{a+b} EI \left[\psi'(x)\right]^2 \mathrm{d}x. \tag{4.61}$$

Using the solutions 4.58, these two expressions become:

$$U_{\mathrm{SH}} = \frac{abF^2}{2\kappa G A(a+b)}, \tag{4.62}$$

$$U_{\mathrm{PB}} = \frac{a^2b^2F^2}{24EI(a+b)}. \tag{4.63}$$

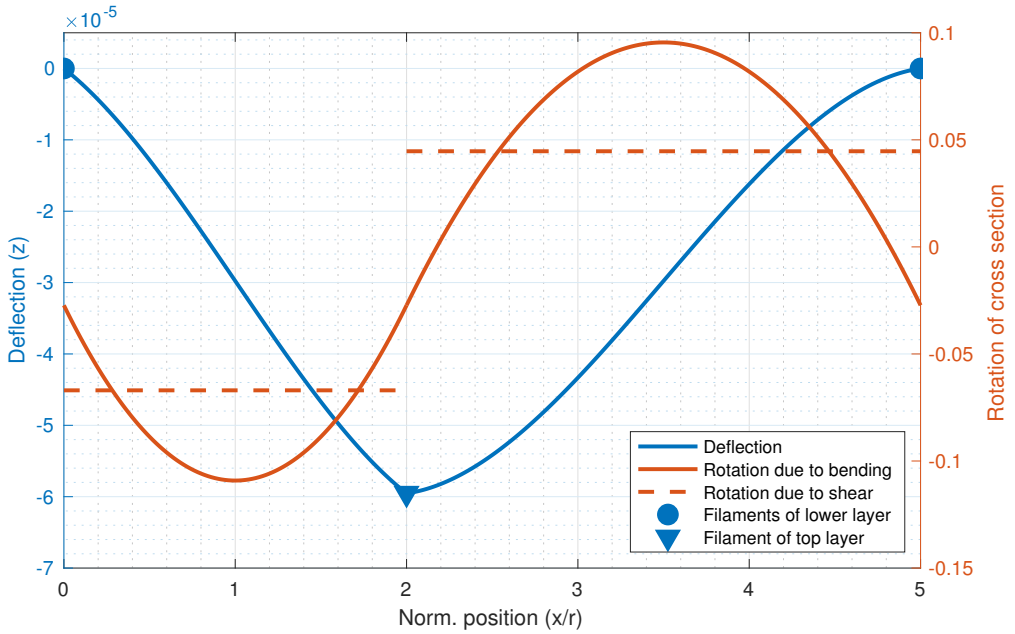


Figure 4.24: Case of a beam under bending where the shear is *not* negligible. The profile of the beam is in solid blue, the rotation of the cross-sections due to bending is in solid orange and the rotation due to shear only is in dashed orange. In this case, the rotation due to shear is an important component of the rotation of the cross section.

To compare these two quantities, we consider the ratio

$$U_{\mathrm{SH,rel}} = \frac{U_{\mathrm{SH}}}{U_{\mathrm{PB}}} = \frac{12EI}{\kappa GAab}. \tag{4.64}$$

This ratio can be rewritten as

$$U_{\mathrm{SH,rel}} = \frac{4I(7+6\nu)}{Aab}, \tag{4.65}$$

using the following expressions

$$G = \frac{E}{2(1+\nu)}, \tag{4.66}$$

$$\kappa = \frac{6(1+\nu)}{7+6\nu}, \tag{4.67}$$

where $\kappa$ is the shear modulus of a circular beam [Cowper, 1966] and $\nu$ the Poisson's ratio.

Substituting the expressions for the second moment of area $I = \frac{\pi}{4}r^4$ and for the area $A = \pi r^2$, we obtain the final expression for the ratio of energy due to shear to energy due to pure bending, in terms of the radius of the filament $r$ and the quantities related

to the span $a$ and $b$ (and the Poisson's ratio of the material):

$$U_{\mathrm{SH,rel}} = (7 + 6\nu)\frac{r^2}{ab}. \tag{4.68}$$

Assuming a Poisson's ratio $\nu = 0.36$ (that of PLA material [Jamshidian et al., 2010]) this ratio takes the final form

$$U_{\mathrm{SH,rel}} = 9.16\frac{r^2}{ab}. \tag{4.69}$$

Interestingly, this quantity *does not* depend on the ratio $\frac{r}{l} = \frac{r}{a+b}$, as one might expect, but on the quantity $\frac{r^2}{ab}$. This can be explained physically as follows. In the case of a beam of length $l = a + b$, with a transverse force applied at a distance $a$ from the left support—see figure 4.22, the contribution due to shear becomes relevant when $a$ is sufficiently small *or* when $b$ is sufficiently small, no matter the length of the beam. This is because in such cases, the force would be applied close to one of the supports. We remind that this problem is equivalent to two cantilever beams joined at the point where the force is applied, hence this would result in a short cantilever beam on one side, where the shear would not be negligible. To provide a numeric example of this, we consider a case where the span is $l = a + b = 10\,\mathrm{mm}$. We aim to find the range of values of $a$ that give $U_{\mathrm{SH,rel}} < 0.1$, given the value of $r$. With this example, the idea is to simulate a situation where we consider the shear to be negligible if $U_{\mathrm{SH}} < 10\%U_{\mathrm{PB}}$. Mathematically, this translates to solving the following inequality (remember equation 4.69 and that in this example $l = a + b = 10\,\mathrm{mm}$):

$$U_{\mathrm{SH,rel}} = 9.16\frac{r^2}{a(10 - a)} < 0.1. \tag{4.70}$$

Rearranging the terms, we obtain

$$a^2 - 10a + 91.6r^2 < 0. \tag{4.71}$$

We can now fix values of $r$ and solve this inequality. To start, we consider $r = 0.2\,\mathrm{mm}$. In this case we obtain the solution $0.38\,\mathrm{mm} < a < 9.62\,\mathrm{mm}$ (a symmetric interval with respect to the midpoint of the beam). With $r = 0.5\,\mathrm{mm}$ we obtain $3.55\,\mathrm{mm} < a < 6.45\,\mathrm{mm}$. This means that the distance at which the force can be applied for the shear to be negligible increases with the radius (i.e. the symmetric interval centred at the middle of the beam shrinks). This is intuitively correct, as the ratio $r/a$ decreases when $a$ increases. This can be observed in figure 4.25, where we plot $U_{\mathrm{SH,rel}}$ (left side of inequality 4.70) as a function of $r$ and $a$, together with the plane representing $U_{\mathrm{SH,rel}} = 0.1$. The intervals just found for $a$ where $U_{\mathrm{SH,rel}} < 0.1$ are also shown on this plot (green and blue lines, the points represent the extremes of the intervals). Two observations can be made: if we set $r = 0.6\,\mathrm{mm}$ there is no real solution, meaning that no matter the choice of $a$, the energy due to shear is not negligible; if we set $a = l/2 = 5\,\mathrm{mm}$, which is the limit case of the shrinking of the symmetric interval, we can find the values for the radius that

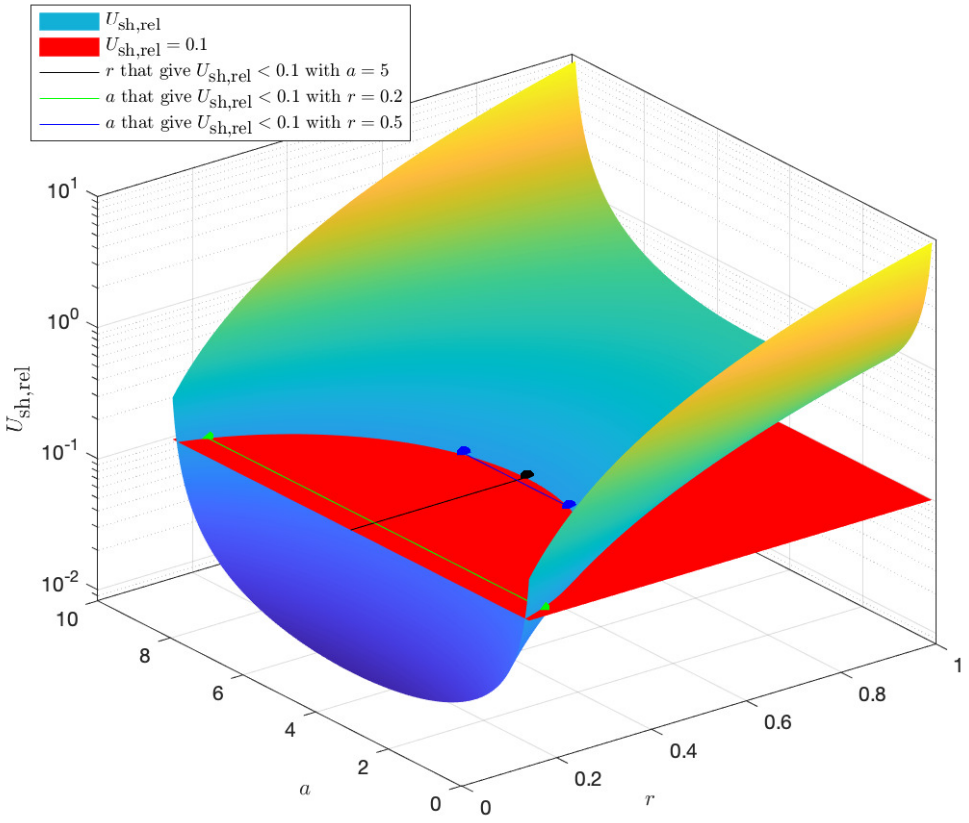


Figure 4.25: Plot of $U_{\text{SH,rel}}$, the ratio of energy due to shear to the energy due to pure bending (left side of inequality 4.70) as the yellow-blue surface. The red surface represents the case $U_{\text{SH,rel}} = 0.1$. The part of the blue surface below the red plane represents the case where $U_{\text{SH,rel}} < 0.1$ (i.e. the energy due to shear is less than 10% of the energy due to pure bending). The green line in the plot represents the range of values of $a$ for which $U_{\text{SH,rel}} < 0.1$, when $r = 0.2\,\text{mm}$. The blue line represents the range of values of $a$ for which $U_{\text{SH,rel}} < 0.1$, when $r = 0.5\,\text{mm}$. The black line represents the range of $r$ that gives $U_{\text{SH,rel}} < 0.1$ when $a = 5\,\text{mm}$ (force is applied at the centre of the beam). The dots represent the extremes of the interval of the same color (where $U_{\text{SH,rel}} = 0.1$).

give $U_{\text{SH,rel}} < 0.1$, the black line on figure 4.25. Additionally, we note that $r = 0.52\,\text{mm}$ (the black dot on the figure) is the minimum value for $r$ that still gives $U_{\text{SH,rel}} < 0.1$ for a central load ($a = 5\,\text{mm}$). This means that for any greater radius, the energy due to shear is never less than 10% of the energy due to pure bending, hence it is not negligible by our definition.

## 4.5 Conclusions

The capability of variable extrusion demonstrated in the previous chapter was taken forward to fabricate bi-layer lattice structures with variations in the stiffness of the struts using prescribed spatial functions. Samples of such functionally graded lattice structures

were tested in the laboratory and the asymmetric deflection profile was recorded. This profile was seen to be in excellent agreement with theoretically predicted ones, based on linear buckled shapes of lattice structures with spatially varying stiffness.

We have seen that the variation in the diameter is achieved by a concatenation of short extrusions where the diameter is changed between extrusions but kept constant for each extrusion. The flow-like properties of the molten polymer then ensure that these variations are smooth between extrusions with different diameter. This does not correspond to a perfectly linear variation in the diameter, however, we use the linear variation in the diameter as a model. We then verified that the mechanical response of the manufactured part be in agreement with the model. This leads to the conclusion that the manufactured part is mechanically continuous and the variation in the diameter can be considered continuous for modelling purposes.

In addition to the analysis for bending response under buckling, in order to provide support to experimental observations, this chapter also provides a number of mathematical models for the description of functionally graded lattices and films. A model for the compression of lattices that includes the deformations due to shear is analysed by the method of matched solutions for a general staggered lattice with significant shear effects that are likely to become important for dense lattices.

In the next chapter, the manufacturing technique will be further expanded for the production of films that exhibit variable stiffness in two directions. This poses a number of challenges which will be addressed and discussed. Additionally, bending profiles post-buckling will be performed and compared with results obtained from finite element analysis.

# Chapter 5

# Fabrication & characterisation of bi-directionally graded lattice films

Structures with spatially varying material properties are of great practical interest. Such structures with varying stiffness or strength were conceived primarily to optimise material usage, because different parts of a structure are differently stressed, which requires spatial variation in their apparent elastic modulus or failure stress for their optimal performance. Such variation in properties is ideally desirable in all three directions. Having demonstrated previously in Chapter 4, that FDM filaments with variable cross-sectional diameter can be achieved by under- or over-extrusion, here we explore the possibility of generalising this to two dimensions for a film-like structure. Manufacture as well as characterisation of such 2D-spatially-graded lattice films will be presented in this chapter. Chapter 4 dealt with spatial variation of stiffness in one direction, while the diameter of filaments in the other orthogonal direction was kept fixed. Here, we modify the manufacturing technique to be able to add a second layer of variable-diameter filaments to explore the feasibility of the two layers bonded together during the FDM process, thus providing bidirectionally graded films. An adjustment required for this is to account for non-flatness of the first layer due to spatially varying diameter, before the second layer could be placed.

Bi-directionally graded films fabricated in this work were characterised experimentally for their mechanical response. This is essential to ensure the technique developed can produce films whose property variation is as intended, before new possibilities of fabrication and application could be explored. A high number of subsequent functionally graded layers is not ideal, due to the uneven layer height that they introduce as a consequence of the variable diameter of the extruded filaments. However, a few well-placed functionally graded layers within a larger object could be used to provide the additional freedom to control both the local mechanical behaviour of the structure as well as its overall behaviour and response. Using these functionally graded layers as infill, would also avoid a

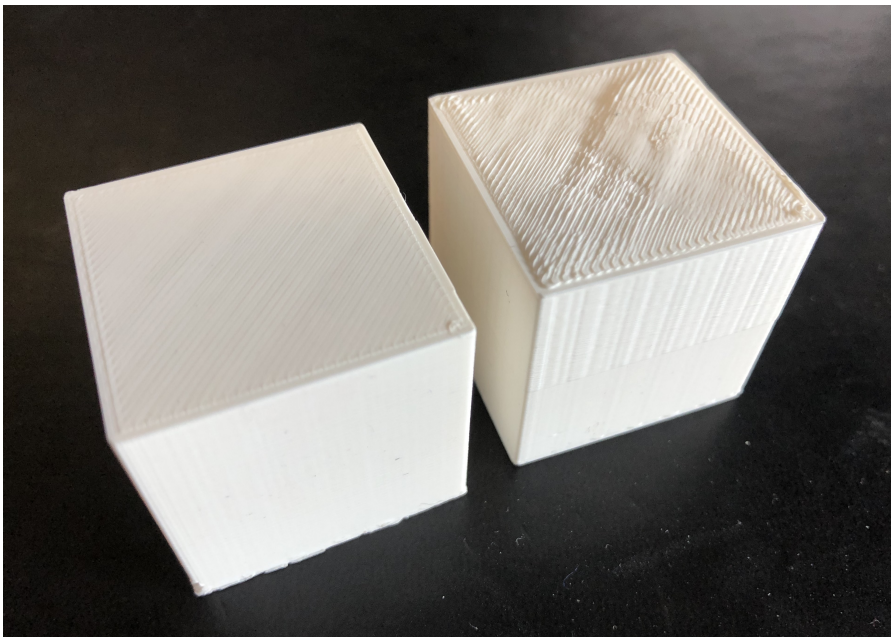

Figure 5.1: On the left, a standard cube made with Solidworks, sliced using Cura and 3D printed with using a nozzle of size 0.4 mm. On the right, a cube obtained with a manipulated version of the G-code. It has been manipulated so that the top half of the cube is printed with a thicker filament, 0.6 mm.

drop in the surface finish quality. Figure 5.1 shows the result of manipulating the G-code of an object to introduce functional gradation throughout—as opposed to only its infill or only in a few layers—as explained in section 3.5. The quality of the surface finish of the cube on the right drastically dropped. This is the second main reason why these functionally graded films are best used as infill. Alternatively, porous structures with no external surface that might be affected could also be manufactured.

Theoretical characterisation of the stiffness of the fabricated films has been carried out using finite element analysis. The purpose of this is to assess the predictive capability, so that other similar structures could be designed without the need to test each structure during a design search exercise. The possibility to manufacture films whose functional gradation is effective and produces tangible changes in the behaviour of the film has been shown with the experimental results. If consistency of the results between the finite element analysis and the experimental results are observed, and the response is robustly predictable, then it would further allow material microstructure design and fabrication to suit bespoke needs.

## 5.1 Fabrication of bi-directionally graded films

### 5.1.1 Methodology

Here we describe a method to manufacture lattice films with properties varying spatially in two directions. Subsequently, the bending response of such a functionally graded structure will be characterised experimentally. In the previous chapter, rectangular strips with two layers were fabricated, in which the bottom layer had filaments with fixed diameter. The next layer above this had variable diameter along its length. Now the bottom later too has variable diameter. This leaves the top surface over which the second layer needs depositing slightly inclined to the horizontal. This slope of the lower layer needs to be accounted for while printing the top layer. We remind again that we are interested in the mechanical response of the structure, hence we will use the term *continuous variation* to indicate that the structure is mechanically continuous (i.e. the mechanical response can be modelled by modelling its filaments as filaments with a linearly-variable diameter).

The films fabricated were manufactured using a Prusa i3 MK3 3D printer [Prusa Research, 2020]. The feeder material used is white, standard poly-lactic acid (PLA). The dimensions of the square films are 100 mm by 100 mm, consisting of two orthogonal layers. All extruded filaments were manufactured using the discretisation approach to obtain continuously variable diameter as explained in Section 3.1.1, and programmed within the range 0.7 mm to 0.4 mm. Two samples with the same intended structure were fabricated and tested as described in the next section.

These films, however, cannot be printed directly on the print-bed of the 3D printer. The use of a base layer to be subsequently removed becomes necessary to obtain the desired filament diameters. This layer is slightly larger than the film fabricated for subsequent mechanical testing as can be seen in Figure 5.2. The detailed reason for this procedure is described in Section 5.1.4. Four layers need to be manufactured: the first two layers serve as a sacrificial base, while the two subsequent layers are separated from the base and used in subsequent studies. The two layers used to form the base are of square shape, with each side of 120 mm length, made of filaments with a constant diameter that corresponds to the nominal diameter of the nozzle, 0.4 mm. These filaments have spacing of 1.25 mm, the same as that for the film on top.

The third and the fourth layers have filaments running along the $x$-axis and $y$-axis of the printer respectively, and are printed using a variable diameter that goes from 0.7 mm to 0.4 mm. To vary the diameter, the technique described in section 3.1.1 is used. Thus, each of the 100 mm-long filaments is divided into 20 segments—which we refer to with indices $i = 1, ..., 20$—each printed with a constant value of the diameter $d(i)$. The left-most of these 20 segments, segment $i = 1$, is printed with a diameter of $d(1) = 0.7$ mm. The right most segment corresponding to $i = 20$, has a diameter $d(20) = 0.4$ mm. The diameters

| | Extrusion temp. (°C) | Layer height (mm) | Feed rate (mm/min) | Fan Speed (% of max) |
|---|---|---|---|---|
| Layer 1: first layer of base | 210 | 0.20 | 1000 | 60 |
| Layer 2: last layer of base | 210 | 0.32 | 2000 | 100 |
| Layer 3: first layer of film | 200 | 0.54 | 2000 | 100 |
| Layer 4: last layer of film | 210 | 0.32 | 2000 | 60 |

Table 5.1: Manufacturing parameters used to manufacture the film (third and fourth layers) and the sacrificial base (layers one and two). The difference in the parameters in each layer is dictated by the need to ensure proper adhesion between layer 1 and 2, reduced adhesion between layer 2 and 3, and proper adhesion between layer 3 and 4. This facilitates the detaching of the base from the film after manufacturing and avoids damaging the film.

of the segments are calculated with a simple linear interpolation: $d(i) = 0.7 - \frac{0.3}{19}(i-1)$ for $i = 1, ..., 20$. The flowing nature of the melted polymer during its deposition and solidification results in a variation in the diameter that is considered continuous and linear. Again, this assumption refers to the mechanical behaviour of such structure. If the mechanical response of the film matches that of a film with continuous gradation, then we can say that the film we manufactured is effectively continuous in this sense. This is an hypothesis that will be confirmed by the matching of the results to the FEA results. The second layer of the film has the same geometric characteristics as the layer just described, only rotated 90 degrees anti-clockwise. This means that for this layer, the filaments run along the $y$-axis of the printer (see Figure 5.2) and have a diameter of 0.7 mm at the front end and 0.4 mm at the back end, with the same variation described before, $d(i) = 0.7 - \frac{0.3}{19}(i-1)$ for $i = 1, ..., 20$.

We now list the most important parameters used to print each layer, remembering that the first two layers belong to the sacrificial base, while the third and fourth layers belong to the film to be tested. Due to the presence of a sacrificial base which needed to be removed before testing, the adhesion between the base and the film needed to be reduced to facilitate their separation without damaging the film. We have achieved this by quickly cooling the last layer of the base followed by a pause where the heated print bed would turn off and cool down (2 minutes). The first layer of the film was then printed with an increased layer thickness $z_{\text{inc}}$ and reduced temperature, again to reduce adhesion, and lastly, the last layer of the film was printed with an increased extrusion temperature and decreased speed for the cooling fan to ensure proper adhesion between the two layers of the film. The values for the parameters used for each layer can be seen in table 5.1. Note the low layer height and low extrusion speed for the first layer to ensure the first layer adheres to the buildplate.

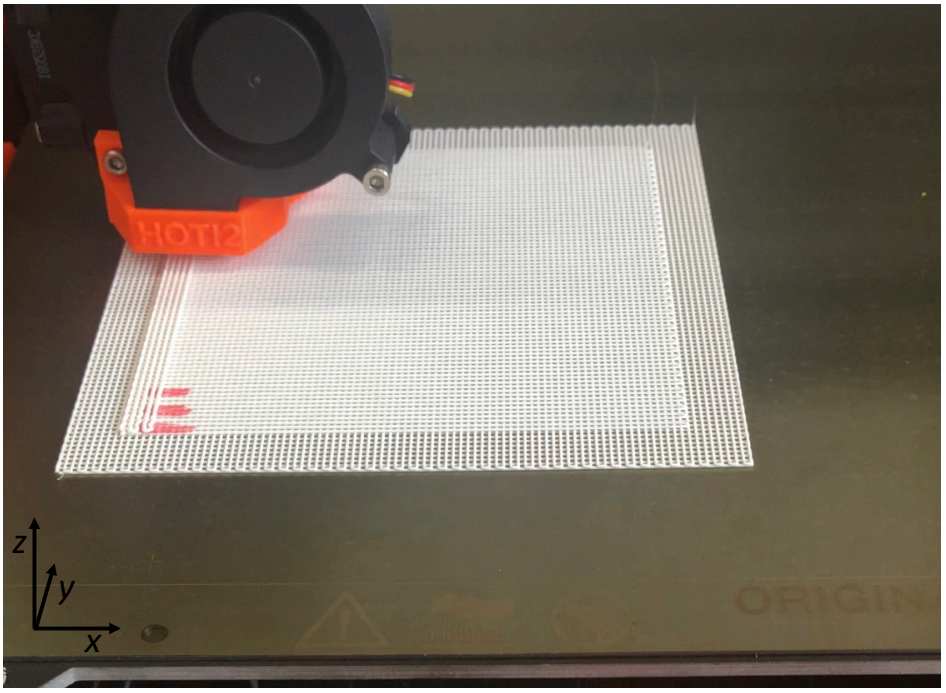


Figure 5.2: The 2-layer film of interest lies on two larger base layers. This allows the film to be made of two layers with comparable diameters, as the layer printed directly on the print-bed is thinner than the rest of the layers.

### 5.1.2 Characterisation of the overlap between filaments of different layers

Practical 3D-printing of lattices with separated cylindrical filaments shows a finite patch over which two cylindrical surfaces contact each other, rather than the mathematically exact point contact between two rigid cylinders. The reason is that while 3D-printing, the extruded polymeric material is still in a state of molten material, which adheres to the layer below by spreading during solidification. This results in an overlap between the two mathematically precise woodpile layers, to be accounted for by an overlap factor. This is necessary because it affects the mechanical behaviour of the structure. If the contact between transverse cylinders is modelled as a point, the cylinders are free to rotate around that point, which adds a degree of freedom that is not present in the manufactured part. This would consequently underestimate the rigidity of the structure and overestimate the deflection. For this reason it is necessary to characterise the overlap that is observed in the manufactured parts, so that the observed amount of overlap could be implemented in the model, in an attempt to maximise fidelity.

When a filament is deposited over a previous layer during the printing process, it fuses with the layer below by an amount that depends on many factors: mainly the extrusion temperature, speed, layer height and nozzle diameter. Two SEM images, figures 5.3(a) and 5.3(b), have been used to calculate a sensible value to use for this parameter. As a measure of this fusion, which we will refer to as *overlap*, we use the ratio between the

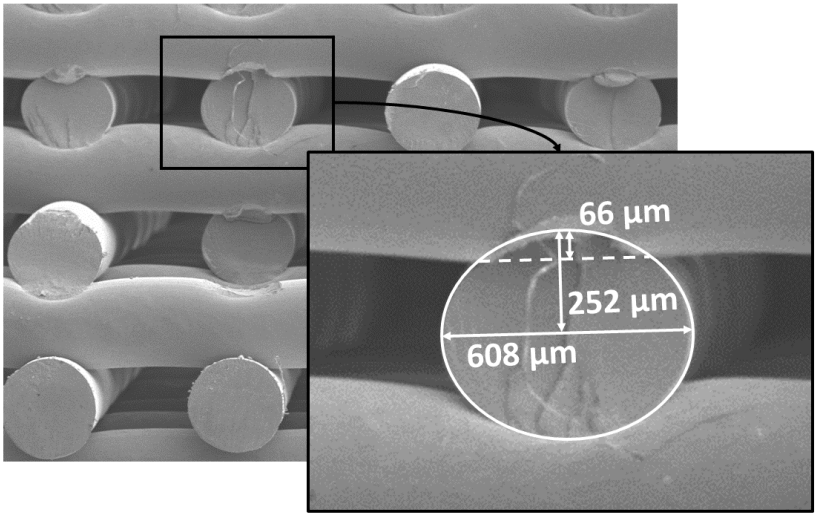


(a)

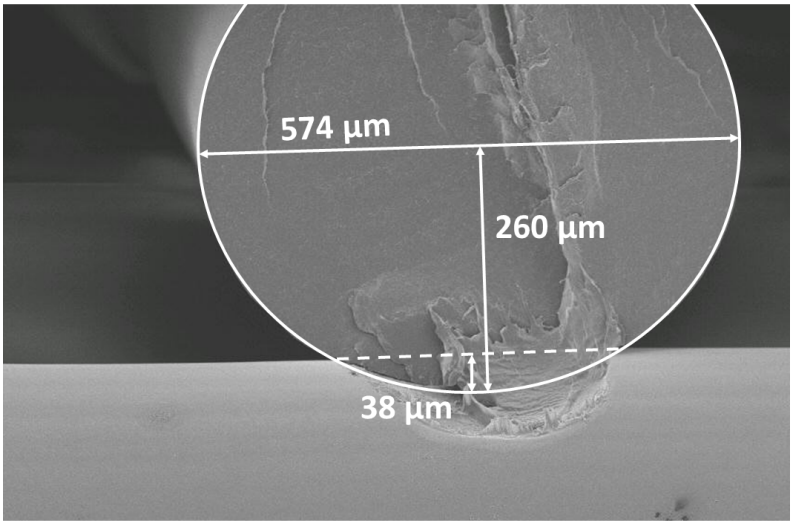


(b)

Figure 5.3: SEM images of the front view of a lattice, in the case of a large overlap between filaments of subsequent layers, (a), and in the case of small overlap, (b). Case (a) is achieved by setting the value for the layer height about 20% smaller than the value for the filament diameter, while case (b) is achieved by setting the value for the layer height close to the value for the filament diameter.

amount of the filament that is embedded in the other layer and the axis of the ellipse in the stacking direction. As an example, for figure 5.3(a), the amount of embedded filament is 66 µm, and the axis of the ellipse in the stacking direction is 504 µm: this results in an overlap of 13.1%. For figure 5.3(b), the overlap is 7.3%. The main difference here is in the layer height chosen. The layer height used to manufacture the films we test in this chapter is close to the layer height used to obtain the sample in Figure 5.3(b), hence an overlap value of 8% was chosen as an estimate for the manufactured films. In the following, the diameter of the filaments in the second layer ($d_2$) will be taken as reference, hence the overlap will be taken as $o = 0.08d_2$.

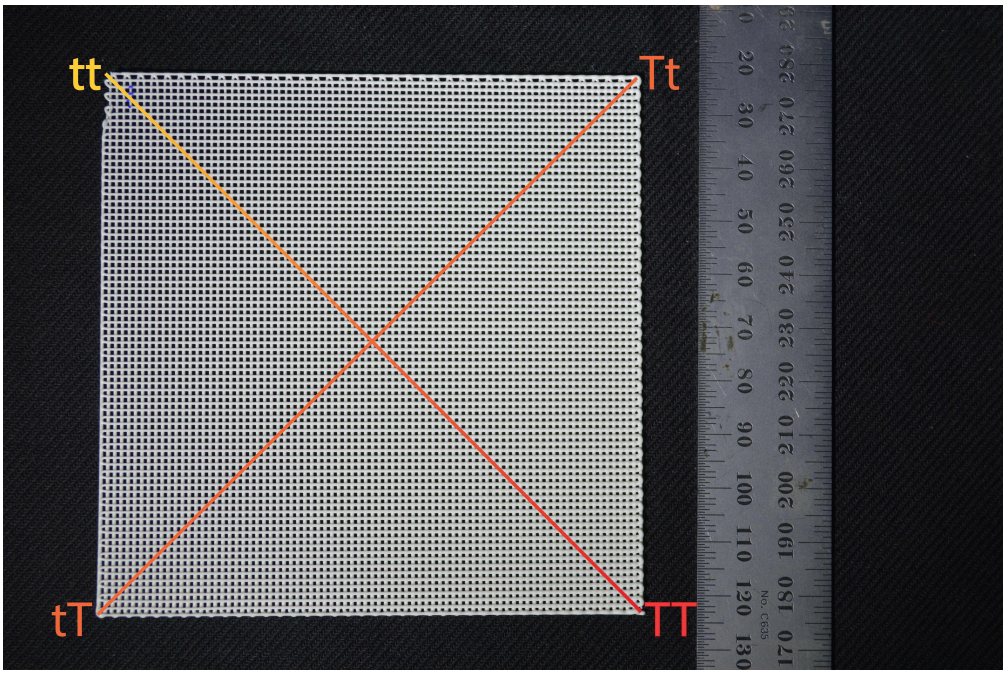


Figure 5.4: The four corners are referred to with a pair of letters depending on the thickness of the two layers of the film at that corner. 'T' is used for thick filaments and 't' for thin filaments, hence we have: tt-corner, TT-corner, tT-corner and Tt-corner. The two diagonals are referred to based on the corners that they connect, hence we have a tt-TT diagonal and a tT-Tt diagonal.

### 5.1.3 The geometry of spatial variation in two dimensions

The fabricated films are made up of two orthogonally stacked layers, each layer providing stiffness variation in one direction. We will refer to the four corners of the films by a pair of letters, referring to the thickness of the filaments at that corner in each of these layers. The letters can either be 't', referring to *thin* filaments with a diameter of 0.4 mm, or 'T', referring to *thick* filaments with a diameter of 0.7 mm. This means that each square sample has a TT-corner, where both layers have thick filaments; a tt-corner, where the layers are both thin, and two corners where one layer is thin and the other is thick, referring them as tT- and Tt-corners. These two corners have equivalence in the sense of having intermediate stiffness, whereas the TT-corner is the stiffest end while the tt-corner is the softest in bending. The two diagonals of the film can then be referred to based on the corners that they connect. The tt-TT diagonal, shown as the yellow-to-red diagonal in figure 5.4, connecting the corner with both thin layers (tt) to the corner with both thick layers (TT); there is also the tT-Tt diagonal, in solid orange, that connects the two corners with one thin and one thick layer bonded together. Figure 5.5 has the top view of the four corners of the film. This image shows the first printed layer in grey and the second layer in blue. Detail A shows the tt-corner, detail B the tT-corner, detail C the Tt-corner and detail D the TT-corner. The diameters reported are the diameters of the filaments at that end of the film, in each direction.

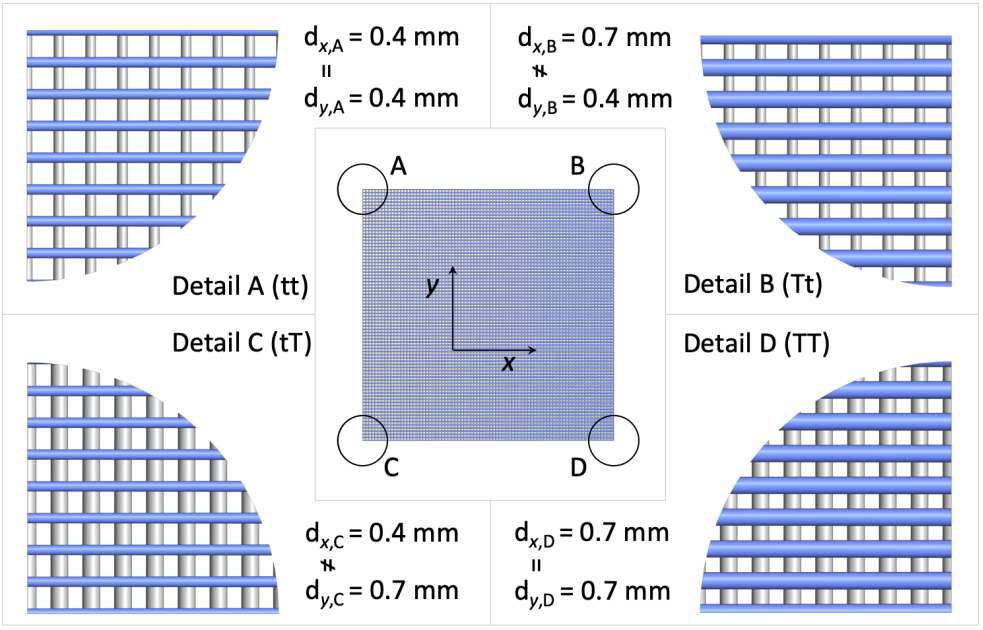


Figure 5.5: Top view of the four corners of the film, at a scale of 10:1 with respect to the film represented in the centre of the image. One layer, along $y$, is shown in grey, while the second layer, along $x$, in blue. Detail A shows the top view of the corner where both layers are made of thin filaments, 0.4 mm in diameter, referred to as tt. Detail B and C show the corners at which one of the layers is 0.4 mm and the other is 0.7 mm, referred to as tT and Tt. Detail D shows the top view of the corner where both layers are made of thick filaments, 0.7 mm in diameter, referred to as TT.

Porosity $\rho$, and its two-dimensional variation over the $x$-$y$ plane, can be calculated from the geometry. The unit cells within a cuboid volume of the structure under consideration are shown in the top row of Figure 5.6. The word unit cell should not be ideally used because there is no strict translational periodicity, since the strut diameter keeps changing from one cell to another. The apparent porosity of the structure can be calculated from material and void within these cuboids. For simplification, the diameter of filaments is taken as constant within such a volume, but varying with $x$ and $y$ over the structure. The size of such a unit cell is given by the spacing of the filaments $s = 1.25$ mm, so the variation in diameter over this distance would only be 0.003 75 mm, which can be ignored. The porosity is calculated from these unit cells dividing the volume of void space within a cell by the volume of the whole cell. The parameters involved to calculate the volume of the cell are the diameter of the filaments in one layer, $d_1$; the diameter of the filaments in the other layer, $d_2$; the spacing of the filaments in both layers, $s$, and the overlap between the layers, $o = 0.08d_2$ (see section 5.1.2). To calculate the volume of the filaments $V_{fil}$, we made use of Solidworks to take the overlap into account, however, this showed that the volume of the overlap is negligible in this case, hence $V_{fil} = \frac{\pi}{4}s(d_1^2 + d_2^2)$. The volume of the cell, on the other hand, is $V_{cell} = (d_1 + d_2 - o)s^2$, where the overlap

is not negligible. The formula used to calculate this porosity is then

$$\rho = \frac{V_{\text{cell}} - V_{\text{fil}}}{V_{\text{cell}}} = 1 - \frac{\pi}{4s}\frac{d_1^2 + d_2^2}{d_1 + d_2 - o}. \tag{5.1}$$

The values of the geometric parameters and the corresponding values of porosity at the different corners of the films are shown in Figure 5.6. The porosity varies from 0.54 at the TT-corner, where the filaments of both layers are 0.7 mm in diameter, to 0.74 at the tt-corner, where the filaments of both layers are 0.4 mm. This changes throughout the sample as the diameters of the filaments change. Figure 5.7 shows how the porosity varies spatially throughout the sample. In this figure, at coordinates $(0, 0)$ we have the TT-corner and at coordinates $(100, 100)$ we have the tt-corner, the contour lines are spaced at intervals of equal values of porosity, each line corresponding to a labelled value of porosity. Thus by choosing the spacing and the diameter of the filaments appropriately, one can not only spatially vary the mechanical properties of the film, but also somewhat *independently* vary its porosity. In the example described above, the porosity changes as a consequence of the variation in the diameter of the filaments, however, this is only because the spacing $s$ between the filaments is kept constant at 1.25 mm. By accounting for the variation in the diameter, the spacing can be varied in such a way that the gap between filaments is constant. We use the word *spacing* to refer to the distance between the axis of the filaments, hence it does not take into account the changing diameter. If we want to keep constant the separation, or *gap*, between the filaments, the diameter needs to be accounted for. The porosity can then be kept constant while varying the diameter, if necessary, simply by varying the spacing between filaments accordingly. On the other hand, the bending stiffness can be kept constant while changing the porosity, as seen in Section 4.1 and in particular Figure 4.3. This was achieved modifying the spacing of filaments while keeping their diameters constant, similar to the work done by Sobral et al. [2011]. By combining spacing variations with diameter variations, the control over the micro structure increases drastically.

A note of caution on how to vary the spacing to obtain the desired porosity. Let's consider two films similar to the one in figure 5.4 with the same porosity, one with constant-diameter filaments and one with variable-diameter filaments, to simulate a case where the manufactured film has the desired porosity but not the desired properties. If we manufacture the constant-diameter film first and we want to manufacture the variable-diameter one so that the porosity is the same in the two films, it is not sufficient to vary the spacing in the variable-diameter one to keep the gap the same as in the constant-diameter case. This is because the variation in the diameter affects the layer *height*. The calculation needs to be done using the expression for the porosity 5.1. We can calculate the value of the porosity in the film with constant-diameter filaments using the expression 5.1 and setting $d_1 = d_2 = d$, as the diameter of the filaments is constant, using $s = s_{\text{const}}$ as the constant value for the spacing between filaments and setting

| corner | TT | Tt | tt |
|---|---|---|---|
| sketch | 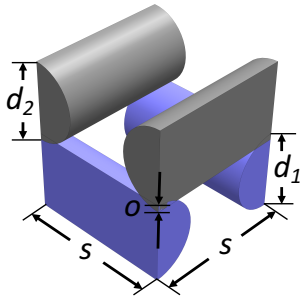 | 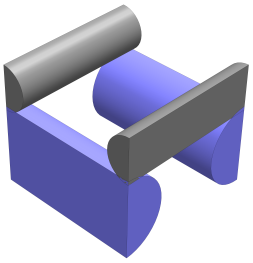 | 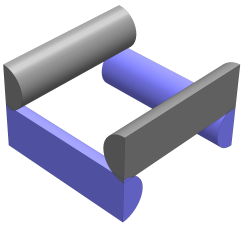 |
| $d_1$ | 0.7 mm | 0.7 mm | 0.4 mm |
| $d_2$ | 0.7 mm | 0.4 mm | 0.4 mm |
| $o$ (=0.08$d_2$) | 0.056 mm | 0.032 mm | 0.032 mm |
| $s$ | 1.25 mm | 1.25 mm | 1.25 mm |
| $\rho$ | 54.19% | 61.76% | 73.82% |

Figure 5.6: Unit cells of the film graded in two dimensions. The assumption is that, within a cell, the diameter of the filaments can be considered constant. $d_1$ is the diameter of the filaments in the first layer, $d_2$ is the diameter of the filaments in the second layer. The overlap between the two layers, $o$, is 8% of $d_2$, and the spacing between filaments is indicated with $s$. The porosity $\rho$ is the ratio of the void volume to the volume of the cell, as per equation 5.1.

$o = 0.08d$. We can then equate this value of porosity to the porosity of the film with variable-diameter, calculated using again expression 5.1 and setting $o = 0.08d_2$, to obtain the necessary spacing in the variable-diameter film:

$$s(d_1, d_2) = s_{\text{const}} \frac{d_1^2 + d_2^2}{d_1 + 1.92d_2} \frac{1.92}{2d}. \tag{5.2}$$

This expression allows to calculate the spacing between the filaments at each point in the film as a function of the diameter of the filaments in the two layers $d_1$ and $d_2$, for fixed values of the diameter of the regular lattice, $d$, and its spacing $s_{\text{const}}$. The value of $d_1$ and $d_2$, in turn, can be chosen by the user to satisfy the requirements in terms of mechanical properties. In doing so, it is essential to keep in mind the capabilities of the manufacturing process used to ultimately manufacture the film in order to avoid obtaining values for the spacing that are too low or too high for a successful manufacturing of the part. Additionally, the variable spacing leads to the filaments not being parallel. If the variation in the spacing is too big, as the number of filaments increases, the external dimensions of the part could be affected.

The last observation is that the bending stiffness has a symmetry with respect to the vertical plane passing through the tt-TT diagonal. The main geometric parameter that

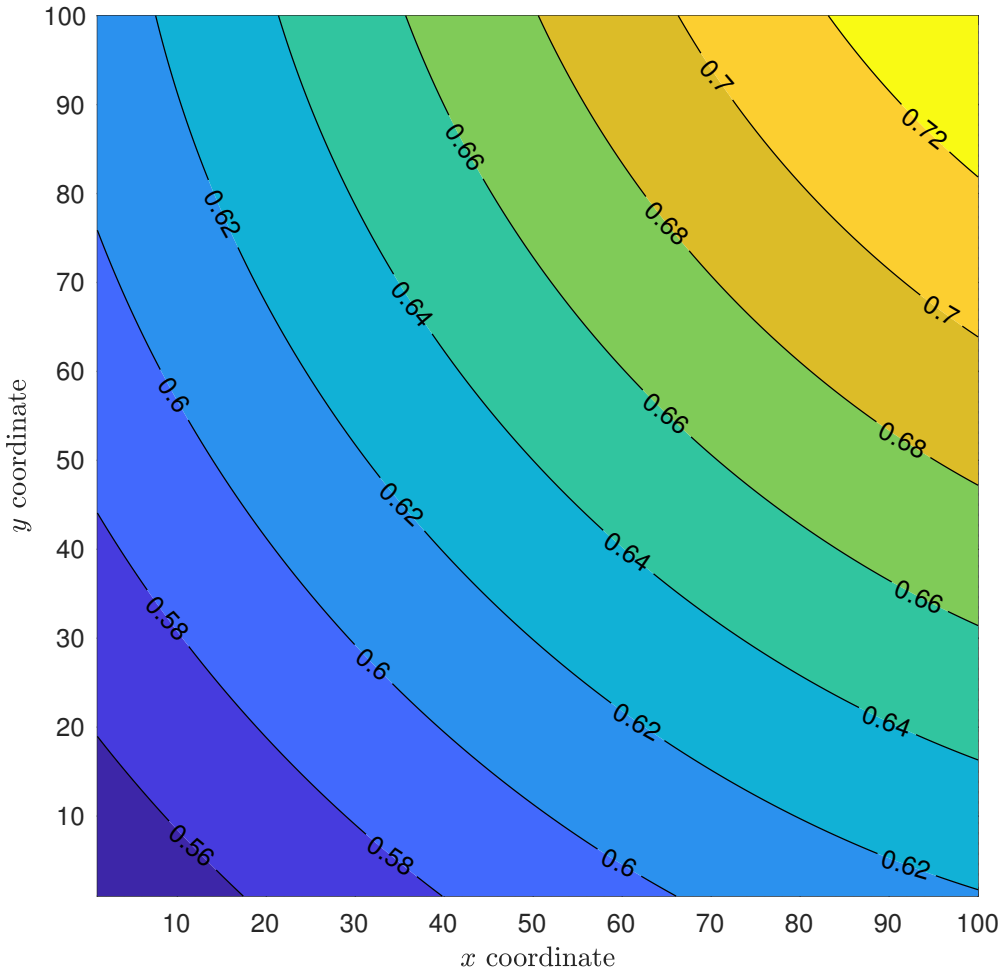


Figure 5.7: Design pore size variation within the film. At coordinate $(0, 0)$ is the TT corner, while at coordinate $(100, 100)$ is the tt corner. The porosity varies from 0.54 to 0.74. The black lines connect unit cells with the same local porosity, whose value is shown.

affects the bending stiffness is the diameter of the filaments. Each point on the sample can be defined by the diameter $d_a$ of the top filament and the diameter $d_b$ of the bottom filament. At a symmetrically placed point, we have the same values but in a different order: $d_a$ is now the diameter of the bottom filament and $d_b$ the diameter of the top filament. This symmetry in the geometry and properties results in a symmetry in the bending stiffness with respect to the tt-TT diagonal.

### 5.1.4 Challenges associated with fabrication

As described in the methodology section, a base-structure is needed that is peeled off from the bi-directionally graded film, as shown in figure 5.2. A challenge that needed to be overcome is the effect that the layer printed directly on the print-bed had on the mechanical properties of the test-film. The issue comes from this first layer having a different thickness than the others. This is because the thickness for the first layer needs

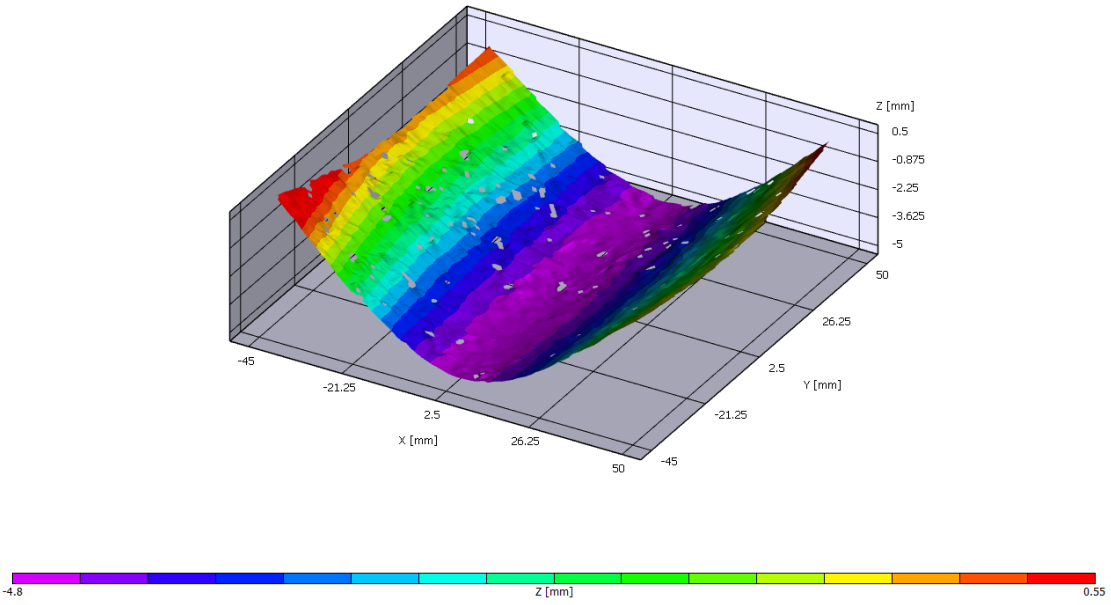


Figure 5.8: Cylindrical deformation due to one of the two layers being stiffer that the other. The first layer that is printed on the print-bed is made of thinner filaments, which are the ones to deform, leaving the filaments in the other direction to remain almost undeformed.

to be small enough to ensure, during printing, adhesion to the print-bed. Due to this, the first layer is made of filaments with a cross section that is much closer to a flat stadium shape than a circle or ellipse, resulting in a layer that is much thinner than the other layers. The films manufactured for this work have a thickness of only two layers, hence its effect was very pronounced since one layer was much thinner than the other. When the first films were tested in bending, the second layer, much thicker than the first layer, was also much stiffer, resulting in a cylindrical deformation of the film, as can be seen in Figure 5.8. In other words, the first layer would bend, while the filaments in the second layer would remain largely undeformed. Assuming the cross section to be an ellipse for ease of comparison, and calling $2a$ the major axis, or width of the filament, and $2b$ the minor axis, or thickness of the filament, the second moment of area would be $I = \frac{\pi}{4}ab^3$. The value of $b$ (thickness), observed to be about half for the first layer, led to its bending stiffness being about 8 times smaller than that of the second layer.

The issue was resolved by adding two sacrificial layers, over which the test-film was printed. The film is then carefully removed from its base after manufacturing and is ready to be tested. To be able to detach the film from the base, a number of printing parameters had to be modified when printing the first layer of the film, to ensure *low adhesion of the film to the sacrificial base structure*, as explained in Section 5.1.1. This has been achieved by increasing the layer height, decreasing the extruding temperature and adding a pause between the printing of the base and that of the film, during which the heated print-bed was turned off for it to reach room temperature. These modifications were put in place so that the *adhesion between the base and the film was much lower than between the*

*layers* of the film. This prevents damaging the film during the detachment of the base. The addition of a sacrificial base allowed to test a film that represents two functionally graded layers well, that could be used as an infill to a 3D-printed structure, without the interference of a first layer. When used as infill, the functionally graded layer will always rest on previous layers and not directly on the build plate. Additionally, we observed that by tuning the manufacturing parameters, it is possible to introduce sacrificial layers that can be later detached: this can be useful to manufacture functionally graded porous structures, even from the first layer. Another viable option could be to manufacture the base using a soluble material such as a polyvinyl alcohol (PVA) filament, which would be dissolved rather than detached, further reducing the risk of damaging the porous structure.

The choice of the printer was dictated largely by the position of the feeder in this machine. In the previous chapters, good results were obtained with Ultimaker 3D printers, however, with the switch to 2D in this chapter, a machine that could more accurately respond to variations in the amount of material extruded was desirable. As explained previously, the novel technique we proposed makes use of an in-house bespoke G-code to modify the amount of material that is pushed through the nozzle. This is achieved by varying the speed at which the *feeder* rotates. Therefore, the position of the feeder is important to achieve accurate response to the demands dictated by the G-code. In the Prusa 3D printer, the feeder is exactly on top of the printhead, while in the Ultimaker printers it is at the back of the printer, much further away from the print head. Hence, our own G-code which controls the amount of material pushed, achieves this with less latency the closer the feeder is to the print head. Prusa i3 MK3 3D printer affords this desirable feature.

## 5.2 Imaging of two-dimensionally-bent functionally-graded lattice films using Digital Image Correlation (DIC)

The films manufactured using the technique described in Section 5.1 are now tested to characterise their spatially varying stiffness. Loading a transversely loaded square shaped film is difficult for uncertainties concerning loading and boundary conditions. A relatively easier approach to characterise the spatial variation of stiffness is to measure the post-buckled shape of the film after compressing it. A film with spatially varying stiffness, as described previously, has a relatively soft corner opposite a stiff corner on a square sample, the other two corners have intermediate stiffness. The bent out-of-plane shape was imaged using digital image correlation (DIC). These tests validate the capability of the manufacturing technique proposed here to produce films with two-dimensional stiffness variation. Buckling is easy to setup, in addition to allowing the edge view of the sample to the imaging cameras, which otherwise would be obstructed by the loading apparatus. Following the discussion on symmetry, as presented in Section 5.1.3,

a buckling test performed along *both* diagonals of the film would lead to two different deflected bent profiles. The tT-Tt diagonal, would exhibit a symmetric response; while a test along the other diagonal, tt-TT, would result in an asymmetric bent shape. The comparison of these two gives a measure of the asymmetric stiffness of the sample. This section explains the laboratory tests performed on the films and validates the effectiveness of the novel fabrication technique. Section 5.3 provides computational evidence of the two-dimensional spatial variation of stiffness achieved by the proposed technique and a quantitative comparison with the observed asymmetric deflection profile.

### 5.2.1 Fundamentals of Digital Image Correlation (DIC)

DIC is an optical technique used to measure the displacement field within structural specimens during mechanical testing in laboratory [Sutton et al., 2009]. It uses a sequence of images captured by a stereo camera system, tracking points on the specimen's surface to find the full-field deformation. Before the mechanical tests are performed, an image of the undeformed state is captured. During the mechanical tests, the DIC system captures a series of images, which is then processed by the DaVis software to find the deformation field of the sample.

The points on the surface of the specimen are tracked by the DIC system. They can either be part of the surface texture of the sample, or alternatively, a random speckled pattern can be sprayed on the specimen before testing. A good speckled pattern is essential to obtain good results with DIC [Pan, 2018]. In the following, the films that will be tested have been sprayed with black paint, to provide a speckle pattern on the surface of the films. A region of interest (ROI) needs to be selected on the images that are captured, namely the surface of the specimen of which the displacement field is required. Additionally, a few seeding points need to be selected to ensure that the software tracks the correct points. This is done by selecting a few speckles on the undeformed image and telling the software where these points are located on one of the images of the deformed state. The region of interest is then divided into squares (facets). The displacement at the centre of these squares is then computed and used to obtain the field of deformation within the region of interest. The dimension of these squares can be thought of as a mesh, which determines the number of points that are tracked. It is recommended that the size of these squares be roughly 3-5 times the size of the speckles on the surface. The way the displacements in these facets can be correlated can be found in Hild and Roux [2006].

The best results are obtained when the surface to be tracked is perpendicular to the direction of pointing of the cameras [Díaz et al., 2020]. If the surface deforms so that it becomes close to parallel to the direction of view of the cameras, no tracking will be obtained. If the view of the cameras is blocked, for example by a loading probe or weight, or by parts of the specimen, the DIC system cannot compute the deformation field. An

edge view of post-buckled profile does not pose these practical problems. The way the facets are generated by the DIC driving software means that they cannot be present all the way to the edges of the sample. There would be a region around the edges, smaller than the dimension of the facets, that will not be tracked. This method works well for the general deformation field but cannot generally be used when boundary deformations are needed. DIC is well suited for our work however, as it provides quantification of the asymmetry in the flexural stiffness which can be inferred from the post-buckled shape.

### 5.2.2 Materials and methods

Guided by the need to bring out asymmetry of the deformed shapes of lattice films with prescribed spatially varying stiffness in two-dimensions, and manageable methods to map deflections over a two-dimensional domain, buckled shapes were characterised experimentally. The chosen spatial variation of the stiffness over area is such (see Section 5.1.3) that symmetry with respect to the tt-TT diagonal exists. However, along the tT-Tt diagonal the film is asymmetric. Films with fixed extruded filament diameter, on the other hand, would exhibit symmetry along both diagonals. Therefore, a square film with 2D stiffness gradation compressed *along* the tt-TT diagonal should show an asymmetric post-buckling bent shape. This would happen if the functional gradation in the mechanical properties of the film is significant. A compression test along the tT-Tt diagonal should result in a symmetric response.

Instron 4204 Electromechanical Test machine was used to perform the tests in displacement control mode. The films were imaged using Digital Image Correlation (DIC) technology, in particular, two LaVision E-lite 5MPx cameras (image resolution: $2455 \times 2057$ pixels) with Nikon 50mm lenses with LaVision DaViS processing software. Before the tests could be carried out, the system needed to be calibrated. Images of a calibrating plate of known dimensions and characteristics where taken and processed, so that the relative position of the cameras would be properly computed by the software. The setup of the experiment is shown in figure 5.9. The film was mounted on the machine using two identical custom fixtures, as that in figure 5.10. We used a flat plate with a cavity, combined with masking tape, to prevent the film from sliding during testing and to limit its rotation. The slit in the masking tape accommodates one of the corners of the sample during testing. The resulting alignment of the sample in the machine allows for the load to be applied *along* the diagonal that runs between the two corners of the film in the two slits. The testing machine applies displacement at a rate of 0.5 mm/s at the top corner, while the bottom corner remains fixed. The displacement of the film is recorded using the DIC equipment, while the Instron machine carries out the compression test in the post-buckled state. One image every second is recorded while the tensile testing machine applies displacement. Each image recorded differs from the previous by an incremental vertical displacement of 0.5 mm.

Two lattice films with the same geometry were manufactured under identical conditions. Each structure was tested along the two diagonals, during which 15 images were recorded with incremental displacement. This results in a vertical displacement that can be at most 7.5 mm, which is 5.3% of the length of the diagonal. The testing machine and the DIC equipment needed to be started separately, hence the imaging was always started first to make sure the undeformed shape was recorded. This results in some of the tests having a few initial images where there is no appreciable displacement. Also, consequently, this results in a maximum displacement that is less than 7.5 mm. However, the magnitude of displacement is irrelevant because we are interested in demonstrating primarily that spatially varying stiffness can be achieved from the proposed additive manufacturing method by over- and under-extrusion. Further, we will show later that the buckled shape is approximately preserved regardless of the amount of deformation. Only recordings with an appreciable displacement will be considered in the following, hence some tests will have less than 15 stages of deformation shown. This is because, when normalising, noise in the data is amplified and this does not result in a smooth curve. The noise comes from the fact that filaments of different layers are on slightly different planes away from the camera, hence at different $z$ values with respect to the DIC optical probe. When the $z$-displacement is comparable to the thickness of the film, readings on different layers affect the accuracy of the results adversely. Therefore, noisy measurements for the stages of deformation that did not result in a smooth curve when normalised were excluded. The LaVision DaViS processing software was then used to extract displacement values along the diagonal as well as the surface plot of the bent film, at each recorded stage. To do this, a subset size of 51 pixels was selected, with a step size of 25 pixels. The displacement values extracted using the DaViS software are then imported into Matlab, where the relevant two-dimensional displacement field was post-processed.

A suite of Matlab scripts and functions were developed to post-process the data extracted from the DaVis software. Firstly, the stages of deformation that show an appreciable displacement are selected and plotted. As the tt-TT diagonal would show asymmetry, a measure of asymmetry of a curve about its mid-point needs to be introduced. A simple measure of asymmetry used here is to treat the deflection values as probability density functions to calculate their skewness. In statistics, skewness is used to determine the asymmetry of a distribution with respect to its mean value. Secondly, the measured post-buckled shapes of the structure will be compared with Finite Element Analysis in section 5.3. For the purpose of characterising the asymmetry in deflected shape affected by spatial variation of stiffness, the amplitude of deformation is arbitrary. Therefore, measured shapes have been normalised in amplitude: the point where the maximum displacement occurs has been normalised to a displacement of value 1 and the rest of the points have been scaled proportionally. This allows a comparison of the deformed two-dimensional shape for different stages of post-buckling. Any systematic trends in the

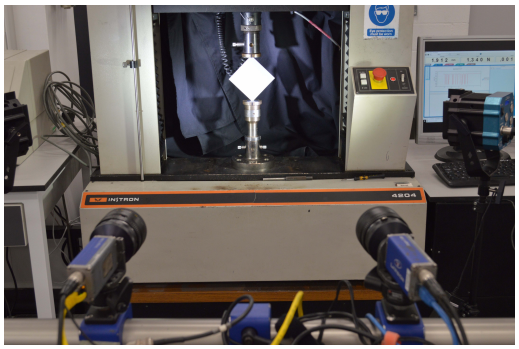

Figure 5.9: Set-up of the buckling experiment. The film is mounted on the fixtures with the diagonal along the loading axis.

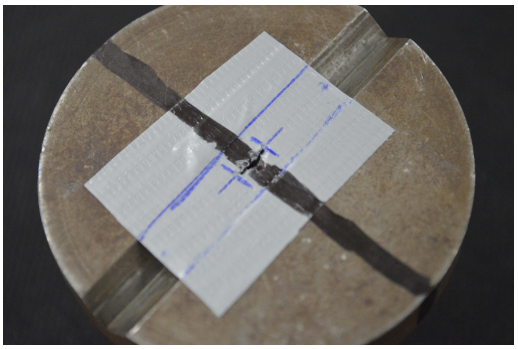

Figure 5.10: The customised fixture uses a round flat plate with a ridge, over which masking tape was added to prevent the rotation of the sample during testing.

change in the shape can then be attributed to non-linearity. On the other hand, a near-invariant scaled shape would confirm that the effect of non-linearities on the deformed shape is negligible. The diagonal in the direction of compression becomes progressively shorter during a test. This needs to be accounted for while comparing deflection shapes of the subsequent stages and also those obtained with the finite element analysis (section 5.3). Therefore, a normalisation along the diagonal has also been carried out. All of the shapes have been transformed so that the leftmost point is $-1$ and so that the rightmost point is 1. Following these normalisations, all the deformed states are transformed so that the two corners of the tested diagonal correspond to position $-1$ and 1, and so that the maximum value of deformation is 1.

### 5.2.3 Results

The commercial software (DaVis) that captures and processes data from the DIC machine divides the sample into square-shaped regions that are tracked during the deformation by the DIC software, as can be seen at the edges of the film in figure 5.11. A surface plot of a film tested along the tt-TT diagonal is shown in figure 5.12(a) and the edge view of the same can be seen in figure 5.12(b). This image shows asymmetry of the profile with respect to the middle point $x = 0$, with largest curvature at the softest corner. Quantification of asymmetry is carried out only along the diagonal along which the compressive displacement was applied. More complex characterisation of the bent surface is unnecessary, as we are primarily interested in demonstrating the capability of the fabrication approach proposed here and to quantitatively compare the laboratory observations with computational predictions. FE analysis is carried out in the next section to address the latter question. The displacement along the diagonal that runs between the two corners

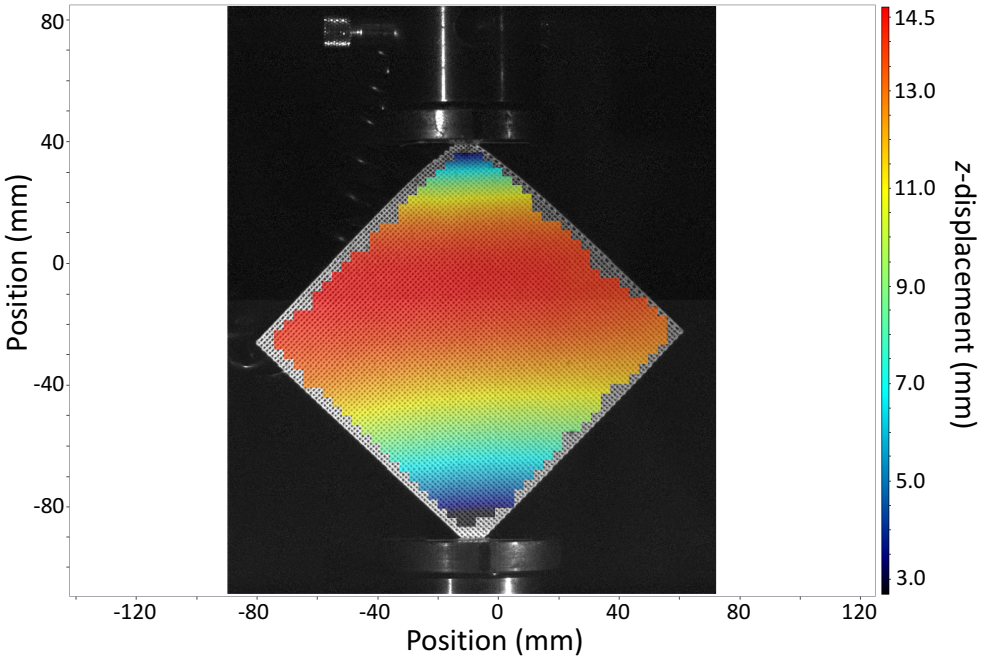


Figure 5.11: Overlayed deformation of film with an asymmetric response. Image obtained from the software DaVis.

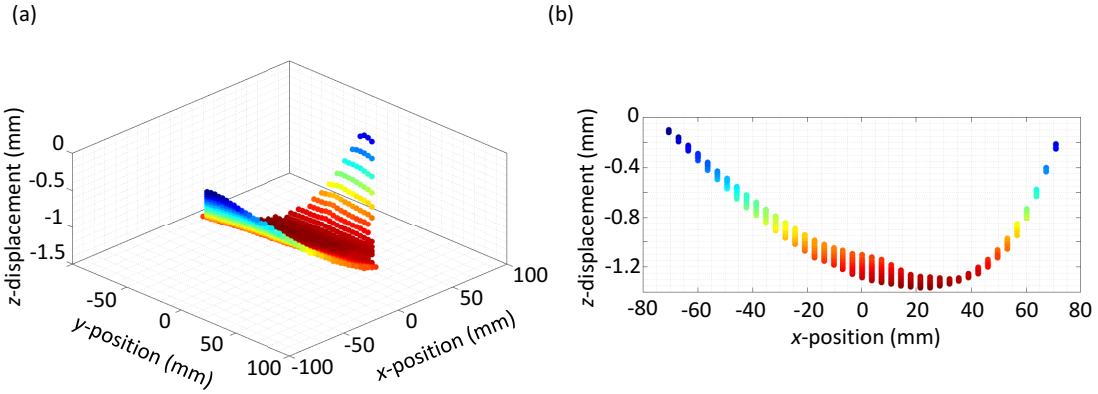


Figure 5.12: (a) Surface plot of the deformation in Figure 5.11. (b) Side view of the deformed film. The asymmetry of the deformed shape is visible, with respect to position $x = 0$.

in the fixtures is extracted from the DaVis software and imported into the Matlab environment. As explained in section 5.2, out of the 15 stages of deformation recorded, only those with an appreciable amount of displacement have been considered, as this ensures suppression of noise associated with very low transverse deflection values. Therefore, less than 15 stages will be considered as to exclude data from very noisy measurements of very small post-buckling deflections. Comparisons with FEA simulations are presented in section 5.3.

Figure 5.13 shows the deformation obtained when testing the film along the tT-Tt diagonal. The response, when the sample is compressed along this diagonal, is expected to be symmetric, since the stiffness distribution has a mirror symmetry about the plane perpendicular to this diagonal. In Figure 5.13, 9 stages of post-buckled shape are presented. The transverse displacement is not normalised, while the position along the diagonal is normalised between $-1$ and 1 in order to ensure that all graphs fit in the same range on the horizontal axis. Visually, all of the shapes are symmetric within the band of experimental measurements and manufacturing tolerances. To quantify this visual appearance further, next we consider these shapes as probability density functions and we compute their skewness, in order to evaluate symmetry about the mid-point. The average value obtained is 0.06. This value is close to the expected value of 0, which would indicate a perfectly symmetrical result. Departure from the theoretical zero value can be attributed to a number of reasons associated with laboratory experimentation, such as the fixtures (refer back to figure 5.10) that hold the film in place during testing. The slit in the masking tape that prevents the film from rotating and sliding out of place, could provide imperfect clamping. Therefore, fixture would not act as a perfect pin joint and would possess resistance during bending. This resistance is hard to control and could be unequal at the two fixtures, resulting in a slight asymmetry in the response. Figure 5.14 shows the stages of deformation of the previous figure after normalising the transverse displacement. There is an almost perfect overlap between the shapes that correspond to different stages of post-buckling, which indicates that the shape of the buckled film remains nearly unchanged and the non-linearity is insignificant.

Figure 5.15 shows the 10 stages of deformation for the bi-layer film tested along the tt-TT diagonal. The position along the diagonal has been normalised in the range from $-1$ to 1 on the $x$-axis, while the transverse displacement is kept as recorded by the DIC system. The response is visually asymmetric with largest curvature at the softest corner, confirming a successful fabrication of variable stiffness structure. Treating these profiles again as probability density functions, the average skewness is 0.27. To put this value into perspective, consider a triangular distribution in the range from $-1$ to 1 on the $x$-axis with the peak at $-1$ and decreasing linearly to a zero value at $+1$ on the $x$-axis. This can be considered to be the limiting case of a bent film with peak at $-1+\delta$, with $\delta$ approaching zero. In this extreme case of asymmetry, the skewness can be found analytically. In the limit $\delta \to 0$, this equals $\frac{2\sqrt{2}}{5} = 0.57$. The skewness obtained for the

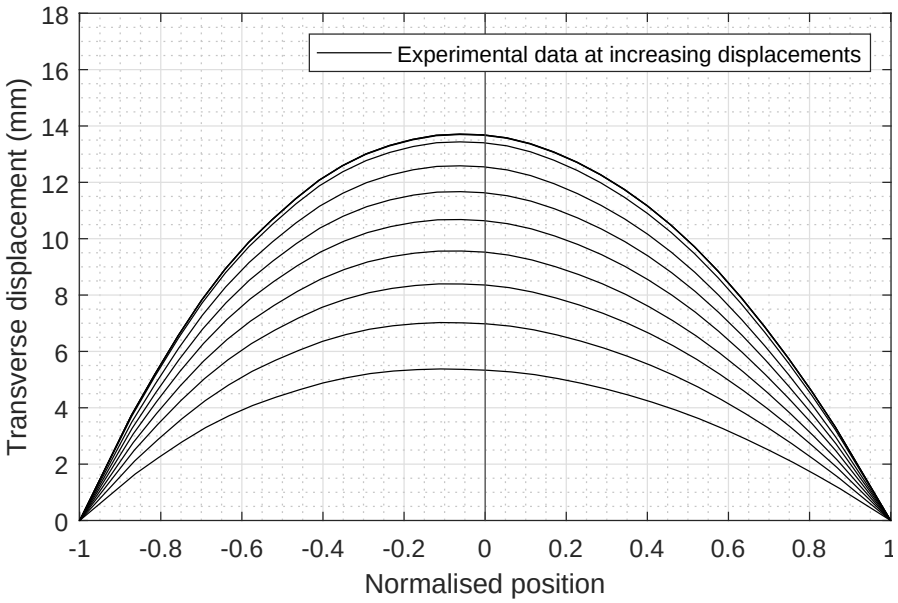


Figure 5.13: The non-normalised stages considered for Sample 2, along the diagonal with symmetric behaviour.

buckled mode along the tt-TT diagonal is then 47.4% of that for the extreme case, while the skewness for the buckled mode shape along the tT-Tt diagonal is 10.5%. Figure 5.16 shows the results with transverse displacement normalised to be between 0 and 1. The near invariance of the shape of the deflection profile regardless of the magnitude is clear in this case too. This enables us to make meaningful comparisons with *linear* buckling mode shapes obtained from FEA calculations.

The above measurements clearly demonstrate the manufacturing capability of the proposed approach to fabricate structures with spatially varying stiffness. The approach of over-extrusion and under-extrusion, introduced in chapter 3 and further developed for 2D stiffness variation in this chapter, effectively provides us a method to *vary the filament diameter* during the 3D-printing process to obtain filaments that behave the same as filaments with a continuously variable diameter. Having shown that the deformed shape does not depend on the amplitude of deformation, we now proceed to the FE analysis performed with software Abaqus [Abaqus/CAE, 2014]. Buckling modes are independent of the amplitude and only the deformed shape, or buckled mode, is significant. We will then compare the normalised deformed shapes obtained experimentally in this section to the normalised results obtained from simulations in the next section. This will complete the picture, showing that the developed technique is reliable and predictable.

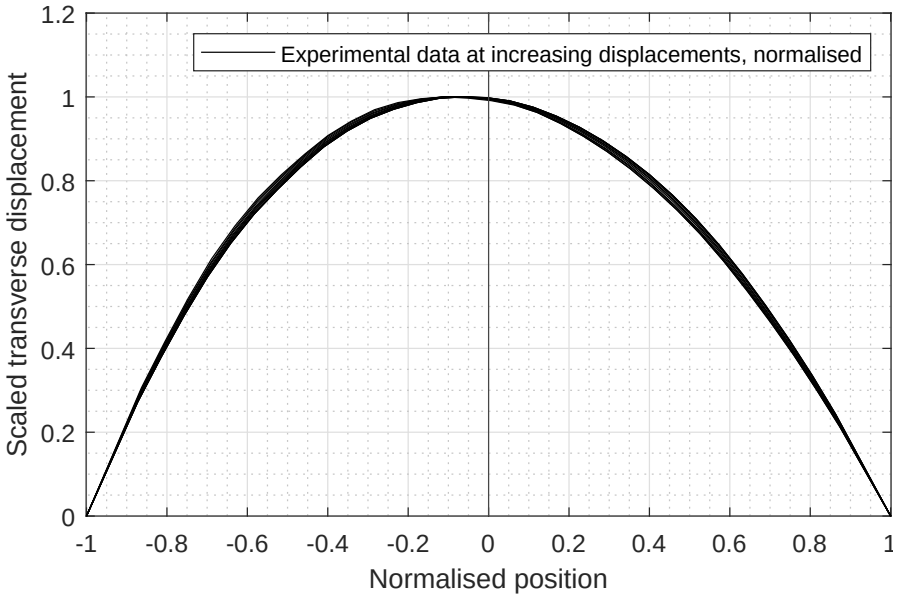


Figure 5.14: The normalised stages considered for Sample 2, along the diagonal with symmetric behaviour.

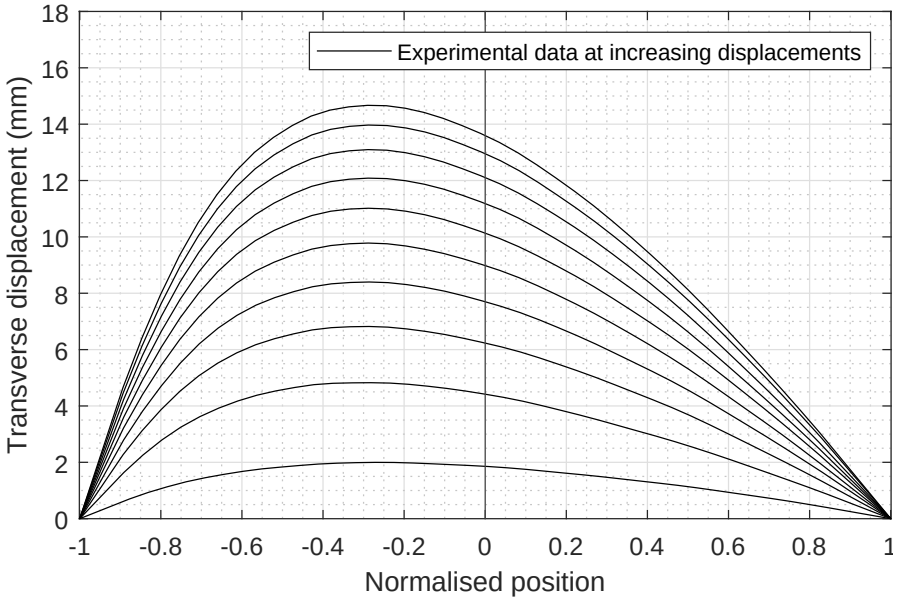


Figure 5.15: The non-normalised stages considered for Sample 2, along the diagonal with asymmetric behaviour.

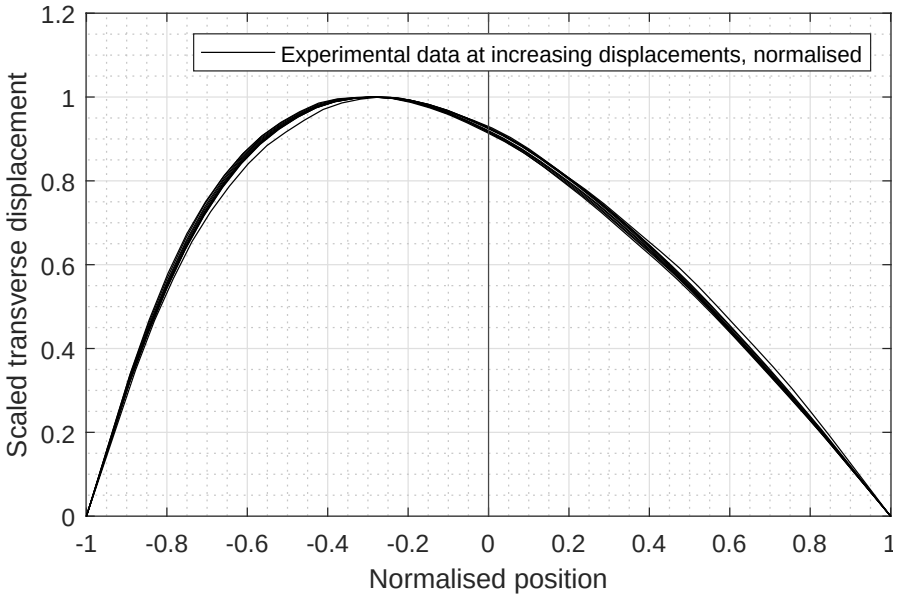


Figure 5.16: The normalised stages considered for Sample 2, along the diagonal with asymmetric behaviour.

## 5.3 Computational response calculation of bi-directionally graded lattice structures

The bending response of structures with stiffness varying in two directions is now assessed using Finite Element Analysis (FEA). A comparison between experimental results and those from FE simulations is presented now.

### 5.3.1 Finite element modelling of the film with spatially varying stiffness in two dimensions

A CAD model of the film was created using the commercial software Solidworks. The geometry and the material properties were the same as the two-layer film experimentally studied in the previous section. The dimensions of the film are 100 mm by 100 mm, the number of filaments along each of the two directions is 80, and the diameter of these filaments varies from 0.7 mm to 0.4 mm along the two directions. The overlap between the filaments of the two layers was chosen according to the characterisation in Section 5.1.2, where an estimate for the overlap was given: 8% of the diameter of the filaments in the second layer. The geometry was then exported from Solidworks into the ABAQUS finite element code in the *.igs* format.

A small difference between the physical 3D-printed samples and the FE model is at the edges of the film. The filaments running along the four edges, in the 3D model, have been cut in half. This can be seen in the details in Figure 5.17. This allows to obtain

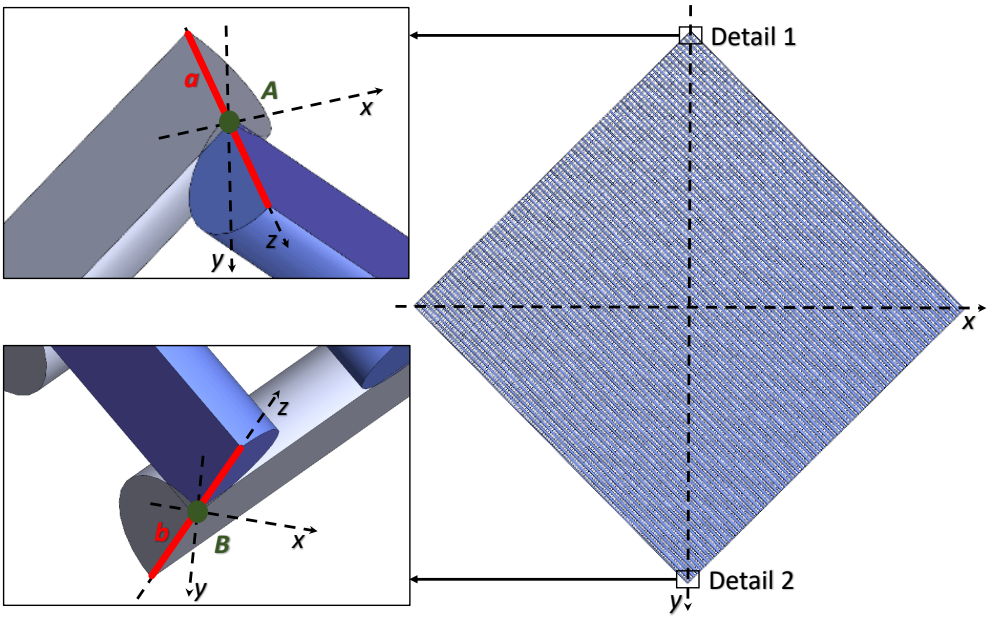


Figure 5.17: The image shows the full lattice and its axis for reference. The $x-y$ plane represents the plane of the film, while the $z$ direction, parallel to segments $a$ and $b$, is the direction out of plane. Along segment $a$, displacement along $x$ is blocked, while at point $A$ displacement is blocked along $x$ and $z$. The point force is applied at point $A$, in the $y$ direction. Along segment $b$, displacement along $x$ is blocked, while at point $B$ displacement is blocked along all directions, $x$, $y$ and $z$.

segments $a$ and $b$ and points $A$ and $B$ where the necessary boundary conditions can be applied, as presented later.

### 5.3.2 Computational assessment of spatially varying stiffness using finite element analysis

Once the 3D geometry has been imported into the commercial finite element software Abaqus, three *main* subsequent steps in the analysis could proceed. The first step is to create another coordinate system. This new coordinate system would have one of the axis along one diagonal of the film and another axis parallel to the other diagonal. The boundary conditions and the load could be applied correctly in this new coordinate system.

The second step is to create a mesh for the model, which can be seen in Figure 5.18. The low diameter of the filaments involved and the relatively large scale of the film, compared to the diameters, result in a relatively large number of elements required in the mesh. The resulting mesh has slightly less than four million elements. The element type chosen is called C3D10: a tetrahedron, part of the 3D stress family in the standard library, with quadratic geometric order. The approximate global size has been set to 0.5 and the maximum deviation factor under the curvature control setting has been set to

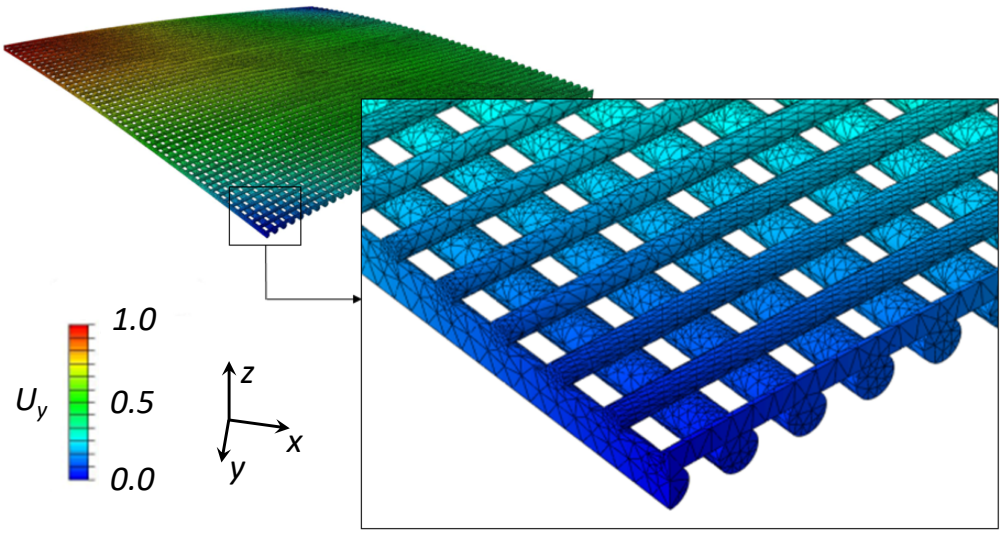


Figure 5.18: The image shows the mesh used for the simulation, as well as an example of the results obtained from Abaqus.

0.1. The deformation step has been set to Buckle, under the Linear Perturbation type. The material properties have been set to $E = 2.29\,\text{GPa}$ and $\nu = 0.36$, respectively for the Young's modulus [Cuan-Urquizo et al., 2015] and the Poisson's ratio [Jamshidian et al., 2010] of PLA filament. These values however, could depend on the properties of the PLA used, for example the molecular weight. For this reason, for critical work it is advisable to test the material that is going to be used for manufacturing and obtain more specific values.

The third step is to apply the correct boundary conditions and loading, which is a force along a diagonal. Point A in Detail 1 of Figure 5.17 is the point at which this force is applied, along direction $y$. This point also needs to be free to move only in the direction of applied load, hence its movement along $x$ and $z$ is constrained. The points belonging to segment $a$ need to be fixed in the $x$ direction to prevent sideways movement and rotation of the film—mimicking the tape used in the fixture of the experimental set-up, as shown in Figure 5.10. The boundary conditions at the other end of the diagonal, shown in Detail 2 of Figure 5.17 are as follows: point B is fixed in space to prevent rigid body translations, segment b is fixed in the $x$ direction to prevent sideways movement and rotation. This allows point A to get closer to point B along the $y$ direction, while the film buckles without unwanted rotations or translations.

### 5.3.3 Computational results for spatially varying structure & comparisons with experimental measurements

Two films were computationally analysed. For each, two simulations were run, one along each diagonal. Displacement components in all directions of the whole bi-layered structure were obtained, see Figure 5.18. However, only the displacement along the tested diagonal has been extracted, normalised both in length and in amplitude and used in the following. These results are now compared with those from experiments presented in the previous section.

Figure 5.19 shows the transverse displacement extracted on the tT-Tt diagonal, as a function of position, from the FE analysis using black dots, and black solid line for experimentally measured post-buckled displacement. This profile corresponds to the maximum deformation in Figure 5.13, and this includes inevitable yet small non-linear response post-buckling. Along the tT-Tt-diagonal, bending stiffness does not vary. Hence the expected response is symmetric. The profile observed here is symmetrical, with a skewness of 0.02 for the computational result. The small discrepancy between the FEA results and the results of the experiments—in which the skewness was 0.06—can be attributed to several factors such as imperfection in mounting, errors in measurement, potential errors in mesh-asymmetry, etc. The fixture with masking tape did not act as a perfect pin joint, rather, it introduced a clamping effect that can be seen at position $x = -1$ in figure 5.19. Here, the left part of the film does not seem to have the same freedom of movement as the end at $x = 1$, resulting in two different curvatures at the two ends.

Figure 5.20 shows the transverse deflection profile of the tt-TT diagonal that is expected to show asymmetry about the mid-point. The image shows the last stage of deformation of the laboratory experiments in solid black, while the FEA results are shown as black dots. These results have all been normalised both in length as well as in amplitude. This result shows a very good overlap of the experimental and FEA buckled shapes: the skewness of the profile obtained with FE analysis is 0.26, the one of the experimental results was 0.27. In this case, we can note that the effect of clamping introduced by the tape is negligible, as opposed to the previous case.

Results obtained here are in line with the expectations as the FEA results overlap closely with those obtained experimentally. This implies that the functional gradation that has been introduced in the film using the developed technique is consistent. The expected diameters of the filaments and the expected variation in the bending properties is close to what is obtained with the 3D printed film. The novel manufacturing technique is then able to produce films graded in two dimension, and the results can be predicted with finite element methods. This is the last step that was necessary to ensure that the developed technique could be applied to real structures to obtain predictable spatially-varying properties, the aim of this chapter.

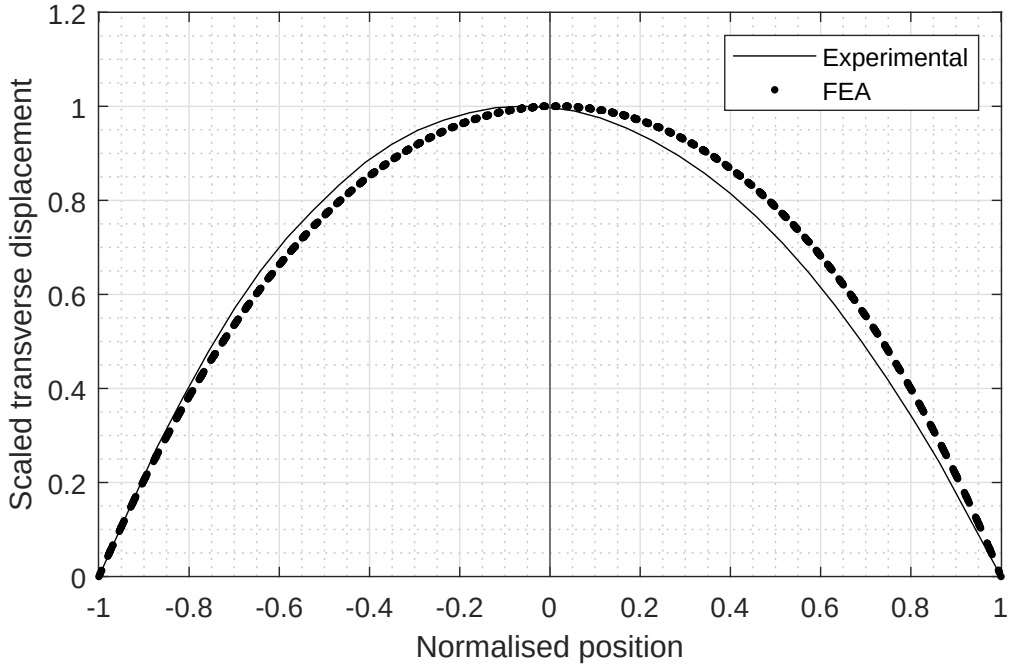


Figure 5.19: The last stage of deformation along the diagonal with non-graded properties, tT-Tt, is shown in solid black. The FE analysis results are reported with black dots. Both are normalised in length and in amplitude for ease of comparison.

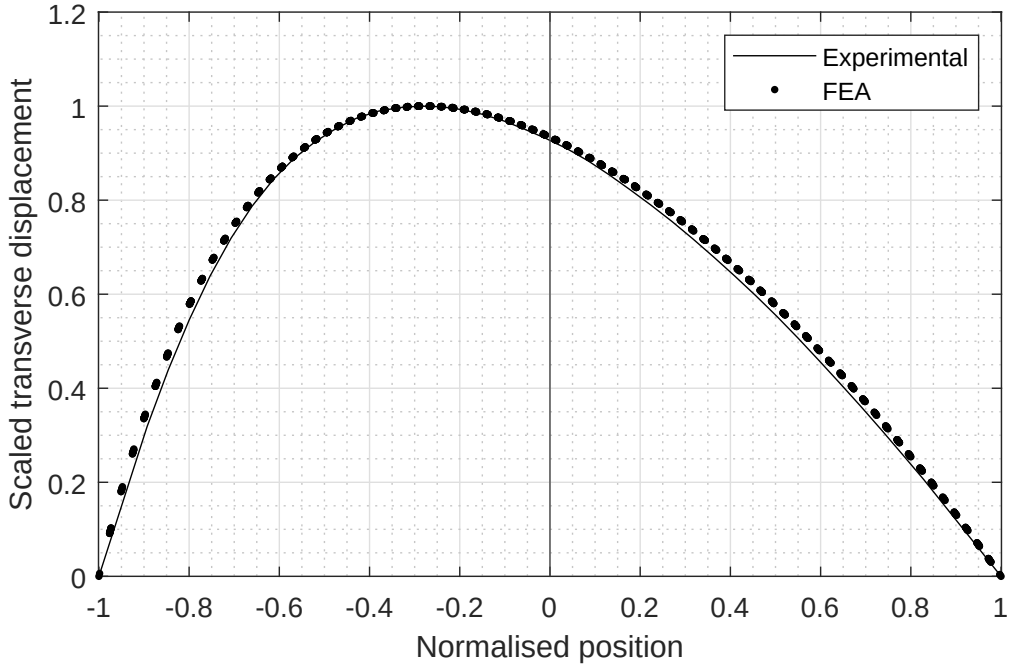


Figure 5.20: The last stage of deformation along the diagonal with graded properties, tt-TT, is shown in solid black. The FE analysis results are reported with black dots. Both are normalised in length and in amplitude for ease of comparison.

## 5.4 Conclusions

Bi-layer lattice films with bi-directionally varying stiffness were successfully fabricated. Planar lattice samples of square shape were fabricated with diameter of struts varying according to a specified function. Following the fabrication of several structural samples, laboratory testing was carried out to observe structural response when properties vary spatially. These samples had the stiffest corner and the softest corner located at opposite edges. Spatial variation in bending stiffness was brought out by testing such bi-directionally graded planar lattice structures by compressing along the diagonal with strongest property variation. The post-buckled profile provides a convenient way of characterising the spatial variation in the stiffness of the structure. The asymmetric bent profile of the diagonal, measured using digital image correlation technique (DIC) confirms the spatially varying stiffness of the struts. Further, the largest curvature was observed in region of smallest stiffness, which is consistent with our expectations.

Finally, FE analysis was carried out to extract the buckling mode shapes of such bi-directionally graded lattice bi-layer structures. Results from the linear FE analysis are in very good agreement with those from the laboratory results. Minor discrepancies between the computationally obtained bent profile and observed shape is attributed to measurement errors, modelling errors and modelling exclusions such as geometric non-linearities.

Successful fabrication, experimental measurement, computation and their agreement show that the fabrication technique developed in this work is not only capable of manufacturing films with graded stiffness, but also that the variation in the property of these films is predictable. The technique can be further applied to real structures to obtain properties that vary in space in a prescribed way, at will. It is also possible to combine the technique developed in this work with a technique similar to that used by Sobral et al. [2011]: use the spacing between filaments to vary the porosity. If the spacing is varied in such a way that accounts for the variation in the diameter that is introduced with our technique, then the porosity and the mechanical properties can be varied somewhat independently by means of variation in spacing and diameter. The limitations to this independence mostly arise from limits in the manufacturing capabilities (presence of large overhangs, for example) or shape retention.

# Chapter 6

# Conclusions and future work

## 6.1 Conclusions

This work presents a novel technique for the production of structures with functionally graded stiffness. Using affordable 3D printers based on fused deposition modelling, we were able to produce variable extrusion using a fixed bore nozzle. This was achieved by controlling a process parameter, which results in over-extrusion or under-extrusion over the nominal bore size. The achieved variations in the extrusion effected by controlling the process parameters were characterised for size and ellipticity. Parameters to describe the range of adaptability of a fixed diameter nozzle for continuously varying extrusion were defined—they are simple measures of the gain in size, axial stiffness and flexural stiffness of the filaments thus produced. In effect, the proposed approach provides a variable diameter nozzle without any hardware modifications.

The appropriate relation between the process parameter and the diameter of the extruded filament was then used to obtain filaments with a diameter that is continuously changing within a lattice structure. This allowed us to obtain extrusions that can be considered having a diameter that changes continuously throughout a rectangular sample. As remarked many times, we have verified that the variations in the diameter that have been introduced are mechanically equivalent to a linear continuous variation in the diameter of the filaments. This is because the films we have manufactured and tested are in agreement with a mathematical model where the variation in the filament diameter is assumed to be linear. Films have been successfully manufactured using the technique developed, first with a variable diameter along *one* direction. The bent shape shows asymmetry due to stiffness varying along its length. The asymmetric shape matches extremely well that predicted using a theoretical model, resulting in the buckling mode shapes. Buckled shapes provide an easy approach to make measurements and record the asymmetric profile. Although linear theory is used, the effects of non-linearity are not so

pronounced and a good agreement between theoretically obtained bent profile and that measured, is obtained.

Following confirmation of the achieved variation in stiffness and its theoretical validation, more realistic lattices with property variations from point-to-point over a plane were realised by controlling the process parameters during FDM 3D printing. Stiffness variation over a plane was prescribed such as two opposite corners have the softest and the stiffest points whereas there is a prescribed variation throughout the two-dimensional domain as per a prescribed function. Again the stiffness variation in bending of a bi-layer square shaped structure is characterised experimentally by the use of Digital Image Correlation (DIC). The bent profile of the diagonal that has intended stiffness variation matches closely with the FE computations that incorporate spatially varying properties as intended during the 3D printing process control.

Finally, encouraged by the experimental realisation of functionally graded structures and their successful validation against theoretical models, several extensions of the analysis concerning mechanics of lattice structures was presented. This included extensions for the response of multiple-layered lattice beams with spatially varying filament size. Also, analysis for the compressive stiffness of woodpile lattices was presented. This is extension of previously known work where filament bending was described by Euler-Bernoulli models, which ignores shear in the struts. The inclusion of shear becomes very significant when the lattice is dense, i.e. when the spacing between struts is comparable to the strut diameter.

The research covered here was inspired by a number of practical applications. Most notably this includes bio-structures such as biomedical scaffolds. However, the fabrication capability demonstrated by this work has the potential of tailoring properties of micro-structured matter in other contexts such as lightweight constructions, core of sandwich panels, thermal and acoustic insulation materials, elastic and acoustic meta-materials, to name a few. In particular, if we compare the technique developed here with some of the techniques presented in the literature review, we can better appreciate the main benefits that our technique brings.

The first difference is that the technique developed does not need hardware modifications and can then be applied to any 3D printer that can be driven using G-code files, as opposed to, for example, the patent by Jin [2016]. A possible alternative technique to obtain a spatial variation in the properties would be to extrude multiple filaments with no gap in between, to obtain a strand of polymer that is thicker than the nominal size of the nozzle. This method however would only be able to produce strands with a *width* that is a multiple of the nozzle diameter, while the *thickness* of the layer would remain the same. Our technique operates on a different length scale: we are able to produce filaments with a diameter that varies between the nozzle diameter and double the nozzle diameter. Additionally, our change also affects the layer thickness rather than only affecting the

width. Lastly, it is possible to follow the methodology of some of the works available in literature to vary the porosity of the structure [Di Luca et al., 2016, Sobral et al., 2011], and couple this with our technique to obtain a change in the mechanical properties. To some extent, these techniques can be considered independent. Not in the sense that one does not affect the other, but it is possible to modify each technique to take into account the changes introduced by the other and obtain structures where it is possible to modify the porosity without affecting the mechanical properties and viceversa. Some limitations to this independence are due to the change in the external dimensions that would arise for large changes in the spacing between filaments, or the layer height. However, these limitation are less stringent when these techniques are used for infill (where the external appearance is taken care of by additional layers) or for porous structures.

## 6.2 Future work

Several possibilities for future work have arisen from the present work. They are itemised below.

- The technique of variable extrusion developed in this work can be implemented directly into slicing software to make it available for use to all users of 3D printers. This has a number of issues to overcome, such as the uneven layer height due to the variable diameter, however, a few layers can easily be introduced as infill where required.
- A standalone application can be developed to modify the G-code of parts to obtain a functionally graded version of the same part, similar to what has been described in Section 3.5.
- A software could optimise the internal architecture to include variable-diameter filaments, based on a loading scenario applied to the part.
- Users of FDM 3D printers can apply these technique directly adapting it to their application and needs.
- A technique could be developed to overcome the issue related to the variable layer height. Correct positioning of extra filaments or partial layers could bring the layer height back to constant after the FG layers have been inserted where required.
- The comparison between mathematical models and experimental results could benefit from a study on the mechanical properties of the base material. For instance, users of 3D printers could test their own material to find the Young's modulus and the Poisson's ratio.

- Mathematical models can be developed for 2D and 3D lattice structures with variable-diameter filaments. Based on the needs of the application, simple mathematical models based on the apparent stiffness described in Section 4.4.1 can be developed.
- The functionally graded version of the woodpile lattice under compression studied in chapter 4 could be developed.
- Operating conditions combining parameters such as nozzle speed, extrusion speed, temperature, etc., could be optimised so as to increase the adaptability of the nozzle output, thus increasing the range of the variable nozzle further.
- A detailed imaging study such as that provided by micro-CT could be used to characterise the variable extrusion process more thoroughly.
- Fracture properties could be analysed and tested.

# Bibliography


Tobias A. Schaedler and William B. Carter. Architected cellular materials. *Annual Review of Materials Research*, 46(1):187–210, 2016. ISSN 1531-7331 1545-4118. doi: 10.1146/annurev-matsci-070115-031624.

Daekeon Ahn, Jin-Hwe Kweon, Soonman Kwon, Jungil Song, and Seokhee Lee. Representation of surface roughness in fused deposition modeling. *Journal of Materials Processing Technology*, 209(15):5593 – 5600, 2009. ISSN 0924-0136. doi: https://doi.org/10.1016/j.jmatprotec.2009.05.016. URL http://www.sciencedirect.com/science/article/pii/S0924013609002039.

V. S. Deshpande, N. A. Fleck, and M. F. Ashby. Effective properties of the octet truss lattice material. *J. Mech. Phys. Solids*, (49):1747–1769, 2001a.

Granta. Granta: CES Selector materials selection software. http://www.grantadesign.com/products/ces/, 2012.

Li Yang, Ola Harrysson, Harvey West, and Denis Cormier. Mechanical properties of 3d re-entrant honeycomb auxetic structures realized via additive manufacturing. *International Journal of Solids and Structures*, 69–70:475–490, 2015. ISSN 0020-7683. doi: http://dx.doi.org/10.1016/j.ijsolstr.2015.05.005.

Andrea Di Luca, Barbara Ostrowska, Ivan Lorenzo-Moldero, Antonio Lepedda, Wojcech Swieszkowski, Clemens Van Blitterswijk, and Lorenzo Moroni. Gradients in pore size enhance the osteogenic differentiation of human mesenchymal stromal cells in three-dimensional scaffolds. *Scientific Reports*, 6:22898, 2016. doi: 10.1038/srep22898https://www.nature.com/articles/srep22898#supplementary-information. URL https://doi.org/10.1038/srep22898.

J. M. Sobral, S. G. Caridade, R. A. Sousa, J. F. Mano, and R. L. Reis. Three-dimensional plotted scaffolds with controlled pore size gradients: Effect of scaffold geometry on mechanical performance and cell seeding efficiency. *Acta Biomater*, 7(3):1009–18, 2011. ISSN 1878-7568 (Electronic) 1742-7061 (Linking). doi: 10.1016/j.actbio.2010.11.003. URL https://www.ncbi.nlm.nih.gov/pubmed/21056125.

Cheon Deok Jin. 3D printer having variable-nozzle mechanism and management method of the same, patent number KR20140152155 [transl. from Korean], 2016.

Manufacturing Guide Sweden AB. Additive manufacturing. https://www.manufacturingguide.com/en/additiv-tillverkning. Accessed: 29-01-2021.

Sigma-Aldrich. Bioprinting: Bioink selection guide. https://www.sigmaaldrich.com/technical-documents/articles/materials-science/3d-bioprinting-bioinks.html. Accessed: 29-01-2021.

Claudia Di Bella, Serena Duchi, Cathal D. O'Connell, Romane Blanchard, Cheryl Augustine, Zhilian Yue, Fletcher Thompson, Christopher Richards, Stephen Beirne, Carmine Onofrillo, Sebastien H. Bauquier, Stewart D. Ryan, Peter Pivonka, Gordon G. Wallace, and Peter F. Choong. In situ handheld three-dimensional bioprinting for cartilage regeneration. *Journal of Tissue Engineering and Regenerative Medicine*, 12(3):611–621, 2018. ISSN 1932-7005. doi: 10.1002/term.2476. _eprint: https://onlinelibrary.wiley.com/doi/pdf/10.1002/term.2476.

Farzad Shahangi. 3D printing Polycaprolactone (PCL) Structures and modelling and finite element analysis (FEA) of the internal structure to predict properties of auricular structures. *University of Wollongong Thesis Collection 2017*, January 2018.

Tuan D. Ngo, Alireza Kashani, Gabriele Imbalzano, Kate T. Q. Nguyen, and David Hui. Additive manufacturing (3D printing): A review of materials, methods, applications and challenges. *Composites Part B: Engineering*, 143:172–196, June 2018. ISSN 1359-8368. doi: 10.1016/j.compositesb.2018.02.012.

Xin Wang, Man Jiang, Zuowan Zhou, Jihua Gou, and David Hui. 3D printing of polymer matrix composites: A review and prospective. *Composites Part B: Engineering*, 110: 442–458, February 2017. ISSN 1359-8368. doi: 10.1016/j.compositesb.2016.11.034.

D. T. Sarathchandra, S. Kanmani Subbu, and N. Venkaiah. Functionally graded materials and processing techniques: An art of review. *Materials Today: Proceedings*, 5(10, Part 1):21328–21334, January 2018. ISSN 2214-7853. doi: 10.1016/j.matpr.2018.06.536.

L. J. Gibson and M. F. Ashby. *Cellular solids: Structure and Properties*. Cambridge University Press, Cambridge, UK, 1997.

R. Lakes. Materials with structural hierarchy. *Nature*, (361):511–515, 1993.

L. Valdevit, A. J. Jacobsen, J. R. Greer, and W. B. Carter. Protocols for the optimal design of multi-functional cellular structures: from hypersonic to micro-architected materials. *J. Am. Ceram. Soc.*, (94):S15–34, 2011.

CMI Inc. Cellular materials international inc. http://www.cellularmaterials.net/, 2019. Accessed: 12/01/2020.

CellMat. CellMat Technologies. http://www.cellmattechnologies.com/en/home/cellular-materials/, 2015. Accessed: 31/01/2017.

K. F. Leong, C. K. Chua, N. Sudarmadji, and W. Y. Yeong. Engineering functionally graded tissue engineering scaffolds. *J Mech Behav Biomed Mater*, 1(2):140–52, 2008. ISSN 1878-0180 (Electronic) 1878-0180 (Linking). doi: 10.1016/j.jmbbm.2007.11.002. URL https://www.ncbi.nlm.nih.gov/pubmed/19627779.

e-NABLE. Enabling The Future. http://enablingthefuture.org/, 2020. Accessed: 24/03/2020.

D. W. Hutmacher. Scaffolds in tissue engineering bone and cartilage. *Biomaterials*, 21 (24):2529–2543, 2000a. ISSN 0142-9612. doi: 10.1016/s0142-9612(00)00121-6. URL <GotoISI>://WOS:000089861700006.

M.f Ashby. The properties of foams and lattices. *Philosophical Transactions of the Royal Society A: Mathematical, Physical and Engineering Sciences*, 364(1838):15–30, January 2006. doi: 10.1098/rsta.2005.1678.

Ulrike G. K. Wegst, Hao Bai, Eduardo Saiz, Antoni P. Tomsia, and Robert O. Ritchie. Bioinspired structural materials. *Nature Materials*, 14:23, 2014. doi: 10.1038/nmat4089. URL https://doi.org/10.1038/nmat4089https://www.nature.com/articles/nmat4089.

T. J. Lu, L. Valdevit, and A. G. Evans. Active cooling by metallic sandwich structures with periodic cores. *Prog. Mater. Sci.*, (50):789–815, 2005.

J. Tian, T. J. Lu, H. P. Hodson, D. T. Queheillalt, and H. N. G. Wadley. Cross flow heat exchange of textile cellular metal core sandwich panels. *Int. J. Heat Mass Transf.*, (50):2521–2536, 2007.

A. G. Evans, M. Y. He, V. S. Deshpande, J. W. Hutchinson, A. J. Jacobsen, and W. B. Carter. Concepts for enhanced energy absorption using hollow micro-lattices. *Int. J. Impact Eng.*, (37):947–959, 2010.

Zhuang Li and Malcolm J. Crocker. Effects of thickness and delamination on the damping in honeycomb–foam sandwich beams. *Journal of Sound and Vibration*, 294(3):473–485, June 2006. ISSN 0022-460X. doi: 10.1016/j.jsv.2005.11.024.

I. S. Golovin and H. R. Sinning. Damping in some cellular metallic materials. *Journal of Alloys and Compounds*, 355(1):2–9, June 2003. ISSN 0925-8388. doi: 10.1016/S0925-8388(03)00241-X.

António J. Salgado, Olga P. Coutinho, and Rui L. Reis. Bone Tissue Engineering: State of the Art and Future Trends. *Macromolecular Bioscience*, 4 (8):743–765, 2004. ISSN 1616-5195. doi: 10.1002/mabi.200400026. _eprint: https://onlinelibrary.wiley.com/doi/pdf/10.1002/mabi.200400026.

Qizhi Chen and George A. Thouas. Metallic implant biomaterials. *Materials Science and Engineering: R: Reports*, 87:1–57, January 2015. ISSN 0927-796X. doi: 10.1016/j.mser.2014.10.001.

F. Rengier, A. Mehndiratta, H. von Tengg-Kobligk, C. M. Zechmann, R. Unterhinninghofen, H.-U. Kauczor, and F. L. Giesel. 3D printing based on imaging data: Review of medical applications. *International Journal of Computer Assisted Radiology and Surgery*, 5(4):335–341, July 2010. ISSN 1861-6429. doi: 10.1007/s11548-010-0476-x.

W. Y. Yeong, C. K. Chua, K. F. Leong, and M. Chandrasekaran. Rapid prototyping in tissue engineering: challenges and potential. *Trends Biotechnol*, 22(12):643–52, 2004. ISSN 0167-7799 (Print) 0167-7799 (Linking). doi: 10.1016/j.tibtech.2004.10.004. URL https://www.ncbi.nlm.nih.gov/pubmed/15542155.

Antonios G Mikos, Amy J Thorsen, Lisa A Czerwonka, Yuan Bao, Robert Langer, Douglas N Winslow, and Joseph P Vacanti. Preparation and characterization of poly(l-lactic acid) foams. *Polymer*, 35(5):1068–1077, March 1994. ISSN 0032-3861. doi: 10.1016/0032-3861(94)90953-9.

David J. Mooney, Daniel F. Baldwin, Nam P. Suh, Joseph P. Vacanti, and Robert Langer. Novel approach to fabricate porous sponges of poly(d,l-lactic-co-glycolic acid) without the use of organic solvents. *Biomaterials*, 17(14):1417–1422, July 1996. ISSN 0142-9612. doi: 10.1016/0142-9612(96)87284-X.

Lisa E. Freed, Gordana Vunjak-Novakovic, Robert J. Biron, Dana B. Eagles, Daniel C. Lesnoy, Sandra K. Barlow, and Robert Langer. Biodegradable Polymer Scaffolds for Tissue Engineering. *Bio/Technology*, 12(7):689–693, July 1994. ISSN 1546-1696. doi: 10.1038/nbt0794-689.

H. Lo, M. S. Ponticiello, and K. W. Leong. Fabrication of controlled release biodegradable foams by phase separation. *Tissue Engineering*, 1(1):15–28, 1995. ISSN 1076-3279. doi: 10.1089/ten.1995.1.15.

R. C. Thomson, M. J. Yaszemski, J. M. Powers, and A. G. Mikos. Fabrication of biodegradable polymer scaffolds to engineer trabecular bone. *Journal of Biomaterials Science. Polymer Edition*, 7(1):23–38, 1995. ISSN 0920-5063. doi: 10.1163/156856295x00805.

K. Whang, C. H. Thomas, K. E. Healy, and G. Nuber. A novel method to fabricate bioabsorbable scaffolds. *Polymer*, 36(4):837–842, January 1995. ISSN 0032-3861. doi: 10.1016/0032-3861(95)93115-3.

Y. Y. Hsu, J. D. Gresser, D. J. Trantolo, C. M. Lyons, P. R. Gangadharam, and D. L. Wise. Effect of polymer foam morphology and density on kinetics of in vitro controlled release of isoniazid from compressed foam matrices. *Journal of Biomedical Materials Research*, 35(1):107–116, April 1997. ISSN 0021-9304. doi: 10.1002/(sici)1097-4636(199704)35:1<107::aid-jbm11>3.0.co;2-g.

Li Yuan, Songlin Ding, and Cuie Wen. Additive manufacturing technology for porous metal implant applications and triple minimal surface structures: A review. *Bioactive Materials*, 4:56–70, December 2019. ISSN 2452-199X. doi: 10.1016/j.bioactmat.2018.12.003.

Y. Chen, J. E. Frith, A. Dehghan-Manshadi, H. Attar, D. Kent, N. D. M. Soro, M. J. Bermingham, and M. S. Dargusch. Mechanical properties and biocompatibility of porous titanium scaffolds for bone tissue engineering. *J Mech Behav Biomed Mater*, 75:169–174, 2017. ISSN 1878-0180 (Electronic) 1878-0180 (Linking). doi: 10.1016/j.jmbbm.2017.07.015. URL https://www.ncbi.nlm.nih.gov/pubmed/28734258.

Y. W. Gu, M. S. Yong, B. Y. Tay, and C. S. Lim. Synthesis and bioactivity of porous ti alloy prepared by foaming with tih2. *Materials Science and Engineering: C*, 29(5):1515–1520, 2009. ISSN 09284931. doi: 10.1016/j.msec.2008.11.003.

M. Bram, C. Stiller, H. P. Buchkremer, D. Stöver, and H. Baur. High-porosity titanium, stainless steel, and superalloy parts. *Advanced Engineering Materials*, 2(4):196–199, 2000. ISSN 1438-1656. doi: 10.1002/(SICI)1527-2648(200004)2:4<196::AID-ADEM196>3.0.CO;2-K. URL https://doi.org/10.1002/(SICI)1527-2648(200004)2:4<196::AID-ADEM196>3.0.CO;2-K.

A. Maiti, W. Small, J. P. Lewicki, T. H. Weisgraber, E. B. Duoss, S. C. Chinn, M. A. Pearson, C. M. Spadaccini, R. S. Maxwell, and T. S. Wilson. 3D printed cellular solid outperforms traditional stochastic foam in long-term mechanical response. *Scientific Reports*, 6(1):1–9, April 2016. ISSN 2045-2322. doi: 10.1038/srep24871.

Gibson L. J., Ashby M. F., Schajer G. S., Robertson C. I. . The mechanics of two-dimensional cellular materials. *Proc. R. Soc. Lond. A*, 382:25 – 42, 1982. doi: https://doi.org/10.1098/rspa.1982.0087.

Gibson I. J., Ashby M. F. The mechanics of three-dimensional cellular materials. *Proc. R. Soc. Lond. A*, 382:43 – 59, 1982. doi: https://doi.org/10.1098/rspa.1982.0088.

A. G. Evans, J. W. Hutchinson, and M. F. Ashby. Multifunctionality of cellular metal systems. *Prog. Mater. Sci.*, (43):171–221, 1999.

H. B. G. Wadley, N. A. Fleck, and A. G. Evans. Fabrication and structural performance of periodic cellular metal sandwich structures. *Compos. Sci. Technol.*, (63):2331–2343, 2003.

M. Alkhader and M. Vural. *Effect of Microstructure in Cellular Solids: Bending vs. Stretch Dominated Topologies*. Ieee, New York, 2007. ISBN 978-1-4244-1056-9. doi: 10.1109/RAST.2007.4283965. Pages: 136-+ Publication Title: 2007 3rd International Conference on Recent Advances in Space Technologies, Vols 1 and 2 WOS:000250805000030.

M. G. Rashed, Mahmud Ashraf, R. A. W. Mines, and Paul J. Hazell. Metallic microlattice materials: A current state of the art on manufacturing, mechanical properties and applications. *Materials & Design*, 95:518–533, 2016. ISSN 02641275. doi: 10.1016/j.matdes.2016.01.146.

Tobias Maconachie, Martin Leary, Bill Lozanovski, Xuezhe Zhang, Ma Qian, Omar Faruque, and Milan Brandt. Slm lattice structures: Properties, performance, applications and challenges. *Materials & Design*, 183:108137, 2019. ISSN 0264-1275. doi: https://doi.org/10.1016/j.matdes.2019.108137. URL http://www.sciencedirect.com/science/article/pii/S0264127519305751.

G. Ryan, A. Pandit, and D. P. Apatsidis. Fabrication methods of porous metals for use in orthopaedic applications. *Biomaterials*, 27(13):2651–70, 2006. ISSN 0142-9612 (Print) 0142-9612 (Linking). doi: 10.1016/j.biomaterials.2005.12.002. URL https://www.ncbi.nlm.nih.gov/pubmed/16423390.

B.M. M Tymrak, M. Kreiger, and J M Pearce. Mechanical properties of components fabricated with open-source 3-D printers under realistic environmental conditions. *Materials and Design*, 58:242–246, June 2014. doi: 10.1016/j.matdes.2014.02.038.

Russell A. Giordano, Benjamin M. Wu, Scott W. Borland, Linda G. Cima, Emanuel M. Sachs, and Michael J. Cima. Mechanical properties of dense polylactic acid structures fabricated by three dimensional printing. *Journal of Biomaterials Science, Polymer Edition*, 8(1):63–75, January 1997. ISSN 0920-5063. doi: 10.1163/156856297X00588. _eprint: https://doi.org/10.1163/156856297X00588.

J. E. Smay, J. Cesarano, and J. A. Lewis. Colloidal inks for directed assembly of 3-D periodic structures. *Langmuir*, 18(14):5429–5437, July 2002. ISSN 0743-7463. doi: 10.1021/la0257135. WOS:000176627000018.

E. Cuan-Urquizo. *Mechanical properties of woodpile lattice materials fabricated using additive manufacturing*. PhD thesis, University of Southampton, 2016.

E Cuan-Urquizo, S Yang, and A Bhaskar. Mechanical characterisation of additively manufactured material having lattice microstructure. *IOP Conference Series: Materials Science and Engineering*, 74:012004, February 2015. ISSN 1757-8981. doi: 10.1088/1757-899x/74/1/012004.

O. Cansizoglu, O. Harrysson, D. Cormier, H. West, and T. Mahale. Properties of ti–6al–4v non-stochastic lattice structures fabricated via electron beam melting. *Materials Science and Engineering: A*, 492(1-2):468–474, 2008. ISSN 09215093. doi: 10.1016/j.msea.2008.04.002.

J. Harbusch-Hecking and A. Öchsner. Simulating the mechanical properties of three-dimensional printed artificial bone scaffolds. *Materialwissenschaft und Werkstofftechnik*, 47(5-6):549–563, 2016. ISSN 1521-4052. doi: 10.1002/mawe.201600531. _eprint: https://onlinelibrary.wiley.com/doi/pdf/10.1002/mawe.201600531.

V. S. Deshpande, M. F. Ashby, and N. A. Fleck. Foam topology: bending versus stretching dominated architectures. *Acta Mater.*, (49):1035–1040, 2001b.

Xiaoyu Zheng, Howon Lee, Todd H. Weisgraber, Maxim Shusteff, Joshua DeOtte, Eric B. Duoss, Joshua D. Kuntz, Monika M. Biener, Qi Ge, Julie A. Jackson, Sergei O. Kucheyev, Nicholas X. Fang, and Christopher M. Spadaccini. Ultralight, ultrastiff mechanical metamaterials. *Science*, 344(6190):1373–1377, June 2014. ISSN 0036-8075, 1095-9203. doi: 10.1126/science.1252291.

X. P. Tan, Y. J. Tan, C. S. L. Chow, S. B. Tor, and W. Y. Yeong. Metallic powder-bed based 3d printing of cellular scaffolds for orthopaedic implants: A state-of-the-art review on manufacturing, topological design, mechanical properties and biocompatibility. *Mater Sci Eng C Mater Biol Appl*, 76:1328–1343, 2017. ISSN 1873-0191 (Electronic) 0928-4931 (Linking). doi: 10.1016/j.msec.2017.02.094. URL https://www.ncbi.nlm.nih.gov/pubmed/28482501.

D. F. Sievenpiper, M. E. Sickmiller, and E. Yablonovitch. 3d wire mesh photonic crystals. *Phys. Rev. Lett.*, (76):2480–2483, 1996.

J. Christensen, M. Kadic, O. Kraft, and M. Wegener. Vibrant times for mechanical materials. *MRS Commun.*, (5):453–462, 2015.

Nejc Novak, Matej Vesenjak, and Zoran Ren. Auxetic cellular materials - a review. *Strojniški vestnik – Journal of Mechanical Engineering*, 62(9):485–493, 2016. ISSN 00392480. doi: 10.5545/sv-jme.2016.3656.

K.E. Evans and A. Alderson. Auxetic materials: Functional materials and structures from lateral thinking. *Advanced Materials*, 12(9):617–628, 2000.

Xiao Kuang, Devin J. Roach, Jiangtao Wu, Craig M. Hamel, Zhen Ding, Tiejun Wang, Martin L. Dunn, and Hang Jerry Qi. Advances in 4D Printing: Materials and Applications. *Advanced Functional Materials*, 29(2): 1805290, 2019. ISSN 1616-3028. doi: 10.1002/adfm.201805290. _eprint: https://onlinelibrary.wiley.com/doi/pdf/10.1002/adfm.201805290.

Kamran Shah, Izhar ul Haq, Ashfaq Khan, Shaukat Ali Shah, Mushtaq Khan, and Andrew J. Pinkerton. Parametric study of development of inconel-steel functionally graded materials by laser direct metal deposition. *Materials & Design (1980-2015)*, 54:531–538, 2014. ISSN 02613069. doi: 10.1016/j.matdes.2013.08.079.

Ankit Gupta and Mohammad Talha. Recent development in modeling and analysis of functionally graded materials and structures. *Progress in Aerospace Sciences*, 79:1–14, 2015. ISSN 03760421. doi: 10.1016/j.paerosci.2015.07.001.

A. Sola, D. Bellucci, and V. Cannillo. Functionally graded materials for orthopedic applications - an update on design and manufacturing. *Biotechnol Adv*, 34(5):504–31,

2016a. ISSN 1873-1899 (Electronic) 0734-9750 (Linking). doi: 10.1016/j.biotechadv.2015.12.013. URL https://www.ncbi.nlm.nih.gov/pubmed/26757264.

W. Pompe, H. Worch, M. Epple, W. Friess, M. Gelinsky, P. Greil, U. Hempel, D. Scharnweber, and K. Schulte. Functionally graded materials for biomedical applications. *Materials Science and Engineering: A*, 362(1-2):40–60, 2003. ISSN 09215093. doi: 10.1016/s0921-5093(03)00580-x.

T. B. F. Woodfield, C. A. Van Blitterswijk, J. De Wijn, T. J. Sims, A. P. Hollander, and J. Riesle. Polymer scaffolds fabricated with pore-size gradients as a model for studying the zonal organization within tissue-engineered cartilage constructs. *Tissue Engineering*, 11(9-10):1297–1311, 2005a. ISSN 1076-3279. doi: 10.1089/ten.2005.11.1297. URL <GotoISI>://WOS:000233347300002.

Milind Singh, Nathan Dormer, Jean R. Salash, Jordan M. Christian, David S. Moore, Cory Berkland, and Michael S. Detamore. Three-dimensional macroscopic scaffolds with a gradient in stiffness for functional regeneration of interfacial tissues. *Journal of biomedical materials research. Part A*, 94(3):870–876, 2010. ISSN 1552-4965 1549-3296. doi: 10.1002/jbm.a.32765. URL https://www.ncbi.nlm.nih.gov/pubmed/20336753https://www.ncbi.nlm.nih.gov/pmc/PMC2926291/.

B. Edenhofer, D. Joritz, M. Rink, and K. Voges. 13 - Carburizing of steels. In Eric J. Mittemeijer and Marcel A. J. Somers, editors, *Thermochemical Surface Engineering of Steels*, pages 485–553. Woodhead Publishing, Oxford, January 2015. ISBN 978-0-85709-592-3. doi: 10.1533/9780857096524.3.485.

B. Kieback, A. Neubrand, and H. Riedel. Processing techniques for functionally graded materials. *Materials Science and Engineering: A*, 362(1-2):81–106, 2003. ISSN 09215093. doi: 10.1016/s0921-5093(03)00578-1.

J. Werner, B. Linner-Krcmar, W. Friess, and P. Greil. Mechanical properties and in vitro cell compatibility of hydroxyapatite ceramics with graded pore structure. *Biomaterials*, 23(21):4285–4294, 2002. ISSN 0142-9612. doi: 10.1016/s0142-9612(02)00191-6. URL <GotoISI>://WOS:000177451800013.

A. Tampieri, G. Celotti, S. Sprio, A. Delcogliano, and S. Franzese. Porosity-graded hydroxyapatite ceramics to replace natural bone. *Biomaterials*, 22(11):1365–1370, 2001. ISSN 0142-9612. doi: 10.1016/s0142-9612(00)00290-8. URL <GotoISI>://WOS:000168325200019.

J. Zeschky, T. Hofner, C. Arnold, R. Weissmann, D. Bahloul-Hourlier, M. Scheffler, and P. Greil. Polysilsesquioxane derived ceramic foams with gradient porosity. *Acta Materialia*, 53(4):927–937, 2005. ISSN 1359-6454. doi: 10.1016/j.actamat.2004.10.039. URL <GotoISI>://WOS:000226774500004.

B. A. Harley, A. Z. Hastings, I. V. Yannas, and A. Sannino. Fabricating tubular scaffolds with a radial pore size gradient by a spinning technique. *Biomaterials*, 27(6):866–874, 2006. ISSN 0142-9612. doi: 10.1016/j.biomaterials.2005.07.012. URL <GotoISI>://WOS:000234095800007.

Yoshimi Watanabe, Yoshifumi Inaguma, Hisashi Sato, and Eri Miura-Fujiwara. A novel fabrication method for functionally graded materials under centrifugal force: The centrifugal mixed-powder method. *Materials*, 2(4):2510–2525, 2009. ISSN 1996-1944. doi: 10.3390/ma2042510.

A. Sola, D. Bellucci, and V. Cannillo. Functionally graded materials for orthopedic applications - an update on design and manufacturing. *Biotechnol Adv*, 34(5):504–31, 2016b. ISSN 1873-1899 (Electronic) 0734-9750 (Linking). doi: 10.1016/j.biotechadv.2015.12.013. URL https://www.ncbi.nlm.nih.gov/pubmed/26757264.

J. K. Sherwood, S. L. Riley, R. Palazzolo, S. C. Brown, D. C. Monkhouse, M. Coates, L. G. Griffith, L. K. Landeen, and A. Ratcliffe. A three-dimensional osteochondral composite scaffold for articular cartilage repair. *Biomaterials*, 23(24):4739–4751, 2002. ISSN 0142-9612. doi: 10.1016/s0142-9612(02)00223-5. URL <GotoISI>://WOS:000178414900006.

S. J. Kalita, S. Bose, H. L. Hosick, and A. Bandyopadhyay. Development of controlled porosity polymer-ceramic composite scaffolds via fused deposition modeling. *Materials Science & Engineering C-Biomimetic and Supramolecular Systems*, 23(5):611–620, 2003. ISSN 0928-4931. doi: 10.1016/s0928-4931(03)00052-3. URL <GotoISI>://WOS:000185869400008.

T. B. F. Woodfield, J. Malda, J. de Wijn, F. Peters, J. Riesle, and C. A. van Blitterswijk. Design of porous scaffolds for cartilage tissue engineering using a three-dimensional fiber-deposition technique. *Biomaterials*, 25(18):4149–4161, 2004. ISSN 0142-9612. doi: 10.1016/j.biomaterials.2003.10.056. URL <GotoISI>://WOS:000220945400023.

T. B. F. Woodfield, C. A. Van Blitterswijk, J. De Wijn, T. J. Sims, A. P. Hollander, and J. Riesle. Polymer scaffolds fabricated with pore-size gradients as a model for studying the zonal organization within tissue-engineered cartilage constructs. *Tissue Engineering*, 11(9-10):1297–1311, 2005b. ISSN 1076-3279. doi: 10.1089/ten.2005.11.1297. URL <GotoISI>://WOS:000233347300002.

3DPrintingIndustry. The Free Beginner's Guide - 3D Printing Industry. https://3dprintingindustry.com/3d-printing-basics-free-beginners-guide#04-processes.

Markforged. Introduction to 3D Printing | Markforged. https://markforged.com/learn/3d-printing-introduction/.

3DHubs. Introduction to FDM 3D printing. https://www.3dhubs.com/knowledge-base/introduction-fdm-3d-printing/.

Lai-Chang Zhang and Liang-Yu Chen. A Review on Biomedical Titanium Alloys: Recent Progress and Prospect. *Advanced Engineering Materials*, 21(4): 1801215, 2019. ISSN 1527-2648. doi: 10.1002/adem.201801215. _eprint: https://onlinelibrary.wiley.com/doi/pdf/10.1002/adem.201801215.

Brian N. Turner, Robert Strong, and Scott A. Gold. A review of melt extrusion additive manufacturing processes: I. process design and modeling. *Rapid Prototyping Journal*, 20(3):192–204, 2014. ISSN 1355-2546. doi: 10.1108/rpj-01-2013-0012.

János Plocher and Ajit Panesar. Mechanical Performance of Additively Manufactured Fiber-Reinforced Functionally Graded Lattices. *JOM*, 72(3):1292–1298, March 2020. ISSN 1543-1851. doi: 10.1007/s11837-019-03961-3.

Manuela Galati and Paolo Minetola. Analysis of Density, Roughness, and Accuracy of the Atomic Diffusion Additive Manufacturing (ADAM) Process for Metal Parts. *Materials*, 12(24):4122, January 2019. doi: 10.3390/ma12244122.

T. J. Horn and O. L. Harrysson. Overview of current additive manufacturing technologies and selected applications. *Sci Prog*, 95(Pt 3):255–82, 2012. ISSN 0036-8504 (Print) 0036-8504.

H. Sahasrabudhe, S. Bose, and A. Bandyopadhyay. Chapter 17 - Laser-Based Additive Manufacturing Processes. In Jonathan Lawrence, editor, *Advances in Laser Materials Processing (Second Edition)*, Woodhead Publishing Series in Welding and Other Joining Technologies, pages 507–539. Woodhead Publishing, January 2018. ISBN 978-0-08-101252-9. doi: 10.1016/B978-0-08-101252-9.00017-0.

S. M. Ahmadi, R. Hedayati, R. K. Ashok Kumar Jain, Y. Li, S. Leeflang, and A. A. Zadpoor. Effects of laser processing parameters on the mechanical properties, topology, and microstructure of additively manufactured porous metallic biomaterials: A vector-based approach. *Materials & Design*, 134:234–243, 2017. ISSN 0264-1275. doi: https://doi.org/10.1016/j.matdes.2017.08.046. URL http://www.sciencedirect.com/science/article/pii/S0264127517307980.

Ferry P. W. Melchels, Jan Feijen, and Dirk W. Grijpma. A review on stereolithography and its applications in biomedical engineering. *Biomaterials*, 31(24):6121–6130, August 2010. ISSN 0142-9612. doi: 10.1016/j.biomaterials.2010.04.050.

P.F. Jacobs, D.T. Reid, Computer, and Automated Systems Association of SME. *Rapid Prototyping & Manufacturing: Fundamentals of Stereolithography*. Society of Manufacturing Engineers, 1992. ISBN 9780872634251. URL https://books.google.co.uk/books?id=HvcN0w1VyxwC.

A. J. Jacobsen, W. Barvosa-Carter, and S. Nutt. Micro-scale truss structures formed from self-propagating photopolymer waveguides. *Advanced Materials*, 19(22):3892–+, 2007. ISSN 0935-9648. doi: 10.1002/adma.200700797. URL <GotoISI>://WOS:000251383900023.

J. R. Tumbleston, D. Shirvanyants, N. Ermoshkin, R. Janusziewicz, A. R. Johnson, D. Kelly, K. Chen, R. Pinschmidt, J. P. Rolland, A. Ermoshkin, E. T. Samulski, and J. M. DeSimone. Continuous liquid interface production of 3d objects. *Science*, 347(6228):1349–1352, 2015. ISSN 0036-8075. doi: 10.1126/science.aaa2397. URL <GotoISI>://WOS:000351219600038.

Nanoscribe GmbH. 3D printing on the micrometer scale. http://www.nanoscribe.de/en/, 2007. Accessed: 12-02-2017.

Alessandro Maggi, Jessica Allen, Tejal Desai, and Julia R. Greer. Osteogenic cell functionality on 3-dimensional nano-scaffolds with varying stiffness. *Extreme Mechanics Letters*, 13:1–9, 2017. ISSN 2352-4316. doi: http://dx.doi.org/10.1016/j.eml.2017.01.002. URL //www.sciencedirect.com/science/article/pii/S2352431616302097http://ac.els-cdn.com/S2352431616302097/1-s2.0-S2352431616302097-main.pdf?_tid=806daa02-e3b7-11e6-976d-00000aab0f02&acdnat=1485428975_fff8bab5b7c9c72d5ecee09eb4656476.

N. Cubo, M. Garcia, J. F. del Canizo, D. Velasco, and J. L. Jorcano. 3d bioprinting of functional human skin: production and in vivo analysis. *Biofabrication*, 9(1):12, 2017. ISSN 1758-5082. doi: 10.1088/1758-5090/9/1/015006. URL <GotoISI>://WOS:000390344900004http://iopscience.iop.org/article/10.1088/1758-5090/9/1/015006/pdf.

Ying Wang, Ranjith Kumar Kankala, Kai Zhu, Shi-Bin Wang, Yu Shrike Zhang, and Ai-Zheng Chen. Coaxial Extrusion of Tubular Tissue Constructs Using a Gelatin/GelMA Blend Bioink. *ACS Biomaterials Science & Engineering*, 5(10):5514–5524, October 2019. doi: 10.1021/acsbiomaterials.9b00926.

Xiao Liu, Sarah-Sophia D. Carter, Max Jurie Renes, Juewan Kim, Darling Macarena Rojas-Canales, Daniella Penko, Cameron Angus, Stephen Beirne, Christopher John Drogemuller, Zhilian Yue, Patrick T. Coates, and Gordon G. Wallace. Development of a Coaxial 3D Printing Platform for Biofabrication of Implantable Islet-Containing Constructs. *Advanced Healthcare Materials*, 8(7):1801181, April 2019. ISSN 2192-2640. doi: 10.1002/adhm.201801181. WOS:000467973400008.

J. Deckers, J. Vleugels, and J. P. Kruthl. Additive manufacturing of ceramics: A review. *Journal of Ceramic Science and Technology*, 5(4):245–260, 2014. ISSN 2190-9385. doi: 10.4416/jcst2014-00032. URL <GotoISI>://WOS:000347265400001.

Andrea Zocca, Paolo Colombo, Cynthia M. Gomes, and Jens Günster. Additive manufacturing of ceramics: Issues, potentialities, and opportunities. *Journal of the American*

*Ceramic Society*, 98(7):1983–2001, 2015. ISSN 1551-2916. doi: 10.1111/jace.13700. URL http://dx.doi.org/10.1111/jace.13700.

Yee Ling Yap, Chengcheng Wang, Swee Leong Sing, Vishwesh Dikshit, Wai Yee Yeong, and Jun Wei. Material jetting additive manufacturing: An experimental study using designed metrological benchmarks. *Precision Engineering*, 50:275–285, October 2017. ISSN 01416359. doi: 10.1016/j.precisioneng.2017.05.015.

Jamison Go, Scott N. Schiffres, Adam G. Stevens, and A. John Hart. Rate limits of additive manufacturing by fused filament fabrication and guidelines for high-throughput system design. *Additive Manufacturing*, 16:1–11, 2017. ISSN 2214-8604. doi: https://doi.org/10.1016/j.addma.2017.03.007. URL http://www.sciencedirect.com/science/article/pii/S2214860416302834.

All3DP. 3d print stringing: 5 easy ways to prevent it. https://all3dp.com/2/3d-print-stringing-easy-ways-to-prevent-it/. Accessed: 29-01-2021.

Scott A. Gold and Brian N. Turner. A review of melt extrusion additive manufacturing processes: Ii. materials, dimensional accuracy, and surface roughness. *Rapid Prototyping Journal*, 21(3):250–261, 2015. ISSN 1355-2546. doi: 10.1108/RPJ-02-2013-0017. URL https://doi.org/10.1108/RPJ-02-2013-0017.

R. J. Shipley, G. W. Jones, R. J. Dyson, B. G. Sengers, C. L. Bailey, C. J. Catt, C. P. Please, and J. Malda. Design criteria for a printed tissue engineering construct: A mathematical homogenization approach. *Journal of Theoretical Biology*, 259(3):489–502, 2009. ISSN 0022-5193. doi: https://doi.org/10.1016/j.jtbi.2009.03.037. URL http://www.sciencedirect.com/science/article/pii/S002251930900143X.

J. Wu, N. Aage, R. Westermann, and O. Sigmund. Infill optimization for additive manufacturing—approaching bone-like porous structures. *IEEE Transactions on Visualization and Computer Graphics*, 24(2):1127–1140, 2018. ISSN 1077-2626. doi: 10.1109/TVCG.2017.2655523.

C. Schumacher, B. Bickel, J. Rys, S. Marschner, C. Daraio, and M. Gross. Microstructures to control elasticity in 3d printing. *ACM Trans. Graph.*, 34(4):1–13, 2015. ISSN 0730-0301. doi: 10.1145/2766926.

Bastian Brenken, Eduardo Barocio, Anthony Favaloro, Vlastimil Kunc, and R. Byron Pipes. Fused filament fabrication of fiber-reinforced polymers: A review. *Additive Manufacturing*, 21:1–16, May 2018. ISSN 2214-8604. doi: 10.1016/j.addma.2018.01.002.

Silvan Gantenbein, Kunal Masania, Wilhelm Woigk, Jens P. W. Sesseg, Theo A. Tervoort, and André R. Studart. Three-dimensional printing of hierarchical liquid-crystal-polymer structures. *Nature*, 561(7722):226–230, 2018. ISSN 1476-4687. doi: 10.1038/

s41586-018-0474-7. URL https://doi.org/10.1038/s41586-018-0474-7https://www.nature.com/articles/s41586-018-0474-7.pdf.

L. Moroni, J. R. de Wijn, and C. A. van Blitterswijk. Three-dimensional fiber-deposited peot/pbt copolymer scaffolds for tissue engineering: Influence of porosity, molecular network mesh size, and swelling in aqueous media on dynamic mechanical properties. *Journal of Biomedical Materials Research Part A*, 75A(4):957–965, 2005. doi: doi: 10.1002/jbm.a.30499. URL https://onlinelibrary.wiley.com/doi/abs/10.1002/jbm.a.30499.

William Bonfield. Designing porous scaffolds for tissue engineering. *Philosophical Transactions of the Royal Society A: Mathematical, Physical and Engineering Sciences*, 364 (1838):227–232, January 2006. doi: 10.1098/rsta.2005.1692.

Sam L. Francis, Claudia Di Bella, Gordon G. Wallace, and Peter F. M. Choong. Cartilage Tissue Engineering Using Stem Cells and Bioprinting Technology-Barriers to Clinical Translation. *Frontiers in Surgery*, 5:70, 2018. ISSN 2296-875X. doi: 10.3389/fsurg.2018.00070.

Frederic Gilbert, Cathal D. O'Connell, Tajanka Mladenovska, and Susan Dodds. Print Me an Organ? Ethical and Regulatory Issues Emerging from 3D Bioprinting in Medicine. *Science and Engineering Ethics*, 24(1):73–91, February 2018. ISSN 1471-5546. doi: 10.1007/s11948-017-9874-6.

Francoise Marga, Adrian Neagu, Ioan Kosztin, and Gabor Forgacs. Developmental biology and tissue engineering. *Birth Defects Research Part C: Embryo Today: Reviews*, 81(4):320–328, 2007. ISSN 1542-9768. doi: 10.1002/bdrc.20109. _eprint: https://onlinelibrary.wiley.com/doi/pdf/10.1002/bdrc.20109.

M. S. Steinberg. Reconstruction of tissues by dissociated cells. Some morphogenetic tissue movements and the sorting out of embryonic cells may have a common explanation. *Science (New York, N.Y.)*, 141(3579):401–408, August 1963. ISSN 0036-8075. doi: 10.1126/science.141.3579.401.

Dietmar W. Hutmacher. *Scaffolds in tissue engineering bone and cartilage*, pages 175–189. Elsevier Science, Oxford, 2000b. ISBN 978-0-08-045154-1. doi: https://doi.org/10.1016/B978-008045154-1.50021-6. URL http://www.sciencedirect.com/science/article/pii/B9780080451541500216.

S. J. Simske, R. A. Ayers, and T. A. Bateman. Porous Materials for Bone Engineering. /MSF.250.151, 1997. ISSN 1662-9752. Conference Name: Porous Materials for Tissue Engineering Library Catalog: www.scientific.net Pages: 151-182.

Anh-Vu Do, Rasheid Smith, Timothy M. Acri, Sean M. Geary, and Aliasger K. Salem. 9 - 3D printing technologies for 3D scaffold engineering. In Ying Deng and Jordan Kuiper,

editors, *Functional 3D Tissue Engineering Scaffolds*, pages 203–234. Woodhead Publishing, January 2018. ISBN 978-0-08-100979-6. doi: 10.1016/B978-0-08-100979-6.00009-4.

R. P. del Real, J. G. C. Wolke, M. Vallet-Regi, and J. A. Jansen. A new method to produce macropores in calcium phosphate cements. *Biomaterials*, 23(17):3673–3680, 2002. ISSN 0142-9612. doi: https://doi.org/10.1016/S0142-9612(02)00101-1. URL http://www.sciencedirect.com/science/article/pii/S0142961202001011.

P. Weimin, L. Dan, W. Yiyong, H. Yunyu, and Z. Li. Tendon-to-bone healing using an injectable calcium phosphate cement combined with bone xenograft/bmp composite. *Biomaterials*, 34(38):9926–36, 2013. ISSN 1878-5905 (Electronic) 0142-9612 (Linking). doi: 10.1016/j.biomaterials.2013.09.018. URL https://www.ncbi.nlm.nih.gov/pubmed/24075477.

Adnan Haider, Sajjad Haider, Madhusudana Rao Kummara, Tahseen Kamal, Abdul-Aziz A Alghyamah, Faiza Jan Iftikhar, Bushra Bano, Naeem Khan, Mohammad Amjid Afridi, Sung Soo Han, Ali Alrahlah, and Rawaiz Khan. Advances in the scaffolds fabrication techniques using biocompatible polymers and their biomedical application: A technical and statistical review. *Journal of Saudi Chemical Society*, 24(2):186–215, February 2020. ISSN 1319-6103. doi: 10.1016/j.jscs.2020.01.002.

Bin Duan, Min Wang, Wen You Zhou, Wai Lam Cheung, Zhao Yang Li, and William W. Lu. Three-dimensional nanocomposite scaffolds fabricated via selective laser sintering for bone tissue engineering. *Acta Biomaterialia*, 6(12):4495–4505, December 2010. ISSN 1742-7061. doi: 10.1016/j.actbio.2010.06.024.

I. Zein, D. W. Hutmacher, K. C. Tan, and S. H. Teoh. Fused deposition modeling of novel scaffold architectures for tissue engineering applications. *Biomaterials*, 23(4):1169–85, 2002. ISSN 0142-9612 (Print) 0142-9612.

Wei Long Ng, Chee Kai Chua, and Yu-Fang Shen. Print Me An Organ! Why We Are Not There Yet. *Progress in Polymer Science*, 97:101145, October 2019. ISSN 0079-6700. doi: 10.1016/j.progpolymsci.2019.101145.

Yang Cui, Yi Liu, Yi Cui, Xiabin Jing, Peibiao Zhang, and Xuesi Chen. The nanocomposite scaffold of poly(lactide-co-glycolide) and hydroxyapatite surface-grafted with l-lactic acid oligomer for bone repair. *Acta Biomaterialia*, 5(7):2680–2692, 2009. ISSN 1742-7061. doi: http://dx.doi.org/10.1016/j.actbio.2009.03.024. URL //www.sciencedirect.com/science/article/pii/S1742706109001172.

Qiang Fu, Eduardo Saiz, Mohamed N. Rahaman, and Antoni P. Tomsia. Bioactive glass scaffolds for bone tissue engineering: state of the art and future perspectives. *Materials Science and Engineering: C*, 31(7):1245–1256, 2011. ISSN 0928-4931. doi: http://dx.doi.org/10.1016/j.msec.2011.04.022. URL //www.sciencedirect.com/science/article/pii/S0928493111001275.

S. F. Hulbert, F. A. Young, R. S. Mathews, J. J. Klawitter, C. D. Talbert, and F. H. Stelling. Potential of ceramic materials as permanently implantable skeletal prostheses. *Journal of Biomedical Materials Research*, 4(3):433–456, 1970. ISSN 1097-4636. doi: 10.1002/jbm.820040309. URL http://dx.doi.org/10.1002/jbm.820040309.

A. J. W. Johnson and B. A. Herschler. A review of the mechanical behavior of cap and cap/polymer composites for applications in bone replacement and repair. *Acta Biomaterialia*, 7(1):16–30, 2011. ISSN 1742-7061. doi: 10.1016/j.actbio.2010.07.012. URL <GotoISI>://WOS:000284795300002.

Vassilis Karageorgiou and David Kaplan. Porosity of 3d biomaterial scaffolds and osteogenesis. *Biomaterials*, 26(27):5474–5491, 2005. ISSN 0142-9612. doi: http://dx.doi.org/10.1016/j.biomaterials.2005.02.002. URL //www.sciencedirect.com/science/article/pii/S0142961205001511.

K. A. Hing, B. Annaz, S. Saeed, P. A. Revell, and T. Buckland. Microporosity enhances bioactivity of synthetic bone graft substitutes. *J Mater Sci Mater Med*, 16(5):467–75, 2005. ISSN 0957-4530 (Print) 0957-4530. doi: 10.1007/s10856-005-6988-1.

Jan Genzer. Templating surfaces with gradient assemblies. *The Journal of Adhesion*, 81 (3-4):417–435, 2005. ISSN 0021-8464. doi: 10.1080/00218460590944855. URL https://doi.org/10.1080/00218460590944855.

Cécile M. Bidan, Krishna P. Kommareddy, Monika Rumpler, Philip Kollmannsberger, Peter Fratzl, and John W. C. Dunlop. Geometry as a factor for tissue growth: Towards shape optimization of tissue engineering scaffolds. *Advanced Healthcare Materials*, 2 (1):186–194, 2013. doi: doi:10.1002/adhm.201200159. URL https://onlinelibrary.wiley.com/doi/abs/10.1002/adhm.201200159.

T. C. Lim, K. S. Chian, and K. F. Leong. Cryogenic prototyping of chitosan scaffolds with controlled micro and macro architecture and their effect on in vivo neo-vascularization and cellular infiltration. *J Biomed Mater Res A*, 94(4):1303–11, 2010. ISSN 1552-4965 (Electronic) 1549-3296 (Linking). doi: 10.1002/jbm.a.32747. URL https://www.ncbi.nlm.nih.gov/pubmed/20694998.

Amir A. Zadpoor. Bone tissue regeneration: the role of scaffold geometry. *Biomaterials Science*, 3(2):231–245, 2015. ISSN 2047-4830. doi: 10.1039/C4BM00291A. URL http://dx.doi.org/10.1039/C4BM00291A.

S. Nag and R. Banerjee. Fundamentals of medical implant materials. *ASM Handb.*, 6: 17, 2012. URL www.scopus.com.

Jae-Young Rho, T. Y. Tsui, and G. M. Pharr. Elastic properties of human cortical and trabecular lamellar bone measured by nanoindentation. *Biomaterials*, 18(20):1325–1330, 1997. ISSN 0142-9612. doi: http://dx.doi.org/10.1016/S0142-9612(97)00073-2. URL http://www.sciencedirect.com/science/article/pii/S0142961297000732.

D. L. Kopperdahl and T. M. Keaveny. Yield strain behavior of trabecular bone. *Journal of Biomechanics*, 31(7):601–608, 1998. ISSN 0021-9290. doi: http://dx.doi.org/10.1016/S0021-9290(98)00057-8. URL http://www.sciencedirect.com/science/article/pii/S0021929098000578.

M. I. Z. Ridzwan, S. Shuib, A. Y. Hassan, A. A. Shokri, and M. N. Mohammad Ibrahim. Problem of stress shielding and improvement to the hip implant designs: A review. *Journal of Medical Sciences*, 7(3): 460–467, 2007a. URL https://www.scopus.com/inward/record.uri?eid=2-s2.0-34249854037&partnerID=40&md5=5b1cfe53dd62a5f70360437afbeda74f.

R. Huiskes, H. Weinans, and B. van Rietbergen. The relationship between stress shielding and bone resorption around total hip stems and the effects of flexible materials. *Clin Orthop Relat Res*, (274):124–34, 1992. ISSN 0009-921X (Print) 0009-921x.

H. M. Frost. Wolff's law and bone's structural adaptations to mechanical usage: an overview for clinicians. *Angle Orthod*, 64(3):175–88, 1994. ISSN 0003-3219 (Print) 0003-3219. doi: 10.1043/0003-3219(1994)064<0175:wlabsa>2.0.co;2.

Mohamad Ridzwan, Solehuddin Shuib, Hassan A.Y, Amran Ahmed Shokri, and Mohamad Ibrahim. *Problem of Stress Shielding and Improvement to the Hip Implant Designs: A Review*, volume 7. Journal of Medical Sciences, 2007b. doi: 10.3923/jms.2007.460.467.

C. Mota, D. Puppi, F. Chiellini, and E. Chiellini. Additive manufacturing techniques for the production of tissue engineering constructs. *Journal of Tissue Engineering and Regenerative Medicine*, 9(3):174–190, 2015. ISSN 1932-6254. doi: 10.1002/term.1635. URL <GotoISI>://WOS:000351831900002.

S. L. Sing, J. An, W. Y. Yeong, and F. E. Wiria. Laser and electron-beam powder-bed additive manufacturing of metallic implants: A review on processes, materials and designs. *J Orthop Res*, 34(3):369–85, 2016. ISSN 1554-527X (Electronic) 0736-0266 (Linking). doi: 10.1002/jor.23075. URL https://www.ncbi.nlm.nih.gov/pubmed/26488900.

Dawei Li, Wenhe Liao, Ning Dai, Guoying Dong, Yunlong Tang, and Yi Min Xie. Optimal design and modeling of gyroid-based functionally graded cellular structures for additive manufacturing. *Computer-Aided Design*, 104:87–99, 2018. ISSN 0010-4485. doi: https://doi.org/10.1016/j.cad.2018.06.003. URL http://www.sciencedirect.com/science/article/pii/S0010448518300381.

Roberto Scaffaro, Andrea Maio, Emmanuel F. Gulino, and Giorgio D. M. Micale. PLA-based functionally graded laminates for tunable controlled release of carvacrol obtained by combining electrospinning with solvent casting. *Reactive and Functional Polymers*, 148:104490, March 2020. ISSN 1381-5148. doi: 10.1016/j.reactfunctpolym.2020.104490.

B. V. Krishna, S. Bose, and A. Bandyopadhyay. Low stiffness porous ti structures for load-bearing implants. *Acta Biomater*, 3(6):997–1006, 2007. ISSN 1742-7061 (Print) 1742-7061 (Linking). doi: 10.1016/j.actbio.2007.03.008. URL https://www.ncbi.nlm.nih.gov/pubmed/17532277.

Helena N Chia and Benjamin M Wu. Recent advances in 3D printing of biomaterials. *Journal of Biological Engineering*, 9, March 2015. ISSN 1754-1611. doi: 10.1186/s13036-015-0001-4.

William K. Durfee and Paul A. Iaizzo. Chapter 21 - Medical Applications of 3D Printing. In Paul A. Iaizzo, editor, *Engineering in Medicine*, pages 527–543. Academic Press, January 2019. ISBN 978-0-12-813068-1. doi: 10.1016/B978-0-12-813068-1.00021-X.

Syed A. M. Tofail, Elias P. Koumoulos, Amit Bandyopadhyay, Susmita Bose, Lisa O'Donoghue, and Costas Charitidis. Additive manufacturing: scientific and technological challenges, market uptake and opportunities. *Materials Today*, 21(1):22–37, 2018. ISSN 13697021. doi: 10.1016/j.mattod.2017.07.001.

D. A. Zopf, S. J. Hollister, M. E. Nelson, R. G. Ohye, and G. E. Green. Bioresorbable airway splint created with a three-dimensional printer. *N Engl J Med*, 368(21):2043–5, 2013. ISSN 1533-4406 (Electronic) 0028-4793 (Linking). doi: 10.1056/NEJMc1301237. URL https://www.ncbi.nlm.nih.gov/pubmed/23697529.

Connected at the heart | MHealth.org. https://www.mhealth.org/blog/2017/july-2017/conjoined-twins-separated-at-university-of-minnesota-masonic-childrens-hospital, 2017.

Y. He, G. H. Xue, and J. Z. Fu. Fabrication of low cost soft tissue prostheses with the desktop 3d printer. *Sci Rep*, 4:6973, 2014. ISSN 2045-2322 (Electronic) 2045-2322 (Linking). doi: 10.1038/srep06973. URL https://www.ncbi.nlm.nih.gov/pubmed/25427880.

S. V. Murphy and A. Atala. 3d bioprinting of tissues and organs. *Nat Biotechnol*, 32 (8):773–85, 2014. ISSN 1546-1696 (Electronic) 1087-0156 (Linking). doi: 10.1038/nbt.2958. URL https://www.ncbi.nlm.nih.gov/pubmed/25093879.

Susmita Bose, Sahar Vahabzadeh, and Amit Bandyopadhyay. Bone tissue engineering using 3d printing. *Materials Today*, 16(12):496–504, 2013. ISSN 13697021. doi: 10.1016/j.mattod.2013.11.017.

J. A. Inzana, D. Olvera, S. M. Fuller, J. P. Kelly, O. A. Graeve, E. M. Schwarz, S. L. Kates, and H. A. Awad. 3d printing of composite calcium phosphate and collagen scaffolds for bone regeneration. *Biomaterials*, 35(13):4026–34, 2014. ISSN 1878-5905 (Electronic) 0142-9612 (Linking). doi: 10.1016/j.biomaterials.2014.01.064. URL https://www.ncbi.nlm.nih.gov/pubmed/24529628.

M. S. Mannoor, Z. Jiang, T. James, Y. L. Kong, K. A. Malatesta, W. O. Soboyejo, N. Verma, D. H. Gracias, and M. C. McAlpine. 3d printed bionic ears. *Nano Lett*, 13(6):2634–9, 2013. ISSN 1530-6992 (Electronic) 1530-6984 (Linking). doi: 10.1021/nl4007744. URL https://www.ncbi.nlm.nih.gov/pubmed/23635097.

J. S. Miller, K. R. Stevens, M. T. Yang, B. M. Baker, D. H. Nguyen, D. M. Cohen, E. Toro, A. A. Chen, P. A. Galie, X. Yu, R. Chaturvedi, S. N. Bhatia, and C. S. Chen. Rapid casting of patterned vascular networks for perfusable engineered three-dimensional tissues. *Nat Mater*, 11(9):768–74, 2012. ISSN 1476-1122 (Print) 1476-1122 (Linking). doi: 10.1038/nmat3357. URL https://www.ncbi.nlm.nih.gov/pubmed/22751181.

Nadav Noor, Assaf Shapira, Reuven Edri, Idan Gal, Lior Wertheim, and Tal Dvir. 3D Printing of Personalized Thick and Perfusable Cardiac Patches and Hearts. *Advanced Science*, 6(11):1900344, 2019. ISSN 2198-3844. doi: 10.1002/advs.201900344. _eprint: https://onlinelibrary.wiley.com/doi/pdf/10.1002/advs.201900344.

A. Butscher, M. Bohner, S. Hofmann, L. Gauckler, and R. Müller. Structural and material approaches to bone tissue engineering in powder-based three-dimensional printing. *Acta Biomaterialia*, 7(3):907–920, March 2011. ISSN 1742-7061. doi: 10.1016/j.actbio.2010.09.039.

Garrett E. Ryan, Abhay S. Pandit, and Dimitrios P. Apatsidis. Porous titanium scaffolds fabricated using a rapid prototyping and powder metallurgy technique. *Biomaterials*, 29(27):3625–3635, September 2008. ISSN 0142-9612. doi: 10.1016/j.biomaterials.2008.05.032.

An Liu, Guang-huai Xue, Miao Sun, Hui-feng Shao, Chi-yuan Ma, Qing Gao, Zhong-ru Gou, Shi-gui Yan, Yan-ming Liu, and Yong He. 3d printing surgical implants at the clinic: A experimental study on anterior cruciate ligament reconstruction. *Scientific Reports*, 6:21704, 2016. doi: 10.1038/srep21704. URL https://doi.org/10.1038/srep21704.

Fumio Watari, Atsuro Yokoyama, Fuminori Saso, Motohiro Uo, and Takao Kawasaki. Fabrication and properties of functionally graded dental implant. *Composites Part B: Engineering*, 28(1):5–11, January 1997. ISSN 1359-8368. doi: 10.1016/S1359-8368(96)00021-2.

Dalia Mahmoud and Mohamed Elbestawi. *Lattice Structures and Functionally Graded Materials Applications in Additive Manufacturing of Orthopedic Implants: A Review*, volume 1. Journal of Manufacturing and Materials Processing, 2017. doi: 10.3390/jmmp1020013.

Alice Melocchi, Federico Parietti, Alessandra Maroni, Anastasia Foppoli, Andrea Gazzaniga, and Lucia Zema. Hot-melt extruded filaments based on pharmaceutical grade

polymers for 3d printing by fused deposition modeling. *International Journal of Pharmaceutics*, 509(1):255–263, 2016. ISSN 0378-5173. doi: https://doi.org/10.1016/j.ijpharm.2016.05.036. URL http://www.sciencedirect.com/science/article/pii/S0378517316304161.

J. Zhang, X. Feng, H. Patil, R. V. Tiwari, and M. A. Repka. Coupling 3d printing with hot-melt extrusion to produce controlled-release tablets. *Int J Pharm*, 519(1-2): 186–197, 2017. ISSN 0378-5173. doi: 10.1016/j.ijpharm.2016.12.049.

Nayan G. Solanki, Md Tahsin, Ankita V. Shah, and Abu T. M. Serajuddin. Formulation of 3d printed tablet for rapid drug release by fused deposition modeling: Screening polymers for drug release, drug-polymer miscibility and printability. *Journal of Pharmaceutical Sciences*, 107(1):390–401, 2018. ISSN 0022-3549. doi: https://doi.org/10.1016/j.xphs.2017.10.021. URL http://www.sciencedirect.com/science/article/pii/S0022354917307190.

Ultimaker. Ultimaker: 3D printers. https://ultimaker.com/en, 2011. Accessed: 23-02-2017.

MATLAB. *version 9.0.0 (R2016a)*. The MathWorks Inc., Natick, Massachusetts, 2016.

Photoshop. *https://www.adobe.com/uk/products/photoshop.html*. Adobe, Seattle, Washington, 2019.

Marcin P. Serdeczny, Raphaël Comminal, David B. Pedersen, and Jon Spangenberg. Experimental validation of a numerical model for the strand shape in material extrusion additive manufacturing. *Additive Manufacturing*, 24:145 – 153, 2018. ISSN 2214-8604. doi: https://doi.org/10.1016/j.addma.2018.09.022. URL http://www.sciencedirect.com/science/article/pii/S2214860418304585.

S. Berariu. Manufacture and structural characterisation of 3D printed materials, 2016. Undergraduate project.

C.M. Wang, C.Y. Wang, and J.N. Reddy. *Exact solutions for buckling of structural members*. CRC Press, Boca Raton, Florida, 2005. ISBN 0-8493-2222-7. URL www.crcpress.com.

G.M. Murphy. *Ordinary Differential Equations and their Solutions*. Van Nostrand, 1960. URL https://books.google.co.uk/books?id=TJE-AAAAIAAJ.

WebPlotDigitizer. WebPlotDigitizer - Extraxct data from plots, images, and maps. https://automeris.io/WebPlotDigitizer/, 2010. Accessed: 21-11-2017.

G. R. Cowper. The Shear Coefficient in Timoshenko's Beam Theory. *Journal of Applied Mechanics*, 33(2):335–340, 06 1966. ISSN 0021-8936. doi: 10.1115/1.3625046. URL https://doi.org/10.1115/1.3625046.

Majid Jamshidian, Elmira Arab Tehrany, Muhammad Imran, Muriel Jacquot, and Stéphane Desobry. Poly-Lactic Acid: Production, Applications, Nanocomposites, and Release Studies. *Comprehensive Reviews in Food Science and Food Safety*, 9 (5):552–571, 2010. ISSN 1541-4337. doi: 10.1111/j.1541-4337.2010.00126.x. _eprint: https://onlinelibrary.wiley.com/doi/pdf/10.1111/j.1541-4337.2010.00126.x.

Prusa Research. Prusa3D - Open-Source 3D printers by Joseph Prusa. https://www.prusa3d.com, 2020. Accessed: 12-03-2020.

Michael A Sutton, Jean Jose Orteu, and Hubert Schreier. *Image correlation for shape, motion and deformation measurements: basic concepts, theory and applications*. Springer Science & Business Media, 2009.

Bing Pan. Digital image correlation for surface deformation measurement: Historical developments, recent advances and future goals. *Measurement Science and Technology*, 29(8):082001, June 2018. ISSN 0957-0233. doi: 10.1088/1361-6501/aac55b.

F. Hild and S. Roux. Digital Image Correlation: From Displacement Measurement to Identification of Elastic Properties – a Review. *Strain*, 42(2):69–80, 2006. ISSN 1475-1305. doi: 10.1111/j.1475-1305.2006.00258.x. _eprint: https://onlinelibrary.wiley.com/doi/pdf/10.1111/j.1475-1305.2006.00258.x.

F. A. Díaz, J. M. Vasco-Olmo, E. López-Alba, L. Felipe-Sesé, A. J. Molina-Viedma, and D. Nowell. Experimental evaluation of effective stress intensity factor using thermoelastic stress analysis and digital image correlation. *International Journal of Fatigue*, 135:105567, June 2020. ISSN 0142-1123. doi: 10.1016/j.ijfatigue.2020.105567.

Abaqus/CAE. *version 6.14-3*. Dassault Systèmes, Providence, RI, USA, 2014. URL https://www.3ds.com/products-services/simulia/products/abaqus/. Accessed: 14-03-2020.